NUMERICAL INVESTIGATION OF THE BEHAVIOUR OF CIRCULAR SYNTHETIC JETS FOR EFFECTIVE FLOW SEPARATION CONTROL

A thesis submitted to the University of Manchester for the degree of Doctor of Philosophy in the Faculty of Engineering and Physical Sciences

2010

Jue Zhou

School of Mechanical, Aerospace and Civil Engineering

Contents

Final word count: 76,924

List of Figures

List of Tables

Nomenclature

A_o	Orifice cross-sectional area
C_f	Non-dimensional shear stress
c_f	Skin friction coefficient (= $\tau_w/0.5\rho U_\infty^2$)
$C_{L\max}$	Maximum lift coefficient
C_μ	Jet momentum coefficient (= $2(h/c)(U_o/U_\infty)^2$)
d	Ratio of boundary layer thickness to orifice diameter (= δ/D_o) (Chapter 2, 5-8); Width of slot (Chapter 2)
D_c	Cavity diameter
D_o	Orifice diameter
f	Diaphragm oscillation frequency
F^+	Non-dimensional forcing frequency (= fx_{ref}/U_{ref})
h	Orifice depth
H	Cavity height
I_o	Jet impulse
L	Dimensionless stroke length ($L = L_o/D_o$)
L_o	Stroke length, $L_o = \overline{U}_o T$
M	Mach number
p	Pressure
P	Velocity program factor
r	Radius of diaphragm, cavity or orifice
r_c	Radius of diaphragm
Re	Reynolds number
Re_I	Reynolds number (= $I_o/\mu A_o$)
Re_L	Reynolds number (= $\overline{U}_o L_o/\nu$)
Re_U	Reynolds number (=$\overline{U}_o D_o/\nu$)
Re_{Upeak}	Reynolds number (=$U_{peak} D_o/\nu$)
Re_Γ	Reynolds number (= Γ/ν)
S	Stokes number (= $\sqrt{2\pi f D_o^2/\nu}$) (Chapter 2, 4); point of separation (Chapter 2); symmetric component of the velocity gradient tensor (Chapter 3, 5-8)

S_b	Jet spreading rate
Str	Strouhal number (= $fD_o/\overline{U}_o$ in quiescent condition, = fD_o/U_∞ or = $f\delta/U_\infty$ in cross flows)
t	Time
T	Period of diaphragm oscillation cycle
u	Velocity
u_o	Instantaneous jet velocity
$\widetilde{u}_o$	Instantaneous space-averaged jet velocity
U_o	Space-averaged jet velocity
$\overline{U}_o$	Time-averaged jet blowing velocity over the entire cycle
U_{peak}	Peak jet velocity
U_∞	Freestream velocity
VR	Velocity ratio (=$\overline{U}_o/U_\infty$ or = U_{peak}/U_∞)
υ	Velocity
w	Orifice depth
x	Streamwise distance from orifice exit
y	Normal distance from orifice exit
z	Spanwise distance from orifice exit

Greek Symbols

α	angle of attack
Γ	Vortex circulation
Γ_o	Initial (or total) circulation
δ	Boundary layer thickness
Δ	Peak-to-peak displacement at diaphragm centre
μ	Molecular dynamic viscosity
ν	Molecular kinematic viscosity
ρ	Density
τ_w	Wall shear stress
ω	Vorticity
Ω	Vorticity

Subscripts

c	Cavity value
o	Orifice value
w	Wall value
x	Value in *x* direction
ref	Reference value

Abstract

Abstract of thesis entitled “Numerical Investigation of the Behaviour of Circular Synthetic Jets for Effective Flow Separation Control” submitted to the University of Manchester for the degree of Doctor of Philosophy by Jue Zhou in 2010.

The stringing regulation on greenhouse gases emissions coupled with the rising fuel price and the growth in aviation transportation have imposed increasing demands on the aircraft industry to develop revolutionary technologies to meet such challenges. Methods of delaying flow separation on aircraft high lift systems have been sought which can lead to an increase in the aircraft performance and ultimately a reduction in aircraft operational costs and its impact on the environment.

Synthetic jet actuators are a promising method of delivering flow control for aircraft applications due to their ability to inject momentum to an external flow without net mass flux and their potential in being integrated in MEMS through micro-fabrication with relative ease. It has been demonstrated in many laboratory experiments that synthetic jets are capable of delaying flow separation on aerodynamic bodies of various shapes. However, currently the operating conditions of synthetic jets are mostly chosen by trial-and-error, and thus the flow control effectiveness varies from one experiment to another. In order to deliver an effective flow separation control which achieves a desired control effect at minimum energy expenditure, a better understanding of the fluid mechanics of the behaviour of synthetic jets and the interaction between synthetic jets and a boundary layer are required. The aims of the present research were to achieve such a goal through a series of purposely designed numerical simulations.

Firstly, synthetic jets issued from a circular orifice into quiescent air were studied to understand the effect of dimensionless parameters on the formation and the extent of roll-up of vortex rings. The computational results confirmed that the Stokes number determines the strength of vortex roll-up of a synthetic jet. Based on the computational results, a parameter map was produced in which three different operational regimes of synthetic jets were indentified and a criterion for vortex roll-up was also established.

A circular synthetic jet issued into a zero-pressure-gradient laminar boundary layer was then investigated. The capability of FLUENT in modelling the key characteristics of synthetic jets was validated using experimental data. The formation and evolution of coherent structures produced by the interaction between synthetic jets and a boundary layer, as well as their near-wall effect in terms of the wall shear stress, were examined. A parameter map illustrating how the appearance of the vortical structures and their corresponding shear stress patterns vary as the synthetic jet operating condition changes was established. In addition, the increase in the wall shear stress relative to the jet-off case was calculated to evaluate their potential separation control effect.

Finally, the study moved one step forward to investigate the flow separation control effect of an array of three circular synthetic jets issued into a laminar boundary layer which separates downstream on an inclined plate. The impact of synthetic jets on the boundary layer prior to separation and the extent of flow separation delay on the flap, at a range of synthetic jet operating conditions, were examined and the correlation between them was investigated. Furthermore, the optimal operating conditions for this synthetic jet array in the current study were identified by considering both the flow control effect and the actuator power consumption. The characteristics of the corresponding vortical structures were also examined.

The findings from this work have produced some further insights of the behaviour and the interaction between synthetic jets and a boundary layer, which will be useful for ensuring an effective application of synthetic jets in practical settings.

Declaration

No portion of the work referred to in this thesis has been submitted in support of an application for another degree or qualification of this or any other university or other institute of learning.

Copyright

Acknowledgements

I would first like to thank my supervisor, Dr Shan Zhong, for her invaluable guidance and continual support throughout my project, and for the great deal of time she spent with me getting the work to the stage it is now.

I would also like to acknowledge the financial support from both The University of Manchester and Universities UK. The latter provided the Overseas Research Student Award Scheme (ORS) for my PhD research.

Thanks are also due to my colleagues Dr Mark Jabbal, Dr Shanying Zhang, Mr Fushui Guo and Dr Hui Tang for their valuable help, support and encouragement.

And last, but by no means least, I am eternally grateful to my parents and my husband, for their constant support throughout my PhD study, particularly during the writing of this thesis.

Chapter 1 Introduction

1.1 The Need for Flow Separation Control

The aviation industry, after decades of growth and development, faces a series of challenges today. At the forefront of the issues are the threat of climate change and the role of aviation in producing emissions of greenhouse gases (Lawrence, 2009). Coupled with the increase in fuel price and the growth in aviation traffic, all parties in the aviation have been seeking greener, cleaner, quieter and more efficient aircraft, in order to minimize the operational costs and to achieve the goal set by the European (ACARE) Vision for 2020 which calls for a 50% reduction in CO_2 emissions, 80% in NO_x emissions and 50% of the perceived noise.

Revolutionary technologies are being developed and implemented on aircraft which are aimed at increasing the operational efficiency of aircraft and reducing the impact on the environment. Amongst these new technologies, flow control has received a great deal of attention.

Flow control has been a research topic for a few decades, and the potential benefits that flow control promises are the reason why it is still pursued today. The term of "flow control" may be described as "… any mechanism or process through which the boundary layer of a fluid flow is caused to behave differently than it normally would were the flow developing along a smooth straight surface" (Gad-el-Hak, 2000). The intent of flow control may be to delay/advance transition, to suppress/enhance turbulence, or to prevent/promote separation. Therefore, its resultant benefits include drag reduction, lift enhancement, mixing augmentation, heat transfer enhancement and flow-induced noise suppression. For flow control implemented on an aircraft, the aerodynamic drag will be reduced, the lift will be increased and the system performance will be improved, resulting in the reduction of fuel consumption, and consequently carbon emissions. Reneaux (2004) suggested that a 1% reduction in drag can lead to a 0.2% reduction in the direct operational costs of a large transport aircraft, which corresponds to other trades-offs like 1.6 tons on the operating empty weight or 10 passengers.

For a commercial aircraft, the multi-element high-lift system has a significant impact on the cost of a typical jet transport, which accounts for somewhere between

6% and 11% of the production cost of a typical jet transport (Rudolph, 1996). It normally consists of a main wing and its leading edge (slat) and trailing edge (flap) devices, allowing a single wing to operate and fulfil the demands of three different flight regimes, i.e. take-off, cruise and landing. Flow control can be applied to an aircraft wing in different manners, as shown in Fig. 1.1: (a) To reduce pressure drag during the take-off and landing phases, separation control technologies would be applied to the leading and trailing edges of the wing; (b) To reduce skin friction drag during cruise flight, laminar, transition and turbulence flow control technologies would be utilized on the main wing element; (c) To reduce wave drag encountered at high Mach numbers during cruise flight, shock control technologies would be utilized. The use of flow control on the multi-element high-lift system can reduce the size and increase the deflection angle of the leading and trailing devices as a result of an enhanced performance (i.e. increase in $C_{L\max}$), which would lead to a saving on weight and a reduction on system complexity (Lin et al, 1994; Harrison, 2006). The improvement in system performance and the decrease in system weight can be translated into a reduction in fuel consumption and pollutant emissions. In the present work, the research interest on flow control is flow separation control, aimed to delay the flow separation using synthetic jet actuators.

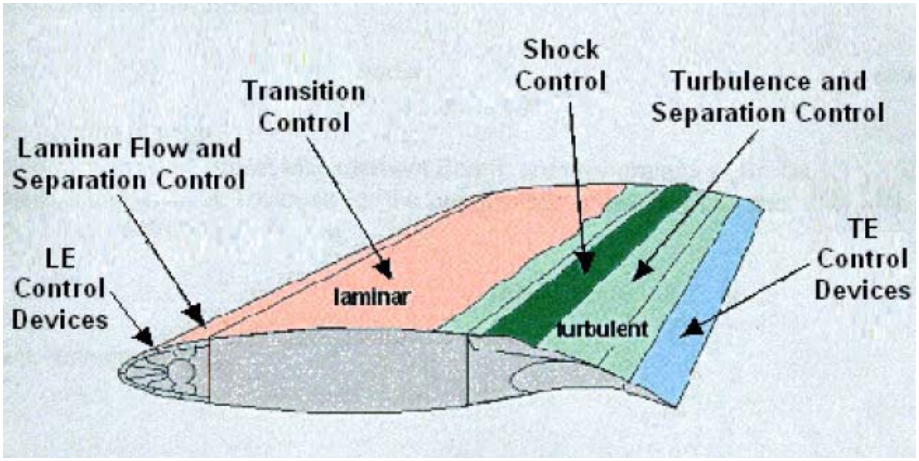

Figure 1.1. Schematic of flow control technologies for aircraft wing application (modified from Sellars, 2003).

Flow control technologies can be classified into passive and active flow control. A classic example of passive flow control is vane vortex generators, which have been routinely used on civil transport aircraft due to their easy implementation.

However, the parasitic drag is produced during cruise flight, and their effectiveness is also limited within a small operational range.

In contrast, active flow control, such as the use of blowing, suction or periodic excitation through slots or orifices on the surface of an aerodynamic body, can be operated "on demand", and therefore the parasitic drag can be avoid when they are not required. Experiments by Prandtl (1904) first demonstrated that suction is an effective method of delaying separation. However, it requires a complex internal piping system, which brings a large weight penalty, and therefore its operational gain is limited. Similarly, blowing via array of steady jets is proved to be effective in preventing or eliminating flow separation. Through injecting high momentum fluid into the boundary layer, the near-wall momentum is enhanced, and thus the boundary layer is more resistant to separation (Schlichting and Gersten, 2000). However, it has a similar problem of suction, that is, compressed air supply and ducting are required which counteract the potential benefits.

In comparison to blowing/suction, periodic excitation is a relatively new method in flow control and has received much attention due to its inherent advantage (Greenblatt and Wygnanski, 2000). By periodically exciting a flow via slots or orifices at adequate actuation frequencies, large scale, phase-locked coherent structures are generated and transport momentum across the boundary layer, which could make the separated flow reattached. It is capable to deliver a similar level of control effect of steady blowing/suction, with a reduced net mass flux. The use of pulsed jets is a good example of periodic excitation (Seifert et al, 1993; Magill and McManus, 2001). Although pulsed jets are proved to be more effective in flow control, they still need a complex air supply system.

1.2 Synthetic Jets

Synthetic jets, as a novel method of periodical excitation without the need for an air supply, have received much more attention since the mid 1990s. A typical synthetic jet actuator (SJA) is shown in Fig. 1.2. It consists of a small cavity with an oscillating diaphragm at the bottom side, and an orifice plate at the opposite side. The volume of the cavity is changed with the vibration of diaphragm. When the diaphragm moves away from the orifice (suction stroke), ambient fluid is entrained

into the cavity and the cavity volume increases. When the diaphragm moves towards the orifice (blowing stroke), the cavity volume is decreased and the fluid in the cavity is expelled, which would form a shear layer along the wall of orifice and subsequently a roll-up of vortex ring at the orifice exit. The alternating blowing and suction produced by the oscillating of diaphragm generate a succession of vortices propagating away from the orifice, and a jet is hence "synthesised".

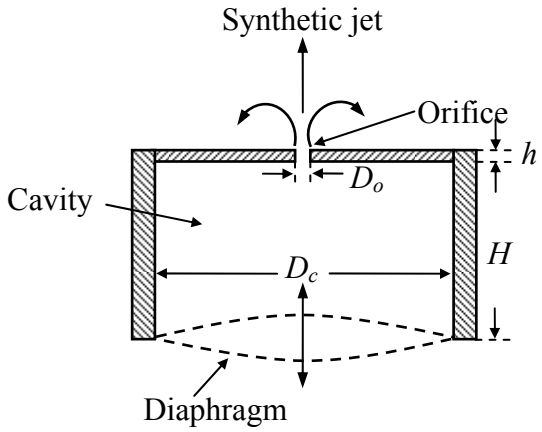

Figure 1.2. Schematic of synthetic jet actuator.

When the SJA is fixed beneath the boundary layer, the vortical structures produced by the periodic excitation would transport momentum within the boundary layer and increase the mixing between the outer and inner regions of the boundary layer. Therefore, the near-wall region is energised and the boundary layer separation is delayed.

The capacity of synthetic jets in delaying or controlling flow separation has been proved by many laboratory-based investigations on aerodynamic bodies such as 2D circular cylinders (Amitay et al, 1997; Rediniotis, 1999; Wood et al, 2000) and aerofoil models (Amitay et al, 1998, 1999, 2001; Smith et al, 1998). In these experiments, the separation line was observed to be pushed downstream significantly and for some aerofoil models, the flow was fully attached under the action of synthetic jets. Therefore, SJAs are promising to be applied to the leading and trailing edges of high-lift system to control flow separation at take-off and landing conditions. Furthermore, SJAs due to their unique advantage also have the potential for Micro-Electro-Mechanical Systems (MEMS) which is required for aircraft implementation.

Although many investigations demonstrated the capacity of synthetic jets in flow separation control and their advantages compared to their counterpart, such as pulsed jets and steady jets, to the knowledge of the author, many of them were undertaken by setting the actuator operating conditions by trial-and-error, and hence the effect of flow control was different from one case to another. This is due to the insufficient understanding of the physical process of the interaction between the synthetic jets and the boundary layer, as well as their induced vortical structures. Therefore, it is required to set up a methodology to find the optimal operating conditions of synthetic jets with the highest effectiveness and the lowest power consumption, by achieving an improved understanding of the nature of synthetic jets and their near wall effects.

Extensive studies aimed at understanding the fluid mechanics of synthetic jets have been undertaken at the University of Manchester since 1998. Crook and Wood (1999, 2000, 2001) successfully applied an array of synthetic jets to a circular cylinder to delay the separation of a turbulent boundary layer. Subsequently, an improved understanding was achieved by investigating the structures of a synthetic jet in quiescent conditions (Tang and Zhong, 2005a, b; Jabbal et al, 2006) as well as the behaviour of synthetic jets issued into a uniform cross flow (Garcillan et al, 2005, 2006) and a boundary layer (Zhong et al, 2005). Three different vortical structures have been identified, and their evolution and characteristics were analysed qualitatively and quantitatively (Jabbal and Zhong, 2008).

However, for synthetic jets in quiescent conditions, the understanding of the formation of vortex rings produced by synthetic jets is not satisfied. And for synthetic jets in an attached boundary layer, the nature of vortical structures produced by synthetic jets, and their impact on the boundary layer in terms of the increase in wall shear stress are still not well understood. Furthermore, for synthetic jet array issued into a separated boundary layer, their effectiveness in delaying flow separation under a range of operating conditions still needs to be indentified, in order to find the optimal operating conditions with high efficiency and effectiveness, which could be chosen for flow control at full-scale flight conditions.

Numerical simulations of synthetic jets have accompanied the experimental work to any significant degree in recent years. It is undoubted that the future of synthetic jets, especially in terms of design and optimization, lies in a research effort that combines both experimental and numerical techniques. The work presented in

this thesis uses Computational Fluid Dynamics (CFD) modelling to simulate the synthetic jets issued into quiescent conditions, a zero-pressure-gradient laminar boundary layer, and a laminar boundary layer which separates downstream on an inclined plate, aimed at gaining a further understanding in the aforementioned areas where no known research has been published.

1.3 Aims and Objectives

The aims of the present research are to achieve an improved understanding of the parameters that affect the formation of vortex rings produced by synthetic jets in quiescent conditions towards developing a vortex roll-up criterion for synthetic jets, and the behaviour of synthetic jets issued into an attached laminar boundary layer and a separated laminar boundary layer in relation to the evolution of vortical structures, their impact on the boundary layer, and the flow control effect, such that the optimal operating conditions which produce the desired vortical structures with the highest flow control effectiveness and lowest power consumption for flow separation control can be identified.

To achieve above aims, numerical simulations were carried out in a complementary manner in parallel with the ongoing experiments at the University of Manchester. The capacity of FLUENT, a commercial CFD package, in modelling a single synthetic jet issued into a zero-pressure-gradient laminar boundary layer, and an array of synthetic jets issued into a laminar boundary layer which separates downstream on an inclined plate, has been validated by the existing experimental data, respectively. On the other hand, the three-dimensional computational results can provide a further insight into the synthetic jets, which are often not available or hard to obtain from the experiments, such as the three-dimensional hierarchy of coherent structures, and their near wall effect in terms of the wall shear stress. The insight of synthetic jets obtained from the numerical simulations is also helpful to explain the phenomena observed in the experiments. In the present study, synthetic jets issued into a laminar boundary layer were chosen in the experiments. Correspondingly, laminar model was employed in the numerical simulation to match the setting of experiments. The use of laminar boundary layer provides a fundamental and first logical step towards understanding the interaction between

synthetic jets and a turbulent boundary layer. In addition, it is believed that there are some commonalities of interaction mechanisms between synthetic jets and a boundary layer irrespective if it is laminar or turbulent.

A series of objectives are specified as follows:

- To investigate the effect of dimensionless parameters on the formation and strength of vortex rings produced by synthetic jets, and to establish a parameter map classifying the different regimes of synthetic jets.
- To study the nature of vortical structures produced by the interaction of a single synthetic jet with an attached laminar boundary layer and their near-wall effects, and to establish a parameter space identifying different types of vortical structures and surface shear stress patterns.
- To investigate the nature of vortical structures produced by an array of synthetic jets in a separated laminar boundary layer, the surface shear stress patterns prior to separation, and the relation between the impact of the vortical structures on the boundary layer prior to separation and the separation delay on the inclined plate.
- To establish a series of parameter maps identifying the transition of vortical structures and surface shear stress patterns on the upstream flat plate, the gain of surface shear stress, the flow control effect and the power consumption of the synthetic jet array, to identify the optimal operating conditions of this synthetic jet array which yield the best flow separation delay, and to examine the characteristics of the associated vortical structures and their near-wall effect.

1.4 Outline of the Thesis

This thesis is presented in the alternative format with its core context provided in the form of published/submitted research papers.

Chapter 2 provides a review of the literature relevant to this project, including flow separation control and the technologies applied for flow separation control, especially the published work on synthetic jet actuators.

Chapter 3 summarizes the papers included in this thesis, and explains the role of each paper and the rationale among these papers.

The following five chapters, Chapter 4 to Chapter 8, include five published or submitted papers that report the candidate's own work.

Finally, Chapter 9 provides the conclusions of this thesis and suggestions for future work.

Chapter 2 Literature Review

This chapter is aimed to provide a comprehensive review of the investigations related to synthetic jets in the context of flow separation control and to identify the areas where further research is required.

The review outlines the phenomenon of flow separation, the concept and means of flow separation control, the behaviour of synthetic jets in both quiescent conditions and cross flow, as well as the CFD techniques in modelling the synthetic jets.

2.1 Flow Separation

2.1.1 Flow Separation

Flow separation is a common phenomenon for most fluid flows. When a solid object is placed in a fluid flow, a boundary layer will form along the object surface due to the viscosity of fluid. In the boundary layer, the velocity of the fluid increases from zero at the wall to its full value corresponding to the external frictionless flow. In some cases, the decelerated fluid particles cannot remain moving along the whole length of the wall, due to the insufficient momentum for them to continue their motion. Thus the near-wall fluid particles will be brought to rest at the separation point (line). And further downstream, the fluid in the boundary layer will become reversed as a result of the action of adverse pressure gradient.

Prandtl (1904) was the first to explain the physical cause of separation at high Reynolds numbers as being associated with the separation of boundary layers that must form on all solid surfaces. In his milestone presentation, Prandtl introduced the boundary layer theory, explained the mechanics of steady separation, and described several experiments in which the boundary layer was controlled.

Figure 2.1 shows the separation of the boundary layer schematically. It can be seen that with the development of the boundary layer, the velocity profile becomes less full, and the velocity gradient at the wall becomes smaller gradually. There exists a separation point at which $\left(\partial u/\partial y\right)_{y=0}=0$. Before this point, the velocity gradient at the wall is positive, while after this point, it is negative.

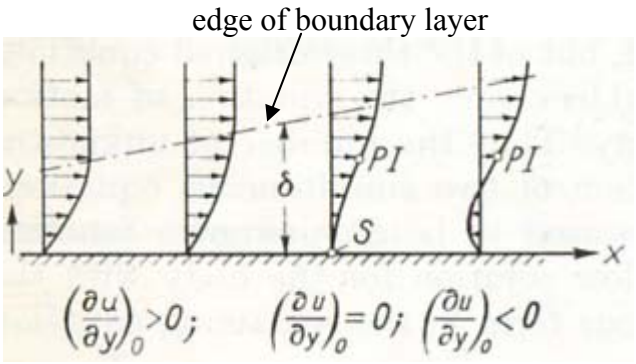

Figure 2.1. Schematic of separation of the boundary layer (S = point of separation; PI = point of inflexion) (Schlichting, 1979).

Prandtl (1904) suggested that the boundary layer separation was intimately connected with the pressure distribution along the wall. If the pressure gradient is favourable (accelerated flow, $dp/dx < 0$), the boundary layer remains attached to the wall. Whereas if the pressure gradient is adverse (decelerated flow, $dp/dx > 0$), the boundary layer tends to separate from the body surface. This is because the velocity in the boundary layer decreases towards the wall, and thus the kinetic energy of the fluid particles in the inner part of the boundary layer is smaller than that at the outer edge of the boundary layer. The closer to the wall, the smaller it is. Hence even a small increase of pressure may cause the fluid particles in the near-wall region to stop and move in the opposite direction of the main flow which forms a recirculation region. This recirculation region can be considered as a characteristic of separated flows.

The fact that separation in steady flow occurs in decelerated flow can be easily inferred from the relationship between the pressure gradient dp/dx and the velocity distribution $u(y)$ with the help of the boundary layer equations (Schlichting, 1979). In the case of steady flow, the boundary layer equations simplify to

$$\frac{\partial u}{\partial x} + \frac{\partial \upsilon}{\partial y} = 0 \tag{2.1}$$

$$u\frac{\partial u}{\partial x} + \upsilon\frac{\partial u}{\partial y} = -\frac{1}{\rho}\frac{dp}{dx} + \nu\frac{\partial^2 u}{\partial y^2} \tag{2.2}$$

with the boundary conditions $y = 0$: $u = 0$, $\upsilon = 0$; $y = \infty$: $u = U(x)$.

Equation 2.2 with the boundary conditions $y = 0$: $u = 0$, $\upsilon = 0$ can be written as

$$\mu\left(\frac{\partial^2 u}{\partial y^2}\right)_{y=0} = \frac{dp}{dx} \tag{2.3}$$

Therefore, the velocity distribution in the boundary layer with pressure decrease or increase can be illustrated as shown in Fig. 2.2. For the accelerated flow, $dp/dx < 0$, and therefore $(\partial^2 u/\partial y^2)_{wall} < 0$ over the whole thickness of the boundary layer. On the other hand, for the decelerated flow $dp/dx > 0$, it is obtained that $(\partial^2 u/\partial y^2)_{wall} > 0$. However, in any case $\partial^2 u/\partial y^2 < 0$ at a large distance from the wall, so there must be a point where $\partial^2 u/\partial y^2 = 0$, and thus the velocity profile in the boundary layer displays a point of inflexion.

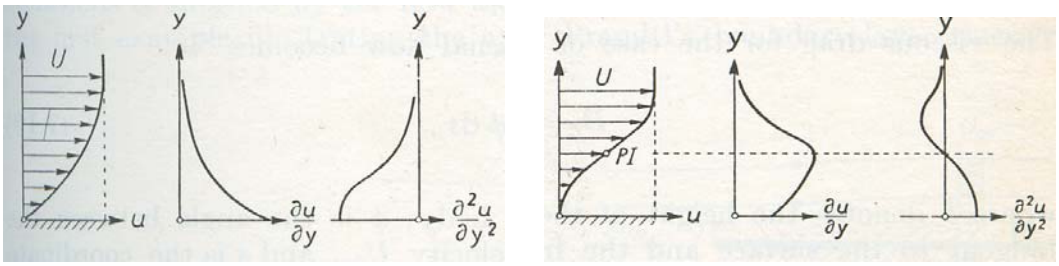

Figure 2.2. Velocity distribution in a boundary layer with (a) pressure decrease and (b) pressure increase (PI = point of inflexion) (Schlichting, 1979).

Since the boundary layer separation is associated with the large energy losses, the performance of many devices is limited at the location of separation (Gad-el-Hak, 2000). For an aerodynamic body, flow separation will cause the drag to increase, especially the pressure drag due to the pressure differential between the front and rear surface, and the lift to decrease. Therefore, separation control is of immense importance to the performance of an aerodynamic body, which, unsurprisingly, has received considerable interests for a century among researchers and engineers in trying to delay or eliminate flow separation.

Typical benefits of flow separation control on aircraft include increased $C_{L\max}$ for greater payload, reduced engine power and noise at take off, shorter runways and reduced approach speed (Gad-el-Hak, 2000). Consequently, the performance of aircraft is improved, billions of money in fuel cost is saved and less greenhouse gases are emitted, which will further be helpful to solve the problem of energy crisis, protect the environment and mitigate the global warming.

High-lift system on civil transport aircraft is one area that could benefit significantly from the application of flow separation control. It changes the lift characteristics of an airfoil to achieve a high $C_{L\max}$ during the takeoff and landing phase, and then is retracted into the wing to allow maximum performance of the airfoil during the cruise phase. High-lift systems generally incorporate two types of devices to increase the maximum lift coefficient: trailing edge flaps and leading edge slats, as shown in Fig. 2.3. The flap increases the camber of the wing and therefore increases the wing's lift coefficient. While the slat, a passageway cut through the leading edge of the wing, enables the wing to pass beyond the normal stalling point without stalling (Lombardo, 1993). Hence, higher lift coefficient is obtained at the higher angle of attack. Like other aerofoils, attempting to obtain the greatest possible performance, high-lift systems are quite close to their performance threshold which is limited by the onset of flow separation on their upper surface. Flow separation control on the slat or flap of high-lift systems has an ability to postpone flow separation under more extreme conditions, and therefore, improve their performance. In addition, with flow separation control, the application of simplified slat/flap geometries becomes possible, and thus the performance can be maintained while the system complexity and weight are reduced. In addition to high-lift systems, flow separation control is also beneficial to other flight control surfaces, such as ailerons (Liddle, 2007) and horizontal tailplane incidence control (Liddle and Crowther, 2008).

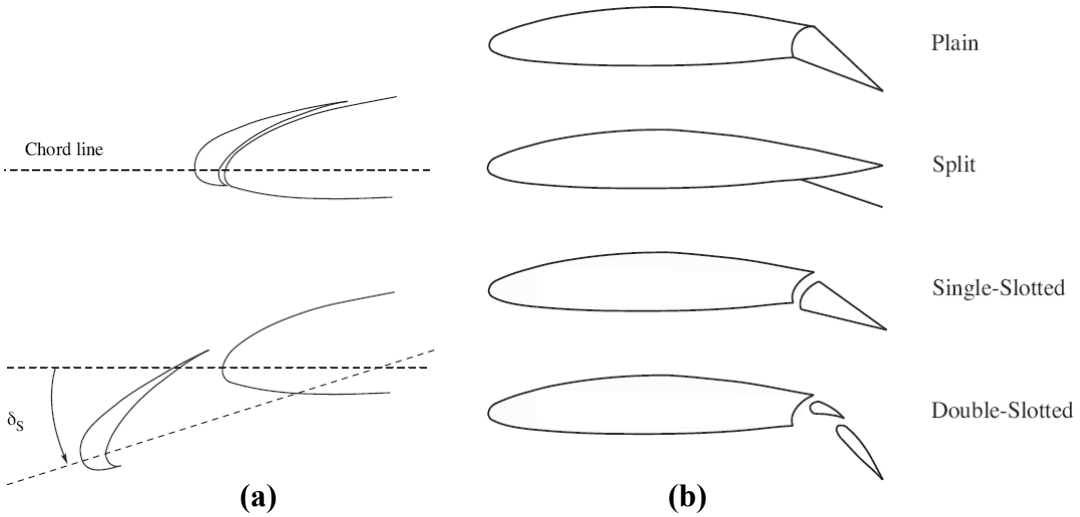

Figure 2.3. Examples of high-lift devices (a) closed and open slat and (b) types of flaps (Hull, 2007).

After understanding the potential of flow control on such industrial devices, it is necessary to build a flow control roadmap to illustrate the physical process involved in attaining an expected flow pattern in a logical manner. Collis et al. (2004) provided a draft of separation delay roadmap which includes a target in terms of flow physics, a mechanism clarifying physical understanding, methods used to achieve the target, and enabling capabilities of each application. Jabbal (2008) refined and enriched this roadmap and presented it in the manner of flow chart as shown in Fig. 2.4.

The delay of (turbulent) boundary layer separation is set as the target because the flow in practical application, i.e. airfoil, is highly turbulent with a Reynolds number having an order of 10^6 to 10^7.

The aforementioned discussion of flow separation indicates that the flow will tend to separate if the near-wall fluid in the boundary layer loses a large amount of kinetic energy which has insufficient momentum to continue its motion, and thus its motion is eventually arrested at the separation point (line). Therefore, in order to delay the boundary layer separation, the mechanism is to increase the streamwise momentum of the near-wall fluid. This is because the increase of near-wall streamwise momentum will increase the near-wall velocity gradient, and consequently the wall shear stress, in terms of the definition of wall shear stress. Hence the mechanism of delaying boundary layer separation is also related to the increase of wall shear stress upstream of the baseline-mean flow separation region.

For the methods to achieve the target of delaying separation, Collis et al. (2004) suggested three existing methods to enhance the near-wall momentum, which are adding high momentum fluid, removing low momentum fluid, and re-distributing momentum across the boundary layer, respectively.

Blowing in the vicinity of the wall is often used to supply the auxiliary power to the surface, whereas suction applied in a region of an adverse pressure gradient can remove the low momentum fluid in the near-wall region. Unlike the former two methods, momentum re-distribution depends on the generation of coherent vorticity which is capable of entraining high momentum fluid from the outer region of the boundary layer into the near-wall region. All the three methods augment the momentum in the near-wall region or enhance the fluid mixing between the inner and outer region of the boundary layer, which make the boundary layer more resistant to separation. This is consistent to the statements by Gad-el-Hak (2000)

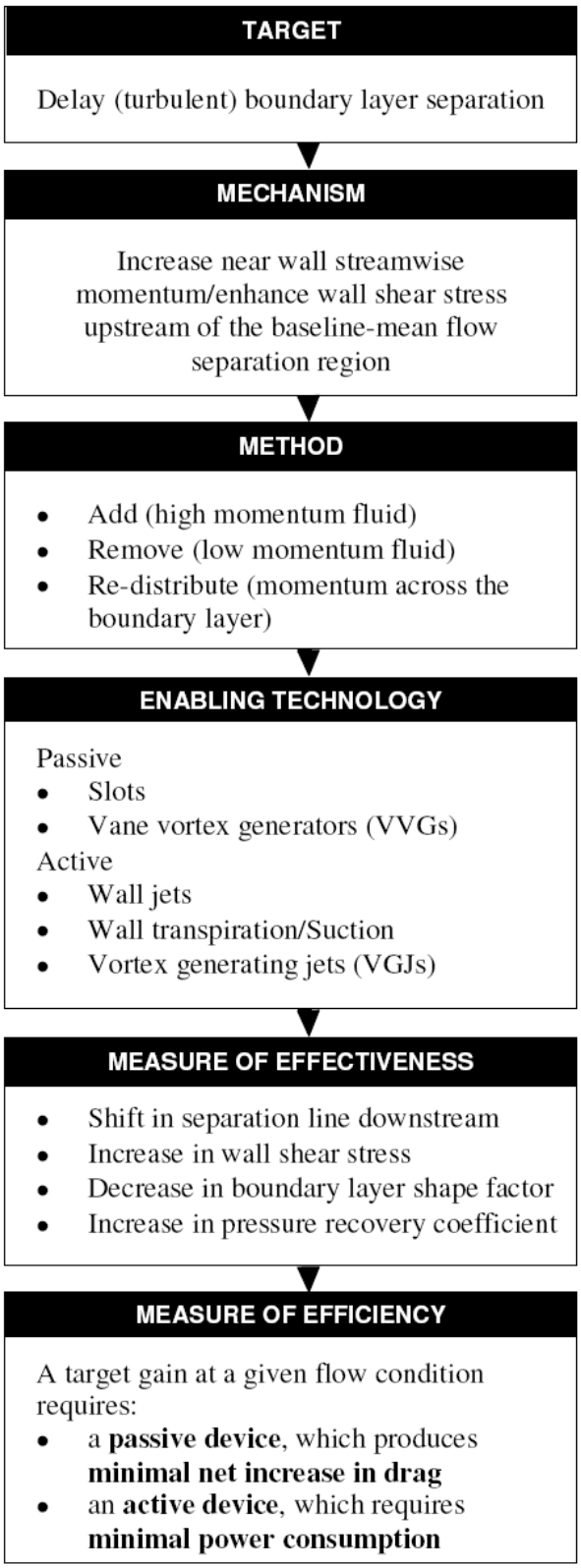

Figure 2.4. Roadmap for flow separation control (Jabbal, 2008).

who suggested that the kernel problem in separation postponement is to add momentum to the very near-wall region of the flow by either transferring momentum

from flow regions further from the wall, or directly adding power drawn from the propulsive system.

To achieve the above control methods, the most studied flow separation control techniques can be classified as active technique, such as tangential blowing and wall jets, and passive technique, such as boundary layer tripping, turbulence enhancement, and vortex generators of various scales. The details of flow control technologies will be introduced in detail in the following section 2.1.2.

Ultimately, the effectiveness of flow control is measured by the extent of performance improvement of a device which will be varied for different research emphases. Nevertheless, some general measures of effectiveness may be considered, such as: (1) Shift in the separation line or a reduction of separation region; (2) Increase in wall shear stress; (3) Decrease in boundary layer shape factor which corresponds to the increase of the fullness of the velocity profile, and therefore implies the enhanced ability of the boundary layer to resist flow separation; (4) Increase in pressure recovery coefficient, thus the boundary layer is capable of withstanding higher adverse pressure gradient (Jabbal, 2008).

Meanwhile, the penalty/input required in flow control process should be considered when seeking a successful and efficient flow control technique. It means that for passive flow control, the device is expected to produce minimal net increase in drag, while for active flow control, the device is required to consume the minimal energy (Jabbal, 2008). Therefore, a desired effective flow control is that the control effectiveness is maximized while the penalty is minimized.

2.1.2 Technologies of Flow Separation Control

Flow control techniques can be classified using different classification schemes. Considering the energy expenditure and the control loop involved, a control device can be passive without requiring auxiliary power and control loop or active requiring energy expenditure, as shown in Fig. 2.5.

Passive flow control techniques, either macro overturn the mean flow using embedded streamwise vortices produced by fixed lifting surface or amplify Reynolds stress which increases the cross-stream momentum transfer, received much attention during the 1970s and 1980s.

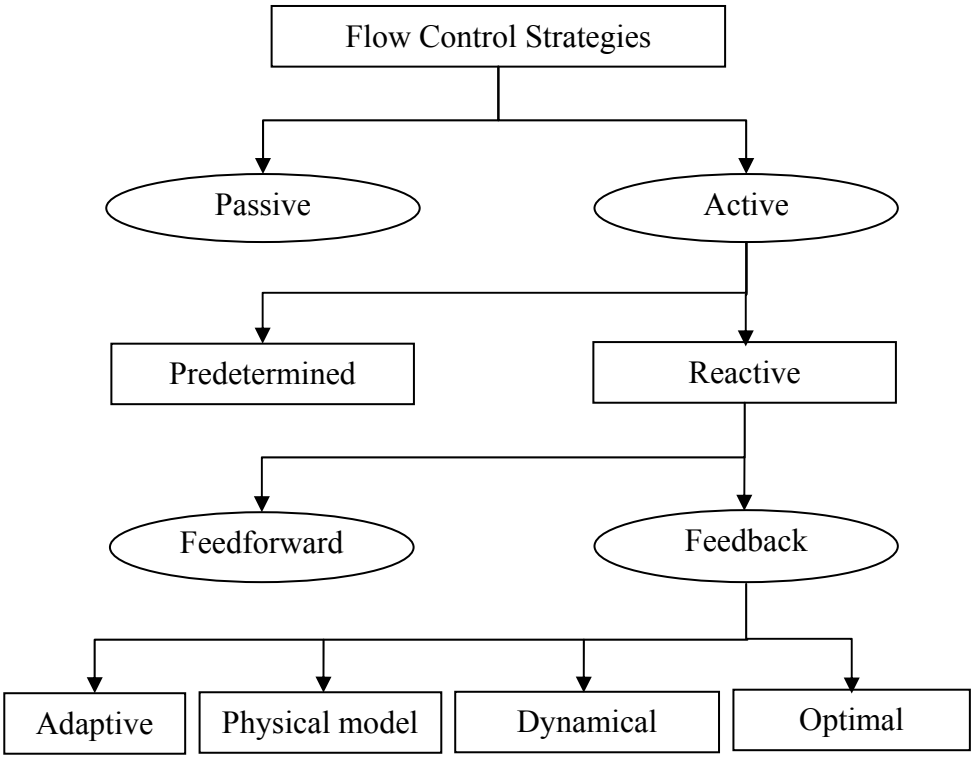

Figure 2.5. Classification of flow control strategies (Gad-el-Hak, 2000).

Passive forms of blowing through leading-edge slats and trailing-edge flaps are inherent features of some high-lift systems. When the high-lift systems are deployed, the fluid (air) from the lower surface of the wing element passes over the upper surface which actually injects the high momentum fluid and therefore energises the boundary layer. Although the blowing intensity is limited due to the pressure difference on the body itself, the effect of passive blowing on lift and drag can be significant (Abbott and von Doenhoff, 1959).

Vortex generators (VGs) are probably the best known conventional passive control technique date from the 1940s (Taylor, 1948). In their basic form, VGs consist of small rectangular, triangular or trapezoidal vanes of approximately boundary layer height in arrays and are set at incidence to the local velocity vector. The VGs may generate array of co-rotating vortices, or pairs of counter-rotating vortices depending on their configuration. The generated vortices entrain higher momentum fluid from the outer region of the boundary layer to the near-wall region and enhance the resistance of the boundary layer to separation. Due to their low weight, robustness and simplicity, VGs have been used in a variety of situations, such as most Boeing aircraft wings (Fig. 2.6a), and BAE systems Hawk aircraft wing (Fig. 2.6b).

(a) **(b)**

Figure 2.6. The application of Vane Vortex Generators (VVGs) on the wing of (a) an Boeing 757 aircraft (www.airliners.net); and (b) a BAE systems Hawk aircraft.

VGs have demonstrated effective flow separation control capacity. But conventional VGs having individual height of the order of the boundary layer thickness δ, produce sizable parasitic drag. Several approaches are now available to improve the performance of VGs. The recent one simply reduces the height of VGs from the order of δ to 0.2δ or less (Rao and Kariya, 1988; Lin and Howard, 1989; Lin et al, 1990). The devices named submerged VGs (Lin et al, 1991), sub boundary layer VGs (Ashill et al, 2002), and low-profile VGs (Lin, 2002) all belong to this category. In comparison with the conventional VGs, the micro VGs can also produce an array of embedded, miniature streamwise vortices to overcome the flow separation, but with reduced parasitic drag. The comparison of different VGs devices by Lin (1999) indicated that the effectiveness of VGs of height 0.2δ is comparable to or better than that of height 0.8δ, while the parasitic drag is greatly reduced.

However, VGs have some shortcomings. They do not have the ability to provide a time-varying control action and therefore they are only effective over a small operational range. Furthermore, the parasitic drag produced by VGs is inevitable.

From the 1990s, the development of dynamic, distributed, and micro-sized systems, which are capable of enhancing the ability to control the unsteady flow in a variety of configurations, makes the research emphasis change from passive flow control to active flow control. Active flow control requiring a control loop can be further divided into predetermined and reactive categories (Fig. 2.5). Predetermined

control inputs steady or unsteady energy without regarding the particular state of the flow, and therefore the control loop is open, as show in Fig. 2.7a. On the other hand, the control input of reactive control is adjusted continuously based on the measurements of sensor, and the control loop can either be open feedforward (Fig. 2.7b) or closed feedback (Fig. 2.7c). The distinction between feedforward and feedback is that the controlled variable differs from the measured variable for feedforward control, but it must be measured, fed back and compared with a reference input for feedback control. And the latter is further divided into four categories listed in Fig. 2.5 (Moin and Bewley, 1994).

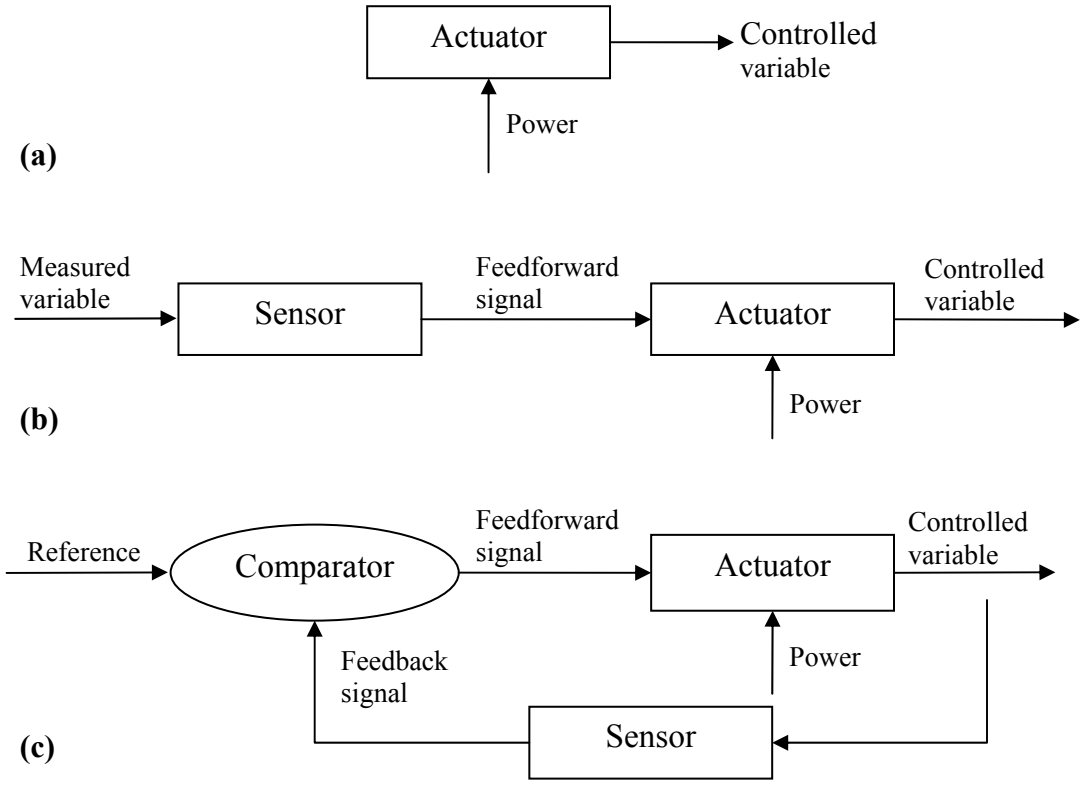

Figure 2.7. Different control loops for active flow control (Gad-el-Hak, 2000).

In comparison to passive flow control, the primary advantages of active flow control were summarized by Kral (1998) as follows: First, active flow control leverages and controls a natural stability of the flow to achieve a large effect at the expense of small, localized energy input. Second, active control can be used to control complex, dynamical processes, since the device of active control can be operative 'on demand' when needed, and its input power level can be varied according to the demands of the local flow condition.

Examples of active flow control techniques listed in Fig. 2.4 include wall jets, wall transpiration (suction), and vortex generating jets.

Wall jets, similar to passive blowing, inject fluid tangentially to the boundary layer to augment the shear layer momentum. It is a straightforward flow separation control technique that has been applied to military fighters and Short Take-Off and Landing (STOL) transports. Separation control by blowing at high speed is covered in the reviews by Delery (1985) and Viswanath (1988).

Wall transpiration or steady suction can be applied through porous surfaces, perforated plates, or carefully machined slots. The effect of suction in preventing flow separation from the surface of a cylinder was first tested by Prandtl (1904) as early as the beginning of the last century. And its remarkable effect was demonstrated on a variety of wind tunnel models and even in flight tests (Lachmann, 1961).

However, both of the above techniques require the complex internal piping to generate the high pressure, mass injection or removal, which carries a large weight penalty. In addition, the aerodynamic gains obtained by blowing or suction are probably offset by the power required to operate these devices. These are the reasons that render them impractical for application.

Vortex generator jets (VGJs), as their name implies, are believed to produce an effect similar to VGs since they generate longitudinal vortices from discrete orifices to enhance fluid mixing in the near-wall region. They are first proposed and studied by Wallis (1952). According to the different jet orifice orientation to the main flow, VGJs can generate arrays of counter-rotating longitudinal vortices (normal jets) or co-rotating longitudinal vortices (pitched and skewed jets), which are similar to that produced by VGs.

Steady jets and pulsed jets are two typical types of VGJs which have been studied extensively (Lin et al, 1990; Johnston, 1990; Seifert et al, 1996; MaManus and Magill, 1996; Bernard et al, 2000; Godard et al, 2006; Godard and Stanislas, 2006a). Especially the pulsed jets, as a relatively new approach using oscillatory or intermittent momentum addition, have obtained much attention recently, since they are capable of delivering similar levels of effectiveness of steady jets with a reduced net mass flux. The effectiveness of steady jets versus pulsed jets for the delay of stall on a thin aerofoil was compared by Seifert et al. (1996). For the same improvements in lift, the pulsed jets were found to require less momentum C_μ = 0.3%, in

comparison to the steady jets, C_μ= 3% (where C_μ is the momentum coefficient, defined as the ratio of jet momentum to the local freestream momentum). Johari and McManus (1997) evidenced a vortex ring production by the pulsed jets, and thus they suggested that in addition to reducing the mass flow rate needed for the control, the impulsive flow enhanced the vorticity production and the boundary layer penetration for the same velocity ratio as compared to the steady jets.

However, both steady jets and pulsed jets require the complexity of internal piping system. In order to circumvent the deficiency incurred by the piping system while maintaining all the other advantages of pulsed jets, synthetic jets, a new means of periodic excitation with zero-net-mass-flux, have been proposed and attracted much more attention in recent years. The schematic of a typical synthetic jet actuator (SJA) is shown in Fig. 1.2.

The primary advantage of SJAs is that they do not require air supply and the weight penalty is smaller compared to the steady and pulsed jets. In addition, they can transfer non-zero momentum to the external fluid, and generate coherent vortices which can provide a favourable control effect. Furthermore, as SJAs only use external fluid for jet production, the energy requirement is reduced and they can be made compact in the design. Hence, SJAs are promising to be applied to high-lift systems for flow separation control (Amitay et al, 1999; Smith and Glezer, 1998; Crook et al, 1999; Seifert and Pack 1999). SJAs have also been used in a variety of active flow control applications besides the flow separation delay, such as thrust-vectoring (Smith and Glezer, 2002), turbulent boundary layer control (Rathnasingham and Breuer, 2003), and mixing augmentation (Ritchie et al, 2000).

SJAs, due to their unique advantages, also have the potential for Micro-Elector-Mechanical Systems (MEMS) which open up a new territory for flow control research. Such systems having micron-sized sensors and actuators, and integrated IC with micro transducers, can execute sense-decision-actuation on a monolithic level, therefore they could reduce the potential density of the actuator systems in the wing, and more importantly, meet a prerequisite for aircraft implementation (Warsop, 2004). It is because the local boundary layer thickness is of the order of 1 to 3 mm on the leading edge devices, and 1 to 10 mm on the trailing edge at the take-off condition, depending on the size of the aircraft. Therefore, considering the boundary layer thickness in practice, it is required to apply MEMS-based micro-scale SJAs.

However, there are some practical problems with using synthetic jets at flight scale. First, a very high driving frequency is required to establish a synthetic jet in time to control the near-wall streak structures individually, which is at least an order of magnitude greater than the turbulent bursting frequency. Second, synthetic jets must have several diaphragm cycles to establish itself that places a limit on their speed of response for controlling the streaks in a turbulent boundary layer. Last, the small size of orifice makes dirt or debris block it easily, especially during the suction stroke. It is a serious issue for aircraft manufacturers since cleaning MEMS would be a demanding operation.

The effectiveness of SJAs in delaying flow separation has been proved by a number of investigations in the laboratory (Amitay et al, 1998; Smith et al, 1998; Amitay et al, 1999; Seifert and Pack, 1999; McCormick, 2000; Wood et al, 2000; Gilarranz et al, 2005; Khodadoust and Washburn, 2007), which will be introduced in detail in section 2.2.2.3. Here only a straightforward result by Wood et al. (2000) is presented.

Wood et al. (2000) investigated the flow control effectiveness of an array of circular synthetic jets normal to the surface of a circular cylinder model upstream of its separation line in a turbulent boundary layer ($Re = 5.5\times10^5$ based on the cylinder diameter), as shown in Fig. 2.8. Oil flow visualization indicated that longitudinal vortices were developed and persisted for a long distance downstream as a result of the interaction between the synthetic jets array and the turbulent boundary layer, and therefore the separation line was pushed downstream where the synthetic jets were actuated at upstream.

Although the capability of SJAs in delaying flow separation has been demonstrated in various manners, the understanding of the physical process, especially the formation of vortex ring, its interaction with the boundary layer and its impact on the near-wall region is still vital, which will be helpful to design and select suitable SJAs in practical application. In the following sections, the characteristics of synthetic jets issued into quiescent conditions, a zero-pressure-gradient attached flow and a separated flow will be reviewed experimentally and numerically.

As a whole, active separation control techniques have their inherent advantages over the passive control techniques, however, they have not been applied widely on high-lift systems of mainstream civil transport aircraft, due to the issues related to reliability, effectiveness and efficiency. For SJAs, a number of issues need

to be addressed in terms of compactness, weight, efficiency, control authority and power density. Hence, this technology is not sufficiently mature for inclusion in the design process.

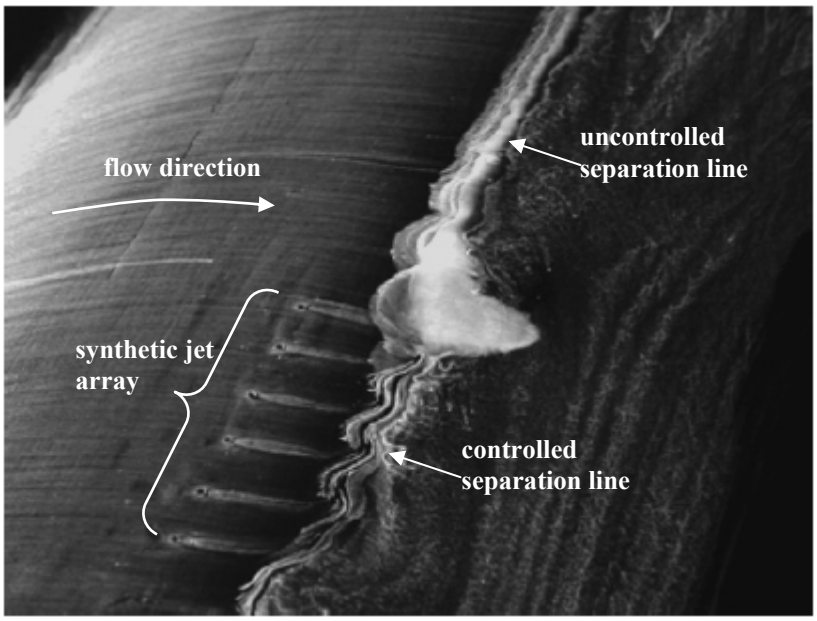

Figure 2.8. Oil flow visualization demonstrating the flow separation control on a cylinder using an array of synthetic jets (modified from Wood et al, 2000).

2.2 Experimental Studies of Synthetic Jets

2.2.1 Synthetic Jets in Quiescent Conditions

In practice, synthetic jets should be applied to the boundary layer aimed to delay flow separation. However, the fluid mechanics of synthetic jets in quiescent conditions is fundamental as a first crucial step.

A typical SJA is a device consisting of three components: a cavity that accommodates a volume of fluid, a diaphragm that creates a volume change in the cavity, and an orifice that delivers the jet to the external flow, as shown in Fig. 1.2. During the suction stroke, the surrounding fluid will be entrained into the cavity, and then the entrained fluid is expelled during the blowing stroke as the diaphragm moves upward, thus a shear layer is formed between the expelled fluid and the surrounding fluid. The vorticity of this shear layer eventually rolls up to form a vortex ring. Repeating this process at a certain frequency, a train of vortex rings is produced and propagates away from the orifice. When the oscillating period and

amplitude are same for blowing and suction stroke, the net-mass-flux-rate is zero, and so the ejected jet is actually 'synthesised' from the working fluid where the SJA is applied. Currently, there are two strategies of SJAs research: one using two-dimensional (2D) slot actuators, while the other using circular, square or ellipse actuators.

Since the mechanical domains (the diaphragm motion) are coupled with fluid domains (the cavity and exits flows), the design of SJAs is quite subtle and affects the performance of synthetic jets greatly. Extensive simulation research has been performed to study the effect of the design of SJAs, which will be reviewed in section 2.3.1.

2.2.1.1 Non-Dimensional Parameters

As shown in Fig. 1.2, the parameters of a typical circular synthetic jet in quiescent conditions can be classified into two categories: one is geometric parameters including orifice diameter D_o, cavity diameter D_c, orifice depth h, and cavity height H, and the other is operating parameters including diaphragm oscillatory frequency f, and displacement Δ. For the purpose of flow separation control, the jet velocity, momentum and vortex strength are considered as the most important performance parameters determining the impact of synthetic jets on the external flow (Tang and Zhong, 2006).

In comparison to the dimensional parameters, the non-dimensional parameters are more useful to compare the synthetic jets with different scales at different operating conditions. Based on the dimensional analysis, four dimensionless parameters are widely used to characterise synthetic jets in quiescent conditions. They are the dimensionless stroke length L, the Reynolds number Re, the Strouhal number Str, and the Stokes number S.

The dimensionless stroke length L can be defined as:

$$L = \frac{L_o}{D_o} \tag{2.4}$$

where L_o is the stroke length. According to the slug model (Smith and Glezer, 1998), the vortex ring is formed from the fluid of velocity U_o being expelled through the nozzle for a time T as a cylindrical fluid slug of length L_o and diameter D_o. therefore the stroke length L_o can be defined as

$$L_o = U_o T \tag{2.5}$$

To account for the changes in velocity programme (U_o varies with time, sinusoidally in the present study), a time-averaged velocity is defined as

$$\overline{U}_o = \frac{1}{T}\int_0^T U_o(t)dt \tag{2.6}$$

where $U_o(t)$ is the instantaneous spatial-averaged velocity over the orifice, T is the actuation cycle. To facilitate a comparison between synthetic jets and steady jets, a slightly different velocity scale was proposed by Smith and Glezer (1998) which has been widely used in the synthetic jet literatures (Smith and Swift, 2003; Holman et al, 2005; Milanovic and Zaman, 2005; Jabbal and Zhong, 2008)

$$\overline{U}_o = \frac{1}{T}\int_0^{T/2} U_o(t)dt \tag{2.7}$$

where $\overline{U}_o$ is the time-averaged blowing velocity over the entire cycle. Note that $\overline{U}_o$ is neither the time-averaged $U_o(t)$ over an entire cycle, which should be zero, nor the time-averaged value over a half cycle, which should be $2\overline{U}_o$. The stroke length (slug length) is now

$$L_o = \int_0^{T/2} U_o(t)dt = \overline{U}_o T \tag{2.8}$$

Substituting Eq. 2.8 to Eq. 2.4, it is obtained that

$$L = \frac{L_o}{D_o} = \frac{\overline{U}_o T}{D_o} \tag{2.9}$$

The formation of synthetic jets is associated with the dimensionless stroke length. The jet will not be formed under certain threshold. The following section 2.2.1.2 will discuss the effect of L on the formation of synthetic jets. In addition, it is known that a formation number (approximately L = 4 proposed by Gharib et al, 1998; Rosenfeld et al, 1998) exists for vortex ring formation, beyond which a tail will be generated behind the vortex ring. Similarly, for synthetic jets, the formation number has been observed in the experiments by Crook and Wood (2000), Milanovic and Zaman (2005) and Jabbal et al. (2006). The experiments of Jabbal et al. (2006) showed that the upper threshold of circular synthetic jets in quiescent conditions occurs at L = 4, above which secondary vortices form due to the saturation of the vortex circulation within the primary vortical structure. However, Milanovic and Zaman (2005) observed that the upper threshold of saturation is L = 5. Note that the

formation number of Gharib et al (1998) depended on the discharge velocity profile and the velocity programme. The numerical simulations of Rosenfeld et al. (1998) showed that non-uniform velocity profiles tend to decrease the formation number significantly, while non-impulsive velocity programmes increase the formation number slightly. Therefore, it is expected that the variations in the formation number are probably due to the different evolution of the discharged velocity profiles.

The Reynolds number has been defined using different characteristic velocity and length scale in the literature. Glezer (1988) found a relationship between the circulation of a vortex ring and the Reynolds number based on the stroke length.

The vortex circulation represents the strength of vortex rings. The initial (or total) circulation at the orifice exit over the whole cycle is

$$\Gamma_o = \int_0^T \frac{1}{2} U_o^2(t)dt = \frac{\overline{U_o^2}T}{2} = \frac{P\overline{U}_o^2 T}{2} = \frac{PL_o^2}{2T} \tag{2.10}$$

where P is a velocity programme factor to account for a specific variation of velocity in the time history.

$$P = \int_0^1 \left(\frac{U_o^2}{\overline{U_o^2}}\right) d\left(\frac{t}{T}\right) = \frac{\overline{U_o^2}}{\overline{U_o^2}} \tag{2.11}$$

Substituting Eq. 2.10 to Eq. 2.8, it is obtained that

$$\frac{2\Gamma_o}{\nu} = \frac{P\overline{U}_o L_o}{\nu} \tag{2.12}$$

The RHS term of Eq. 2.12 is a Reynolds number ($\mathrm{Re}_L = P\overline{U}_o L_o/\nu$). The dimensionless circulation on the LHS term of Eq. 2.12 is also equivalent to an alternative Reynolds number ($\mathrm{Re}_\Gamma = 2\Gamma_o/\nu$). According to Eq. 2.12, the Reynolds number is proportional to the vortex circulation hence it quantifies the strength of a vortex ring. Glezer also proposed another alternative Reynolds number $\mathrm{Re}_I = I_o/\mu A_o$, where $I_o = \rho A_o \int_0^{D_o} U_o^2(t)dt = \rho A_o \overline{U_o^2} T_o$ is the momentum associated with the discharge, and A_o is the orifice area. These three equivalent Reynolds numbers can be used to characterise synthetic jets (Glezer and Amitay, 2002). Both Glezer (1988) and Shuster and Smith (2007) suggested that Re_Γ is a good measure of the laminar-turbulent nature of newly formed vortex rings.

Smith and Swift (2001, 2003) used the Reynolds number $\mathrm{Re}_U = \overline{U}_o D_o / \nu$, based on the time-averaged jet ejection velocity over the whole cycle $\overline{U}_o$ and the orifice diameter D_o, to characterise the synthetic jets. The behaviour of synthetic jets was compared with steady jets of the same Reynolds number, and the self-similar velocity profiles were found to be identical in the far field. Re_U is related to Re_L defined by Glezer, since

$$\mathrm{Re}_L = \frac{\overline{U}_o L_o}{\nu} = \mathrm{Re}_U \frac{L_o}{D_o} = \mathrm{Re}_U \cdot L \tag{2.13}$$

Crook and Wood (2000) used the Reynolds number $\mathrm{Re}_{peak} = U_{peak} D_o / \nu$ based on the peak velocity U_{peak} for circular synthetic jets. A number of distinct states of synthetic jets were observed from smoke visualization depending on Re_{peak}. For a sinusoidal diaphragm oscillation, $U_{peak} = \pi \cdot \overline{U}_o$ (Smith and Swift, 2003), therefore $\mathrm{Re}_{peak} = \pi \cdot \mathrm{Re}_U$.

In the present study, the Reynolds number based on $\overline{U}_o$ and L_o is utilized, i.e. $\mathrm{Re}_L = \frac{\overline{U}_o L_o}{\nu}$.

Strouhal number, as a dimensionless frequency, characterises the jet strength per unit time. For synthetic jets in quiescent conditions, it can be defined as

$$Str = f D_o / \overline{U}_o \tag{2.14}$$

Substituting Eq. 2.14 into Eq. 2.9,

$$L = \frac{L_o}{D_o} = \frac{\overline{U}_o T}{D_o} = \frac{1}{Str} \tag{2.15}$$

Therefore, the Strouhal number is the inverse of the dimensionless stroke length. This relationship has been validated by the investigation of Rediniotis et al. (1999). They studied the effect of the Strouhal number (based on the maximum jet velocity) on the structure of a circular synthetic jet, and found that at lower *Str* = 0.2 (equivalent to high *L*), a vortex ring forms during the blowing stroke and subsequently propagates away from the orifice. However, at higher *Str* = 2 (equivalent to low *L*), the expelled fluid is drawn back into the cavity due to the action of suction stroke and hence no jet forms.

Viscous effects lead to a boundary layer in the orifice whose thickness is governed by the viscosity and the frequency of oscillation, and can be expressed in

terms of a Stokes' length scale, $l_s = \sqrt{\nu/2\pi f}$. The Stokes number, as a measure of viscous effects in oscillating flows, is another important dimensionless parameter for synthetic jets, which is commonly defined as

$$S = \sqrt{2\pi f D_o^2 / \nu} \tag{2.16}$$

Rathnasingham and Breuer (1997) suggested that the Stokes number characterises the viscous effect in the orifice. When the oscillating boundary layer dominates the entire orifice duct at a small *S*, the flow is 'choked' and therefore the jet velocity is proportional to the orifice area. In contrast, when the boundary layer is restricted close to the orifice wall at a large *S*, the flow in the orifice can be considered as inviscid flow and therefore the jet velocity is inversely proportional to the orifice area. Additionally, for a given actuator geometry, an optimal Stokes number was found at which the maximum jet velocity is achieved. And beyond this optimal value, the jet characteristics are governed by inviscid, incompressible theory.

Based on the Buckingham theorem, *L* and Re are identified as the independent parameters determining the characteristics of synthetic jets in question conditions (Smith and Glezer, 1998). The Strouhal number *Str* and the Stokes number *S* are dependent parameters; *Str* is the inverse of the dimensionless stroke length, while *S* is related to *L* and Re via Eq. 2.17.

$$\mathrm{Re}_L = \frac{L^2 S^2}{2\pi} \tag{2.17}$$

However, *S* and *Str* are often quoted in the literature due to their physical meaning.

2.2.1.2 Formation of Synthetic Jet

The vortex rings produced by synthetic jets differ from those produced by a piston arrangement in that the behaviour of the former is strongly affected by the presence of a suction flow in the neighbourhood of the orifice. Therefore, synthetic jets will only form when the vortex rings are able to overcome the effect of suction during the suction stroke. Many research have been undertaken to study the formation of synthetic jets in quiescent conditions both experimentally and numerically (Smith and Glezer, 1998; Mallinson et al, 1999; Crook et al, 1999, 2001; Müller et al, 2001; Kral et al, 1997; Rizzetta et al, 1999; Lee and Glodstein, 2002; Holman et al, 2005; Milanovic and Zaman, 2005; Shuster and Smith, 2007). A comprehensive review of formation of synthetic jets can be found from Glezer and Amitay (2002).

It is known that there are two groups of orifice geometry: one is slot with high aspect ratio, nominally 2D and the other is circular or axisymmetric. The formation of these two groups' synthetic jets is different. The former appears to produce two-dimensional vortex pairs when they just form, but the formed vortex pairs are highly unstable and experience subsequent 'axis swapping' between the major and minor axis of the jet (Ravi et al, 2004; Zhong et al, 2004). While the latter generates successive vortex rings propagating downstream.

Holman et al. (2005) defined synthetic jet formation as "the appearance of a time-averaged outward velocity along the jet axis and corresponds to the generation and subsequent convection or escape of a vortex ring". There are several key parameters determining the jet formation and subsequent roll-up of a vortex ring (vortex pair for 2D synthetic jets). Jet formation is primarily characterised by the dimensionless stroke length. Since the stroke length represents the length of the fluid column ejected during the blowing stroke (Eq. 2.9), which is proportional to the distance that a vortex ring moves away from the orifice exit. If the stroke length is too small, the vortex ring cannot move far away from the orifice before the start the suction stroke, and then will be ingested back to the orifice due to the action of suction. Therefore, there is a minimum stroke length to ensure the jet formation.

For 2D synthetic jets, Smith and Swift (2001) estimated analytically the threshold of $L = 4/\sqrt{\pi} \approx 2.26$, whereas the experimental results indicated the threshold is in the range of $5.5 < L < 6$ assuming the radius at the orifice lip is not present. A series of numerical simulations by Utturkar et al. (2003) and Holman et al. (2005) revealed that the formation criterion is approximately $L > 6.28$ (note that the value presented here has been translated into the dimensionless stroke length defined in Eq. 2.9). The discrepancy of these criteria is probably due to the effect of the geometry of the orifice lip. This statement is supported by the numerical study of Fugal et al. (2005), who found that the formation threshold is approximately $L = 2$ for a sharp lip, and $L = 10$ for a rounded lip.

Experimental jet formation data for the axisymmetric case was published over 50 years ago. Ingard and Labate (1950) used standing waves in an acoustically driven circular tube to induce an oscillating velocity field in the vicinity of an orifice plate and observed the formation of jets from trains of vortex rings on both sides of the orifice without net mass flux. More recently, the experimental investigation of

Smith et al. (1999) provided additional data and suggested that $L > 1$ for synthetic jet formation at high Stokes number $S > 35$. Utturkar et al. (2003) and Holman et al. (2005) supplied the data at lower Stoke number range ($6 \leq S \leq 36$) and revealed that the criterion of $L \approx 0.5$. Shuster and Smith (2004) observed that a vortex ring is unable to fully escape the orifice and consequently a jet is not formed at $L < 0.8$, and recently they modified the criterion to $L < 0.6$ according to dye flow visualization. Milanovic and Zaman (2005) provided a smaller criterion of $L = 0.25$ by observing the centreline velocity profiles, at which an initial peak and subsequent decay happened. The difference in the thresholds of L may be attributed to factors such as the different geometry of orifice lip and the diaphragm velocity programme. Actually, it can be found that many of the experimental observations were undertaken in parallel with the numerical simulations which will be discussed in section 2.3.1, and both of them contributed uniquely to the establishment of jet formation criterion.

Since the synthetic jet is 'synthesised' by a succession of vortex rings which are produced as a result of the roll-up of the shear layer at the orifice edge, the formation of synthetic jet is always accompanied with the roll-up of vortex ring.

The formation process of the vortex ring is directly related to the evolution of the vortex sheet formed at the orifice edge, which would proceed to roll-up into a vortex ring under certain conditions. The velocity across an idealized vortex sheet is discontinuous and consists of a continuous distribution of vortex lines, as shown in Fig. 2.9. Crook (2002) described the formation process as follows:

1. The vortex sheet induces a velocity on itself perpendicular to the plane of the sheet, which achieves its maximum at the leading edge of the sheet.
2. The leading edge of the sheet curves due to the effect of the self-induced velocity.
3. The combined effects of the velocity component induced by the curved vortex sheet on the leading edge and the normal component of the velocity induced by the uncurved sheet, make the roll-up happen.

In consideration of the action of viscosity, the velocity jump across the vortex sheet is not quite discontinuous in reality.

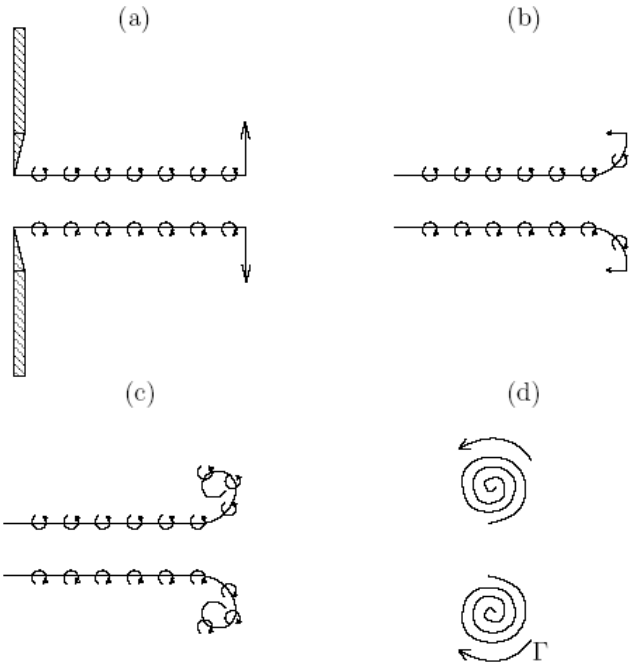

Figure 2.9. Idealized vortex ring formation: (a) creation of vortex sheet through an orifice, (b) … (d) roll-up. Straight lines represent induced velocity, small curved ones vorticity (Crook, 2002).

It is known that vortex rings are able to entrain ambient fluid into their cores by roll-up process, which enhances mixing. And the strength of vortex rings in terms of the level of circulation determines the ability of vortex rings' entrainment. Hence, vortex roll-up, as a prerequisite to vortex ring's strength, is another important characteristic of synthetic jet formation.

Guo and Zhong (2007) studied the behaviour of synthetic jets issued from two orifices of 5×10^{-4} m and 5×10^{-3} m diameter, and suggested that the Stokes number S is the primary parameter characterising the vortex roll-up. For the small orifice of 5×10^{-4} m diameter, no vortex roll-up was observed at a dimensionless stroke length of 4 and a Stokes number of 7. Then they carried out a particle image velocimetry (PIV) measurement on a large orifice of 5×10^{-3} m diameter. Based on a qualitative observation of the experimental data, a minimum Stokes number appears to be about 10 which is required for an appreciable roll-up to be observed within the range of stroke length examined (L = 1.4, 2.9 and 3 respectively). As discussed in section 2.2.1.1, the Stokes number is a measure of the ratio between the unsteady force and the viscous force in the orifice, and thus a higher Stokes number indicates a thinner boundary layer along the orifice wall. Consequently, the velocity profile at the orifice exit will vary from a parabolic shape to a top-hat shape with an increase in

Stokes number. Therefore, a thinner boundary layer along the orifice wall produced at a higher Stokes number is favourable to roll-up.

2.2.1.3 Evolution of Synthetic Jet

It is clear that in the near field of the synthetic jet, its evolution is determined critically by the details of the formation, advection and interaction of the discrete vortices in the presence of the time-periodic reverse flow. A stagnation point along the centreline will be formed as a result of the periodical reversal in flow direction along the jet centreline during the blowing and suction strokes. It is located between the recent vortex and the jet exit and moves along the centreline during the suction stroke, which has been observed by Gilarranz and Rediniotis (2001) and Glzer and Amitay (2002). Hence the suction flow is confined with a finite region near the orifice exit.

The vortex ring produced during the formation process may follow the evolutionary path, namely the transition from laminar to turbulent stage due to azimuthal instabilities (Widnall et al, 1974). At a high Reynolds number, the vortex ring may be turbulent initially. Glezer (1988) suggested that the two parameters Re_L ($\mathrm{Re}_L = \Gamma_o / \nu$) and L might, under some conditions, be sufficient to define the behaviour of the vortex ring throughout its life time. Based on the results of the survey of two orifices diameters, a transition map was created showing the initial flow regime of the vortex ring (laminar or turbulent) for various configurations. The laminar vortex ring is considered to remain laminar at least about 30-40D_o downstream of the orifice exit, while the turbulent vortex ring is thought to be turbulent immediately after its formation. A transitional boundary was found based on the qualitative observation from dye visualization. For small L, the critical Re_{Do} is approximately 2×10^4, while for large L, the critical Re_L is approximately 5×10^4. Therefore, it may conclude that L_o is not important for transition when L is small. On the contrary, D_o is not important for transition when L is large. It was also suggested that the transition to turbulent may be accelerated by Kelvin-Helmholtz type instabilities in the vortex sheet during its formation, even though the exact mechanism was not given. Although some investigations were carried out to study the transition mechanism further (Glezer and Coles, 1990; Shariff and Leonard, 1992;

Lim, 1997), it seems that no universal mechanism describing the transition to turbulent has been suggested.

Shuster and Smith (2007) provided a similar transition map observed by Glezer (1988), using dye flow visualization. And a similar shape of transition boundary was found reaching an apparently asymptotic Reynolds number for large *L*, however at a Reynolds number a factor of 5 smaller.

Crook and Wood (2000) and Cater and Soria (2002) proposed four different flow patterns in the near field of circular synthetic jets observed via dye visualization:

1. At low Reynolds number, a 'laminar jet' is observed where the flow is an apparently steady stream of dye flowing from the orifice with little penetration of ambient fluid as shown in Fig. 2.10a. Here, $\mathrm{Re} = U_o D_o / \nu$, and $Str = fD_o / U_o$, where U_o is a characteristic velocity scale, f is the oscillation frequency, D_o is the orifice diameter.
2. The individual identifiable laminar vortex rings form as shown in Fig. 2.10b. The path of the preceding rings affect the successive rings produced at the orifice, but no agglomeration occurs within the observable flow domain. This type of flow field is termed 'laminar rings'.
3. As the Reynolds number increases, a 'transitional jet' occurs where the rings start to agglomerate within the observable domain and an erratic, intermittent jet is generated as shown in Fig. 2.10c.
4. At highest Reynolds number, a 'turbulent jet' is generated as shown in Fig. 2.10d, which is very similar in appearance to a conventional steady turbulent jet.

The oscillatory nature of synthetic jets flow in the near field leads to a much greater entrainment of ambient fluid than steady jets (Mallinson et al, 2001; Cater and Soria, 2002; Smith and Swift, 2003), therefore both 2D slot synthetic jets and circular synthetic jets, grow more rapidly than steady jets, in terms of jet width and volume flux. Figure 2.11 demonstrates the larger spreading rate of a synthetic jet in comparison to that of an equivalent steady jet based on the momentum flow velocity by dye visualization (Cater and Soria, 2002). However, in the far field of synthetic jets, the vortex rings eventually become indiscernible from the jet flow and travel with the jet mean velocity. For 2D slot synthetic jets, Smith and Glezer (1988) observed that the cross-stream distributions of the time-averaged streamwise and

cross-stream velocity components and the corresponding root-mean-square (rms) velocity fluctuations appear to collapse in the usual similarity coordinates for 2D steady jets. However, the streamwise decrease of the mean centreline velocity is higher in comparison to steady jets. While for circular synthetic jets, both experimental and numerical investigations by Mallinson et al. (2001) indicated that its centreline and cross-stream velocity distributions agree with the theory for a stead jet. Hence, the behaviour of synthetic jets in the far field is similar to that of steady jets.

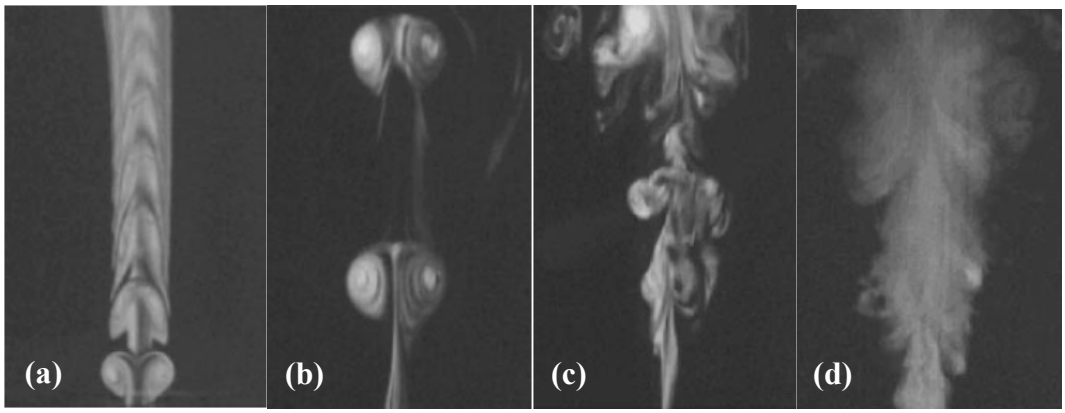

Figure 2.10. Four distinct flow patterns of synthetic jets: (a) laminar jet Re = 3336, *Str* = 0.03; (b) laminar vortex rings Re = 7784, *Str* = 0.012; (c) a transitional jet Re = 11121, *Str* = 0.009; (d) a turbulent jet, Re = 66991, *Str* = 0.009 (Cater and Soria, 2002).

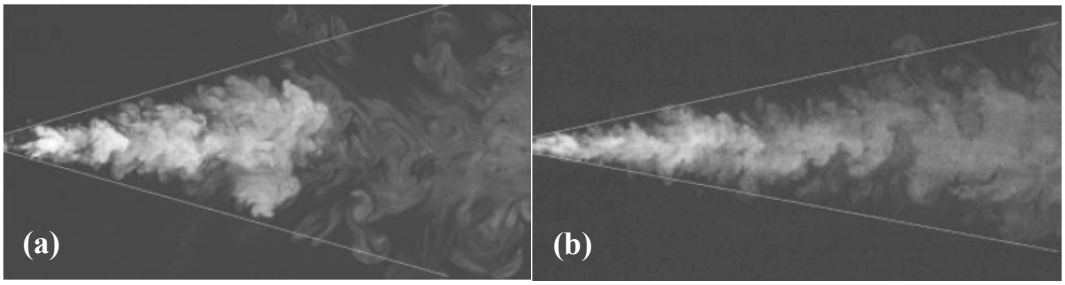

Figure 2.11. Flow visualisation of fluorescent dye marker for (a) a synthetic jet, and (b) an equivalent steady jet. The light-coloured lines drawn on the images indicate the mean boundary of the dye flow. The approximate spreading rates are: (a) $S_b \approx 0.13$, (b) $S_b \approx 0.1$ (Cater and Soria, 2002).

2.2.2 Synthetic Jets in Cross Flow

2.2.2.1 Non-Dimensional Parameters

For a synthetic jet issued into a cross flow, three more physical parameters on which the nature of the synthetic jet depends should be added. They are the local boundary

layer thickness δ, the freestream velocity U_∞, and the local wall shear stress τ_w. Therefore, a wide range of dimensionless parameters can be extracted to describe the interaction of synthetic jets with a cross flow. In addition to L and Re_L discussed in quiescent conditions, the following dimensionless parameters are considered

$$VR = \frac{\overline{U}_o}{U_\infty},\ d = \frac{\delta}{D_o},\ C_f = \frac{\tau_w}{\rho U_\infty^2},\ Str = \frac{f\delta}{U_\infty},\ \mathrm{Re}_\delta = \frac{U_\infty \delta}{\nu} \tag{2.18}$$

where VR represents the jet-to-freestream velocity, which indicates the relative strength between the jet and the freesstream; d represents the ratio of boundary layer thickness to orifice diameter; C_f is the non-dimensional shear stress, which is equivalent to the skin friction coefficient ($c_f = \tau_w / 0.5\rho U_\infty^2$); Str is the Strouhal number defining the non-dimensional spacing of successive vortical structures formed from synthetic jets (the definition of Str in cross flow is different to that in quiescent conditions); and Re_δ is the Reynolds number based on the freestream velocity and the boundary layer thickness.

Considering the interdependence of these parameters, Str can be written as $Str = \frac{VR \cdot d}{L}$, and Re_δ can be written as $\mathrm{Re}_\delta = \frac{\mathrm{Re}_L \cdot d}{L \cdot VR}$. Hence five dimensionless parameters are used to describe the behaviour of synthetic jets interacted with a cross flow

SJA characteristics = $Fn(L, VR, d, \mathrm{Re}_L, C_f)$ (Jabbal and Zhong, 2008) (2.19)

This functional dependence on the dimensionless parameters is supported by the numerical simulations by Raju et al. (2005) and dimensional analysis by Ashill et al. (2005). Raju et al. (2005) used a non-linear regression analysis of the data obtained from numerical simulations, and established a scaling law for the vorticity flux of a synthetic jet in a zero-pressure-gradient laminar boundary layer, which relates the vorticity flux to the Strouhal number based on the jet velocity, a jet-to-freestream velocity ratio, a boundary layer thickness to slot width ratio, and a jet Reynolds number. A similar list of key parameters for production of synthetic jet vortices was also suggested by Ashill et al. (2005).

Since the velocity ratio VR indicates the relative strength between the jet and the freestream velocity, it actually characterises the trajectory of synthetic jets. The investigation of Milanovic and Zaman (2005) showed that at a given streamwise location, the penetration height of synthetic jet depends on the momentum flux ratio

which is equivalent to the velocity ratio. A higher *VR* induces a rapid penetration of vortical structures, and therefore the residual time within the boundary layer becomes shorter which is expected to influence the effect of flow control.

The ratio of boundary layer thickness to orifice diameter, *d*, is directly related to the shear in the boundary layer. For $d \leq 1$, the boundary layer thickness is considered unimportant, since the synthetic jet penetrates the boundary layer quickly and the effect of shear in the boundary layer is negligible. The studies of Crook (2002) and Milanovic and Zaman (2005) focused on the behaviour of synthetic jets under this condition. Contrarily, for $d > 1$, synthetic jets are issued into a large shear flow, and therefore the interaction between the synthetic jets and the boundary layer becomes remarkable. Some investigations are reported under this condition which studied the synthetic jets embedded in a flat plate boundary layer in order to explore the fundamental interaction mechanisms (Smith, 2002; Schaeffler, 2003; Shuster et al, 2005).

The modified Strouhal number *Str* is based on δ and U_∞ instead of D_o and $\overline{U}_o$ in order to emphasize the influence of the freestream flow on the behaviour of synthetic jets. It is known that the vortex rings will be forced to convect with the freestream flow shortly after they form from the orifice, and therefore U_∞ is more suitable than $\overline{U}_o$ in describing the behaviour of synthetic jets in a cross flow. *Str* is usually used to measure the spatial distance between successive vortical structures as it is only related to the oscillating frequency *f* for a fixed δ and U_∞. Chang and Vakili (1995) studied the dynamics and trajectories of vortex rings formed by the pulsation of a jet in a uniform cross flow, and observed that at lower pulsing frequencies (low *Str*), the vortex rings penetrate into the cross flow much deeper than that at high pulsing frequencies (high *Str*). A low pulsing frequency which corresponds to a low *Str*, indicates a large spatial distance between successive vortex rings. Hence the vortex rings at low *Str* move as unit blobs of fluid with little change in their general shape, and the interaction between successive vortex rings is not appreciable. On the other hand, a high *Str* implies a small spatial distance between successive vortex rings, and their interaction is expected to be dominant which reduces their penetration.

2.2.2.2 Interaction with a Zero-Pressure-Gradient Attached Cross Flow

Gordon and Soria (2002) studied velocity vector fields of two circular synthetic jets in cross flow by PIV measurement both in the near field and far field. The circular synthetic jets were characterized by Re_j = 1240, VR = 4.6, Str = 0.016, L = 20 and Re_j = 2960, VR = 7, Str = 0.014, L = 30 respectively, which are based on the average momentum flow velocity U_j, the orifice diameter D_o and the freestream velocity U_∞. Phase-averaged velocity and vorticity fields in the near field showed the formation of vortex ring and its movement into the cross flow with a trailing cylindrical layer of concentrated vorticity. This indicated that the formation of synthetic jet in cross flow exhibits similarities to the free vortex rings with formation number $L/d > 4$ (Gharib et al, 1998), although an asymmetry is visible due to the cross flow. Additionally, they calculated the volume flow rate (which represents the rate of fluid flow in the direction perpendicular to the wall) in the near field ($y/D_o \leq 3$), and found the temporal oscillation of the volume flow rate is similar to the temporal oscillation of centreline velocity of a 2D slot synthetic jet characterized by Str = 0.023 and Re = 600 (Smith and Glezer, 1998), and that of a circular pulsed jet characterized by Str = 0.011 and Re = 6×10^4 (based on the mean velocity) (Bremhorst and Hollis, 1990). Interestingly, there is no cross flow for the 2D slot synthetic jet and the circular pulsed jet. Therefore, it was suggested that the development of synthetic jet in cross flow in the near field is similar to a free synthetic jet near the wall and a free fully pulsed jet at $3D_o$ from the wall. On the other hand, in the far field, it was observed that although fluid ejected from the orifice penetrates much further (the jet penetrations are 15 and $18D_o$ for the jets at VR = 4.6 and 7 respectively based on maximum velocity, at x/D_o = 21), the time-averaged penetration, as indicated by the deflection of the mean streamlines, is only 2-3D_o from the wall. In addition, in the far field, the velocity decay along the jet trajectory was found to be similar to that of a steady jet with 85% of the equivalent momentum ratio.

Similarly, Schaeffler (2003) used the time-averaged displacement of the streamline closest to the wall to measure the behaviour of circular synthetic jets in a turbulent boundary layer at three VRs. At the maximum VR, VR = 0.95 based on the maximum rms velocity, the streamline closest to the wall is lifted up to $1.75D_o$ (88% of the undisturbed boundary layer thickness) at x/D_o = 1.5, as shown in Fig. 2.12a. This effect decreases with the decrease of VR. Hence at VR = 0.36, the displacement of the streamline is reduced to $0.8D_o$ (44% of the undisturbed boundary layer thickness) at the same streamwise location, as shown in Fig. 2.12b. A possible

explanation was suggested as a conflict between cavity entrainment and vortex ring entrainment during the suction stroke. The vortex ring and the cavity are able to balance each other to a higher degree at high *VR*, while at low *VR* the cavity entrainment is able to dominate the ring entrainment making the ring cannot access to the ambient fluid which further limits the strength of the vortex ring. Therefore, the penetration of the synthetic jet at low *VR* is reduced. Schaeffler (2003) also suggested that the creation of a robust vortical structure early in the cycle is necessary to enhance the mixing across the height of the boundary layer.

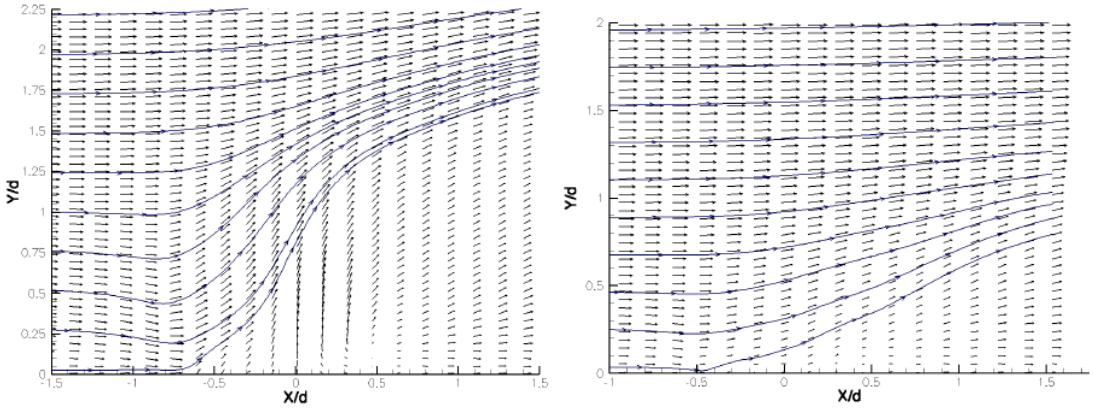

(a) **(b)**

Figure 2.12. Velocity vector maps for the synthetic jets operating at (a) *VR* = 0.95 and (b) *VR* = 0.36 (Schaeffler 2003).

Milanovic and Zaman (2005) used a distance y_{max} to denote the location of the peak in the fundamental (rms) intensity profile in order to measure the penetration of synthetic jets. They found that at a given streamwise location, y_{max} solely depends on *VR*. In addition, for a given cross flow, the overall features of synthetic jets were found to be similar to that of steady jets at $x/D_o = 5$ with the same *VR* (*VR* ≈ 2.45 based on the maximum velocity), in terms of the jet penetration and the cross-sectional distributions of mean velocity, streamwise vorticity and turbulence intensity. Furthermore, the cross-sectional distributions of streamwise mean velocity of synthetic jets from a cluster of orifices having the same orifice area were found to be similar to that from a single orifice, just a few diameter downstream. However the jet penetration of cluster orifices is less than that of the single orifice, as a result of an increased mixing with the cross flow.

Gordon et al. (2004) utilized Planar-laser-induced fluorescence (PLIF) measurement to study the properties of a circular synthetic jet in cross flow, for a

range of Strouhal numbers, Reynolds numbers and velocity ratios. A characteristic jet velocity was proposed to calculate Re, *Str* and *VR*, which can be defined as $U_j = U_{prms}\left(D_c/D_o\right)$, where U_{prms} is the rms diaphragm velocity. Hence $\mathrm{Re} = \frac{U_j D}{\nu}$, $L = 2\left(\frac{D_c}{D_o}\right)^2 \frac{\Delta}{D_o}$, and $Str = \frac{fD_o}{U_j} = \frac{\sqrt{2}}{\pi L}$. Two distinct jet flow patterns were observed: single trajectory jets and multiple trajectory jets, which are distinguished by a critical Strouhal number of $Str_{\mathrm{crit}} = 0.02$, as shown in Fig. 2.13. Single trajectory jets which have similar flow patterns to the ensemble-averaged steady jets represented mixing of the bulk of fluid outside the upstream boundary layer (Fig. 2.13a). While multiple trajectory jets are characterized by two thin regions of high concentration. The upstream vortex ring trajectory is normal to the wall demonstrating greater penetration into the ambient cross flow, whereas the downstream trajectory is parallel to the wall (Fig. 2.13b). Furthermore, for single trajectory synthetic jets (*Str* < 0.02), the jet penetration does not depend on the velocity ratio. And the jet penetration decreases with increasing Reynolds number and Strouhal number, which is similar to the results of pulsed jets by Chang and Vakili (1995).

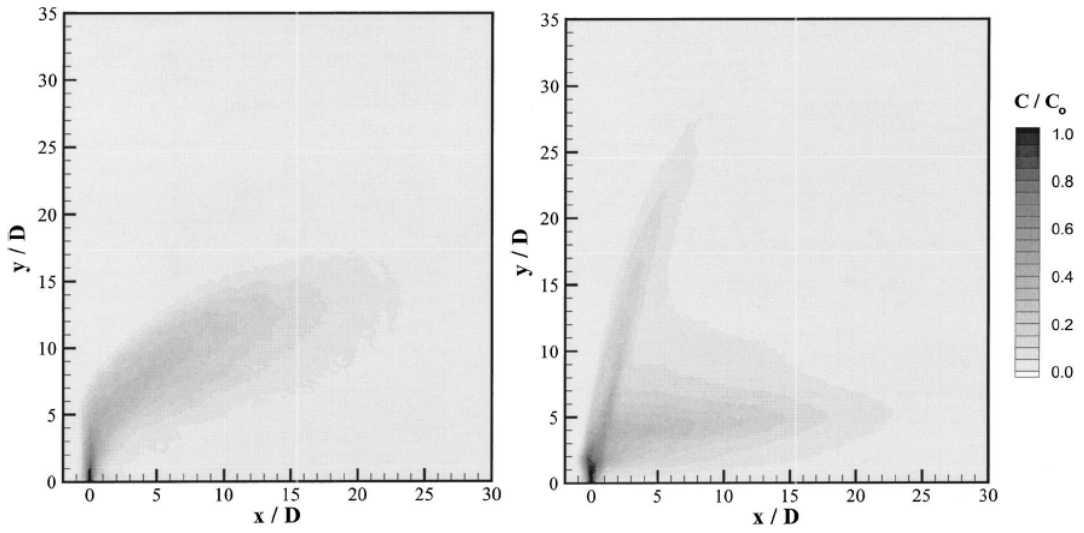

Figure 2.13. Mean intensity images of (a) single trajectory jet at *Str* = 0.014, *VR* = 20, Re = 14080 and (b) multiple trajectory jet at *Str* = 0.077, *VR* = 10, Re = 2640. Cross-flow is from left to right (Gordon et al, 2004).

Despite the evolving understanding of the flow behaviour arising from isolated SJAs in a cross flow, the interaction between multiple synthetic jets has not been addressed with a sufficient level of details.

Smith (2002) investigated the interaction between a 2D slot synthetic jet array and a turbulent boundary layer using hot wire anemometry. The 2D slot synthetic jets were operated at VR = 1.2 based on the average orifice velocity, L = 12.5 and $\mathrm{Re}_{lo} = 1.35\times10^4$. Two distinct flow fields were observed downstream of the synthetic jet array at two configurations. In the spanwise configuration (the major axes of the actuator orifices are coincident and oriented perpendicular to the cross flow direction), the boundary layer was characterised by a wakelike region in the lee side of the jet due to a blockage effect and the maximum penetration height was 0.8δ. In addition, the jet trajectory was found to follow the power law scaling for a steady jet in cross flow indicating the interaction contains a similar counter-rotating vortex pair aligned in the streamwise direction. While in streamwise configuration (the major axes of the orifices are parallel and also parallel to the cross flow direction), the flow structure was consistent with the presence of longitudinal vortices embedded in the boundary layer, and the penetration reached the edge of the boundary layer.

Watson et al. (2003) carried out a preliminary study of flow interaction between a pair of circular synthetic jets in still air, in a laminar boundary layer and in a turbulent boundary layer. With the help of flow visualization, it was found that the trajectory of adjacent synthetic jets would be changed and move toward each other with the decrease of the orifice spacing. A very small orifice spacing would make the two adjacent synthetic jets have immediate interaction out of the orifice, and generate a single, large vortex ring. On the other hand, for a set spacing, the interaction between rings was found to be changed with the decrease of yaw angle. Therefore, they suggested that the combined effect of the yaw angle and the orifice spacing would enhance or reduce the amount of vorticity in the flow. However, quantitative data was required to clarify the variation of vorticity. Subsequently, using oil flow visualization and streamwise velocity contour mapping, Liddle and Wood (2005) demonstrated that the mode of interaction between two circular synthetic jets and a turbulent boundary layer can be controlled by the yaw angle, and the input signal phase can influence the stability and effectiveness of flow structures.

A synthetic jet issued into a cross flow exhibits a rich and complex structure due to the fluid from the two streams meet and interact. The most interesting feature of synthetic jets in cross flow is the counter-rotating vortex pair that is created by the cross flow interaction. The vortical structure transports high momentum fluid from the freestream to the near-wall region, forming a fuller velocity profile that is beneficial to the delay of boundary layer separation. Therefore, the investigation of vortical structures produced by synthetic jets in cross flow, i.e. their formation, evolution and decay, as well as their influence on the near-wall flow, is essential to obtain an improved understanding of this interaction, and is helpful to find the desired vortical structures on delaying flow separation.

Zhong et al. (2005) used dye flow visualization to study the nature of vortical structures produced by circular synthetic jets with Re ranging from 16 to 245, *VR* from 0.06 to 0.7, *Str* from 0.1 to 0.5 and *L* from 0.56 to 1.4. The parameter range was chosen such that reasonably clear dye flow visualization images were obtained for a given synthetic jet actuator and the boundary layer. It turned out that different types of vortical structures were captured at different Re and *VR*. At low Re and *VR*, the vortical structures appear as highly stretched hairpin vortices attached to the wall (Fig. 2.14a). At intermediate Re and *VR*, the structures roll up into vortex rings which experience a considerable amount of tilting and stretching as they enter the boundary layer. Thus the stretched vortex ring type of structures with a weak upstream branch forms (Fig. 2.14b). At high Re and *VR*, the vortex rings appear to experience a certain amount of tilting without obvious stretching, and penetrate the edge of boundary layer in a short time (Fig. 2.14c).

Based on the experimental observations, Zhong et al. (2005) explained that the formation of hairpin vortices is due to the suppression of the upstream branch of the vortex ring by the resident vorticity in the boundary layer, which has the opposite sense of rotation of the upstream branch. Contrarily, the downstream branch is enhanced by the resident vorticity. This asymmetric structure propagates within the boundary layer, and eventually develops to a hairpin vortex with the legs trailing along the wall for a significant distance. On the other hand, when the synthetic jets emerge from the orifice as strong vortex rings, the rings will penetrate the boundary layer at a certain distance downstream of the orifice depending on the strength of the vortex ring, hence the impact on the near-wall flow is found to be limited. Therefore, Zhong et al. (2005) suggested that the hairpin vortices could be the desirable vortical

structures required for effective flow control with minimal power consumption. And the streamwise vortical structures observed by Crook et al. (1999, 2000) on the cylinder model are probably produced by the overlapping legs of hairpin vortices. However, above conjectures need the confirmation of further quantitative measurements.

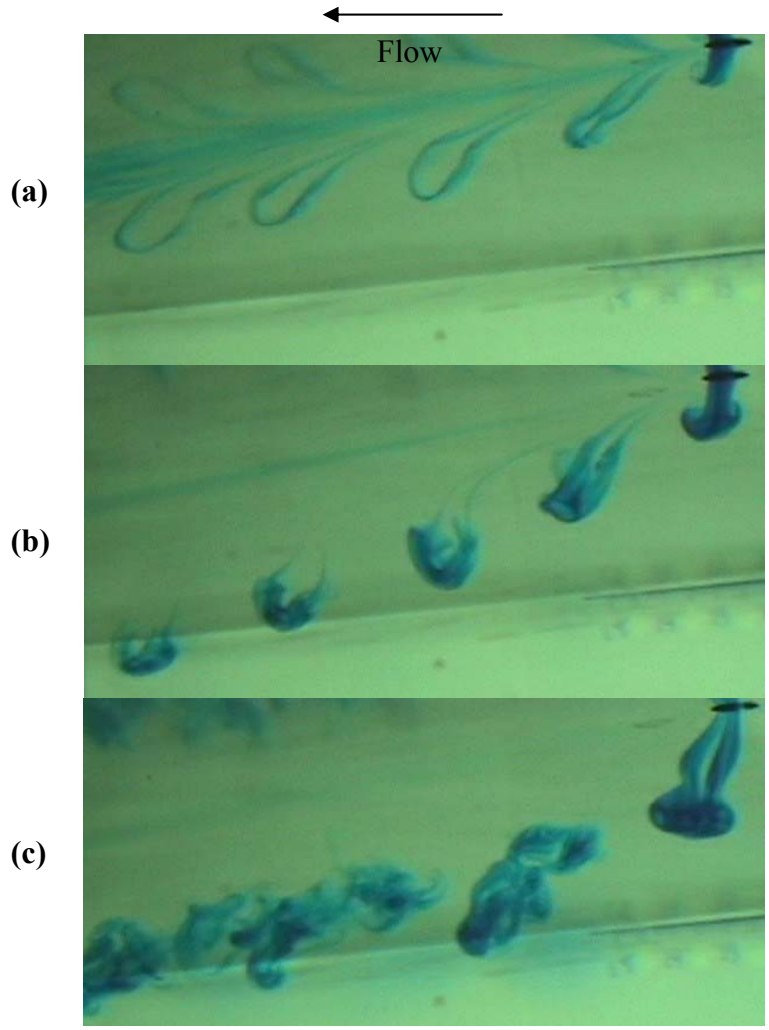

Figure 2.14. Dye visualisation of vortex structures produced by synthetic jets in a laminar boundary layer: (a) hairpin vortices; (b) stretched and tilted vortex rings; and (c) distorted vortex rings (modified from Zhong et al, 2005).

Subsequently, Jabbal and Zhong (2007, 2008) investigated the interaction of a circular synthetic jet with the near-wall region and observed three main synthetic jet structures, namely hairpin vortices, stretched vortex rings and tilted vortex rings, which are similar to the findings of Zhong et al. (2005). The impact of these three types of structures on a laminar boundary layer was quantified and their potential flow separation control effectiveness was compared using wall shear stress. The flow visualization and the corresponding surface liquid crystal visualization indicated that

both hairpin vortices and stretched vortex rings exhibit similar characteristics to a longitudinal vortex pair embedded in a boundary layer, which induces an upwash movement between the counter-rotating legs and a downwash movement outboard of the legs as marked by the thermal footprint (Figs. 2.15a and b). On the contrary, trailing legs associated with the tilted vortex rings induce a tertiary vortex pair in the near-wall region, which produces a common flow towards the wall, and therefore the thermal footprint has a single streak of high heat transfer along the centreline (Fig. 2.15c). By correlating the vortical structures delaying flow separation on a cylinder observed by Crook et al. (1999, 2000), both hairpin vortices and stretched vortex rings appear potentially useful in flow separation control. It also supported the belief that the interaction of a synthetic jet with a laminar boundary layer is essentially same to that with a turbulent boundary layer. Furthermore, parameter maps based on *VR*-*L* and Re_L-*VR* of different vortical structures were established which is useful to identify the conditions that ensure the formation of such structures, as shown in Fig. 2.16. It was found that both hairpin vortices and stretched vortex rings form at *VR* < 0.4 approximately.

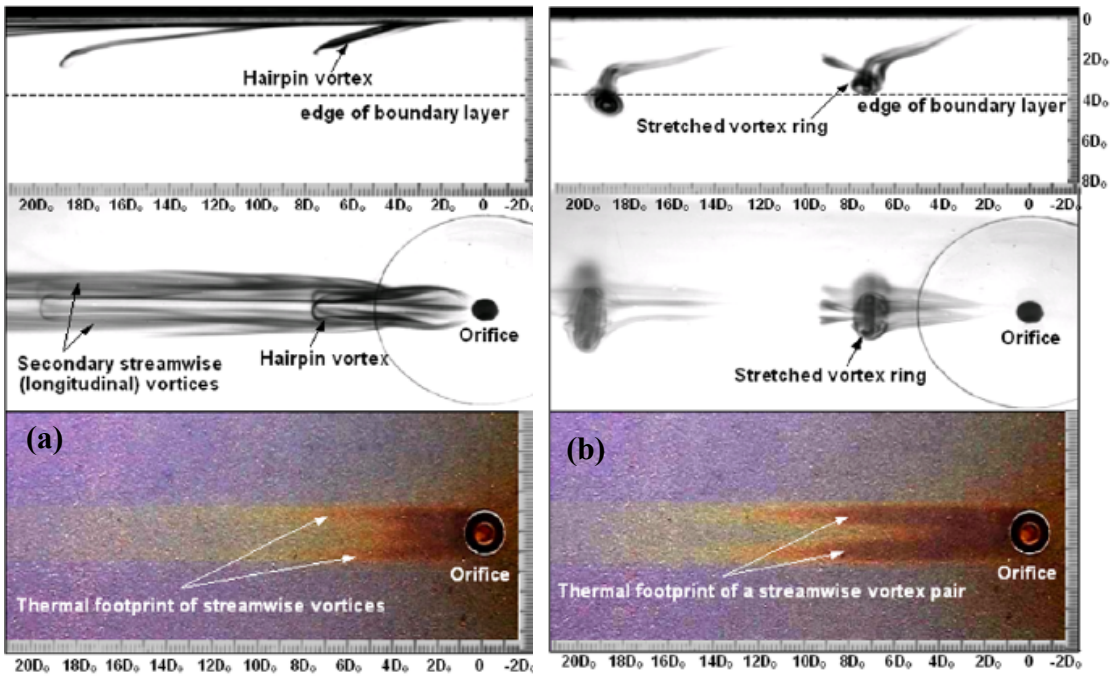

For caption see overleaf

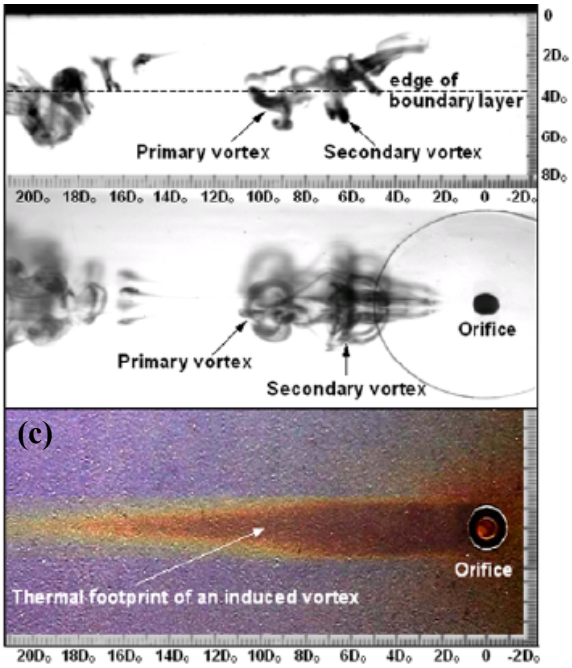

Figure 2.15. Stereoscopic dye and surface liquid crystal images of a synthetic jet showing (a) hairpin vortices at VR = 0.14, Re_L = 46 and L = 1.4; (b) stretched vortex rings, VR = 0.27, Re_L = 182 and L = 2.7; and (c) distorted vortex rings, VR = 0.51, Re_L = 658 and L = 5.1 (Jabbal and Zhong, 2008).

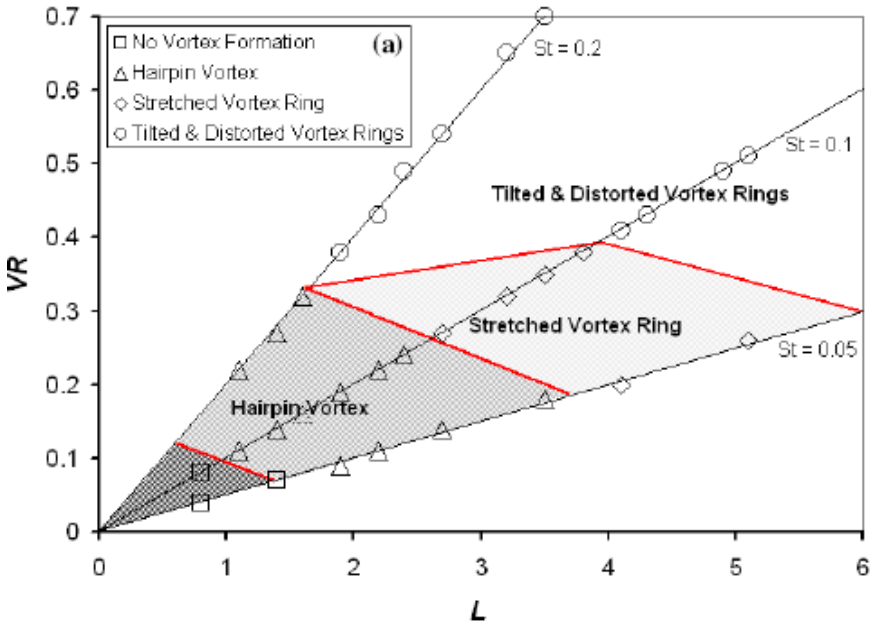

For caption see overleaf

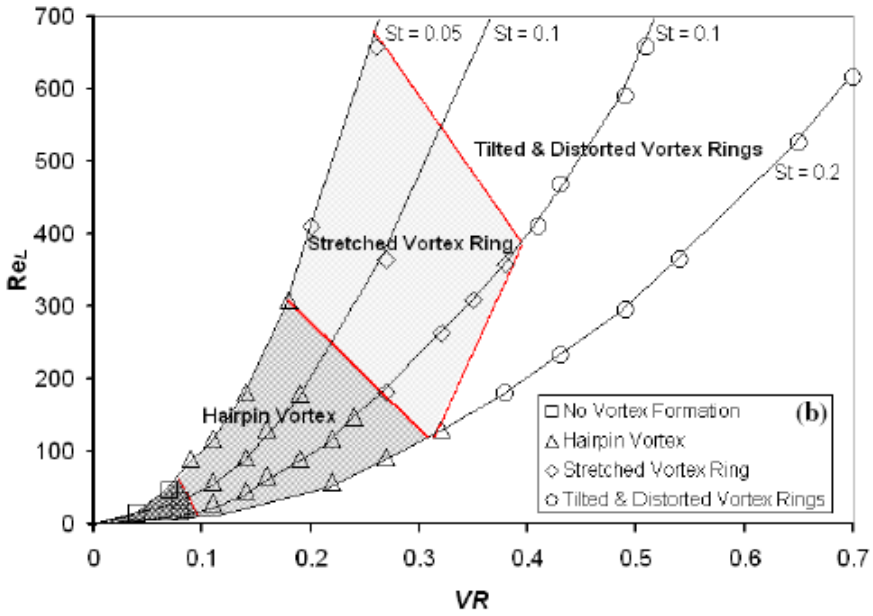

Figure 2.16. (a) *VR-L* and (b) Re_L-*VR* parameter space of the different vortical structures as a result of the interaction between a synthetic jet and a boundary layer (Jabbal and Zhong, 2008).

Garcillan et al. (2005, 2006) used hot wire and PIV measurement to study the evolution of synthetic jets in a turbulent boundary layer. The streamwise velocity contours on the streamwise central plane indicated that for low velocity ratio, the distance from the vortical structures to the near-wall region is small, and thus the effect on the lower part of the boundary layer increases which is beneficial for flow control. In addition, the spanwise flow patterns implied the presence of a pair of streamwise counter-rotating vortices, which are the legs of hairpin vortices. These quantitative findings for synthetic jets in a turbulent boundary layer are similar to those observed by Zhong et al. (2005) and Jabbal and Zhong (2007, 2008) in a laminar boundary.

All the aforementioned qualitative and quantitative investigations arrived at a consensus that the interaction of synthetic jets with a laminar boundary layer and a turbulent boundary layer is essentially similar, which produces hairpin vortices embedded in the boundary layer. Many researchers have suggested hairpin-type vortex is a basic and dominant flow structure in the energy transport within a turbulent boundary layer and is probably responsible for the delay of flow separation. (Theodorsen, 1952; Head and Bandyopadhyay, 1981; Smith, 1984; Acarlar and Smith, 1987a, b; Smith et al, 1991, Robinson, 1991; Haidari and Smith, 1994; Zhou et al, 1999). Figure 2.17 shows a typical hairpin vortex for illustration purpose. It

consists of a vortex head and vortex legs which are mainly aligned in the streamwise direction and close to the wall.

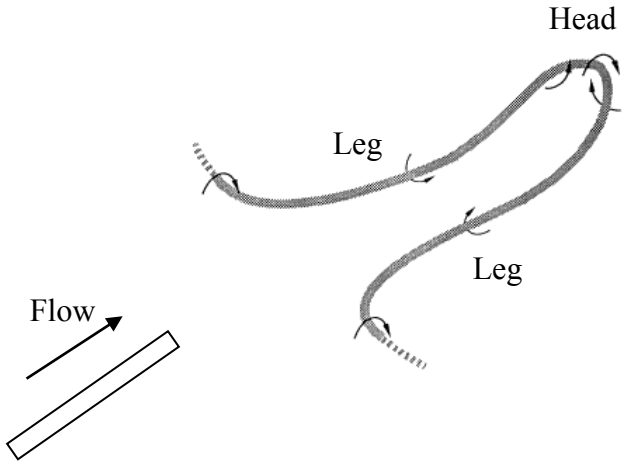

Figure 2.17. Schematic of typical hairpin vortex configuration, with sense of vorticity (modified from Smith et al, 1991).

A hairpin vortex would either decay or grow when developing downstream (Haidari and Smith, 1994). The decaying hairpin vortex imposes little effect on the near-wall flow with the diffusion of initial vorticity. Contrarily, the growing hairpin vortex has a strong interaction with the near-wall flow resulting in sharp fluid eruptions. Consequently, new vortices will be formed both laterally and in its wake under this stimulation, as shown in Fig. 2.18. Both secondary hairpin vortices and subsidiary vortices can be observed accompanied with the primary hairpin vortex. The subsidiary vortices are believed to be associated with the inviscid deformation of the vortex lines comprising the primary vortex (Smith et al, 1991). While the secondary hairpin vortices are formed due to inviscid/viscous interactions between outer-layer fluid and strong eruptions of surface fluid which are caused by the interaction of the primary hairpin vortex with the surface. Figure 2.19 shows the generation of secondary vortices via surface interaction for a hairpin vortex (Smith et al, 1991):

1. Sharp, crescent-shaped ridge develops in the surface flow where the induced pressure gradient near the surface is adverse (Fig. 2.19a). For the symmetric hairpin vortex, an adverse pressure gradient (i.e. an eruption of the surface layer) occurs behind the vortex head and near each trailing leg;

2. The erupting ridge containing concentrated vorticity moves outward rapidly (Fig. 2.19b);
3. The erupting sheet starts to roll over from the tip of the tongue and the roll-over spreads outboard along the rest of the ridge (Fig. 2.19c);
4. A majority of the sheet has rolled up (Fig. 2.19d);
5. Secondary hairpin vortices are generated completely (Fig. 2.19e).

The newly formed secondary hairpin vortices may intertwine with the primary hairpin vortex, or produce further hairpin vortices. Secondary and tertiary vortices have been observed under appropriate conditions (Acarlar and Smith, 1987b; Zhou et al, 1999; Smith et al, 1991)

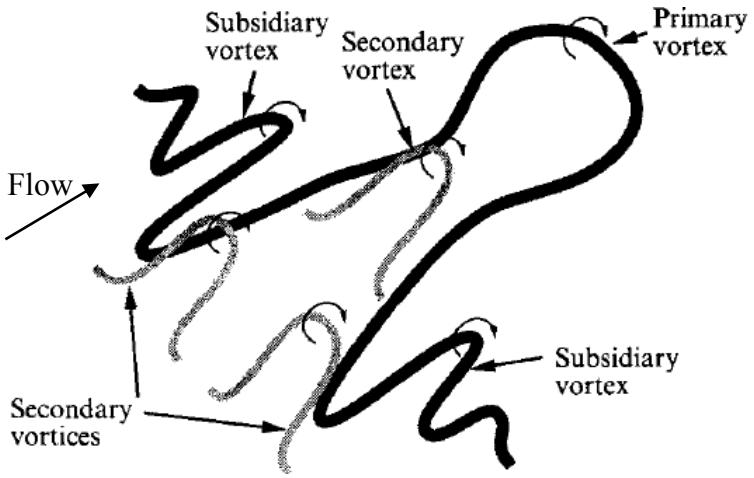

Figure 2.18. Schematic of the hierarchy of hairpin vortices (Haidari and Smith, 1994).

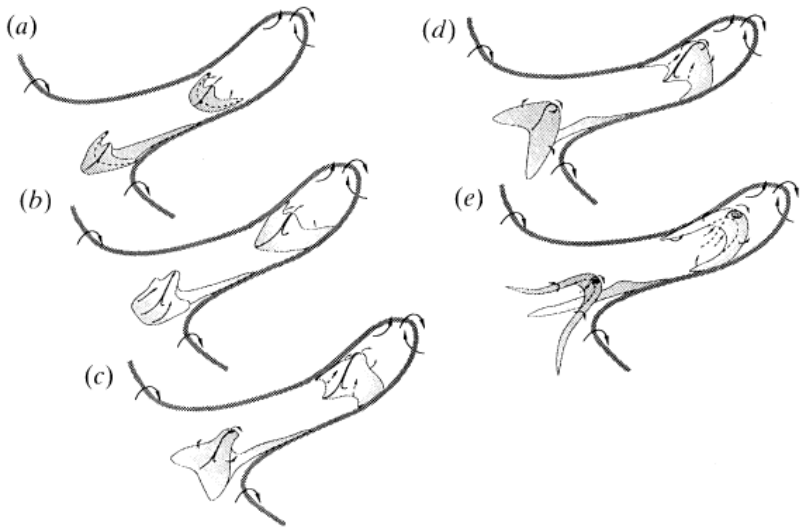

Figure 2.19. The generation of secondary vortices via surface interaction for a hairpin vortex (Smith et al, 1991).

Although the aforementioned hairpin vortices are not produced by synthetic jets, it is believed their development and growth are similar to the hairpin vortices produced by synthetic jets.

2.2.2.3 Interaction with a Separated Flow

The capability of synthetic jets in delaying flow separation has been introduced briefly in section 2.1.2. In this section, more detailed discussion for both 2D slot synthetic jets and circular synthetic jets interacted with a separated flow will be provided.

Currently, 2D slot SJAs have been used to study the flow separation control of a 2D cylinder (Amitay et al, 1998), low-speed aerofoils (Smith et al, 1998; Amitay et al, 1999), and multi-element aerofoils at representative flight Reynolds numbers (Seifert and Pack, 1999; Khodadoust and Washburn, 2007), whereas circular SJAs have been used in the form of an array of round jets on a circular cylinder (Wood et al, 2000).

McCormick (2000) used a 2D slot synthetic jet to control a 2D airfoil leading-edge separation. The synthetic jet, operating at forcing frequency f = 50Hz, was injected at a 4% chordwise location, upstream of the leading-edge separation which was located at 8% chord approximately. The wind tunnel speed was set at M = 0.025 and Re = 2.5×10^5. Hence the non-dimensional forcing frequency F^+ is 2.6. Smoke was introduced just upstream of the leading edge for a post-stall angle of attack (α = 24 deg) to visualize the flow on the airfoil at different levels of forcing represented by momentum coefficient C_μ (Fig. 2.20). As shown in Fig. 2.20a, at C_μ = 0, the flow separates from the leading edge, shedding vortical structures in the shear layer. At C_μ = 0.005, the flow turns towards the airfoil more, and three vortical structures locked to the forcing frequency over the airfoil chord can be observed (Fig. 2.20b). When C_μ varies between 0.01 and 0.015, the flow is fully attached without coherent structures over the airfoil, which implies that the synthetic jet delivers its full capability to suppress the flow separation by energizing the boundary layer (Fig. 2.20c). If the level of forcing increases further to 0.04-0.068, vortical structures are again visible, but with the opposite sense of rotation indicating that the forcing level is above the optimal value (Fig. 2.20d). At this higher level of forcing, the flow

behaviour is analogous to the synthetic jet in quiescent condition, in terms of the sense of rotation of the vortical structures.

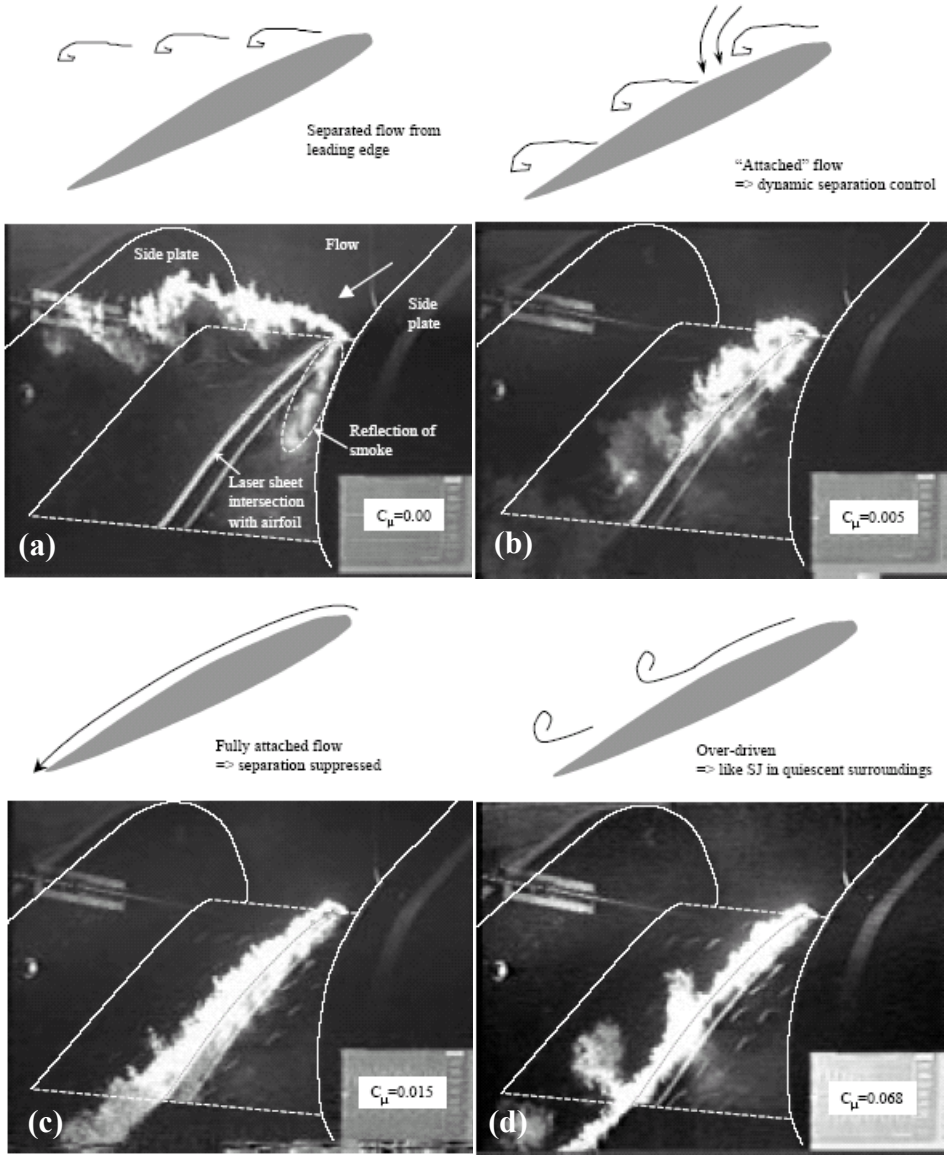

Figure 2.20. Flow separation control on an aerofoil leading edge using synthetic jets: (a) without control, C_μ = 0; (b) under-driven, C_μ = 0.005; (c) fully controlled, C_μ = 0.015; (d) over-driven, C_μ = 0.068 (McCormick, 2000).

Gilarranz et al. (2005) applied a 2D synthetic jet to the flow over a NACA0015 wing at U_∞ = 35 m/s and Re = 8.96×10^5 (based on the wing chord). The exit slot of the actuator was placed at 12% of the chord, on the top surface of the wing (Fig. 2.21a), and was machined to make the jet exit tangentially to the wing surface. Figs. 2.21b and c show the smoke flow visualization without and with synthetic jet actuation at f = 120 Hz, F^+ = 1.13, C_μ = 0.0123 at an angle of attack of

25 deg. Without SJA actuation the flow is separated close to the leading edge, while with SJA actuation the flow is attached over the wing chord.

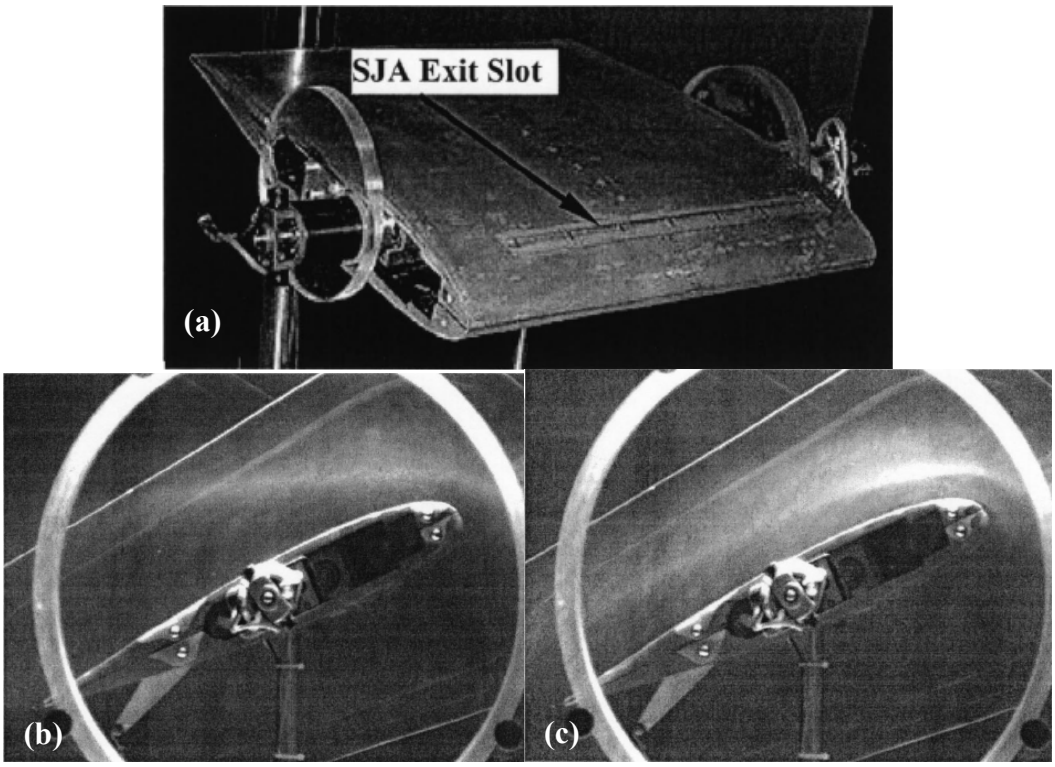

Figure 2.21. Flow separation control over a NACA0015 wing using synthetic jets: (a) the location of the synthetic jets exit slot; (b) flow visualization without actuation and (c) flow visualization with actuation (Gilarranz et al, 2005).

Both aforementioned investigations suggest that there are some primary controlling parameters need to be identified when applying synthetic jets on airfoil, such as dimensionless frequency F^+, excitation level C_μ, excitation location and slot orientation (Greenblatt and Wygnanski, 2000). It is found that for the majority of cases, the optimum dimensionless frequencies vary in the range of $0.3 \leq F^+ \leq 4$, whereas investigations by Glezer and his co-workers suggested that at high reduced frequencies ($F^+ = 10$ or 20), flow separation is also effective and the lift-to-pressure drag ratio appears to be invariant with the actuation frequency (Amitay et al, 2001). The effective excitation level proposed by Greenblatt and Wygnanski (2000) is in the range: $0.01\ \% < C_\mu < 3\ \%$. And the excitation which is applied at or close to the leading edge is found to be effective for a wide variety of airfoil, although the precise location may vary for different airfoils. It is interesting to find that the results of the aforementioned two studies are consistent with the propositions of Greenblatt and Wygnanski (2000) as a whole. Furthermore, it is noticed that McCormick (2000)

and Gilarranz et al. (2005) both employed tangential orientation of slot. This kind of slot orientation coupled with the use of high-powered SJAs indicates that the control method used in these studies inclines to augment the momentum of the boundary layer directly, making the boundary layer more resistant to separation.

Unlike 2D slot synthetic jets, which have been investigated extensively on various aerodynamic models, the array of circular synthetic jets is less well studied. Extensive experimental studies aimed at understanding the fluid mechanics of circular synthetic jets and their potential in delaying flow separation have been undertaken at the University of Manchester since 1998 (Wood et al, 2000; Crook, 2002; Zhong et al, 2005; Garcillan et al, 2005; Jabbal and Zhong, 2008). As shown in Fig. 2.8, the separation line is pushed downstream where the synthetic jets are actuated upstream. And it was observed that the footprints of streamwise vortical structures produced by an array of circular synthetic jets (in the time-averaged view) are quite similar to that produced by passive VGs and active VGJs. Figure 2.22 shows the oil streaklines and the corresponding flow topology of a streamwise vortex pair produced by the synthetic jets issued into a separated turbulent flow (Crook, 2002). As explained in section 2.1.2, these streamwise vortices are capable of entraining the high momentum fluid from outer region of the boundary layer to the near-wall region, and therefore enhancing fluid mixing and energizing the boundary layer to resist the separation.

Although the potential of synthetic jets in flow separation control has been demonstrated in the existing literature, there is a large gap between the SJAs used in laboratory demonstrations and that needed in realistic, full-scale applications, in terms of compactness, weight, efficiency, control authority and power density. Compared with 2D slot synthetic jets, circular synthetic jets may be more attractive in flow control application at civil aircraft scale, especially in MEMS based devices, since they are space saving and easily arranged. This is also the reason why the present study focuses on circular synthetic jets.

2.2.2.4 Synthetic Jet Flow Control Effectiveness

According to the separation control roadmap in Fig. 2.4, some general measures can be used to evaluate the potential flow control effectiveness of a synthetic jet in terms

of an increase in wall shear stress or a decrease in shape factor. Both parameters are linked to an enhanced near-wall fluid mixing.

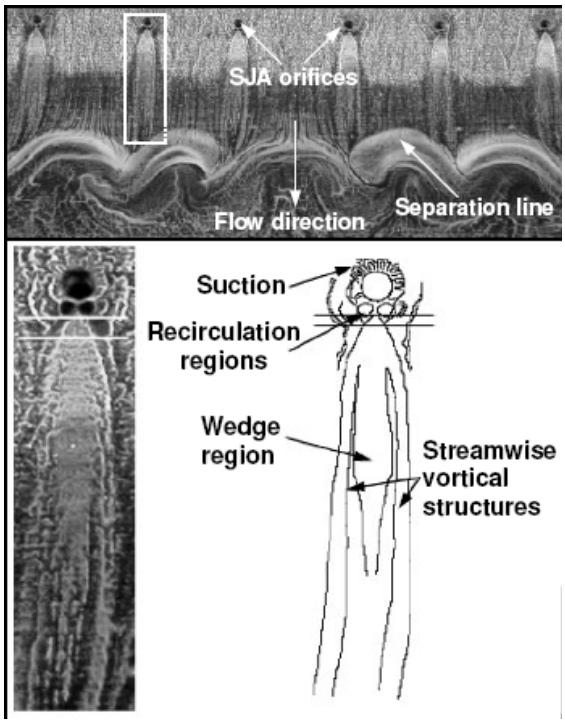

Figure 2.22. Surface flow visualization and topology for the interaction of a synthetic jet with a separated flow (modified from Crook, 2002).

The aforementioned investigations on synthetic jets in attached flows and separated flows indicated that the performance of synthetic jets in flow separation control is governed by the behaviour of vortical structures produced by the interaction of the synthetic jets with the cross flow. Therefore, the type of vortical structures, their strength, and their location in the boundary layer are the important factors affecting the flow control effectiveness. It is also noted that the strength and location of vortical structures dictate their persistency during their streamwise development.

Godard and Stanislas (2006b) discussed briefly about the 'optimal' control with an 'optimal' structure. Both experiments and numerical simulations indicated the streamwise (or more precisely quasi streamwise) vortices play an important role in the near-wall region of the boundary layer. They are capable of transferring the momentum towards the wall and increasing the skin friction. Therefore this kind of vortical structures is considered as a good candidate for an 'optimal' structure. This definition of the 'optimal' structures complies with the mechanism for flow

separation control in section 2.1.1. The studies of VGs for flow separation control also confirm above statement. The results presented by Lin (2002) indicated that the embedded streamwise vortices produced by low-profile VGs (submerged VGs and micro VGs) provide the most effective and efficient means of delaying turbulent boundary layer separation, whereas the spanwise vortices produced by spanwise cylinder do not perform as good as the streamwise vortices. In addition, according to the discussion in section 2.2.2.2, the quasi streamwise vortices in the form of hairpin vortices are the dominant flow structures in turbulent boundary layers, which have been presented in a conceptual model provided by Utami and Ueno (1987) (Fig. 2.23). Therefore, it is possible that the structures shown in Fig. 2.23 are the 'optimal' structures proposed by Godard and Stanislas (2006b).

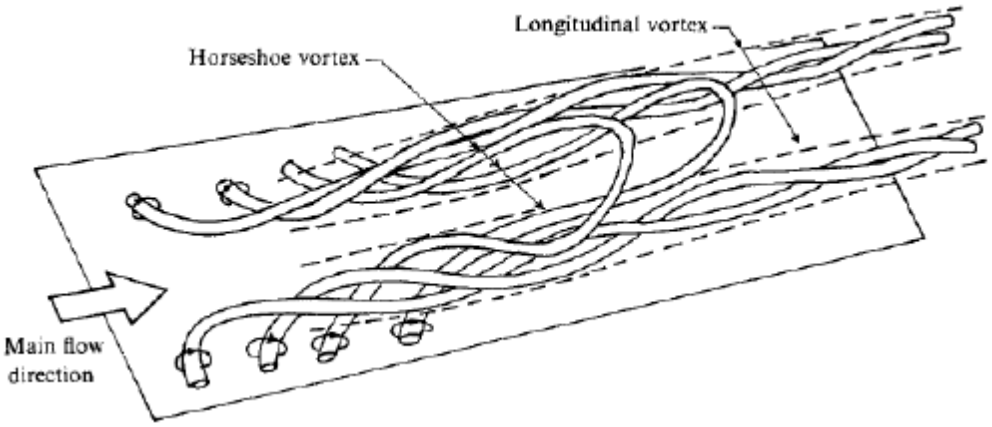

Figure 2.23. Schematic of the proposed, overall structure of turbulence in the wall region of a turbulent boundary layer (Utami and Ueno, 1987).

According to the discussion of dimensionless parameters in section 2.2.2.1, the Reynolds number quantifies the strength of the vortical structures and the velocity ratio characterises the trajectory of synthetic jet. At high Re, the strength of vortical structures is increased which could enhance the near-wall fluid mixing and the wall shear stress via intense momentum redistribution, however a too high Re will cause the vortical structures break through the boundary layer, which reduces their effect on the near-wall region. At high *VR* or very small *d*, the vortical structures will penetrate the boundary layer shortly downstream, and therefore, the effect on the boundary layer is expected to be limited. Furthermore, the scaling law proposed by Raju et al. (2005), for the vorticity flux of a synthetic jet in a zero-pressure-gradient laminar boundary layer, showed that if the geometry and the

boundary layer thickness are fixed, the non-dimensional vorticity flux scales with the natural logarithm of the jet Reynolds number Re_j, a negative power of *Str* based on the jet velocity and a linear function of VR^{-1}. Hence, the vorticity associated with the vortical structures of a synthetic jet is enhanced at a high Re and a low *VR*. It is preferred that the vortical structures would be generated with a high strength, while their trajectory is in the boundary layer to make sure a sufficient impact on the near-wall flow.

Some literature related to vortex generating devices for separation control found that vortex displacement in the outer region of the boundary layer is more effective for enhancing fluid mixing. For VGs applied for delaying flow separation, Chang (1976) suggested that the vortices must stay close to the edge of the boundary layer, in order to produce a substantial interchange between high and low momentum air. Johari and Rixon (2003) compared the behaviour of pulsed jets and steady jets at the same *VR* and indicated that the pulsed jets penetrate further into the boundary layer (50% further than a steady jet), which is probably the reason for the superior performance of pulsed jets observed in flow separation control. Zhang and Collins (1993) studied the effect of longitudinal vortices generated by steady jets on flow and heat transfer control at the wall of a turbulent boundary layer, using numerical simulation, and observed three types of vorticity distribution (corresponding to low, intermediate and high *VR*):

1. Longitudinal vortex is deeply embedded in the turbulent boundary layer – the vortex is diffused rapidly due to the strong turbulent diffusion and can not remain coherent over a long distance downstream;
2. Longitudinal vortex is located at the edge or in the outer region of the boundary layer – a balance is achieved between the vortex diffusion and its ability in flow control. The vortex remains coherent for a suitable distance downstream, and the maximum skin friction coefficient increases rapidly.
3. Longitudinal vortex is located outside of the turbulent boundary layer – although the vortex may be strong and remains coherent, the flow control effect is reduced.

The consensus obtained from the studies on passive VGs, pulsed jets and steady jets appears to be consistent with the scaling law of Raju et al. (2005) who suggested that the synthetic jet is preferred to be operated at low *VR* (equivalent to short distance to the wall). Therefore, the vortical structures produced by synthetic

jets will be located in the outer part of the boundary layer to enhance their persistence and effectiveness via fluid mixing.

The 'optimal' vortical structures for a synthetic jet were summarized by Jabbal (2008) as follows:

1. $L > 1$ to ensure the jet formation and $S > 10$ to ensure the vortex roll-up;
2. *Str* should not be too high, since the strong interaction between successive vortices would impair the strength of vortical structures and make them incoherent.
3. The vortical structures produced by synthetic jets are composed mainly or fully of streamwise vorticity, which is effective for enhancing fluid mixing and wall shear stress.
4. The formed vortices with high strength should be located at the edge of the boundary layer with high strength. Therefore, appropriate Re and *VR* are needed to balance the strength and trajectory of vortices.

It is noted that the aforementioned discussion of synthetic jet effectiveness focuses on finding an 'optimal' vortical structure in delaying or eliminating flow separation, the efficiency of synthetic jet is not considered. As mentioned in section 2.1.1, the ideal flow separation control is to maximize the control effectiveness while minimizing the penalty.

Tang et al. (2007) developed a methodology of designing circular SJAs for full-scale flight conditions. A flow chart summarizing the design procedure is shown in Fig. 2.24. This methodology complies with both the physical constraints imposed on the actuator geometry and the criteria for maximizing the effect of the synthetic jets on the local boundary layer. The physical constraints include the ratio of orifice diameter to the boundary layer thickness ($D_o < 5\sim20\%\delta$) and the selection of H, h and D_c determined by the geometric constraints and the operating conditions. While the criteria for maximizing the control effectiveness may include $S > 10$ to ensure the vortex roll-up, $1 < L < 5$ and $0.1 < VR < 0.5$ to ensure the formation of hairpin vortices, and Helmholtz-resonance operating condition. Finally, they suggested that for a typical wing of a commercial aircraft at the take-off condition, at the trailing edge of the flap where $M = 0.3$, $\delta = 5$ mm, the actuator design should be: $D_o = 0.5$ m, $D_c = 6$ mm, $h = 0.5$ mm, $H = 1$ mm, $\Delta = 0.05$ mm and $f = 5$ kHz.

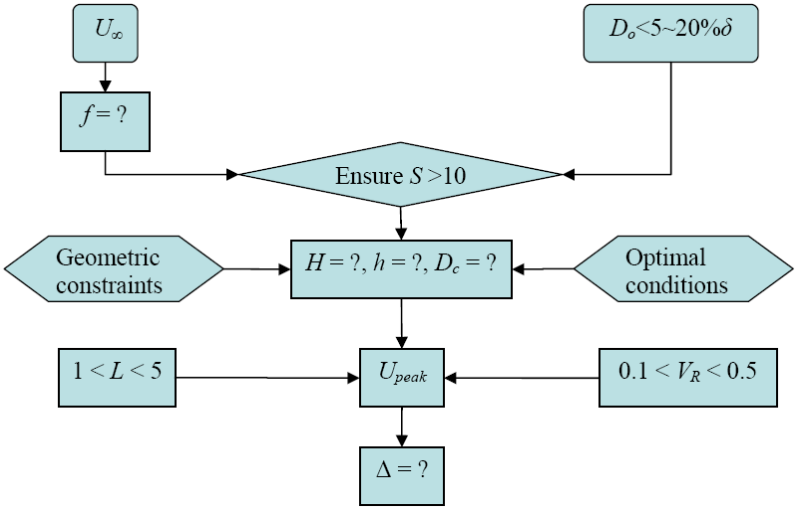

Figure 2.24. The flow chat showing the procedure for designing SJAs for flight conditions (Tang et al, 2007).

Comes et al. (2006) carried out three industrial scale case studies (a flap, a slat, and a cruise for both separation control and shock control) to evaluate the mass and power requirements for a SJAs system applied to an A321 aircraft. The operating conditions of SJAs were selected based on empirical evidence for effectiveness: VR = 1, D_o/δ = 1/5 and the spacing between actuators is $10D_o$. Through the optimization of SJAs, the peak velocity achieves 130 m/s and the peak conversion efficiency is about 15%. The tests results indicated that all system's power requirements were within the limit of an Auxiliary Power Unit (APU) power rating typically found in an aircraft of this class. Although it is possible to realistically design a synthetic jet flow control system within the aircraft performance limit, the question whether the performance benefits outweigh the system cost is still unsolved.

Recently, Jabbal et al. (2009) compared the power and mass costs of implementing four different flow control methods (pulsed jet actuators via direct bleed, electric pulsed jet actuators, SJAs and plasma actuators) in flow separation control applications on an A320 aircraft. The operating conditions of these four actuators are same, and are also identical to that used by Comes et al. (2006). The power conversion efficiency for SJAs is assumed to 10 %. The case study indicated that among these four methods, the power specific mass for the SJA flow control system is the lowest, only 1 kg/kW approximately. In addition, the implementations of more efficient single-crystal piezoelectric diaphragm are helpful to improve the mass efficient of flow system. As a result, the required power and mass of a flap

application could feasibly be reduced to 6 % of engine power and 1 % of flap mass, respectively.

2.3 CFD Simulations of Synthetic Jets

As a result of increases in computer storage capacity and speed, the tremendous increases in CFD capability are transforming flow separation control from an empirical art to a predictive science. The purposes of numerical simulations of synthetic jets are to examine the modelling capacity of CFD codes, to shed light on understanding the complex behaviour of synthetic jets and to complement the vital information which could be difficult to derive from experiments.

2.3.1 Synthetic Jets in Quiescent Conditions

In parallel to the experimental study, extensive studies have been conducted on numerical modelling of synthetic jets generated at quiescent external flow conditions (Kral et al, 1997; Rizzetta et al, 1999; Mallinson et al, 1999, Mittal et al, 2001; Utturkar et al, 2002, 2003; Spencer et al, 2004; Holman et al, 2005; Kotapati and Mittal, 2005; Carpy and Manceau, 2006; Wu and Leschziner, 2006, 2009). A key problem for the synthetic jet simulation is how to establish a more realistic boundary condition, especially at the location of diaphragm. From a numerical point of view, the flow inside and outside the actuator must be resolved to capture the dynamics of the momentum and vortex injection process. However, no consensus was achieved in terms of simulating the flow field inside the cavity and orifice.

Kral et al. (1997) carried out two-dimensional calculations of both laminar synthetic jets and turbulent synthetic jets using an incompressible flow solver, INS2D, and the latter is obtained by the solution of unsteady Reynolds-averaged Navier-Stokes (URANS) equations with Spalart-Allmaras (SA) one-equation turbulence closure. The synthetic jets were similar to the ones studied experimentally by Smith and Glezer (1997). The computational domain encompassed only the region external to the jet without the cavity or oscillating diaphragm. Different analytic velocity profiles at the orifice exit were applied to simulate the presence of jet. Turbulent results for the streamwise variation of the centreline velocity and cross-stream distributions of the streamwise velocity were in good agreement with

the measurements of Smith and Glezer (1997): the near field is dominated by the formation of counter-rotating vortex pairs. However, further away from the jet, vortex cores in the turbulent simulation became smeared by turbulent diffusion and the lack of three-dimensionality in the laminar simulation failed to capture the breakup of the vortex train observed in the experiments.

In the work by Rizzetta et al. (1999), the direct numerical simulation (DNS) of unsteady compressible Navier-Stokes equations was used to investigate two- and three-dimensional flow field of finite aspect-ratio synthetic jets which have been studied by Smith and Glezer (1997) and Kral et al. (1997). An overset deforming zonal mesh system and a high-order compact-different scheme were used to generate the results of the actuator cavity and the external jet flow field, respectively. The external region, the slot region and jet cavity were linked through a chimera methodology, and the motion of diaphragm was represented by varying the position of approximate boundary points. When flow in the cavity became periodic after several cycles, the velocity profile at the slot plane was sampled and used as a boundary condition at the slot exit in the subsequent cycles. The results of Rizzetta et al. (1999) confirmed the findings of Kral et al. (1997) in terms of the cross-stream distributions of the time-mean velocity profiles. Furthermore, the three-dimensional simulations captured the breakdown of the external flow into a turbulent jet observed in the experiments, which nevertheless was not found in strictly two-dimensional modelling. Mallinson et al. (1999) obtained the same conclusion by comparing their experiments with their URANS simulations. A commercial solver named CFX4.2 was employed to perform the unsteady incompressible simulation. The turbulent flow was computed using the k-ε turbulent model. However, they used the same method as Kral et al. (1997) by assuming an analytic velocity distribution at the slot exit.

Mittal et al. (2001) first included an accurate model of the jet cavity in their simulations using an incompressible Navier-Stokes solver developed by their research group. A second-order accurate central-difference scheme was used for spatial discretization and a mixed explicit-implicit fractional step scheme for time advancement. The pressure Poisson equation was solved using a multigrid algorithm. The diaphragm is modelled as a moving boundary, and therefore the flow inside the cavity was accurately computed. A parametric study has been carried out to investigate the effects of varying diaphragm amplitudes and orifice width to height

ratios on the flow field for 2D synthetic jets in quiescent conditions. For the same synthetic jet geometry, the train of strong, compact vortices was observed at higher diaphragm amplitude ($\Delta/H = 0.1$) (Fig. 2.25a), whereas it was not the case at lower diaphragm amplitude ($\Delta/H = 0.05$) due to the strong effect of the suction stroke (Fig. 2.25b). The orifice width to height ratio h/d in their study seemed to impose little effect on the flow outside and inside the cavity in terms of the vorticity contour (Fig. 2.25c), however the jet velocity profile exhibited more parabolic shape at peak blowing for the higher h/d.

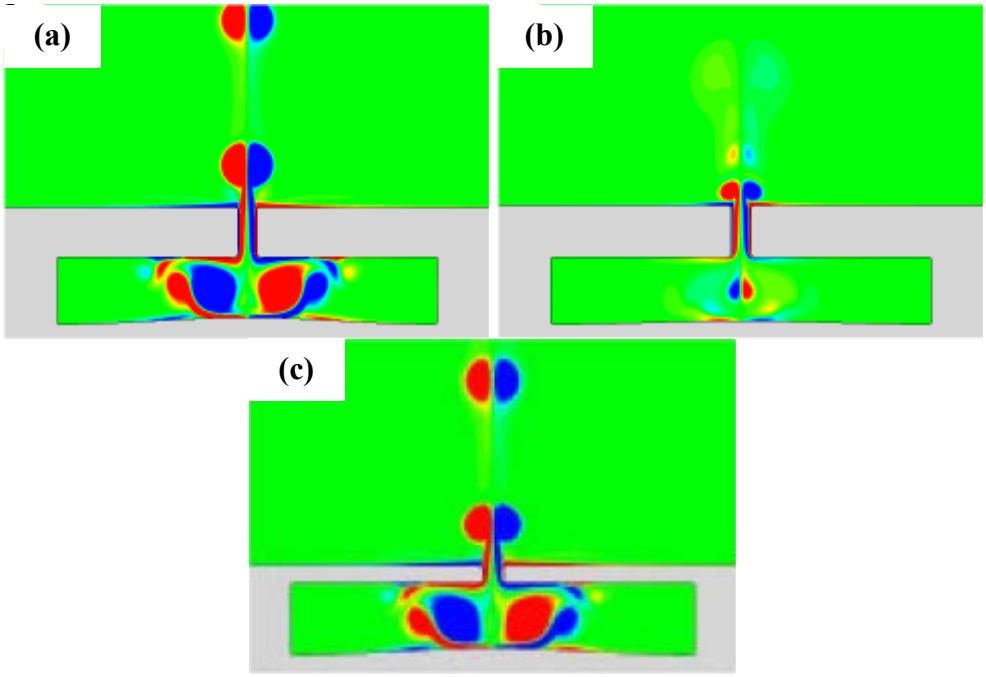

Figure 2.25. Plot of synthetic jet vorticity contours at the minimum volume phase (a) $h/d = 3$, $\Delta/H = 0.1$, (b) $h/d = 3$, $\Delta/H = 0.05$, and (c) $h/d = 1$, $\Delta/H = 0.1$ (Mittal et al, 2001).

Subsequently, a considerable amount of research has been carried out to investigate the effect of the design of SJAs, such as the variations in jet geometric parameters and operating parameters. Nevertheless, some findings are contradicted with each other or with experimental results. Utturkar et al. (2002) carried out a detailed two-dimensional CFD study using the same solver as Mittal et al. (2001). They focused on examining the variations of the diaphragm placement and cavity aspect ratio on the characteristics of the jet. The comparison of vorticity contours showed that when the cavity volume and the cumulative volume displacement of the diaphragm are constant, the external flow is virtually same for all the cases despite

the significant differences in the cavity design. In addition, the comparisons of velocity profiles at the slot exit and the jet momentum coefficient supported the findings of vorticity contours. Therefore, Utturkar et al. (2002) concluded that the details of the cavity design and diaphragm placement do not play an important role in determining the behaviour of the jet. However, they also warned that this conclusion may not be universal as the range of parameters studied is limited and the compressibility effect is not considered.

However, Rizzetta et al. (1999), based on their DNS of synthetic jets from a 2D slot, observed that at the same forcing amplitude, a shorter cavity depth induces a strong vortex which propagates a greater distance over the same length of time. Lee and Goldstein (2002) used an alternative DNS method based on that developed by Kim et al. (1987) to simulate 2D synthetic jets. The Navier-Stokes equations were manipulated to give a fourth-order system of equations which were solved with a Chebyshev-tau method. The simulation results suggested that as cavity becomes shallower, the celerity of the ejected vortices is increased. They believed that the vorticity inside a shallow cavity might be pushed out of the orifice which enhances the vortex roll-up. This finding is consistent with the results of Tang and Zhong (2005a) who showed that for circular synthetic jets, the strength of vortex ring decreases with the increase of H. However, Crook and Wood (2000) observed the opposite trend in their experiments of circular synthetic jets, and they believed that at large H, more vorticity on the wall of the cavity is induced, which may then be contained in the separating shear layer to form the vortex ring.

The study of orifice configuration by Lee and Goldstein (2002) also indicated that a thicker orifice (equivalent to a lower orifice width to depth ratio) increases the celerity of the ejected vortices due to the development of a thicker boundary layer. Crook and Wood (2000) in their experiments also observed that the increasing the orifice depth causes the circulation of the vortex ring to increase, since the thicker shear layer in the orifice creates a larger diameter vortex core, which increases the vorticity and total circulation. However, their results are contradicted to the numerical results by Tang and Zhong (2005a) who revealed that with the decrease of h, a high total circulation is expelled through the virtual pipe, and hence a higher vortex circulation is produced.

Ravi et al. (2004) examined the effect of changes in the slot shape on the flow produced by the synthetic jets using DNS. A 3D Cartesian, incompressible,

Navier-Stokes solver, VICAR3D, employing a second-order accurate central-difference scheme for the spatial discretization and a two-step fractional-step scheme for time advancement, was used for simulation. Three different slot configurations (one square and two rectangular) were investigated. Keeping the same averaged jet velocity and slot area, the iso-surface of eigenvalue contours showed that for the rectangular slot configurations, the rectangular vortex ring formed out of the slot rotates in its own plane by 90º as it convects upwards and subsequently turns to be perpendicular to the slot, as shown in Fig. 2.26a. And this vortex rotation becomes clearer with the increase of aspect ratio. This change is very similar to the 'axis-switching' phenomenon observed for steady jet (Wilson and Demuren, 1997). However, for square slot, only a distinct vortex ring emerged out, and the 'axis-switching' was not observed (see Fig. 2.26b).

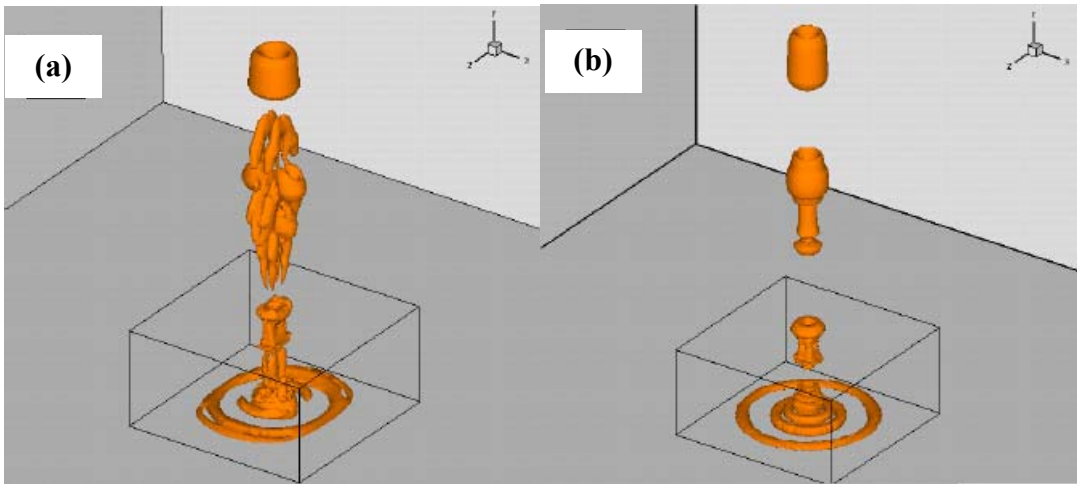

Figure 2.26. Iso-surface of eigenvalue contour, Re_j = 227, (a) rectangular configuration, S = 12 and (b) square configuration, S = 15.2 (Ravi et al, 2004).

Although the aforementioned simulations indicated that the cavity and orifice may affect the external flow field of synthetic jets, many researchers chose to leave out the simulation of the cavity and orifice, since they believe that the simulation inside the cavity with an oscillating piezoelectric diaphragm was beyond the capacity of existing CFD codes (Vatsa and Turkel, 2004). Many researchers modelled the internal cavity of the actuator as a two-dimensional configuration, and utilized a transpiration condition imposed at the diaphragm to simulate the diaphragm motion. Some further imposed a transpiration condition at the bottom of the slot or even directly at the exit of the slot. These researchers suggested that once the unsteady velocity at the slot exit replicates the experimental conditions, details of the cavity

modelling are not crucial for the development of the synthetic jet. For example, Vatsa and Turkel (2004) obtained the peak velocity at the diaphragm surface via numerical iteration to match the measured peak velocity in the experiments. A multigrid-based, multiblock, structured grid, thin-layer Navier-Stokes solver ,TLNS3D, was applied for the simulation. The simulation results agreed with the experimental data in the near field, however, the agreement deteriorated in the far field. Based on all of the aforementioned numerical studies, the author of this thesis believes that it is necessary to include the cavity and orifice in the simulation to ensure the accuracy of the results, especially when the geometry of the cavity and orifice is not complex which will not add much computation costs. The moving boundary condition on the diaphragm has some advantages compared to the velocity boundary condition, as it represents the actual movement of the diaphragm. However, the computation cost and stability need to be considered when using moving boundary condition. It is acceptable to use the velocity boundary condition instead of the moving boundary condition at a small diaphragm displacement.

Besides the parametric investigations, a number of studies focused on the formation of synthetic jets since the jet formation is one of the key features of synthetic jets. The numerical simulation of Mittal et al. (2001) has already observed that the pair of counter rotating vortices could be ingested back into the cavity during the suction stroke at certain conditions, and therefore it was suggested that the vortex pair must be well separated from the orifice exit at the start of the ingestion stroke. Although they found that the separation distance depends on the jet velocity and the strength of the vortex pair, the criterion for the formation of the vortex train was not provided. The DNS of a 2D synthetic jet by Lee and Goldstein (2002) observed that jet formation was highly sensitive to the flow Reynolds number, while jet evolution was affected by the Strouhal number, however no criterion of jet formation was proposed.

The subsequent work by Utturkar et al. (2003) proposed and validated a jet formation criterion for both 2D synthetic jets and circular synthetic jets. A Cartesian grid solver developed by their research group was employed in the simulation. It was found that the criterion of jet formation is $L/\pi = \mathrm{Re}/S^2 > K$, where the constant K is approximately 2 and 0.16 for 2D and circular synthetic jets, respectively. It is noted that this criterion is valid for thick orifice plate with $w/d > 2$ (w the orifice depth and d is the width of the slot or diameter or the orifice), in which the orifice flow can be

considered fully developed. This criterion was subsequently validated and refined by Holman et al. (2005), and found to be valid over a whole range of synthetic jet designs. Independently, Smith and Swift (2001) also reached a similar conclusion for 2D synthetic jets by experiments, but argued that the formation threshold is not a constant. A numerical study using FLUENT by Fugal et al. (2005) indicated that the jet formation for 2D jets is related to the orifice lip geometry. The formation threshold is approximately $L = 2$ for a sharp lip, and $L = 10$ for a rounded lip. In addition, it was suggested that for 2D slot synthetic jets, its near field is scaled on the stroke length, rather than the slot width. Recently, Kotapati et al. (2007) studied the 3D synthetic jet in quiescent air by direction numerical simulations of incompressible Navier-Stokes equations and reaffirmed the findings of Smith and Swift (2001), Utturkar et al. (2003), and Holman et al. (2005), that the jet stoke length (i.e. the Strouhal number) is the key parameter in these flows. They also demonstrated that this parameter governs the vortex trajectory and celerity primarily, and a successful comparison with experiments depends critically on matching it.

Other numerical simulations were carried out in order to match the experiments and to investigate the ability of various turbulent models. In particular, an international workshop, CFDVAL2004, was held in 2004 at NASA Langley Research Centre to assess the state-of-the-art of CFD simulations of aerodynamic flows in the presence of synthetic jets. A number of different groups used a variety of techniques ranging from Reynolds-averaged Navier-Stokes (RANS) computation to DNS, to model the experimental configuration of Yao et al. (2004) who performed a detailed experimental investigation of a piezoelectric-diaphragm-driven synthetic jet exhausting into an ambient quiescent air. Rumsey et al. (2004) provided a good overview of these simulations. He pointed out that different turbulent models could have significant effects, especially further into the flow field, and modelling the cavity does not appear to be a distinct advantage, compared with specifying a jet boundary condition at the surface.

2.3.2 Synthetic Jets Issued into a Zero-Pressure-Gradient Attached Cross Flow

In comparison to the numerical simulation of synthetic jets in quiescent conditions, the numerical simulation of synthetic jets issued into a zero-pressure-gradient

attached flow is more complicated due to the unsteady interaction between the synthetic jets and the cross flow.

Early work by Mittal et al. (2001) studied the interaction of a 2D synthetic jet with a flat plate boundary layer using their in-house Cartesian grid solver. The simulations of three cases having different *VR* and Re showed that the presence of the cross flow results in a significant different flow as evidenced by the dynamics of the vortex structures produced by the synthetic jet and the jet velocity profiles. Perhaps the most revealing aspect of the Mittal et al. (2001) work was in relation to the effect of velocity ratio on the exit velocity profile. Higher velocities were observed near the downstream edge of the orifice than the upstream edge during the ejection phase since the cross flow skewed the profiles. Such exit profiles were also observed in the numerical simulation of square/rectangular synthetic jets by Ravi et al. (2004) and in an experimental study of circular/elliptic synthetic jets in cross flow by Schaeffler (2003). But the study of Mittal et al. (2001) was purely numerical as there was no associated experimental data can be compared.

Similarly, Ravi et al. (2004) carried out a purely three-dimensional numerical study of rectangular synthetic jets in a cross flow using a DNS solver VICAR3D. It was observed that 3D jets with finite aspect ratio had more impulse than their 2D counterpart with infinite aspect ratio in terms of the ability of the formed vortex rings to penetrate the boundary layer, but the unsymmetrical velocity profiles about the central line of the slot were accordant to their 2D counterpart.

Cui et al. (2003) studied 2D synthetic jets in a turbulent boundary layer using a URANS solver INS2D. Two cases, which have the same $VR = 1.25$ based on the averaged jet velocity, were simulated to compare with the experimental data. The discrete vortices scale with the boundary layer thickness (the momentum ratio the jet and the boundary layer $C_\theta = O(10^{-1})$) in one case, and scale with the inner viscous sublayer ($C_\theta = O(10^{-2})$) in the other one. Their simulation results qualitatively agreed with the experimental data on the whole in terms of the phase-averaged velocity vectors and vorticity contours, however were quantitatively different to the experiments, especially in the vicinity downstream of the jet. For the high jet momentum case ($C_\theta = O(10^{-1})$), the discrete vortices were found to penetrate the entire thickness of boundary layer and their influence extended to a larger distance of 4δ in the streamwise direction, due to higher jet momentum; while for the low jet

momentum case (C_θ = $O(10^{-2})$, a smaller penetration (0.2δ) in the cross flow was observed, and their influence distance was about 0.8δ in the streamwise direction.

Wu et al. (2006) investigated a square synthetic jet in a turbulent boundary layer using an in-house finite-volume Large-Eddy Simulation (LES) code STREAM-LES. Proper-Orthogonal-Decomposition (POD) has been employed to identify the energetic structures in the turbulent cross flow. It was observed that two Ω-shaped vortices of two consecutive injection puffs exist in the flow field. One is formed at the orifice with high vorticity magnitude due to the expelled fluid which acts in a manner similar to an obstacle, and the other is in the far field with a lower vorticity magnitude, as shown in Fig. 2.27. The far field Ω-shaped vortices were also observed in the simulation of Ravi et al. (2004) who utilized the iso-surface of eigenvalue contours to identify the vortices. Although the good qualitative agreement indicated the LES has captured the main control effect, the quantitative difference between the hot wire measurement and the simulation data were evident.

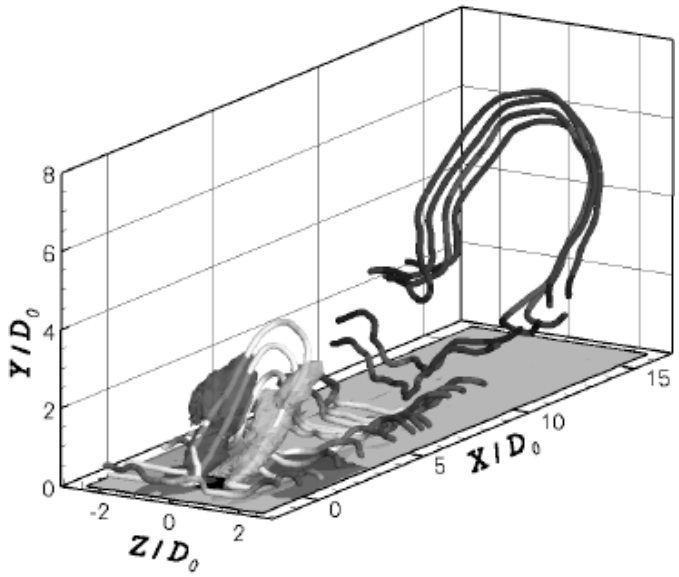

Figure 2.27. Visualization of the flow field: vorticity lines overlaid with the contour of vorticity magnitude ω (light and dark shades indicate high and low value of ω) and iso-surfaces of normalized streamwise vorticity ω_x at ω_x = 1 and -1 (Wu et al, 2006).

Although some consensus were arrived for synthetic jets in attached cross flow, such as the asymmetric flow inside the cavity, the skewness of velocity profile at the orifice exit, and the generation of sequence of clockwise rotating vortices, most of CFD simulations have been undertaken in isolation hence the capabilities of

different classes of computational methodologies are still hard to be assessed. In addition, in comparison to the publications focused on the slot or rectangular (square) jets (2D or 3D), the interaction of circular synthetic jets with a boundary layer has not been studied with much attention using CFD modelling. This may be due to insufficient database for validation.

By far the most extensive investigation for the circular synthetic jets in cross flow was presented at the CFDVAL2004 workshop (Rumsey et al, 2004). PIV and Laser Doppler Velocimetry (LDV) techniques were used to investigate the interactions of a circular synthetic jet with a turbulent boundary layer. Five contributors ran ten separated 3D cases using LES or URANS. In summarising the results of the CFD simulations, Rumsey et al. (2004) pointed out although a good qualitative agreement is obtained in comparison to the experimental results, there are significant variations among the CFD results. The agreement with experimental data was poor for turbulence quantities, hence no one turbulent model stood out as being the best methodology. In other words, the 'state-of-the-art' CFD techniques of today are not fully capable to consistently and accurately predicate these flows. However, this workshop has established a benchmark for the flow involving synthetic jets and turbulent separation control. Additional results of this workshop are available from the CFDVAL2004 website (http://cfdval2004.larc.nasa.gov/index.html).

Recently, Rumsey et al. (2007) performed additional URANS simulations based on 'CFDVAL case2' (Schaeffler and Jenkins, 2004) and 'NASA Glen case' (Milanovic et al, 2005), using a code CFL3D, This code solves the three-dimensional, time-dependant, compressible, RANS equations with an upwind finite-volume formulation. Three different turbulent models in CFL3D were tested, namely one-equation Spalart-Allmaras (SA) model, two-equation Menter k-ω shear-stress transport (SST) model, and explicit algebraic stress model (EASM). For the former case, a circular synthetic jet was issued into a turbulent boundary layer at M = 0.1, Re_{Do} = 14160, d = 3.3, f = 150 Hz, and VR = 1.3 based on the maximum jet velocity, hence the jet effect was mostly contained within the boundary layer. Whereas for the latter case, a circular synthetic jet was operated at M = 0.0175, Re_{Do} = 7530, d = 0.4, f = 24 Hz, and VR = 1.0 based on the maximum jet velocity, hence the jet effect extended beyond the boundary layer edge. Qualitative agreements were observed, but there were many quantitative differences. Furthermore, they emphasized the importance of including the region inside the orifice, since time-dependent top-hat

boundary conditions at the orifice exit was too simple which produced markedly different results.

Wu and Leschziner (2009) used their in-house code STREAM-LES to investigate circular synthetic jets in a turbulent boundary layer, aiming at evaluating the capacity of LES in modelling synthetic jets, and providing detailed insight into the physics of the interaction of the jet with the boundary layer. A pair of streamwise vortices was formed and confirmed as the major feature that is responsible for the control effect of the synthetic jets in the boundary layer. They also suggested that the effectiveness of the synthetic jets is largely determined by the ability of the streamwise vortices to survive over a substantial distance downstream of the orifice exit.

The formation number for circular synthetic jets in quiescent conditions is found to be 4 (Jabbal et al, 2006), however this threshold is expected to reduce in the presence of a cross flow. Sau and Mahesh (2007) utilized DNS to study the passive scalar mixing in vortex rings, and observed the trailing column forms at lower $L = 3$ and $VR = 1.5$, as shown in Fig. 2.28. The iso-surface of pressure is plotted to present the vortical structure. The vortex ring with a considerable downstream side is tilted towards the direction of the cross flow, and the trailing column, which actually is the excess circulation accumulated in the jet, follows the vortex ring and causes a very high pressure gradient in the downstream side. Sau and Mahesh (2007) believed that for this particular case of $VR = 1.5$, the equivalent formation number is certainly less than 3. It is understandable that the entrainment of the cross flow into the vortex core does not allow all of the shear layer fluid to be entrained into the ring even at L less than formation number. Hence, the cross flow reduces the threshold of L above which the trailing column is formed.

2.3.3 Flow Separation Control Using Synthetic Jets

A 2D synthetic jet applied on both stationary and pitching NACA 0015 airfoil for separation control was studied by Rehman et al. (2006) using FLUENT. The simulations were undertaken at $Re = 3.6\times10^5$ based on the chord length of 0.332 m and a freestream velocity of 16 m/s. For a stationary airfoil, the synthetic jet was placed at three different positions (36%, 32% and 28% of the chord length) before the separation point (40% of the chord length at the static stall angle 15 deg). The

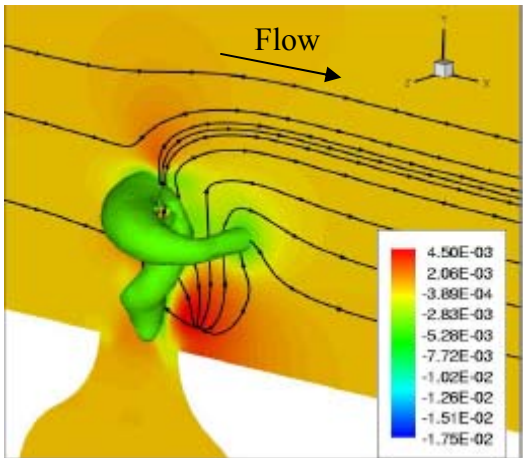

Figure 2.28. Iso-surface of pressure showing the ring and trailing column structure for the case of $L = 3$, $VR = 1.5$. The pressure contours in the symmetry plane along with some in-phase streamlines is also added (Sau and Mahesh, 2007).

comparisons of mean lift and drag coefficients at different synthetic jet locations indicated that both lift and drag are increased as the synthetic jet moves far away from the separation point. Furthermore, both the pressure recovery and the flow pattern at the trailing edge showed that the jet at 28 % of the chord length suppresses the separated flow more effectively than the other locations. Therefore, it was suggested that imparting movement to flow far away from separation point is beneficial to increase the lift, while the location of the synthetic jet close to the separation point is helpful to reduce the drag. The simulation also demonstrated that for the synthetic jet at 28% of the chord length, the increase in lift becomes significant at high incidences (10-20 deg), and the control effectiveness of the synthetic jet is reduced at low incidences (4-10 deg). For a pitching airfoil, the effects of non-dimensional forcing amplitude and forcing frequency were investigated. It was found that higher amplitude is suitable for drag reduction whereas higher frequency is beneficial for lift enhancement.

The importance of the actuation frequency has been discussed in section 2.2.2.3. Similar to the experimental work by Amitay et al. (2001), Dandois et al. (2006) used DNS and LES to investigate the frequency effect of synthetic jets on a rounded ramp at Re = 28,275 based on the step height. Two reduced frequencies based on the separation length of the uncontrolled case and the freestream velocity were examined, which are $F^+ = 0.5$ and 4 respectively. The results of LES demonstrated that two different modes of the synthetic jet have been identified at

two different reduced frequencies. At the low frequency which is close to the natural vortex shedding frequency, a 'vorticity-dominated mode' was observed for which the separation length is reduced by 54% (Fig. 2.29b), in comparison to the uncontrolled case (Fig. 2.29a). It is because the large vortices formed at low frequency increase the entrainment of high momentum fluid from the outflow to the wall. However at the high frequency, an 'acoustic-dominated mode' was observed for which the separation length is increased by 43% (Fig. 2.29c). The increase of separation length is due to a modification of the mean velocity profile as proposed by Stanek et al. (2002a, 2002b) which results in a lower entrainment in the mixing layer.

(a)

(b)

(c)

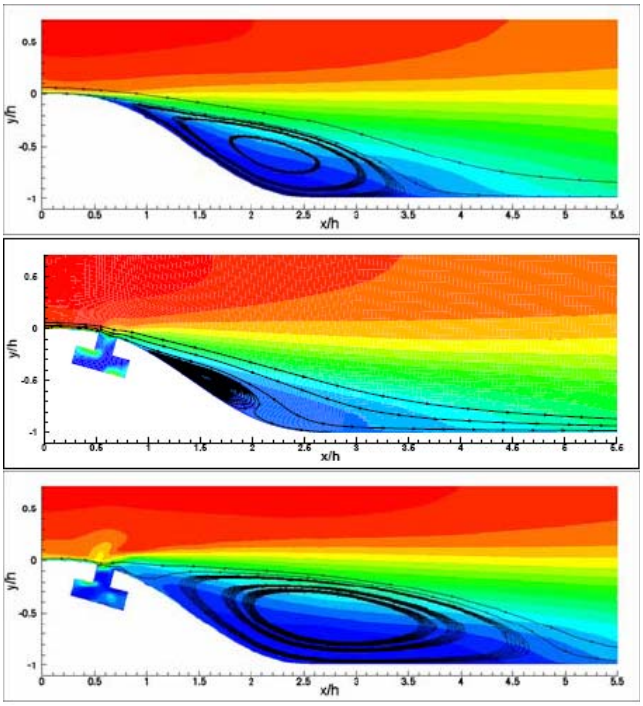

Figure 2.29. Mean streamwise velocity field and streamlines showing the extent of the separation bubble of (a) uncontrolled case, (b) $F^+ = 0.5$ case, and (c) $F^+ = 4$ case (Dandois et al, 2006).

Recently, Kim and Kim (2009) numerically investigated the lift enhancement mechanism of NACA 23012 airfoil using synthetic jets. The 2D unsteady incompressible Navier-Stokes equations were utilized to simulate the separated flow. The simulations were carried out at a freestream velocity of 35.7 m/s and a chord Reynolds number of 2.19×10^6 for various jet velocities and frequencies. A leading edge synthetic jet having an inclined angle of 23 deg with respect to the local tangential airfoil surface was located near the separation point (12% chord from leading edge) of the airfoil at angle of attack 22 deg. It was observed that the actual

flow control mechanism and the flow structure are fundamentally different depending on the range of the synthetic jet frequency, as shown in Fig. 2.30. At a low frequency (F^+ = 1 based on the characteristic length which is defined as the distance between the trailing edge and the jet slot and the freestream velocity), a small vortex penetrates into the large separation flow at the leading edge, which leads to a substantial size reduction of the leading edge separation vortex. At a high frequency (F^+ = 5), the flow near the synthetic jet slot is firmly attached, and therefore, the circulation of the virtual airfoil shape is changed. The maximum lift was obtained when the separation point coincided with the synthetic jet location at F^+ = 1 approximately.

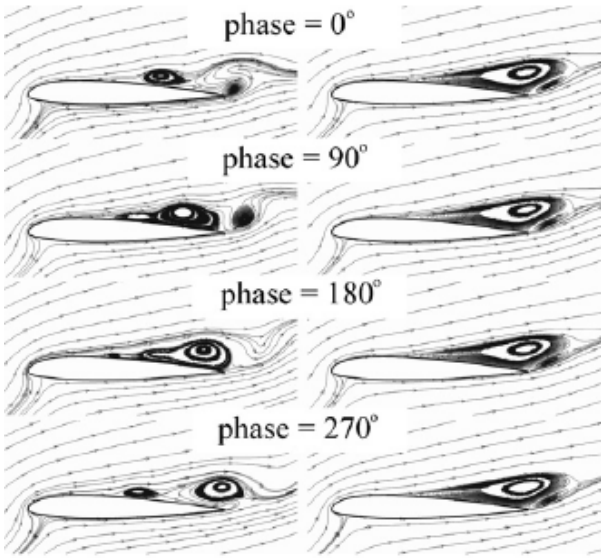

(a) **(b)**

Figure 2.30. Phase locked streamlines of the synthetic jet at 0.12*c*: (a) F^+ = 1 and (b) F^+ = 5. For both case, *VR* = 3 based on the jet peak velocity (Kim and Kim, 2009).

Lesbros et al. (2006) employed a commercial LES code, CFD-ACE, to model a micro synthetic jet in a laminar separation due to an adverse-pressure-gradient. The simulations were carried out to investigate the dependency of the synthetic jet actuation on the forcing frequency, in a focused range of the low Tollmien-Schlichting (T-S) frequencies (F^+ = 0.72~1.41 based on the laminar separation bubble length and the freestream velocity). The results of simulation were validated by the corresponding experimental data (Hong et al, 2002). Both of them reaffirmed that the most effective reduced frequency of a synthetic jet is in an order of $O(1)$.

2.4 Summary

In this chapter, some research related to the flow separation control and the methods used for flow separation control have been reviewed, especially the literature involving synthetic jets and their potential in flow separation control. Although both experimental and numerical investigations have greatly improved the understanding of the behaviour of synthetic jets in quiescent conditions and in cross flow with/without flow separation, several issues still remain unresolved, or at least are not fully resolved. From the author's point of view, these issues are imperative towards setting up a methodology to determine the operating conditions of SJAs for a given flow, which therefore requires an improved understanding of the fluid mechanics of synthetic jets for effective flow control. These issues form the objectives of the present research.

Firstly, to ensure the generated synthetic jets definitely have a vortex roll-up which is beneficial to enhance the mixing within the boundary layer and consequently the potential in flow separation control, there is a need for understanding the effect of non-dimensional parameters, such as S and L on the formation and vortex roll-up of synthetic jets in quiescent conditions, There is also a need to find a criterion of vortex roll-up over a wide parameter space, to refine the existing criterion proposed by Guo and Zhong (2007).

Secondly, in the presence of a boundary layer, there is a need to investigate the characteristics of the vortical structures produced by the interaction of synthetic jets with a boundary layer, over a wide range of synthetic jets operating conditions. The hierarchy of coherent structures, their development and near-wall effect are important for the potential of synthetic jets in delaying flow separation and thus require further research. There is also a need to establish a parameter space for identifying different vortical structures and their wall shear stress patterns.

Finally, it is required to apply an array of synthetic jets to a separated boundary layer to explore their behaviour in delaying flow separation and to evaluate their flow control effect so as to identify the most effective synthetic jet operating conditions, and to find out how the vortical structures deliver the flow control effect on the downstream separation region. Similarly, a series of parameter spaces are required which would be useful to identify the optimal operating conditions of

synthetic jets under which the best flow control effect and highest efficiency can be achieved.

To the best knowledge of the author, no known work has been published in these areas. All the above issues will thus be investigated in this thesis.

Chapter 3 Research Overview

This thesis is written in an alternative format, in which the research methodologies and findings are presented in the form of published or submitted papers. In this chapter, a research overview in this PhD project is provided. The logical relations among these papers, a brief summary of each paper as well as a statement of the author's contribution are stated.

3.1 Research Overview

As mentioned in Chapter 1, the ultimate goal of this project is to identify the optimal operating conditions of the synthetic jet actuators (SJAs) investigated in the current study and the desired vortical structures generated under the optimal conditions for flow separation control, based on an improved understanding of the fluid mechanics of synthetic jets issued into quiescent conditions, a zero-pressure-gradient laminar boundary layer and a laminar boundary layer which separates further downstream over an inclined plate. A numerical investigation using FLUENT is undertaken to achieve this goal. The capability of FLUENT in modelling the synthetic jets has been validated by comparing the simulation results with the corresponding experimental data qualitatively and quantitatively. And a reasonable agreement has been attained.

Firstly, since the strength of the vortex rings in terms of the level of circulation plays an important role in determining the impact of synthetic jets on the external flow, vortex roll-up for synthetic jet in quiescent conditions is studied using numerical simulations, in order to understand the effect of dimensionless parameters on the formation and strength of vortex rings. This work is an in-depth study following the experimental investigation by Guo and Zhong (2007) who suggested a criterion of Stokes number $S \geq 10$ for vortex roll-up at a dimensionless stroke length of around 4. A wider range of operating conditions are examined and finally a parameter map that marks three different regimes of synthetic jets (i.e. no jet, jet formation without vortex roll-up and jet formation with vortex roll-up) is provided (Zhou et al, 2009). Although some criteria for the formation of synthetic jets have been reported by Holman et al. (2005), Milanovic and Zaman (2005) and Shuster and Smith (2007), to the best knowledge of the author of this thesis, it is the first

time that a parameter map is provided which integrates the aforementioned states of synthetic jets with well-defined boundaries. In addition, the difference between the synthetic jet formation and vortex ring roll-up is clarified, and their criteria are provided respectively. This work is helpful for selecting more effective SJAs in which vortex roll-up is required.

Based on the study on the behaviour of synthetic jets in quiescent conditions, a synthetic jet issued into a zero-pressure-gradient laminar boundary layer is then investigated. Unlike other CFD studies of synthetic jets in cross flow, which focus on validating the algorithm model or examining the flow filed, this work provides an insight of the hierarchy of vortical structures produced by the interaction of synthetic jets with a laminar boundary layer, and explains the resultant surface shear stress patterns produced by these structures (Zhou and Zhong, 2009). The computational results are summarized in a non-dimensional parameter space, which identifies two different types of vortical structures (i.e. hairpin vortices and tilted vortex rings) and their corresponding surface shear stress patterns. The conditions at which each type of vortical structures is formed are also provided. Furthermore, the increase in surface shear stress relative to the baseline case without the synthetic jets is also calculated to evaluate the potential separation control effect of synthetic jets.

Upon understanding the potential separation control effect of different vortical structures produced by synthetic jets, the numerical simulation work has moved one step forward to examine the flow separation control using an array of synthetic jets issued into a laminar boundary layer which separates downstream on an inclined plate. The interaction between the adjacent synthetic jets and the existence of the flow separation make the external flow complicated. The impact of synthetic jets on the boundary layer prior to separation and the extent of flow separation delay on the flap, at a range of operating conditions, are quantified and presented in non-dimensional parameter maps respectively. The relationship between the impact of synthetic jets on the boundary layer prior to separation and their downstream flow control effect on the flap has been set up. Furthermore, considering the power required for the synthetic jet actuator and the performance of synthetic jets in delaying flow separation, the optimal operating conditions which generate the desired vortical structures are identified. The characteristics of these resultant vortical structures that yield the best control effect and highest flow efficiency are

also examined which sheds light on the selection of synthetic jet for practical applications on aircraft.

The numerical simulation in this project works in a complementary manner in parallel with the ongoing experiments carried out by the other colleagues in the same research group, supervised by the author's supervisor, Dr. Shan Zhong. The capacity of numerical simulations, for both the synthetic jets issued into a zero-pressure-gradient laminar boundary layer and a laminar boundary layer which separates further downstream over an inclined plate, is validated by the experimental data quantitatively and qualitatively. In return, the computational work also provides guidance for presenting and interpreting the experimental data. In addition, the results of numerical simulation provide some quantitative information which is hard to achieve in the experiments, hence offer a further insight into the fluid mechanics of synthetic jets.

To the best knowledge of the author, it is the first time to present the hierarchy of coherent structures produced by synthetic jets in a laminar boundary layer, and to use these coherent structures to explain the impact of synthetic jets on the boundary layer. A series of parameter maps, not only explain the transition of synthetic jets and their induced wall shear stress patterns with the variation of non-dimensional parameters, but also provide a guide for choosing the optimal synthetic jets operating conditions for flow separation control. Although this guidance is only valid for the SJAs and parameter range investigated in the current study, the work presented in this thesis shows that with an improved understanding of the behaviour of synthetic jets in cross flow and the characteristics of the optimal vortical structures in delaying flow separation, selection and optimization of synthetic jets for full-scale flight conditions are promising.

3.2 Research Methodology

As mentioned previously, at full-scale flight conditions, the highly turbulent boundary layer is very thin of the order of a few millimetres, and therefore, the implementation of SJAs requires orifice diameters of the order of ten to hundreds of micrometer (in MEMS scale). As such, the modelling of synthetic jets at the real scale appears to out of the capability of the existing CFD codes in terms of the

accuracy of the modelling results, which has been confirmed at the CFDVAL2004 workshop (Rumsey et al, 2004). In addition, it is also not achievable for available measurement techniques in the experiment. Therefore, macro scale SJAs, which have orifice diameters of 5 and 2 mm, are used in quiescent and cross flow investigations, respectively. Also, for simplification, the research only considers the synthetic jets issued from normal circular orifices. The compressibility effect is not taken into account in the present study because for synthetic jets in cross flow, water is chosen as flow medium for which the compressibility is negligible. While for synthetic jets in question conditions, air as flow medium can also be treated as incompressible since the actuation frequency is far from the Helmholtz resonance frequency.

For CFD modelling in this thesis, 2D/3D unsteady incompressible flow simulations are performed using a commercial solver, FLUENT 6.3. FLUENT provides two options for solvers: segregated solver and coupled solver. The segregated solver solves the continuity, momentum, energy and species equations sequentially, while the coupled solver solves them simultaneously. The segregated solver has been widely used for incompressible and mildly compressible flows, while the coupled solver is normally used for high-speed compressible flows, highly coupled flows with strong body forces, or flow being solved on very fine meshes. Considering the flow conditions being investigated, segregated solver is selected using a control-volume-based technique. Since the Reynolds numbers of the synthetic jet in the present operating conditions are much lower than the critical value (around 5×104) proposed by Glezer (1988), above which the jet becomes turbulent at the orifice exit, all cases are simulated using laminar flow model. The application of laminar synthetic jets issued into a laminar boundary layer with/without separation is reasonable, since some commonalities exist in the interaction mechanism between synthetic jets and a boundary layer no matter it is laminar or turbulent, and both produce hairpin vortex type structures in the boundary layer (Acarlar and Smith, 1987b; Haidari and Smith, 1994), which has been illustrated in section 2.2.2.2. Experimental evidence also revealed that the hairpin vortex type structures are responsible for the delay of flow separation (Zhang and Zhong, 2010b). Therefore, investigating the interaction of synthetic jets with the laminar boundary layer and the behaviour of vortical structures produced by this interaction will provide an insight of the fluid mechanics of synthetic jets for

practical applications. In the author's opinion, understanding the behaviour of synthetic jets in a laminar flow is the first logical step towards understanding the complex behaviour of synthetic jets in a turbulent flow. Moreover, the computation in the simulation and the measurement in the experiment can be simplified, and the accuracy and reliability of the results can be ensured. The second-order implicit scheme is selected for the unsteady formulation. The pressure and velocity are coupled using the Pressure-Implicit with the Splitting of Operators (PISO) algorithm. The second-order scheme and second-order upwind scheme are selected for pressure discretization and momentum discretization, respectively. The aforementioned schemes are chosen by referring other researchers' work, and their accuracy has been validated in the present study. Discrete Phase Model (DPM) is used to model the particle movement of synthetic jets and the density of the released particles is set as the same as that of water to make sure the particles follow the movement of water closely.

The SJAs and the external flow configurations used in the simulation are identical to that used in the experiment. The movement of diaphragm is modelled by providing the instantaneous velocity of diaphragm at its neutral position during the actuation cycle. For synthetic jets issued into quiescent conditions and a separated boundary layer, a thin rubber diaphragm, which is sandwiched between two metal disks, is driven by a permanent magnetic shaker via a steel rod to oscillate in a sinusoidal manner, and mimics the motion of an oscillatory piston. Hence, the diaphragm displacement Δ and the oscillating frequency f are varied independently in the experiment. Correspondingly, in the simulation, the instantaneous velocity of diaphragm can be defined as

$$\upsilon(t) = \pi \Delta f \cos(2\pi f t) \tag{3.1}$$

Whereas for synthetic jets in the attached boundary layer, a rubber diaphragm is pre-stretched and clamped circumferentially to the back of the cylindrical cavity exhibiting a cone shape instantaneously. The centre of the diaphragm is made to oscillate in a sinusoidal manner by being attached to a permanent magnetic shaker via a steel rod. Hence, the velocity of diaphragm can be defined as

$$\upsilon(r,t) = \pi \Delta f \left(1 - \frac{r}{r_c}\right) \cos(2\pi f t) \tag{3.2}$$

Despite the different expressions of diaphragm velocity for different cases, two important operating parameters: Δ and f, are decoupled all the time, which makes the study on the sole effect of Δ and f on the behaviour of synthetic jet possible.

The velocity boundary condition is specified using User-Defined-Functions (UDFs) supported by FLUENT. The reason for using velocity boundary instead of moving boundary to model the movement of diaphragm is that at small displacement, there is a negligible difference of the jet velocity and the formation of vortex rings when using these two methods, while the latter requires more calculation time.

In the present work, the coherent structures produced by the synthetic jets interacted with the boundary layer is identified using Q-criterion, which is developed by Hunt et al. (1988). Hunt et al. (1998) identified vortices of an incompressible flow as connected fluid regions with a positive second invariant of velocity gradient tensor ∇u . Q, the second invariant of velocity gradient tensor ∇u , can be defined as

$$Q = 0.5\left(\|\Omega\|^2 - \|S\|^2\right) \tag{3.3}$$

where $\|S\| = \left[Tr\left(SS^t\right)\right]^{1/2}$, $\|\Omega\| = \left[Tr\left(\Omega\Omega^t\right)\right]^{1/2}$, $\|\cdot\|$ is the matrix norm, and S and Ω are the symmetric and asymmetric component of ∇u . Hence, Q represents the local balance between the rotation rate $\|\Omega\|^2$ and the strain rate $\|S\|^2$. The positive Q implies the strength of rotation overcomes that of strain, and thus the coherent structure can be defined as a region where $Q > 0$.

The Q-criterion is one of the most widely used local vortex-identification criteria (Dubief and Delcayre, 2000; Chakraborty, et al, 2005; Kolář, 2007). Dubief and Delcayre (2000) examined the behaviour of the Q-criterion in transitional and turbulent flows using an extensive database. Four vortex-eduction methods (low pressure, high vorticity, negative λ_2, and positive Q) were compared for isotropic turbulence, mixing layer, channel flow and backward-facing step flow. Among these four methods, Q-criterion is observed to be more appropriate as it seems to capture all the details of these flows well. Chakraborty et al. (2005) studied the relationship between some popular local schemes based on ∇u (Q-criterion, λ_2-criterion, Δ-criterion and λ_{ci}-criterion), and suggested that in the intense swirling regions (for example a Burgers' vortex at high Re or vortical structures in turbulent flows), given the appropriate choice of the threshold for the different criteria, the resulting vortex

cores are quite similar for all practical purpose of kinematic and dynamic interpretation.

However, a contradictory result regarding the comparison of vortex structures educed using the different local criteria (vorticity magnitude $|\omega|$, Δ-criterion, Q-criterion and λ_2-criterion) was found by Jeong and Hussain (1995) who observed significant differences in various flow examples. They pointed out the Q and λ_2 criteria tend to be similar but often differ from the Δ and $|\omega|$ criteria; however, Q-criterion did not properly represent the vortex geometry where vortex stretching or compression is significant. Wu et al. (2005) made an analytical diagnosis of four local criteria (Δ-criterion, Q-criterion, λ_2-criterion and Q_{2D}-criterion) which indicated that Q and λ_2 criteria may cut a connected vortex into broken segments at locations with strong axial stretching. Although Q-criterion was found to be inadequate for certain vortices mentioned above, these configurations are very unlikely in common turbulent flows. Thus, Q-criterion is widely used to represent the coherent structures.

The main issue in vortex identification for the Q-criterion is subjectivity. As a result, it needs a user-defined threshold to capture the energetic coherent structures without the addition of uncertain small-scale vortices, which relies on previous publications and experience. Dubief and Delcayre (2000) proposed another method to find a critical threshold, by using the contribution of educed coherent vortices to vorticity fluctuations. Therefore, a threshold close to the critical value will represent the most energetic structures in terms of vorticity fluctuations.

3.3 Outline of Published/Submitted Papers

Since this thesis is presented in the alternative format, a total of five published/submitted papers are included as separated chapters with a required re-formatting. In this section, the contents and the logical relations among these included papers are outlined. As to the contributions of the author and other co-authors to the work, except the first paper, which is co-authored one additional researcher, all the other four papers are co-authored by the author and her supervisor, Dr. Shan Zhong. The work in these four papers was undertaken solely by the author under the supervision of Dr. Zhong. Dr. Zhong pointed out the research focus and offered some valuable suggestions to present and explain the simulation results. For

the first paper, as the first author, the author of this thesis carried out the CFD simulations, and data presentation and analysis, except for the relation between the normalized thickness of Stokes layer ε/D_o and the Stokes number S, which is derived from a theoretical estimation by another co-author, Dr. Hui Tang.

3.3.1 Vortex Roll-Up Criterion for Synthetic Jets (Zhou, Tang, and Zhong, 2009)

Authors: J. Zhou, H. Tang, and S. Zhong

Reproduced from: AIAA Journal, Vol. 47, No. 5, pp. 1252-1262, 2009

To ensure the generated synthetic jets definitely have a vortex roll-up, which is beneficial to enhance the mixing within the boundary layer, and consequently the potential in delaying flow separation, the criterion of vortex roll-up for synthetic jets in quiescent conditions is sought. Both theoretical analysis and numerical simulations are undertaken to study the parameters that affect the strength of vortex roll-up of synthetic jets. Firstly, a dimensional analysis reveals that the dimensionless vorticity of vortex roll-up produced by an orifice flow depends on the dimensionless stroke length, Stokes number and the ratio between the orifice diameter and the thickness of the Stokes layer. Based on the results from a fully developed oscillating laminar pipe flow, the Stokes number is found to play an important role in determining the thickness of the Stokes layer inside the orifice hence the shape of the velocity profile. Results from the numerical simulations confirm that the Stokes number also determines the strength of vortex roll-up of a synthetic jet issued from an orifice of a finite depth due to the same reason. Finally, a parameter map, which marks three different regimes of synthetic jets classified as no jet, jet formation without vortex roll-up and jet formation with vortex roll-up, is produced based on the numerical simulation results. It is shown that for the SJA used in the present study, a minimum Stokes number of about 8.5 is required to ensure the occurrence of an appreciable vortex roll-up at a dimensionless stroke length greater than 4. In addition, a very low Stokes number can also suppress the formation of synthetic jets. This study provides a further understanding of the behaviour of synthetic jets in quiescent conditions, which will be useful for designing more effective SJAs for flow separation control where vortex roll-up is desired.

3.3.2 Numerical Simulation of the Interaction of a Circular Synthetic Jet with a Boundary Layer (Zhou and Zhong, 2009)

Authors: J. Zhou and S. Zhong

Reproduced from: Computers and Fluids, Vol. 38, No. 2, pp. 393-405, 2009

On the basis of an improved understanding of the synthetic jets in quiescent conditions, a 3D numerical simulation of circular synthetic jets issued into a laminar boundary layer developing over a flat plate is undertaken in a complementary manner alongside with an experimental study with the aim of achieving an improved understanding of the fluid mechanics underlying the interaction process between the synthetic jets and the boundary layer. The simulation is carried out in FLUENT at two diaphragm operating conditions, which produce two distinctly different vortical structures and shear stress footprints on the wall. The simulation results are validated using experimental data and a good agreement is achieved by comparing the particle movement, surface shear stress footprint, jet trajectory and boundary layer velocity profiles. The jet trajectory obtained from the simulation is nearly identical to that from the experiment. The maximum deviation for the time-averaged velocity is less than 8%, and for the instantaneous velocity is less than 23%. The temporal evolution of coherent structures formed as the result of this interaction is examined using the *Q*-criterion. The hierarchy of the coherent structures is established which provides a credible explanation of the wall shear stress pattern observed in both the experiment and the simulation. The high spatial resolution in the near-wall region and 3D nature of the simulation results provide the information about the flow field which is not only consistent with but also additional to that from the experiment, leading to an improved understanding of the interaction process between the synthetic jets and the boundary layer and the resultant vortical structures.

3.3.3 Coherent Structures Produced by the Interaction between Synthetic Jets and a Laminar Boundary Layer and Their Surface Shear Stress Patterns (Zhou and Zhong, 2010)

Authors: J. Zhou and S. Zhong

Reproduced from: Computers and Fluids, Vol. 39, No. 8, pp. 1296-1313, 2010

The work presented in this paper is an extension of the work by Zhou and Zhong (2009), aimed to investigate the evolution of coherent structures upon the changes in

operating conditions over a wide parameter space and the impact of these structures in the near-wall region in terms of surface shear stress patterns. The configurations of the SJA and the external flow, as well as the numerical method are exactly same to that of the aforementioned work. 3D numerical simulations of circular synthetic jets issued into a zero-pressure-gradient laminar boundary layer developing along a flat plate are undertaken using FLUENT. Non-dimensional parameter maps are established to illustrate the variations in the appearance of these resultant structures and their shear stress footprints upon the changes in the operating conditions of synthetic jets. A parameter boundary separating the two distinct types of vortical structures and surface shear stress patterns is identified. It is found that the location of this boundary correlates closely with the jet-to-freestream velocity ratio of VR = 0.4 when the Strouhal number (Str) is less than 1, whereas for $Str > 1$ the boundary deviates from this trend, approaching the line of dimensionless stroke length of L = 1.6. In order to investigate the potential impact of the synthetic jets on the boundary layer, the increase in the space- and time-averaged skin friction coefficient relative to the baseline case without the synthetic jets is calculated. It appears that in order to maximize the impact on the near-wall flow while keeping the energy expenditure down, it is wise to maximize the accumulated effect of hairpin vortices by keeping the spacing between consecutive hairpin vortices similar to the local boundary layer thickness upstream of the separated flow instead of producing stronger individual structures. The knowledge gained from this study will be useful to understanding the effect of synthetic jets on a separated flow to which flow separation control can be applied. Once the optimal vortical structures which are most effective in delaying flow separation are identified via further studies of synthetic jets issued into a boundary layer which separates further downstream, the knowledge obtained from this study can help the selection of the operating condition of the synthetic jets which ensures the formation of such structures.

3.3.4 A Numerical Investigation of the Interaction of an Array of Synthetic Jets with a Separated Laminar Boundary Layer (Zhou and Zhong, 2010)

Authors: J. Zhou and S. Zhong

Submitted to: Computers and Fluids

In this work, the research moves one step forward to investigate the flow separation control using an array of three circular synthetic jets issued into a laminar boundary layer that separates further downstream over an inclined flap. The 3D simulation results are validated using experimental data and a reasonable agreement is achieved. The simulations are undertaken at three synthetic jet operating conditions, i.e. Case A: $L = 2$, $VR = 0.32$; Case B: $L = 4$, $VR = 0.64$ and Case C: $L = 5$, $VR = 0.81$. Two distinct types of vortical structures, i.e. hairpin vortices (Case A) and tilted vortex rings (Case B and C), are generated by each synthetic jet. Case A exhibits two streaks of high surface shear stress downstream of each jet whereas Case B and C show only one streak of high surface shear stress downstream of each jet. These patterns of surface shear stress are observed in the zero-pressure-gradient boundary layer developing along the horizontal plate upstream to the inclined flap and they persist further downstream resulting in a wavy separation line in the separated flow region. The impact of the middle synthetic jet in the array on the boundary layer prior to separation is evaluated by examining the spatial variations of surface shear stress. It is found that Case A produces the largest space- and time-averaged surface shear stress, whereas Case C produces the highest local peak surface shear stress due to its high velocity ratio. The flow control effectiveness of the middle synthetic jet is also quantified by the size of the surface area over which the flow remains attached. Among the three cases tested here, Case A is found to be most effective as it produces a considerable flow separation delay and a smoother separation line while consuming less energy than the other two cases. The finding from this study suggests that hairpin vortical structures produced at a relatively low *VR* are more desirable structures for effective flow control.

3.3.5 The Near-Wall Effect of an Array of Synthetic Jets and Their Control Effect in a Separated Laminar Boundary Layer (Zhou and Zhong, 2010)

Authors: J. Zhou and S. Zhong

Submitted to: Computers and Fluids

After validating the capacity of FLUENT in modelling an array of three circular synthetic jets issued into a laminar boundary layer which separates further downstream over an inclined flap, the simulations are carried out using FLUENT at a

wide range of actuator operating conditions. Based on the large number of cases simulated, a parameter map illustrating the nature of the primary vortical structures in the orifice near-field is established. The parameter map can be divided into two regimes separated by a well-defined boundary; one regime is characterised by hairpin vortices and the other by tilted vortex rings. The impact of the middle synthetic jet in the array on the boundary layer prior to separation is evaluated by examining the space- and time-averaged surface shear stress. Two regions with a high surface shear stress increment relative to the baseline case are identified; one is associated with the appearance of hairpin vortices and the other is featured by the presence of tilted vortex rings. The flow control effect of the middle jet is also quantified by examining the time-averaged location of the separation line. It is found that the hairpin vortex type of structures is capable of delivering a stronger flow control effect than the tilted vortex ring type of structures and this is correlated with the fact that the former also produces a higher surface shear stress increment upstream. It is found that the best flow control effect occurs when the maximum height of the hairpin structures is about that of the boundary layer with their limbs located at about a half of the boundary layer height. Among all the conditions examined in the current study, operating the synthetic jets at $L = 2$ and $VR = 0.36$ which yields hairpin-like structures with a streamwise spacing about 70% of the local boundary layer thickness at the jet orifices is found to produce the best flow control effect with the lowest power consumption. The evidence from this study also suggests that the flow separation delay produced by the synthetic jet array investigated here is due to the accumulated effect of the vortical structures on the boundary layer as they propagate downstream, rather than the local interaction of these structures with the separated flow.

Paper title:

Vortex Roll-Up Criterion for Synthetic Jets

Authors:

Jue Zhou, Hui Tang and Shan Zhong

Reformatted version of paper originally published in:

AIAA Journal, Vol. 47, No. 5, pp. 1252-1262, 2009

Corrections:

1. Fig 4.1 is modified from Crook (2002).
2. More details of mesh and time step size sensitivity study is added:

   A sensitivity study have been undertaken previously in which the effects of three meshes (5860, 23660, and 94640 mesh cells) and three time step sizes (T/32, T/80, and T/160) were examined in terms of the variation of axial velocity at the orifice exit. It was found there is only 2% difference in the maximum velocity between the medium mesh used in the present study and the fine mesh. And the velocity is not sensitive to the range of time step sizes tested. Therefore, the choices of mesh size and time step size used in the present study are adequate (Tang and Zhong, 2005b).
3. It is more suitable to use "reasonable" agreement instead of "good" agreement on the last line of page 113. Although the centreline velocity from the simulation is slightly larger (Fig. 4.3a), the computational results also show three distinct peaks observed from the PIV measurement, which correspond to the locations of consecutive vortex rings. Therefore, FLUENT is capable of reproducing the key characteristics of synthetic jets observed in the experiments.
4. Figure 4.3a is explained in detail:

   The oscillation of the centreline velocity is due to the existence of a train of vortex rings where the velocity peaks correspond to the centre of the vortex rings. However, as they propagate downstream, the vortex rings decelerate and eventually become indistinguishable from the jet flow due to vortex dissipation. Both the PIV data and the simulation result observe the decay in the velocity oscillation.
5. American spelling should be changed to British spelling, such as "grey", "behaviour", "neighbourhood", "centre", "centreline", "colour" and "millimetre".

6. The near parabolic exit velocity observed at S = 2.32 and 5.68 (Fig. 4.6a) corresponds to a thicker stokes layer, which inhibits the curling up of vortex sheets required for the formation of a vortex ring. Hence no vortex roll-up is observed.
7. The parameter map in Fig. 4.17 only shows the effects of S and L on the jet formation and vortex roll-up of synthetic jets. It is believed that the Reynolds number determines the vortex roll-up strength once the Stokes number is sufficiently high such that a predominant potential core is present in the jet flow.
8. The repeated "Firstly" on the last paragraph of page 132 is removed, and "Firstly" is changed to "First".

Chapter 4 Vortex Roll-Up Criterion for Synthetic Jets

Jue Zhou, Hui Tang and Shan Zhong

School of Mechanical, Aerospace and Civil Engineering, University of Manchester, UK

Abstract

In this paper, both theoretical analysis and numerical simulations are undertaken to study the parameters that affect the strength of vortex roll-up of synthetic jets. Firstly, a dimensional analysis reveals that the dimensionless vorticity of vortex roll-up produced by an orifice flow depends on the dimensionless stroke length, Stokes number and the ratio between the orifice diameter and the thickness of the Stokes layer. Based on the results from a fully developed oscillating laminar pipe flow, the Stokes number is found to play an important role in determining the thickness of the Stokes layer inside the orifice hence the shape of the velocity profile. Results from the numerical simulations confirm that the Stokes number also determines the strength of vortex roll-up of a synthetic jet issued from an orifice of a finite depth due to the same reason. Finally, a parameter map, which marks the three different regimes of synthetic jets classified as no jet, jet formation without vortex roll-up and jet formation with vortex roll-up, is produced based on the numerical simulation results. It is shown that for the synthetic jet actuator used in the present study, a minimum Stokes number of about 8.5 is required to ensure the occurrence of an appreciable vortex roll-up at a dimensionless stroke length greater than 4. In addition, a very low Stokes number can also suppress the formation of synthetic jets. This study provides a further understanding of the behavior of synthetic jets in quiescent conditions, which will be useful for designing more effective synthetic jet actuators where vortex roll-up is desired.

4.1 Introduction

A vortex ring is usually formed by ejecting fluid impulsively from an orifice (Shariff and Leonard, 1992). A vortex sheet separates at the edge of the orifice and rolls up to

form a vortex ring, which moves downstream with a self-induced translational velocity. Vortex rings produced by means of an impulsively started piston have been well studied with the earliest publications dated back to the 1850s. Research has been undertaken both numerically and experimentally to investigate how the characteristic parameters of fully formed vortex rings, such as the ring diameter, the circulation and translational velocity change with the nozzle geometry, the piston stroke and the velocity history of the piston movement (Pullin, 1979; Didden, 1979; Glezer, 1988; Gharbi et al, 1998).

In recent years, more research attention has been given to synthetic jets due to their potential for flow separation control in aerospace applications (Smith and Glezer, 1998; Glezer and Amitay, 2002; Zhong et al, 2007; Tang et al, 2007). A typical synthetic jet actuator consists of a small cavity with an oscillating diaphragm at its bottom side and an orifice plate at the opposite side, as shown in Fig. 4.1. As the result of the alternating of suction and blowing produced by the movement of the diaphragm, a succession of vortex rings is produced and propagates away from the orifice.

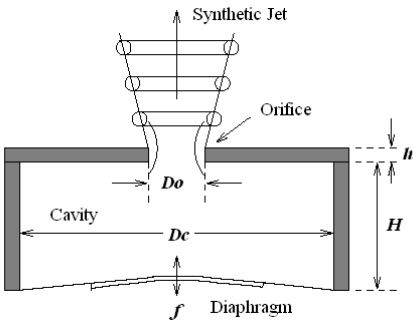

Figure 4.1. Schematic of synthetic jet actuator.

The vortex rings produced by a synthetic jet actuator differ from those produced by a piston arrangement in that the behavior of the former is strongly affected by the presence of a suction flow in the neighborhood of the orifice. As a result, a synthetic jet will only form when the vortex ring is able to overcome the suction velocity during the ingestion stroke. Holman et al. (2005) defined synthetic jet formation as the appearance of a time-averaged outward velocity along the jet axis which corresponds to the generation and subsequent convection of vortex rings. Based on their numerical and experimental studies, a formation criterion for both

two-dimensional and axisymmetric synthetic jets was proposed. It was stated that, in order for the synthetic jet to form, the reciprocal of the Strouhal number $\frac{1}{Str} = \frac{\overline{U}_o}{\pi f D_0}$ should be greater than a threshold value K, where the constant K depends on geometric factors such as orifice/slot shape, radius of curvature and aspect ratio of the slot. For axisymmetric synthetic jets, K is found to be equal to 0.16. Taking into account the relationship between the Strouhal number and the dimensionless stroke length, the preceding criterion can be translated into a dimensionless stroke length of about 0.5 for axisymmetric synthetic jets. A different value (≈ 0.25) was given by Milanovic and Zaman (2005). The difference in the threshold was attributed to factors such as the differences in the lip shape of the orifice and the diaphragm velocity program.

Vortex rings are known for their ability to entrain ambient fluid into their cores which enhances mixing. When a synthetic jet is issued into a boundary layer, the injection of coherent vortices via the initial vortex roll-up results in formation of a hierarchy of vortical structures that are capable of delaying flow separation (Zhou and Zhong, 2009; Jabbal and Zhong; 2008). It is understandable that the strength of vortex rings in terms of the level of circulation will determine the impact of synthetic jets on the external flow. A question remains, however, if a synthetic jet which satisfies the aforementioned formation criterion will definitely have a vortex roll-up. Guo and Zhong (2007) studied the behavior of synthetic jets issued from an orifice of 5×10^{-4} m diameter and observed no vortex roll-up at a dimensionless stroke length of 4 and a Stokes number of 7. This prompted them to investigate the conditions for vortex roll-up by conducting particle image velocimetry (PIV) measurements on a synthetic jet issued from an orifice of 5×10^{-3} m diameter. They found that the Stokes number is an important parameter which determines the strength of roll-up since it affects the shape of the velocity profile at the orifice exit. Based on a qualitative observation of their experimental results, it appears that a minimum Stokes number of about 10 is required for an appreciable roll-up to occur at a dimensionless stroke length of around 4. Nevertheless, a more in-depth examination of this criterion is still needed to provide a theoretical backup and evidence of validation.

To ensure the flow control effectiveness of synthetic jets in practical settings, a better knowledge of the parameters that affect the formation of these vortex rings is required. To the best knowledge of the authors of this paper, however, although there

has been a volume of research work on the roll-up process of vortex rings produced by a single pulsation of a piston (Shariff, 1992; Pullin, 1979; Didden, 1979; Glezer, 1988), the conditions for roll-up of vortex rings produced by synthetic jets have not been reported in the literature. In this paper, both dimensional analysis and numerical simulations are therefore undertaken to investigate the vortex roll-up criterion for synthetic jets issued into quiescent air. The dimensional analysis identifies the parameters which determine the extent of vortex roll-up. Numerical simulations were then undertaken to illustrate how these parameters affect the formation and strength of vortex roll-up for a 5mm diameter synthetic jet. Finally, a parameter map, which marks the three different regimes of synthetic jets classified as no jet, jet without roll-up and jet with vortex roll-up, is produced based on the numerical simulation results. The finding from this study is expected to be useful to the design of synthetic jet actuators for which formation of vortex rings is desired.

4.2 The Computational Methods

In this study, a synthetic jet actuator identical to that used by Guo and Zhong (2007) in their experiment is chosen as the model for the simulations (see Fig. 4.1). The actuator has a cylindrical cavity with a diameter $D_c = 4.5\times10^{-2}$ m and height $H = 1\times10^{-2}$ m. Its orifice has a diameter $D_o = 5\times10^{-3}$ m and depth $h = 5\times10^{-3}$ m, giving an orifice depth-to-diameter ratio h/D_o of 1. This particular orifice depth-to-diameter ratio is chosen since it is near the optimal value which was found to produce the maximum vortex circulation for an actuator of a similar design (Zhong et al, 2007). In the experiment, the thin rubber diaphragm, which is sandwiched between two metal disks, is clamped circumferentially to the end of the cylindrical cavity and the center of the diaphragm is attached to a permanent magnetic shaker via a steel rod. The diaphragm is made to oscillate in a sinusoidal manner at predetermined diaphragm oscillation displacements and frequencies. At small displacements, this diaphragm mimics the motion of an oscillatory piston.

Unsteady incompressible laminar flow simulations are performed using a commercial solver, FLUENT 6.2. To simplify the computation, the flow is treated as axisymmetric. The flow in both the orifice and actuator cavity are included in the simulation in order to ensure the accuracy of the results. The computational

geometry and the boundary conditions used in the simulation are shown in Fig. 4.2. To ensure adequate spatial resolution of the flow structures, the grids are densified in the actuator orifice, the region around the jet central plane and near the walls. The entire computational domain contains 23,660 mesh cells. The time-step used in the simulations is $T/80$. A sensitivity study undertaken previously showed that the choices of mesh size and time-step used in the present study are adequate (Tang and Zhong, 2005b).

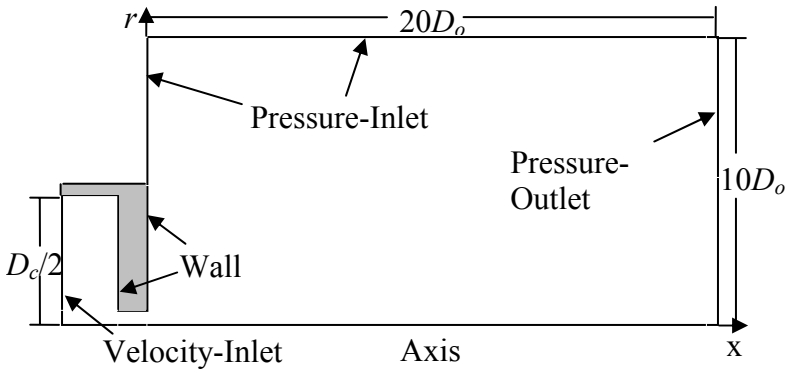

Figure 4.2. Computational geometry and boundary conditions.

In the present study, the instantaneous displacement relative to its neutral position of the oscillating diaphragm is given by:

$$\delta(t) = \frac{\Delta}{2}\sin(2\pi ft) \tag{4.1}$$

where δ is the deformation of the diaphragm relative to its neutral position, and Δ is the peak-to-peak displacement of the diaphragm. To simplify the computation, a velocity boundary condition is applied at the neutral position of the diaphragm. The moving velocity of the diaphragm can be obtained by differentiating Eq. 4.1 with respect to time,

$$\upsilon(t) = \pi\Delta f\cos(2\pi ft) \tag{4.2}$$

The velocity boundary condition is specified using user-defined functions (UDFs) supported by FLUENT.

The numerical method has been validated using data measured with PIV and a hot-wire by Tang and Zhong (2005b). Two figures extracted from their paper illustrating the good agreement between the predicted and measured instantaneous

jet centreline velocity and jet exit velocity profile are shown in Fig. 4.3. It is evident that the computational software with the setting used in this study is capable of reproducing the key characteristics of synthetic jets observed in the experiments.

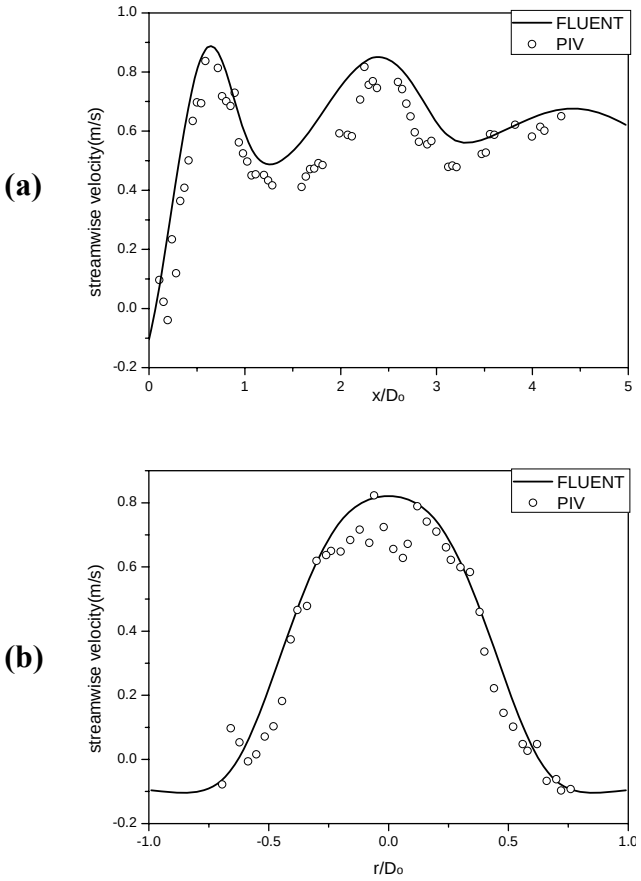

Figure 4.3. Comparisons of streamwise velocity (a) along the jet centerline at t/T = 9/16, and (b) in the spanwise direction at x/D_o = 1, t/T = 14/16 with PIV data (Tang and Zhong, 2005b).

4.3 Dimensionless Parameters of Synthetic Jets

The behavior of synthetic jets issued into a quiescent flow is usually characterized by three non-dimensional parameters, i.e. the dimensionless stroke length L, the Reynolds number Re_L based on stroke length, and the Stokes number S (Zhong et al, 2007). The stroke length of a synthetic jet represents the length of a fluid column that is pushed out during an actuation cycle, i.e.

$$L_o = \overline{U}_o T \text{ (Gelzer, 1988)} \tag{4.3}$$

where $\overline{U}_o$ is the time-averaged blowing jet velocity over an entire cycle and T is the oscillating period. It defines an important dimensionless parameter for synthetic jets called the dimensionless stroke length

$$L = \frac{L_o}{D_o} = \frac{\pi}{Str} \tag{4.4}$$

The Reynolds number defined based on the time-averaged jet velocity $\overline{U}_o$ and the stroke length L_o is given by

$$\mathrm{Re}_L = \frac{\overline{U}_o L_o}{\nu} \tag{4.5}$$

where ν is the kinematic viscosity coefficient. Re_L is often regarded important because it is proportional to the total circulation ejected through the orifice during the blowing cycle (Tang and Zhong, 2006). The Stokes number is commonly defined as

$$S = \sqrt{\frac{2\pi f D_o^2}{\nu}} \tag{4.6}$$

It is found to determine the pressure losses due to friction as well as the entrance and exit flow in the orifice (Raju et al, 2007). Since the Stokes number is related to L and Re_L via $\mathrm{Re}_L = L^2S^2/2\pi$, only two of the preceding three dimensionless parameters are independent.

Along another line of thought, the importance of these three parameters can also be appreciated. The flow inside the actuator is dictated by the counteraction of three forces, i.e. the unsteady force, viscous force and inertia force. Here the unsteady force is referred to as the force arising from the oscillating pressure field imposed by the oscillating diaphragm. If D_o, $\overline{U}_o$ and T are chosen as the characteristic length, velocity and time scale, the representative inertia force, viscous force and unsteady force in this case can be expressed as, $\frac{\overline{U}_o^2}{D_o}$, $\frac{\nu\overline{U}_o}{D_o^2}$ and $\frac{\overline{U}_o}{T}$ respectively. The ratio of the unsteady force and the inertia force yields the

dimensionless stroke length, justifying its appearance in the jet formation criterion as to if the inertia force overcomes the suction effect imposed by the unsteady force. Similarly, the ratio of the inertia force and viscous force gives the Reynolds number, justifying the use of Reynolds number as an important parameter that determines the state of the jet as it comes out of the orifice (Glezer, 1988). Finally, the ratio of the unsteady force and viscous force gives the Stokes number. In the rest of this paper, it will be shown that the Stoke number is also an important parameter which affects the behavior of synthetic jets through the strength of vortex roll-up.

4.4 Dimensionless Parameters Determining the Strength of Vortex Roll-Up

The formation of vortex rings is believed to be directly related to the evolution of the vortex sheet produced in the orifice (Shariff, 1992).When fluid is ejected from an orifice, a vortex sheet is formed which then proceeds to roll up into a vortex ring. The velocity across an idealized vortex sheet is discontinuous and consists of a continuous distribution of vortex lines. Crook (2002) described the roll-up process as follows (see Fig. 4.4):

1. The vortex sheet induces a velocity on itself perpendicular to the plane of the sheet and this induced velocity is maximum at the leading edge of the sheet;
2. The self-induced velocity causes the leading edge of the sheet to curl;
3. The curled vortex sheet continues to induce a velocity component on the leading edge, which together with the normal component of the velocity induced by the uncurled sheet, is responsible for the roll-up observed in Fig. 4.4d.

Note that in reality the velocity jump across the vortex sheet is not discontinuous due to the action of viscosity.

The strength of a vortex sheet can be measured by the level of vorticity Ω. Based on the definition of vorticity, if $\partial \upsilon / \partial x$ is ignored, the vorticity on a cylindrical vortex sheet can be expressed as

$$\Omega = \frac{\partial \upsilon}{\partial x} - \frac{\partial u}{\partial r} \approx -\frac{\partial u}{\partial r} \tag{4.7}$$

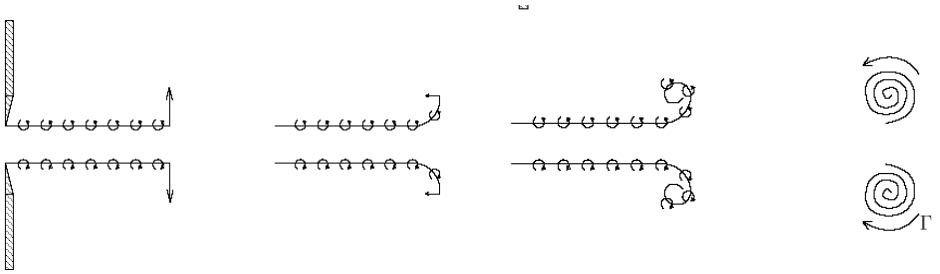

Figure 4.4. Idealized vortex ring formation: (a) creation of vortex sheet through an orifice, (b) and (c) curling up of vortex sheet, (d) roll-up. Straight arrows represent induced velocity and small curved ones represent vorticity (Crook, 2002).

The order of magnitude of vorticity on the vortex sheet can be estimated as

$$\Omega \sim \frac{\overline{U}_o}{\varepsilon} = \frac{LfD_o}{\varepsilon} = Lf\frac{D_o}{\varepsilon} \tag{4.8}$$

where ε is the thickness of the Stokes layer in the orifice, which is defined as the radial distance between the position of the velocity peak and the wall at the orifice exit.

Taking into account the scale effect, one can get the dimensionless form of the vorticity

$$\frac{\Omega D_o^2}{\nu} \sim L \cdot S^2 \cdot \frac{D_o}{\varepsilon} \tag{4.9}$$

Equation (4.9) reveals that the dimensionless vorticity is approximately proportional to the dimensionless stroke length L, Stokes number S and the ratio D_o/ε. It also indicates that, to obtain a similar roll-up, vorticity Ω should be much higher for a synthetic jet issued from a smaller orifice. This is true because the vortex ring of small scale has a higher curvature, which demands a higher level of vorticity on the vortex sheet.

By integrating the velocity jump along the stroke length L_o, the integrated strength of the finite vortex sheet, i.e. the circulation of the vortex ring, can be estimated as

$$\Gamma \sim \Omega \cdot \varepsilon \cdot L_o \sim U_o L_o = (LfD_o) \cdot (LD_o) = L^2 fD_o^2 \tag{4.10}$$

Its non-dimensional form becomes

$$\frac{\Gamma}{\nu} \sim L^2 \frac{fD_o^2}{\nu} = \frac{L^2 S^2}{2\pi} \sim \mathrm{Re}_L \tag{4.11}$$

Equation (4.11) indicates the dimensionless vortex circulation can be characterized by the Reynolds number Re_L, which is consistent with the previous finding by Glezer (1988).

The normalized thickness of the Stokes layer ε/D_o is expected to depend on both L and S. Assuming a fully developed oscillating laminar pipe flow, i.e. the flow velocity does not change with the streamwise distance, ε/D_o is found to be a function of the Stokes number only. Figures 4.5a and b show the variation of ε/D_o and its inverse against the Stokes number S, respectively. Figure 4.5a indicates that the Stokes layer extends to the center of the orifice exit when $S < 10$, whereas it retreats rapidly towards the orifice wall as S increases above 10. Being a measure of the ratio between the unsteady force and the viscous force, a higher Stokes number is expected to result in a thinner boundary layer along the orifice wall. Figure 4.5a shows that D_o/ε increases exponentially as S increases above 10. Hence, according to Eq. 4.9, the vorticity strength will subsequently experience a tremendous increase.

The thickness of the Stokes layer directly affects the location of the peak velocity in the velocity distribution hence the exit velocity profile. This will affect the concentration of vorticity in the vortex sheet hence its capability to form a vortex ring. At $S < 10$, the maximum velocity occurs at the center of the orifice exit hence a 'thick' cylindrical vortex sheet dominates the entire orifice. Consequently, the leading edge of the vortex sheet will be unable to curl due to the axisymmetry and continuum of the flow. When S is greater than 10, however, a potential core appears at the center of the orifice, allowing the vortex sheet to curl and a vortex ring to form.

The preceding discussion is based on the assumption that the oscillating flow in the orifice is fully developed. For actuators in which the orifice depth-to-diameter ratio h/D_o is too small to allow the flow in the orifice to become fully developed, the requirement on the Stokes number loosens since a potential core tends to exist due to the entrance effect.

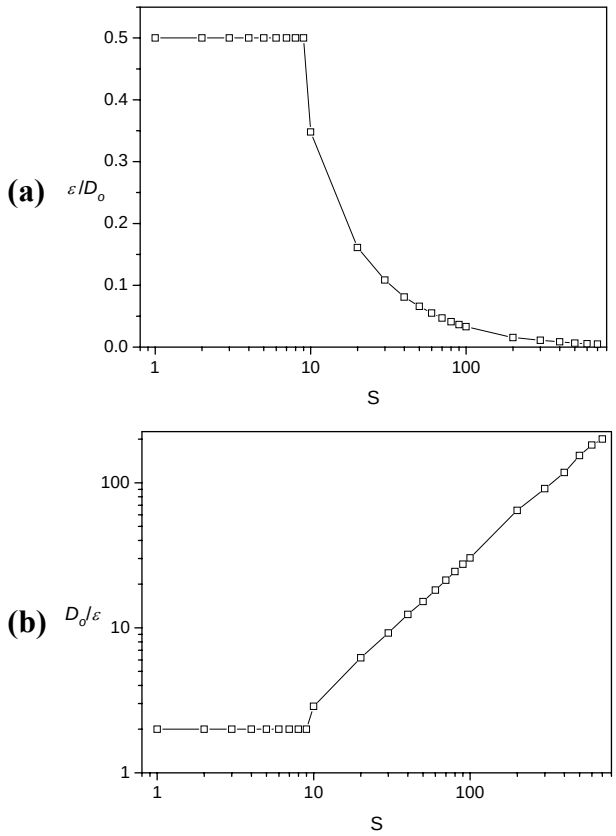

Figure 4.5. Variation of the thickness of the Stokes layer in an oscillating pipe flow (a) ε/Do vs. S (b) Do/ε vs. S.

4.5 Effects of the Dimensionless Parameters on Vortex Roll-Up of Synthetic Jets

Based on Eq. 4.9, both S and L will affect the strength of vortex roll-up. The aforementioned analysis reveals that for a fully developed oscillating orifice flow, the Stokes number plays an important role in determining the exit velocity profile hence the tendency and strength of vortex roll-up. In this section, numerical simulations are used to illustrate the effect of changing S and L on the exit velocity profile and the strength of vortex roll-up of synthetic jets issued from an orifice with a finite length (h/D_o = 1) attached to a cavity. The simulations were undertaken on the actuator described in section 4.2 for two groups of selected test cases in which either L or S was made the same by using different combinations of diaphragm displacements and frequencies. The exit velocity profiles normalized by the mean velocity $\overline{U}_o$ at the instant of maximum expulsion are then compared and the extent of vortex roll-up is examined.

As shown in Fig. 4.6a, at the same dimensionless stroke length (L = 3) the exit velocity profile changes gradually from a near parabolic shape to a top-hat shape as S increases from 2.32 to 14.7. A Similar trend was also observed in the experiment by Guo and Zhong (2007). The observed variation in the exit velocity profile is consistent with the finding from the fully developed oscillating flow discussed in the previous section, i.e. an increasing Stokes number results in a decrease in the thickness of the Stokes layer. In Fig. 4.6b, the normalized velocity profiles at the same Stokes number (S = 14.7) but different L are compared. It is shown that, although to a lesser extent, the dimensionless stroke length also affects the shape of the exit velocity profiles considerably, especially the central part of the profile. A lower L due to the use of a smaller diaphragm displacement results in a dip in the central region which is commonly observed in an oscillating pipe flow. This phenomenon tends to enhance the effect of the Stokes number at low L since the Stokes layer becomes thinner as the result of the velocity peak being closer to the wall (see Fig. 4.6b). As the dimensionless stroke length increases, the dip stretches itself out as the result of an increase in the jet momentum.

To illustrate how the extent of vortex roll-up is affected by the magnitude of the Stokes number, the flow fields at the corresponding test conditions in Fig. 4.6a are examined in detail. The velocity vector fields at four different phases during the diaphragm oscillation cycle at S = 14.7 are shown in Fig. 4.7. The velocity vectors are color coded with the local velocity magnitude. To make weak vortices more visible, velocity vectors of the same length are used despite the differences in their velocity magnitudes. It can be seen at the maximum blowing phase (corresponding to the diaphragm at the neutral position in the blowing cycle) a vortex pair associated with a strong rotational motion is formed at the orifice exit (see Fig. 4.7a). This vortex pair propagates downstream progressively along with the central region of high velocity during the entire cycle.

To enable a confirmation of the presence of vortex roll-up which is accompanied by entrainment of ambient fluid into the vortex core, the patterns of particle tracers at the corresponding phases are shown in Fig. 4.8. The particle tracers are released into the flow at short intervals of time from both the orifice exit and parallel lines in space which are $0.02D_o$ apart outside the orifice. To allow the particles which originate from inside the orifice to be distinguished from those which originate from outside, the particles released from the orifice exit are shown in gray

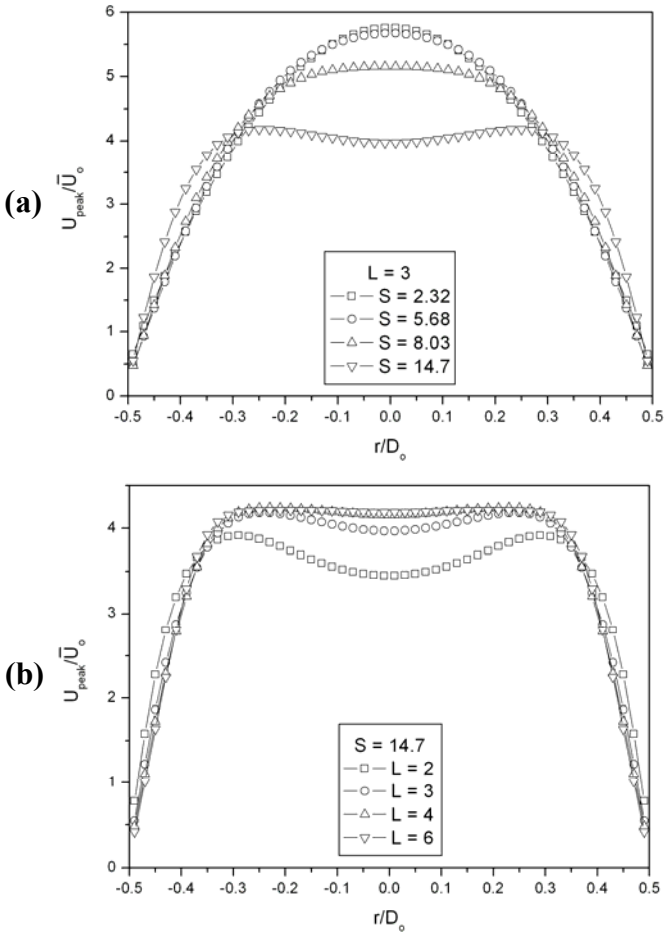

Figure 4.6. Comparisons of exit velocity profiles of a synthetic jet at the phase of maximum expulsion at different (a) Stokes numbers; (b) dimensionless stroke lengths.

and those from the outside are shown in black. At the phase of maximum blowing (Fig. 4.8a), the timelines on the wings of the structure, which is produced by the ejected fluid, curl upstream due to an intense local rotational motion. As the blowing cycle proceeds, the black tracers are seen to be drawn into the wings of this structure and swirl around it, indicating that the ambient flow near the orifice exit is being entrained into this structure. The location of the center of the vortex pair revealed by the velocity vectors appears to coincide with the region of the structure where the ambient fluid is entrained into, indicating that this vortex pair is responsible for the entrainment activity revealed by the timelines. This vortex pair is believed to be a part of a vortex ring caused by vortex roll-up of the ejected fluid from the orifice. This case is considered to be a typical case where a strong vortex roll-up is present.

As the Stokes number is reduced to 8.03, a vortex pair similar to that observed at S = 14.7 also appears, although its strength is relatively weaker as indicated by a smaller velocity magnitude (Fig. 4.9). The pattern of particle tracers (Fig. 4.10), however, indicates that the amount of entrainment brought about by this vortex pair is only marginal. Hence, this case is considered to be a transitional case for vortex roll-up.

At S = 5.68, a vortex pair also appears at the orifice exit at the phase of maximum blowing (Fig. 4.11a). It is weaker than those observed at S = 8.03 and 14.7 since it is associated with a lower velocity magnitude. The vortex pair disappears shortly downstream at the phase of maximum suction (corresponding to the diaphragm at the neutral position in the suction cycle) (see Fig. 4.11c). Although the timelines on the wings of the structure produced by the ejected fluid still curl towards the stem of the jet, a rotational motion is barely visible. In addition, almost no entrainment of ambient fluid is revealed by the particle tracers (Fig. 4.12). In fact, the vortex pair which is revealed by the velocity vectors appears to be located outside the region that is occupied by the fluid ejected from the orifice. Hence it is not a part of a vortex ring. As the jet does appear to advance downstream during the cycle as shown by the timelines, this case is considered to be one which has jet formation but no vortex roll-up.

It can be seen that a much weaker vortex pair of a similar nature to that observed at S = 5.68 also occurs at the smallest Stokes number, S = 2.32 (see Fig. 4.13a). The external timelines are deformed into a "Ω" shape in the blowing stroke due to the fluid expulsed from the orifice exit (Figs. 4.14a and b). Again no entrainment of ambient fluid into the flow structure produced by the jet is seen. During the suction cycle, a substantial amount of ejected fluid is ingested into the cavity such that the most downstream part of the timelines shows no forward movement during the entire cycle, indicating that the jet does not propagate away from the orifice (Figs. 4.14c and d). Hence a synthetic jet is not formed.

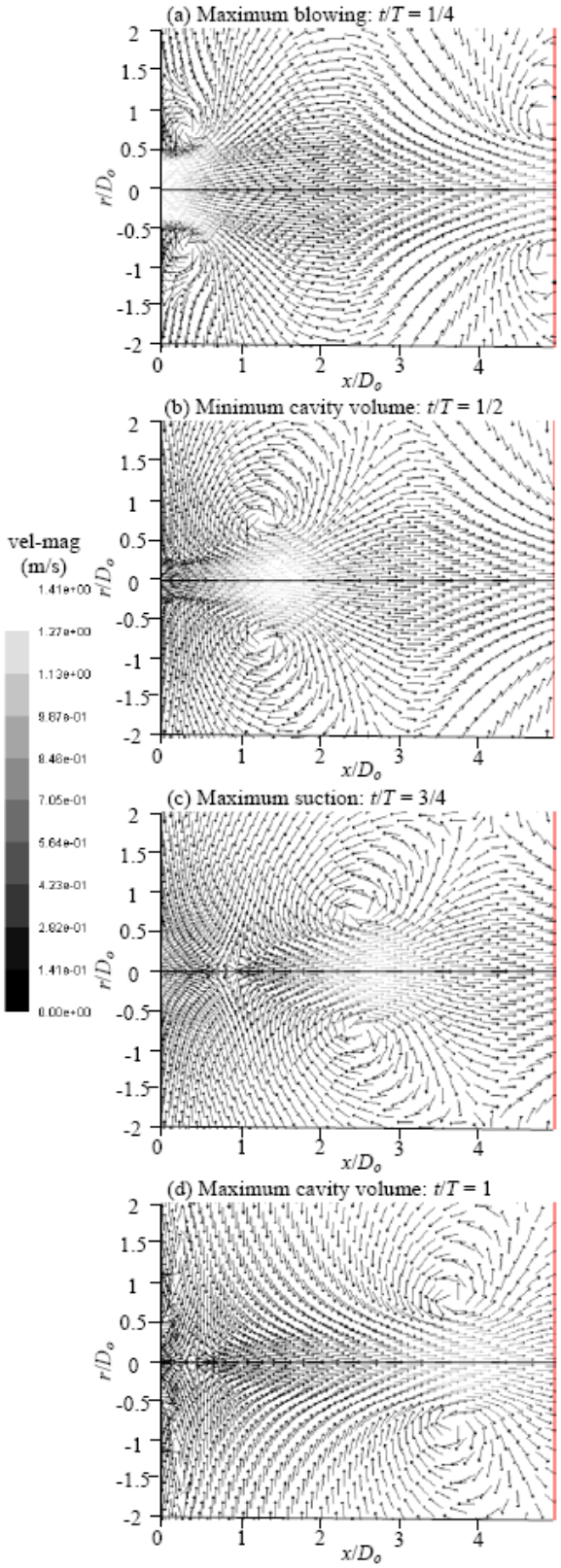

Figure 4.7. A time sequence of velocity vector field at S = 14.7 and L = 3.

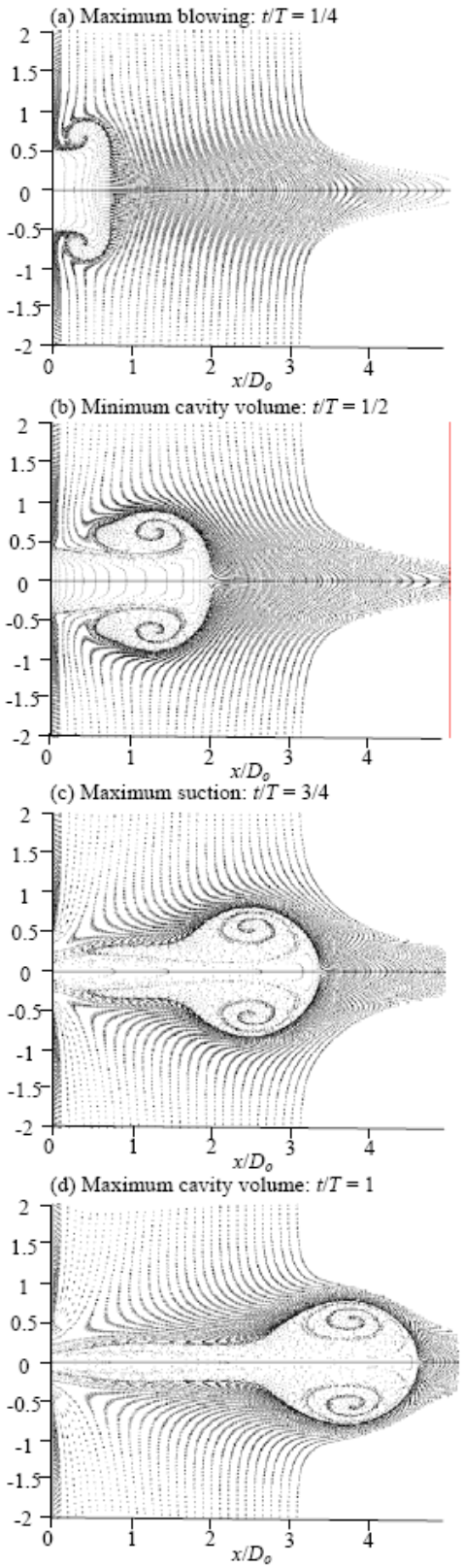

Figure 4.8. A sequence of patterns of timelines at S = 14.7 and L = 3.

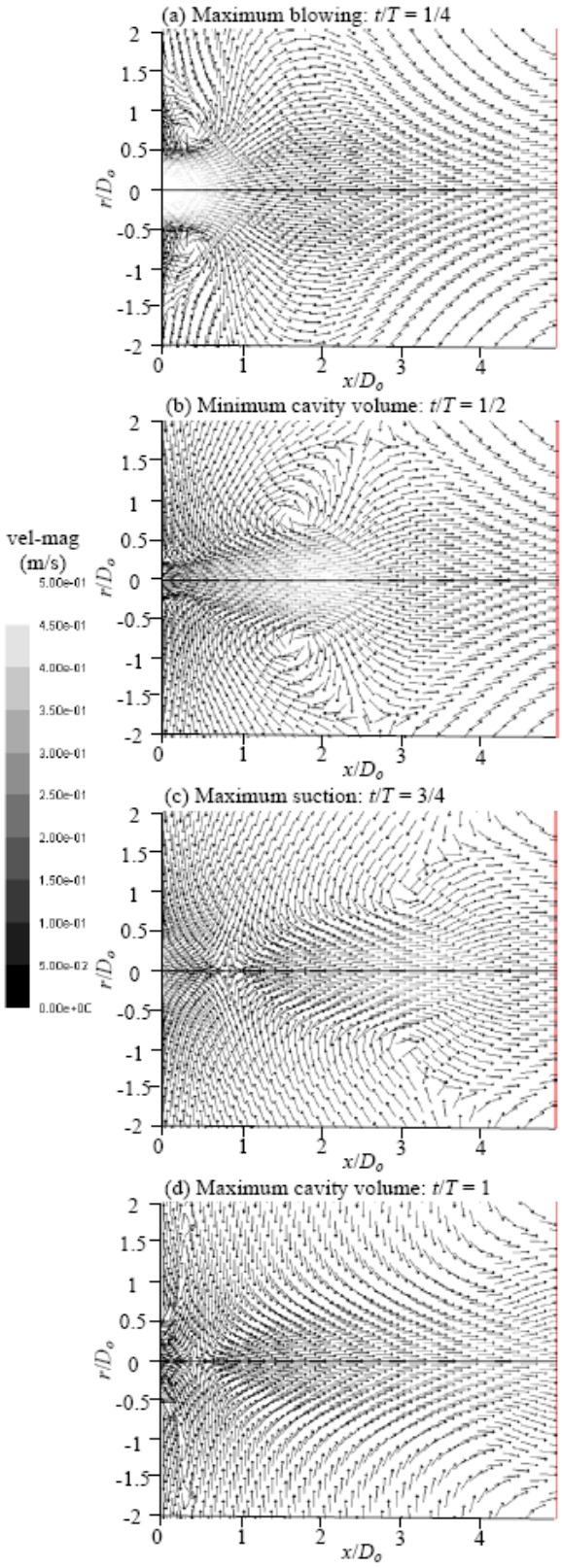

Figure 4.9. A time sequence of velocity vector field at S = 8.03 and L = 3.

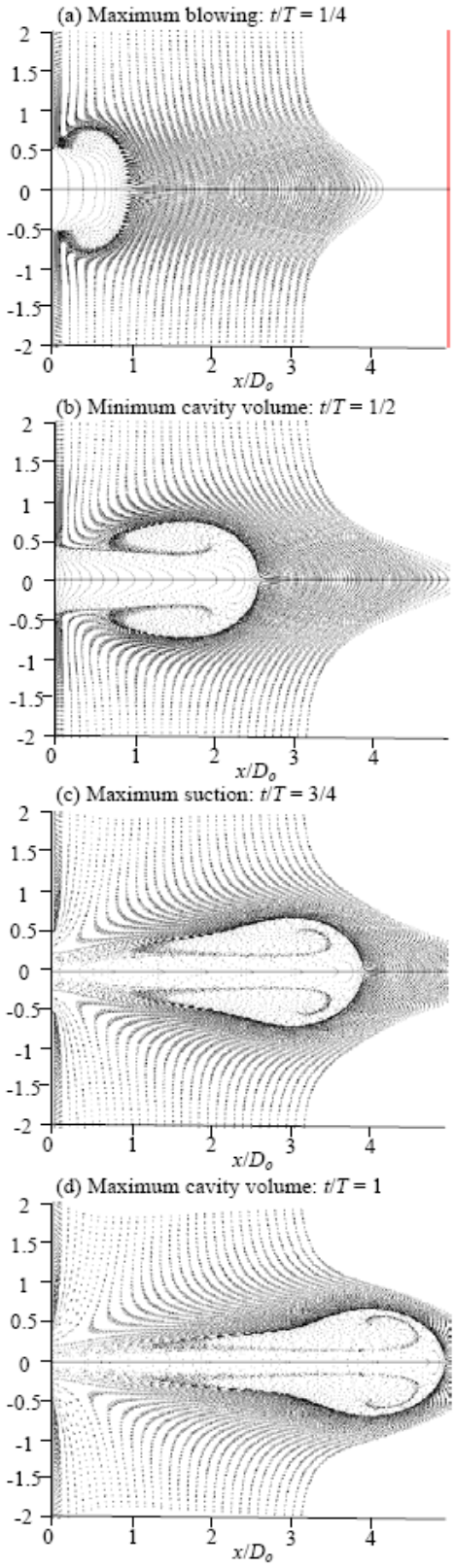

Figure 4.10. A sequence of patterns of timelines at S = 8.03 and L = 3.

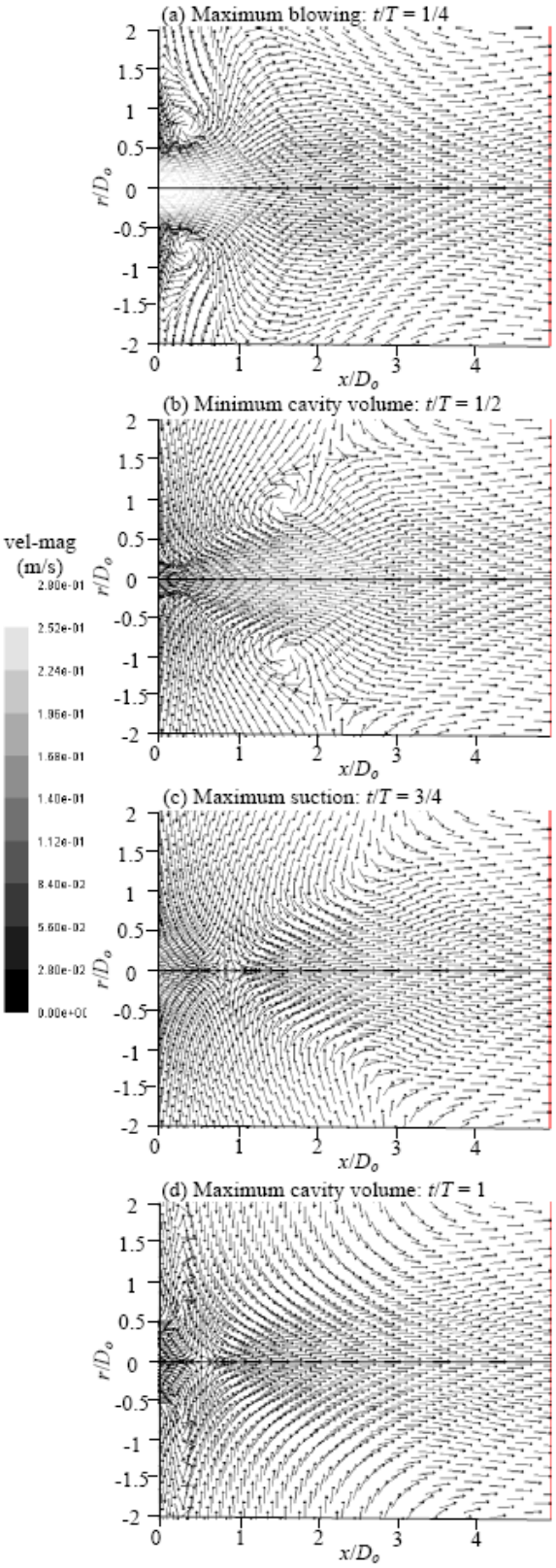

Figure 4.11. A time sequence of velocity vector field at S = 5.68 and L = 3.

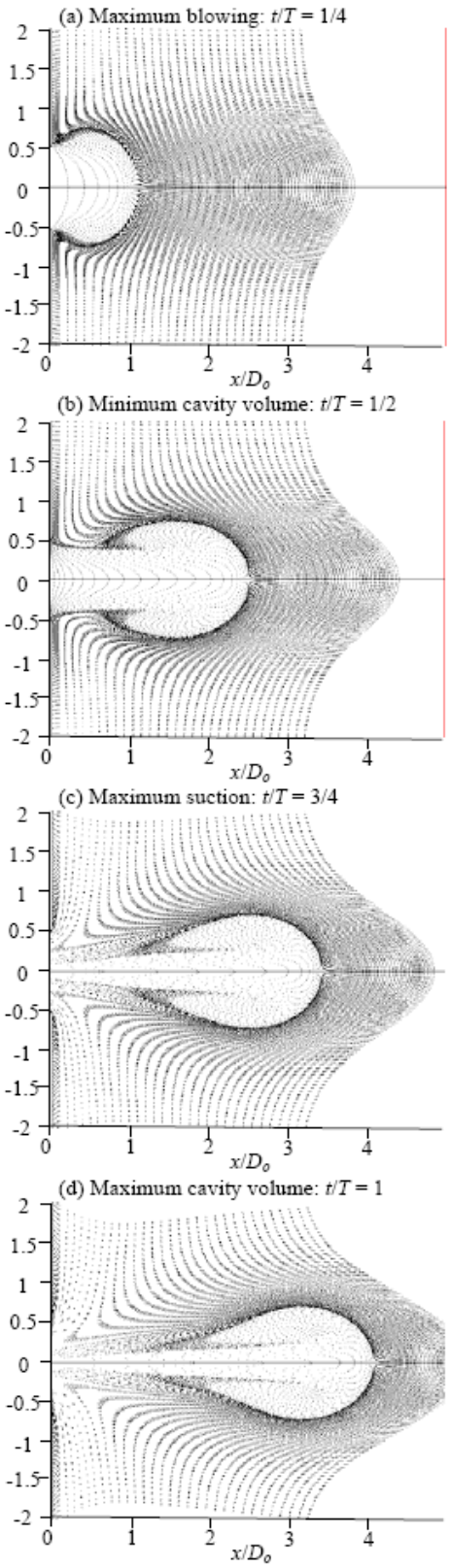

Figure 4.12. A sequence of patterns of timelines at S = 5.68 and L = 3.

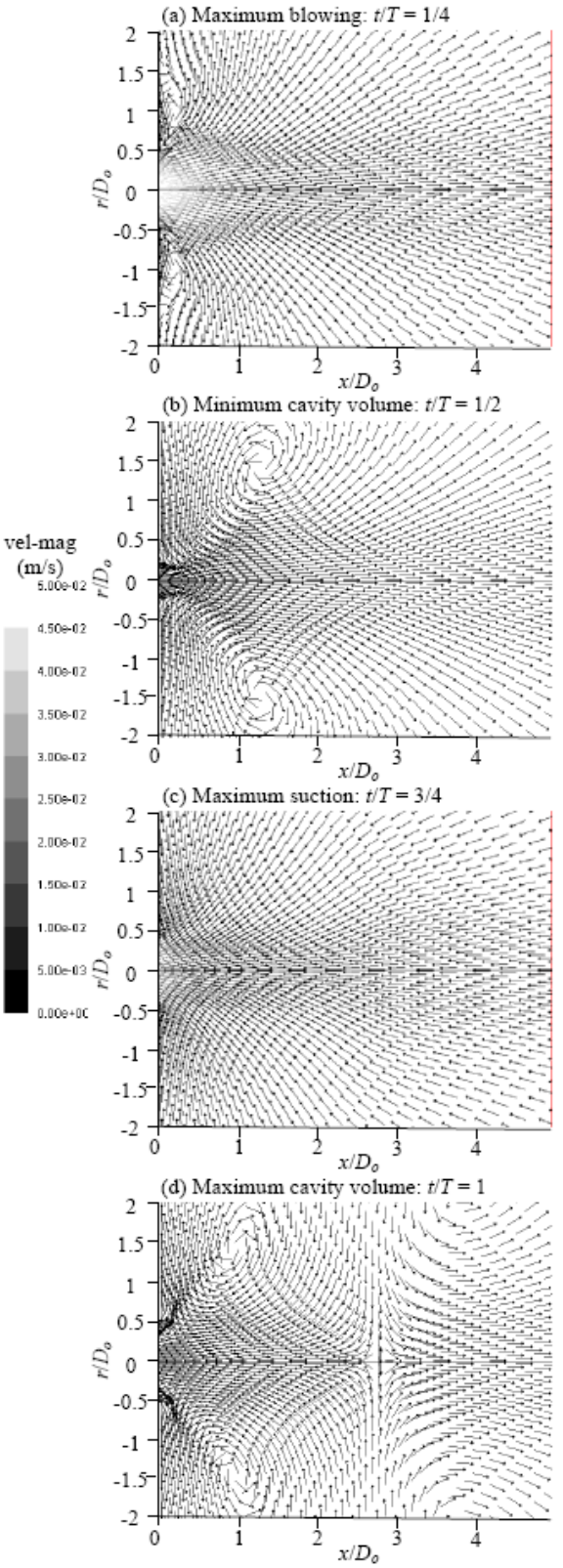

Figure 4.13. A time sequence of velocity vector field at S = 2.32 and *L* = 3.

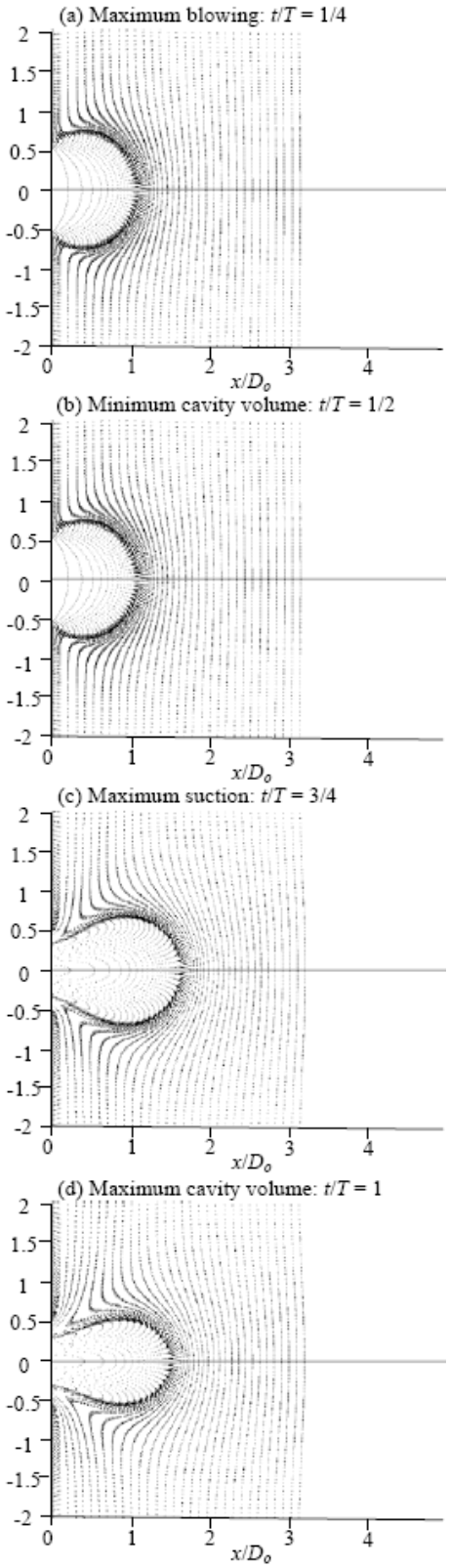

Figure 4.14. A sequence of patterns of timelines at *S* = 2.32 and *L* = 3.

Figure 4.15 shows the instantaneous centerline streamwise velocity for the corresponding cases in Figs. 4.7 to 4.14 at four phases. At S = 2.32, the magnitude of the streamwise velocity at the centerline decreases sharply at all phases and drops to almost zero within a distance of approximately $2D_o$ from the orifice (see Fig. 4.15a), confirming that no jet is formed in this case. At S = 5.68, the magnitude of velocity fluctuations is a lot higher (Fig. 4.15a). Although its value indicates the presence of only one distinct structure and a subsequent rapid decay within $4D_o$ from the orifice, a non-zero streamwise velocity is observed at a distance of $12D_o$ downstream from the orifice exit. Hence a synthetic jet should have been formed despite its weak strength. As S increases further, not only the magnitude of velocity increases but also multiple velocity peaks are observed indicating the propagation of a train of structures downstream (see Figs. 4.7a and c). This is what would be expected when vortex rings are formed.

(a)

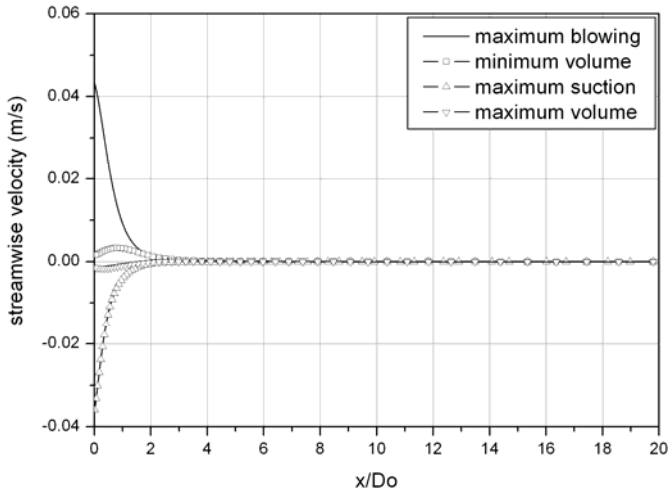

(b)

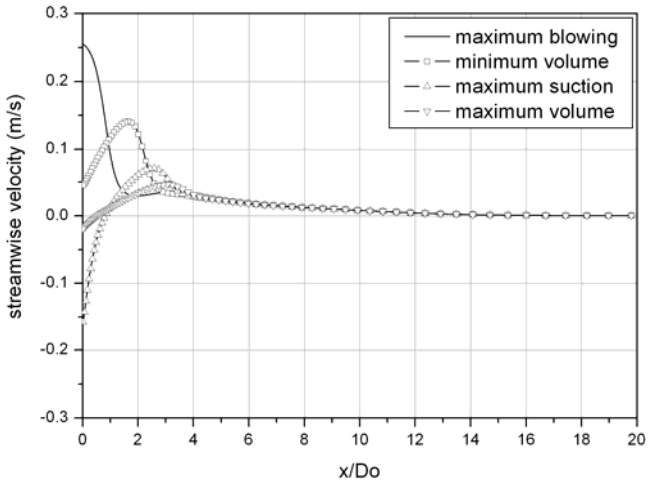

For caption see overleaf

(c)

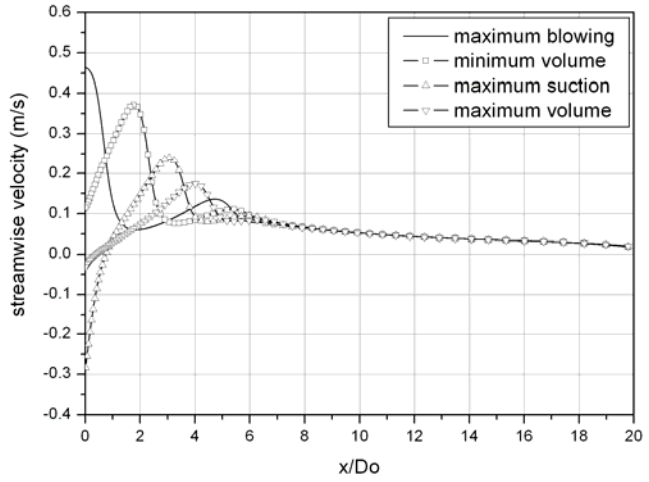

(d)

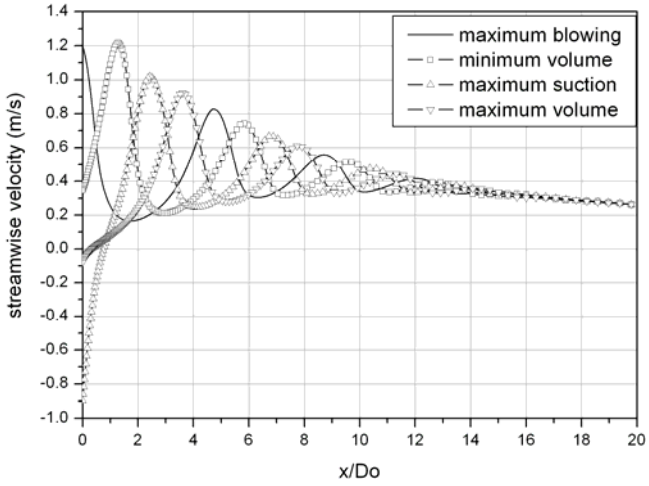

Figure 4.15. Instantaneous streamwise velocities at the jet centerline for the cases at L = 3, (a) S = 2.32; (b) S = 5.68; (c) S = 8.03; and (d) S = 14.7.

From the preceding discussion of the four cases, it can been seen that when the dimensionless stroke length is kept constant, as the Stokes number increases the synthetic jets go through three different regimes from no jet formation, jet formation without vortex roll-up to jet formation with vortex roll-up. The near parabolic exit velocity profile at S = 2.32 and 5.68 is believed to be the reason that no vortex roll-up is observed in these cases, since a thick Stokes layer inhibits the curling up of vortex sheets required for the formation of a vortex ring. Based on the preceding visual impressions, it is confirmed that a minimum Stokes number is required for an appreciable roll-up to occur within the range of dimensionless stroke length examined here. Furthermore, it should be noted that although the dimensionless stroke length L is 3, which is well above the jet formation criterion of L = 0.5 proposed by Holman et al, a jet formation fails to occur at S = 2.32 (see Figs. 4.13

and 4.14). Hence it appears that the Stokes number also has to be large enough to ensure jet formation even at a large stroke length.

As shown in Eq. 4.11, the Reynolds number Re_L characterizes the level of vortex circulation of a synthetic jet. The current study suggests, however, that there is an exception when the Stokes number is below a threshold value. Figure 4.16 shows the vorticity contour superimposed on the velocity vector field for two test cases, which have the same Reynolds number (Re_L =137) but different S hence two distinctly different exit velocity profiles. At S = 14.7, the exit velocity profile has a top-hat shape, and the core of the roll-up vortex is found to almost coincide with the location of peak vorticity. Since the potential core is irrotational, all circulation produced by the blowing part of the cycle is likely to be contained in the vortex ring. At S = 7.35, however, the exit velocity profile has a near parabolic shape. At this Stokes number, an offset exists between the center of the vortex roll-up and the location of peak vorticity in the shear layer. It appears that only a small portion of the total circulation produced by the blowing part of the cycle is accumulated in the vortex and the rest is deposited in the shear layer which extends to the jet centerline. This suggests that although Re_L determines the total circulation ejected through the orifice, the Stokes number moderates the proportion that will be collected in the initial roll-up. Nevertheless, when the Stokes number is sufficiently high such that a predominant potential core is present in the jet flow, it may become more adequate to state that the Reynolds number determines the roll-up strength since a majority of the total circulation is pumped into the vortex ring.

4.6 Parameter Map for Jet Formation and Vortex Roll-Up

From the preceding discussion, it has become clear that the Stokes number plays an important role in determining the strength of vortex roll-up of a synthetic jet since it affects the shape of the exit velocity profile significantly. It appears that the Stokes number also has to be large enough to ensure jet formation even at a large dimensionless stroke length. In order to appreciate the effect of both Stokes number and dimensionless stroke length on the state of a synthetic jet, it is useful to establish a parameter space in which the different regimes of synthetic jets classified as no jet

formation, jet formation without roll-up and jet formation with vortex roll-up are identified for the present actuator.

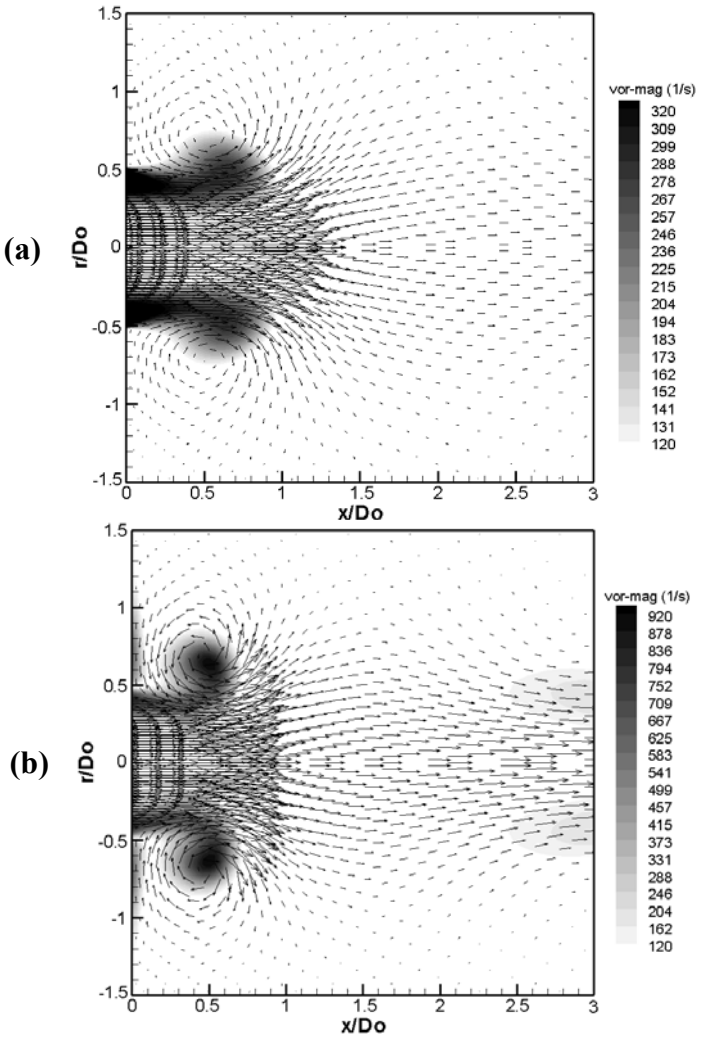

Figure 4.16. Comparison of synthetic jets at the same Re_L showing how the Stokes number moderates the strength of vortex roll-up (a) $L = 4$ and $S = 7.35$ ($Re_L = 137$) at $t/T = 1/4$; (b) $L = 2$ and $S = 14.7$ ($Re_L = 137$) at $t/T = 3/8$.

In this study, numerical simulations of 70 cases have been undertaken using different combinations of diaphragm displacements and frequencies which cover the range of $0.5 < L < 10$ and $2 < S < 26$. The timeline method described in the previous section is used to display the results and to determine the state of the synthetic jets in a semi-qualitative manner. A parameter map containing all the test cases is shown in Fig. 4.17. The parameter map can be divided into three regimes, corresponding to no jet formation, jet formation without vortex roll-up and jet formation with vortex roll-up. Transitional boundaries between different regimes are obtained by best fitting the data shown in Fig. 4.17.

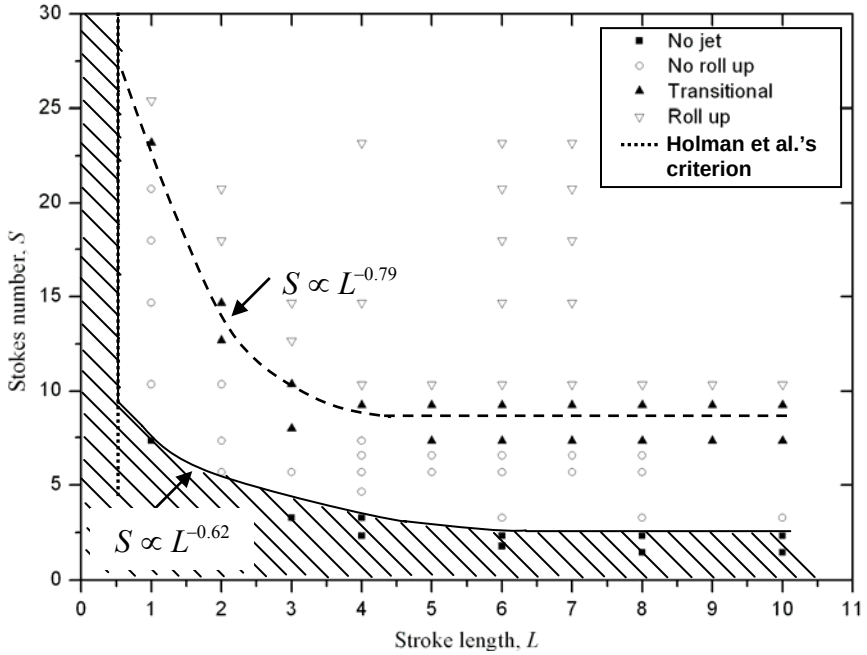

Figure 4.17. Parametric map showing different regimes of synthetic jet formation.

From this graph it is seen that the synthetic jet can not be formed when the Stokes number is low even at very high stroke lengths and the threshold value of Stokes number for jet formation increases as the dimensionless stroke length decreases. A best fit of the boundary between no jet and jet formation without roll-up shows that on the boundary $S \propto L^{-0.62}$. It is believed that the reason that the jet does not form at very low Stokes numbers is the viscous effect being too high to allow the periodic formation of the jet. In the jet formation criterion proposed by Holman et al. (2005), only the counteraction of the inertia force and the unsteady force is considered, resulting in the dimensionless stroke length being the only parameter that affects jet formation.

For the present actuator, jet formation is observed at the dimensionless stroke length of $L = 1$ when $S > 7.5$. Here a boundary between no jet formation and jet formation without vortex roll-up is drawn at $L = 0.5$ on the graph based on the formation criterion given by Holman et al. (2005).

There is a reasonably well-defined transitional boundary separating the jets with and without vortex roll-up. For $L < 4$, the threshold of S for vortex roll-up increases as the dimensionless stroke length decreases. The transitional boundary has an expression of $S \propto L^{-0.79}$. For $L > 4$, the transitional boundary is asymptotic to a

horizontal line at about S = 8.5, suggesting that the threshold of S for vortex roll-up remains constant at large L. Hence at large dimensionless stroke lengths, the Stokes number is the only parameter which determines if a vortex roll-up will occur. The need to have a sufficiently high Stokes number for vortex roll-up to occur in a synthetic jet is consistent with the finding from the theoretical analysis of a fully developed oscillating pipe flow discussed in section 4.4. The slightly lower threshold value than the theoretical predicted value of 10 is believed to be caused by the relatively short length of the orifice which encourages the exit velocity profile to acquire a top-hat shape. It should be noted that the threshold value of S = 8.5 for vortex roll-up is obtained specifically for the synthetic jet actuator studied in this paper. Hence a deviation from this value is expected for actuators which have a different orifice lip shape, orifice depth-to-diameter ratio and velocity program.

According to its definition, the Stokes number decreases linearly with the orifice diameter and increases linearly with the square root of the actuation frequency. Since the orifice diameter is expected to be in the range of a few tenths or hundredths of a millimeter for flow control purposes in aerospace applications, the Stokes number may become undesirably low with the use of a very small orifice, resulting in no vortex roll-up or even no jet formation. Based on the finding from this study, to ensure the flow control effectiveness of synthetic jets in practical settings, as the scale of the actuator reduces, the actuator operating frequency has to increase substantially in order to satisfy the condition for vortex roll-up. On the other hand, since the displacement of an actuator driven by a piezoelectric diaphragm decreases significantly at high frequencies, achieving a sufficient dimensionless stroke length so as to ensure jet formation can also become more challenging. Therefore both the jet formation criterion and the vortex roll-up criterion should be considered in conjunction with each other when one is designing the synthetic jet actuators for aerospace applications.

4.7 Conclusions

In this paper, both theoretical analysis and numerical simulations are undertaken to study the parameters that affect the strength of vortex roll-up of synthetic jets. Firstly, Firstly, a dimensional analysis reveals that the dimensionless vorticity of vortex roll-

up produced by an orifice flow depends on the dimensionless stroke length, Stokes number and the ratio between the orifice diameter and the thickness of the Stokes layer. Based on the results from a fully developed oscillating laminar pipe flow, the Stokes number is found to play an important role in determining the thickness of the Stokes layer inside the orifice hence the shape of the velocity profile. Results from the numerical simulations confirm that the Stokes number also determines the strength of vortex roll-up of a synthetic jet issued from an orifice of a finite depth due to the same reason. Finally, a parameter map, which marks the three different regimes of synthetic jets classified as no jet, jet formation without vortex roll-up and jet formation with vortex roll-up, is produced based on the numerical simulation results. It is shown that for the synthetic jet actuator used in the present study, a minimum Stokes number of about 8.5 is required to ensure the occurrence of an appreciable vortex roll-up at a dimensionless stroke length greater than 4. In addition, a very low Stokes number can also suppress the formation of synthetic jets. This study provides a more in-depth understanding of the behavior of synthetic jets in quiescent conditions, which will be useful for designing more effective synthetic jet actuators where vortex roll-up is desired.

Paper title:

Numerical Simulation of the Interaction of a Circular Synthetic Jet with a Boundary Layer

Authors:

Jue Zhou and Shan Zhong

Reformatted version of paper originally published in:

Computers and Fluids, Vol. 38, No. 2, pp. 393-405, 2009

Corrections:

1. Figure 5.1 is modified from Crook (2002).
2. The freestream velocity is fixed at 0.05m/s in the experiment in order to obtain the best quality results from the dye flow visualization experiment.
3. The domain size shown in Fig. 5.5 is chosen to make sure there is enough space for the development of vortical structures produced by the synthetic jets, while the computation cost is minimized.
4. The symmetric boundary condition is used on the surface opposite to the streamwise central plane since this boundary is located far enough from the orifice such that the flow does not change in the spanwise direction. Although this artificial boundary condition imposes a restriction on the flow close to the boundary which inevitably causes a difference between the simulation and the experiment, in the current study, this deficiency is acceptable. The adequacy of boundary conditions used in the present work has also been validated.
5. Figures 5.11 and 5.12 show the comparison of time-averaged and phase-averaged boundary layer velocity profiles. It can be found that computed profiles match the measured profiles reasonably well. The deviation of the time-averaged velocity is no more than 8%, whereas the deviation of the phase-averaged velocity at some locations close the edge of the boundary layer is higher, about 23%.
6. On page 151 line 5, phase 1corresponds to the instant when “the blow cycle begins”, not “the diaphragm is in its neutral position”.
7. “Magus force” on the second paragraph of page 151 should be “Magnus force”.
8. The Magnus effect can be explained as follows:

   The cross flow exerts a downward Magnus force on the upstream branch of the ring, and the downstream branch experiences an upward Magnus force. Thus the

Magnus force generates a rotational moment around the centre of the vortex ring resulting in its upstream branch being closer to the wall than its downstream branch.

9. The reason why the threshold of L drops in cross-flow is added:
   The reduction of threshold of L in cross-flow is because the vortex ring not only entrains the shear layer fluid from the orifice, but also entrains the cross flow fluid. However, the entrainment of the cross flow fluid does not allow all the shear layer fluid from the orifice to be entrained into the ring. Therefore, a trailing column is formed behind the vortex ring.
10. “In turns” on page 153 should be “In turn”.

Chapter 5 Numerical Simulation of the Interaction of a Circular Synthetic Jet with a Boundary Layer

Jue Zhou and Shan Zhong

School of Mechanical, Aerospace and Civil Engineering, University of Manchester, UK

Abstract

In this work, a 3D numerical simulation of circular synthetic jets issued into a laminar boundary layer developing over a flat plate was undertaken in a complementary manner alongside with an experimental study with the aim of achieving an improved understanding of the fluid mechanics underlying the interaction process between the synthetic jets and the boundary layer. The simulation was carried out in FLUENT at two diaphragm operating conditions, which produced two distinctly different vortical structures and shear stress footprints on the wall. The simulation results were validated using experimental data and a good agreement was achieved. The temporal evolution of coherent structures formed as the result of this interaction was examined using the *Q*-criterion. The hierarchy of the coherent structures was established which provided a credible explanation of the wall shear stress pattern observed in both the experiment and the simulation. The high spatial resolution in the near-wall region and 3D nature of the simulation results provide the information about the flow field which is not only consistent with but also additional to that from the experiment, leading to an improved understanding of the interaction process between the synthetic jets and the boundary layer and its resultant structures.

5.1 Introduction

A typical synthetic jet actuator consists of a small cavity with an oscillating diaphragm at its bottom side and an orifice plate at the opposite side, as shown in Fig 5.1. As the result of the alternating of suction and blowing produced by the

movement of diaphragm, a succession of vortex rings is produced and propagates away from the orifice; an oscillating jet is hence "synthesised".

The potential application of synthetic jet actuators in delaying boundary layer separation on aircraft has been the driver behind the intense research on synthetic jets in recent years. It has been demonstrated in laboratory experiments that they are capable of delaying or eliminating flow separation on circular cylinders (Crook et al, 1999; Glezer and Amitay, 2002; Tensi et al, 2002) and aerofoil models (McCormick, 2000; Amitay and Glezer, 2002; Kim and Kim, 2006). It is believed that the interaction of the coherent trains of vortices formed out of a circular synthetic jet with a local boundary layer produces streamwise-aligned vortical structures, which entrain faster moving fluid from the freestream to the near-wall region resulting in the delay of flow separation. However, there is still a lack of sufficient understanding of the interaction process which leads to the formation of these streamwise structures and their near-wall effect. This knowledge is essential to the determination of the operating conditions of synthetic jets which deliver desired flow control effects in practical settings (Zhong et al, 2007; Tang et al, 2007).

Although a certain amount of CFD studies of synthetic jets in crossflow has been reported (Mittal et al, 2001; Ravi et al, 2004; Dandois and Garnier, 2006; Rumsey et al, 2007; Remsey et al, 2006), to the best knowledge of the authors of this paper, they were focused on validating the computational algorithm and examining the time-averaged velocity fields. The numerical study reported in this paper is undertaken in a complementary manner in parallel with an ongoing experimental study at Manchester University for the purpose of achieving an improved understanding of the fluid mechanics underlying the aforementioned interaction process. In the experiment, a circular synthetic jet is issued into a laminar boundary layer developing along a flat plate. Two test cases, which produce distinctly different patterns in wall shear stress, are identified. Upon a successful validation of the CFD model using the dye flow visualization images and PIV data, the simulation results are used to provide an insight of the hierarchy of vortical structures produced by the interaction between the synthetic jets and boundary layer as well as an explanation of the resultant wall shear stress pattern.

In the present work, the interaction of synthetic jets with a laminar boundary layer is studied for which commercial CFD software are capable of producing results with credibility. In the authors' opinion, understanding the behaviour of synthetic

jets in a laminar flow is the first logical step towards understanding the complex behaviour of synthetic jets in a turbulent flow.

5.2 Experimental and Computational Methods

5.2.1 Experimental Methods

The synthetic jet actuator used in the numerical study is identical to that used in the experiment (see Fig. 5.1). The cavity of the actuator has a diameter of D_c = 45 mm and a height of H = 20 mm. The orifice diameter D_o is 5 mm and its height h is also 5 mm. The centre of the rubber diaphragm is attached to a permanent magnetic shaker via a steel rod. The diaphragm is made to oscillate in a sinusoidal manner at predetermined diaphragm oscillation displacements and frequencies.

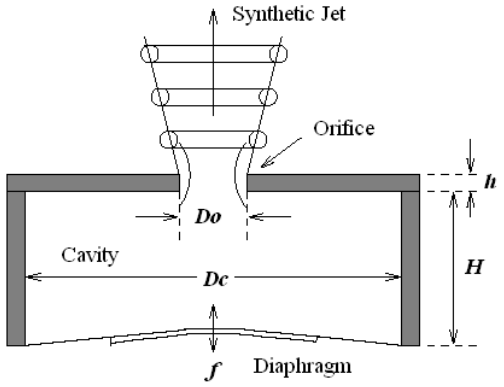

Figure 5.1. Schematic of synthetic jet actuator.

The experiment is conducted in a tilting water flume, as shown in Fig. 5.2. The flat test plate, along which a laminar boundary layer develops, is placed horizontally across the whole width of the test section with its test surface facing downwards. The synthetic jet actuator is mounted to the back of the test plate and the centre of its orifice is located at 0.7 m downstream of the leading edge of the plate.

In the dye flow visualization experiment, dye is introduced into the actuator cavity by gravity. A video camera is used to capture the dye pattern from two orthogonal views simultaneously from side and below (see Fig. 5.2a). The thermal footprints of the flow structures are also revealed using a layer of thermochromic liquid crystals which is coated on the heated test surface. The liquid crystals change

colour in response to the passage of the flow structure which causes a localized variation of convective heat transfer.

For the PIV measurement, the images of the seeded fluid flow are taken on a series of streamwise planes normal to the test surface at 60 equally-spaced phases during one diaphragm oscillation cycle using a continuous laser and a high-speed camera (see Fig. 5.2b). One hundred images pairs are used to obtain each phased-averaged velocity field. In the experiments, both the dye and PIV seeding have a density close to the density of water to ensure that they follow the motion of the fluid flow closely. In addition, the test surface is only heated to a few degrees above the water temperature such that the buoyancy effect in the boundary layer is negligible.

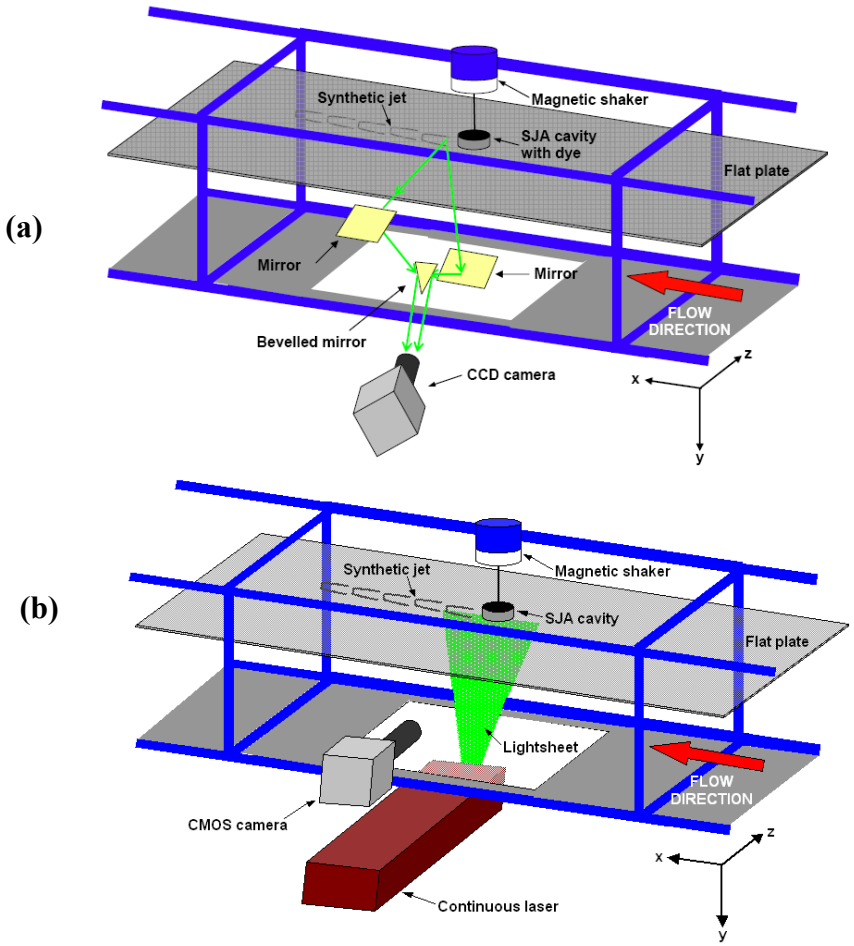

Figure 5.2. Schematic layout of experimental set up for (a) dye flow visualization and (b) PIV measurement in the water flume (Jabbal and Zhong, 2007).

In the experiment, the free stream velocity is fixed at 0.05 m/s. The boundary layer approaching the orifice of the synthetic jet is laminar as confirmed by the

velocity profile measured using PIV and the local boundary layer thickness is about four times of the orifice diameter. The characteristics of the synthetic jets are varied by changing the diaphragm oscillation displacements and frequencies.

Dimensional analyses have shown that in a given laminar boundary layer the jet-to-freestream velocity ratio, VR, dimensionless stroke length, L, Reynolds number based on the stroke length, Re_L, are the key dimensionless parameters that determine the behaviour of synthetic jets (Jabbal and Zhong, 2006). The jet-to-freestream velocity ratio is defined as

$$VR = \frac{\overline{U}_o}{U_\infty} \tag{5.1}$$

where U_∞ is the freestream velocity and $\bar{U}_o$ is the time-averaged blowing velocity over the entire cycle.

$$\overline{U}_o = \frac{1}{T}\int_0^{T/2} \tilde{u}_o(t)dt \tag{5.2}$$

where $\tilde{u}_o(t)$ is the instantaneous space-averaged velocity at the orifice exit. The definition of $\overline{U}_o$ was originally proposed by Smith and Glezer (1998) to facilitate a comparison between synthetic jets and steady jets. The dimensionless stroke length is defined as

$$L = \frac{L_o}{D_o} = \frac{\overline{U}_o}{fD_o} \tag{5.3}$$

where L_o is the stroke length, which, according to the slug model (Glezer, 1988), represents the length of the fluid column expelled during the blowing stroke. Finally, the Reynolds number is defined as

$$\mathrm{Re}_L = \frac{\overline{U}_o L_o}{\nu} \tag{5.4}$$

Among the actuator operating conditions tested in the experiments, two typical test cases are selected. In both cases, the diaphragm peak-to-peak displacement is fixed at 0.5 mm hence the dimensional stroke length is the same. The diaphragm oscillating frequency is set at f = 1 Hz in Case A and at f =2 Hz in Case B. The actuator operating conditions and non-dimensional parameters are given in Table 5.1. Details of the experimental setup and discussion of results can be found in Jabbal and Zhong (2006, 2007).

Table 5.1 Operating conditions and dimensionless flow parameters of the two synthetic jet structures

Case	f (Hz)	Δ (mm)	VR	L	Re_L
A (hairpin vortices)	1	0.5	0.27	2.7	182
B (tilted vortex rings)	2	0.5	0.54	2.7	364

Dye visualization reveals that in both cases a vortex ring forms at the orifice exit and the ring experiences an anti-clockwise tilt as a result of the torque produced by the Magnus force acting on the upstream and downstream branches of the vortex ring. However, due to the relative low velocity ratio, the upstream branch of the vortex ring in Case A is located in the near-wall region. Its circulation is eventually cancelled out by the strong residential vorticity which has the opposite sign, resulting in a highly stretched hairpin vortex as shown in Fig. 5.3a. In Case B, having a relatively higher velocity ratio and stronger roll up, the upstream branch of the vortex ring survives and the main structure appears as a tilted vortex ring (see Fig. 5.4a). In Case A the passage of the structures produces two streamwise streaks of high surface heat transfer, whereas in Case B a single streak of high surface heat transfer is observed. By Reynolds Analogy, a high heat transfer region corresponds to a region of high surface shear stress.

It is not surprising that the streamwise counter-rotating legs of a highly stretched hairpin vortex in Case A produces a region of high surface shear stress in the outboard of each leg. However, it is less obvious how a tilted vortex ring located in the outer part of a boundary layer in Case B produces a region of high surface shear stress. Since the PIV data are only available on streamwise planes, a numerical simulation is subsequently undertaken so as to provide an insight of the hierarchy of vortical structures produced by the interaction between the synthetic jets and boundary layer as well as an explanation of the resultant wall shear stress pattern.

5.2.2 Computational Methods

5.2.2.1 Numerical Solver

The commercial CFD software, FLUENT 6.2, is utilized to compute the unsteady 3D incompressible flow. Since the Reynolds numbers of the jet in the present study are

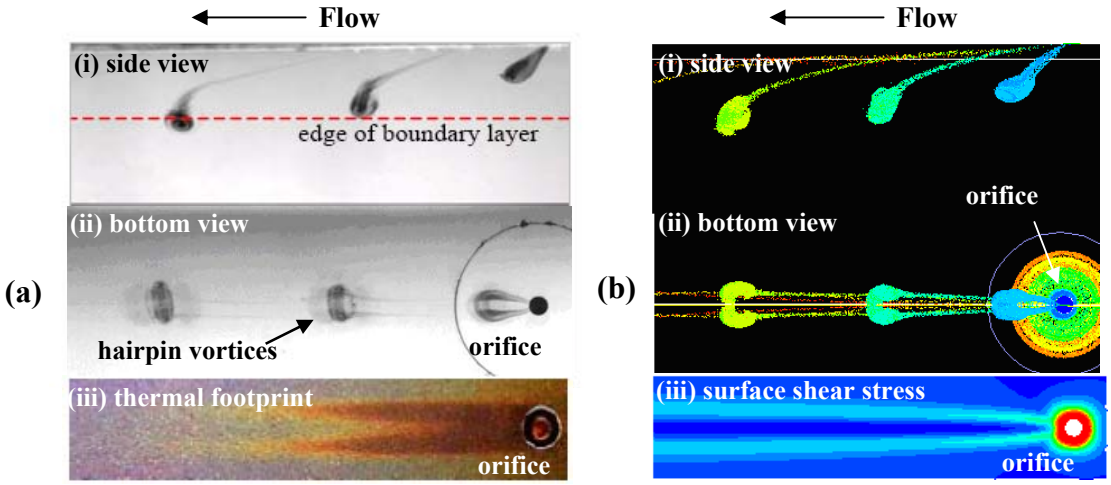

Figure 5.3. A comparison of (a) dye and liquid crystal visualization from experiments and (b) particle trace and surface shear stress from simulations of hairpin vortices (Case A).

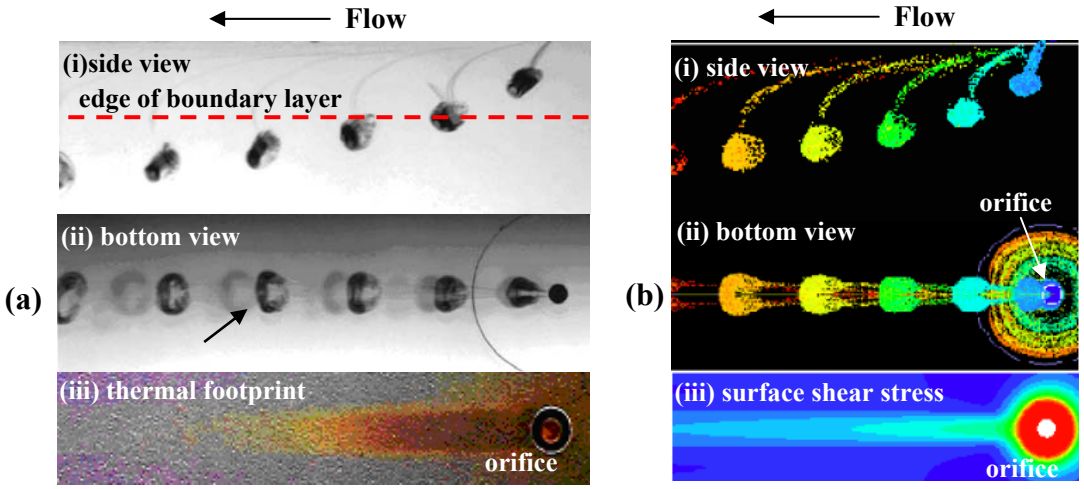

Figure 5.4. A comparison of (a) dye and liquid crystal visualization from experiments and (b) particle trace and surface shear stress from simulations of tilted vortex rings (Case B).

much lower than the critical value above which the jet becomes turbulent (Glezer, 1988), the laminar model is employed to compute the flow field. The second-order implicit scheme is selected for unsteady formulation, and the second-order upwind scheme for both space discretization and pressure discretization. Pressure-Implicit with Splitting of Operators (PISO) scheme is applied for pressure-velocity coupling, which is more efficient than SIMPLE and SIMPLEC algorithms. Discrete Particle Model (DPM) is used to simulate the particle movement of synthetic jets. The density of the particles is set as the same as the density of water to ensure that the particles follow the movement of fluid closely.

5.2.2.2 Geometry and Boundary Conditions

The computational geometry and boundary conditions used in the simulation are shown in Fig. 5.5. The inlet of the flow domain is located 75 mm ($15D_o$) upstream of the orifice of synthetic jet, and the outlet is set at 300 mm ($60D_o$) downstream of synthetic jet. The height and width of computation domain are 150 mm ($30D_o$) and 50 mm ($10D_o$) respectively. Since the flow field is expected to be symmetric relative to the central plane of the orifice, only a half of flow field is modeled in order to save the computational time. A comparison of the distributions of the time-averaged wall shear stress at $x = 50D_o$ for Case A computed with a half-plane domain and a full-plane domain confirms that the use of a half-plane domain is justifiable (see Fig. 5.6). Another comparison of the time-averaged wall shear stress using a domain width specified in Fig. 5.5 and that twice as large reveals only a difference of less than 1.3 %, indicating that the width of computation domain of $10D_o$ is reasonable (see Fig. 5.7).

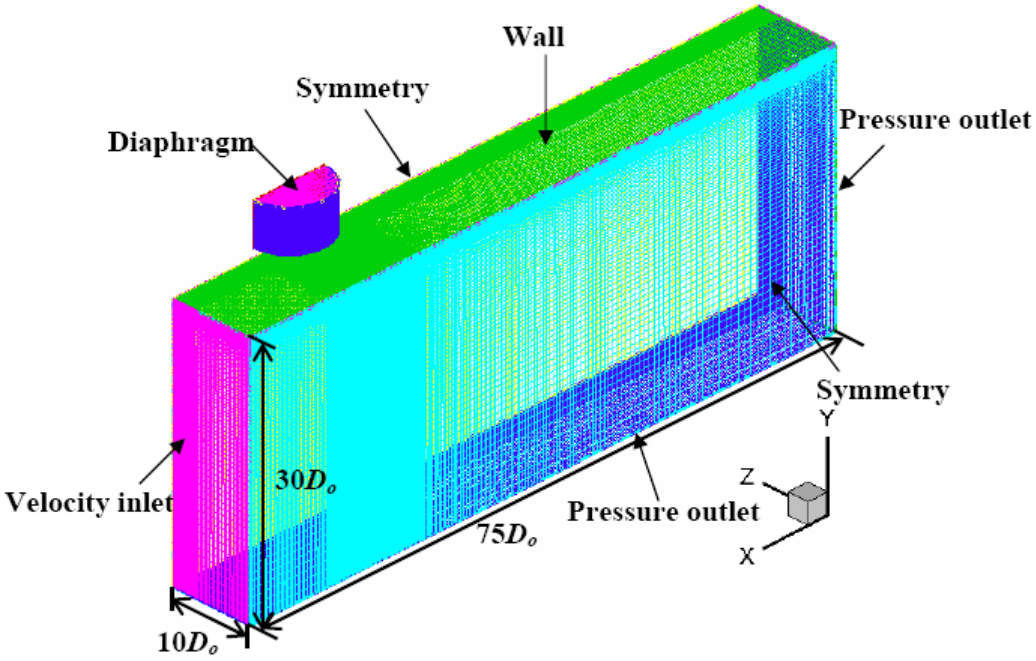

Figure 5.5. Computational geometry and mesh.

The inlet condition is specified using the Blasius velocity profile. Since the flow domain is symmetric relative to the streamwise plane that bisects the orifice exit, a symmetric boundary condition is applied on this plane. A symmetric boundary condition is also used on the surface opposite to the streamwise central

plane. The pressure outlet condition is employed at both the outlet of the flow domain and the freestream boundary opposite to the flat plate. The adequacy of boundary conditions used in the present work has been checked by comparing the computed wall shear stress distribution along the wall of the baseline case without turning on the synthetic jets with the theoretical value given by the Blasius solution, and a good agreement is achieved.

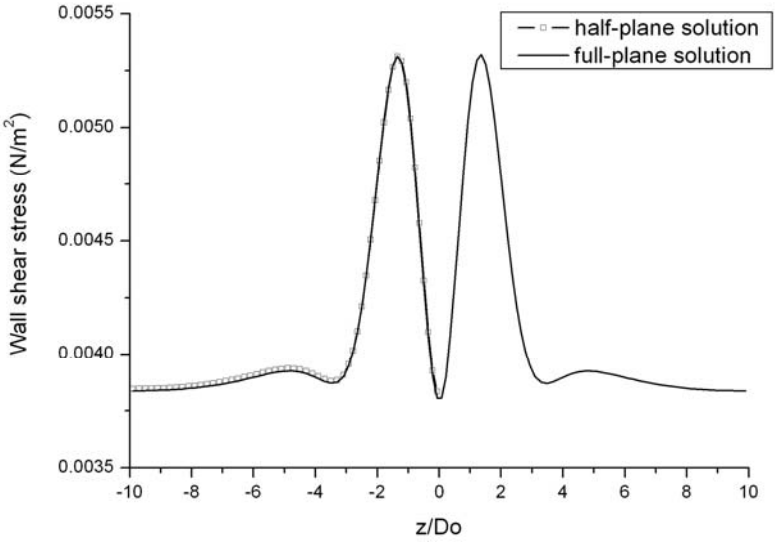

Figure 5.6. A comparison of spanwise distributions of wall shear stress at $x = 50D_o$ for Case A when a half-plane domain and full-plane domain are used in the simulation.

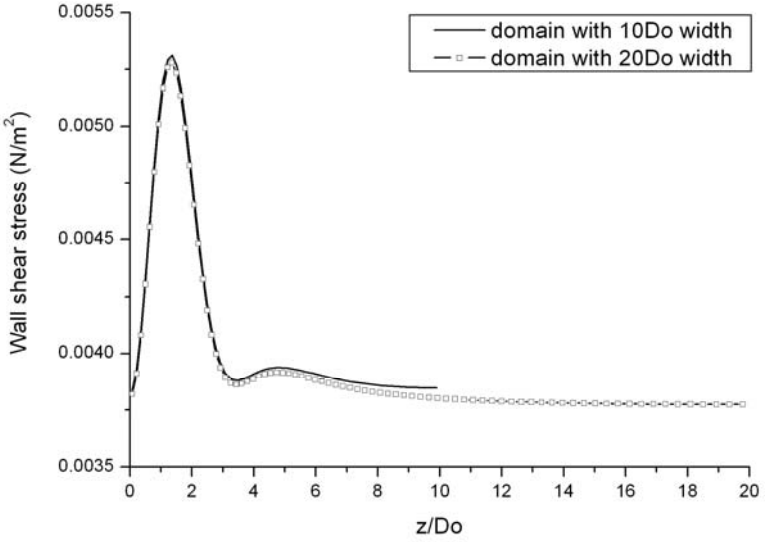

Figure 5.7. Spanwise wall shear stress for different domain width at $x = 50D_o$ for Case A.

Both the orifice duct and actuator cavity are included in the simulation and a velocity boundary condition is applied at the neutral position of the diaphragm. In the present study, the instantaneous shape of the oscillating diaphragm can be described as

$$\varepsilon(r,t) = \frac{\Delta}{2}\left(1 - \frac{r}{r_c}\right)\sin(2\pi ft) \tag{5.5}$$

where ε is the deformation of diaphragm relative to its neutral position, r is the distance from the centre of diaphragm, and Δ is the peak-to-peak displacement of the diaphragm. Differentiation of Eq. 5.5 with respect to time gives the moving velocity of diaphragm

$$\upsilon(r,t) = \pi\Delta f\left(1 - \frac{r}{r_c}\right)\cos(2\pi ft) \tag{5.6}$$

The velocity boundary condition is specified using user-defined functions (UDFs) supported by FLUENT.

5.2.2.3 Sensitivity Study of Mesh Size and Time Step

Three different mesh partitions are investigated before the final settings are selected (see Table 5.2). In order to simulate the flow field with an adequate spatial resolution, denser meshes are used in the orifice, boundary layer and the region close to the central surface for all three meshes. Figure 5.8a shows the spanwise distributions of time-averaged wall shear stress at $x = 50D_o$ using three different meshes for Case A. It is found that the results of the three different meshes are nearly identical. The difference between medium mesh and fine mesh is only 1 %. Therefore the medium mesh partition is chosen in the present study as a compromise of computational accuracy and time.

Table 5.2 Mesh refinement cases

Mesh designation	Coarse	Medium	Fine
Cavity	64×24×60	80×30×75	118×44×112
Orifice	16×24×16	20×30×20	30×44×30
Out flow domain	206×44×64	264×56×85	391×81×122
Total mesh	714,665	1,434,796	4,358,783

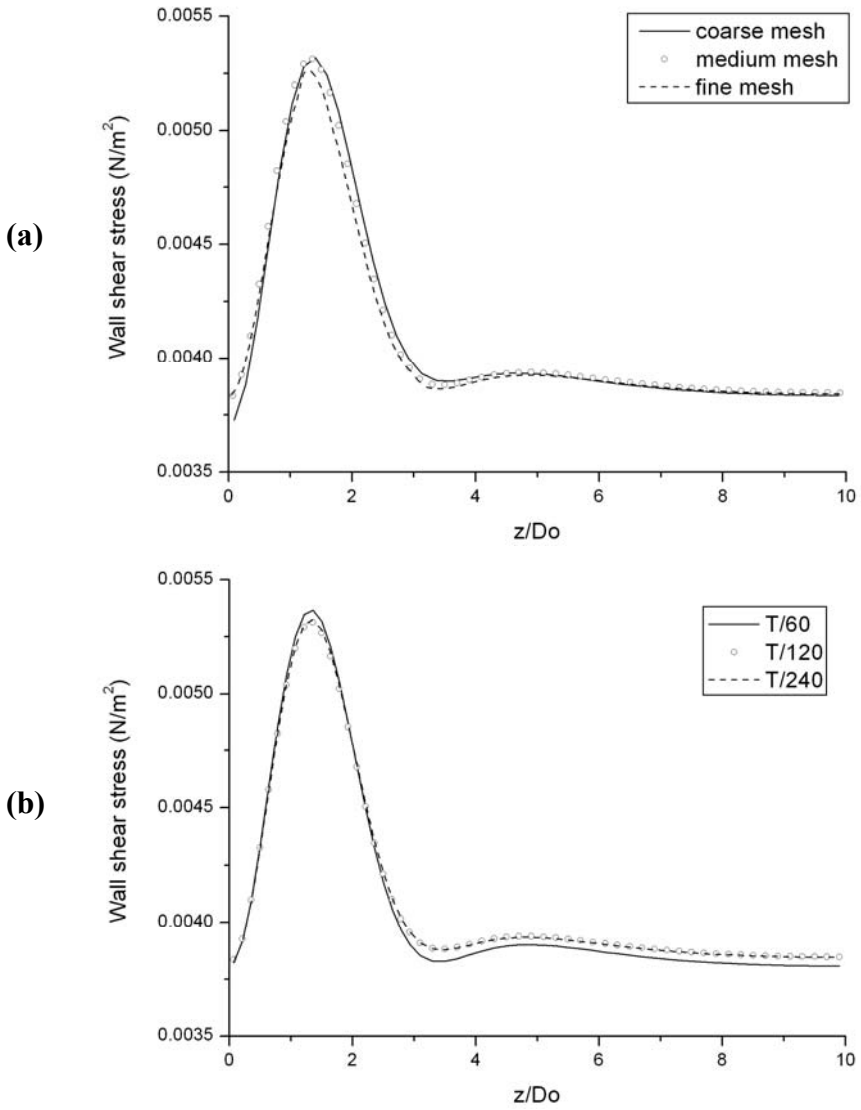

Figure 5.8. Spanwise wall shear stress distributions for (a) different mesh size (b) different time step sizes at $x = 50D_o$ for Case A.

The effect of time step size is also investigated by using 60, 120 and 240 steps per cycle for Case A. A comparison of the wall shear stress distribution using these three time step sizes confirms that the use of the medium time step size is adequate (see Fig. 5.8b).

In the simulation, the synthetic jet is turned on when the simulation of the flow field of the jet-off case has converged after several time's iteration. The flow field will eventually exhibit a stable periodicity after sufficient numbers of iteration. The number of iteration required depends on the condition of flow field. Two points on the central plane at $x = 50D_o$ are selected to monitor the progress of iteration, one is inside and the other outside the boundary layer. Figure 5.9 shows the variation of streamwise velocity at these two points with the number of iterations in Case A. It is

clearly shown that after several time's iteration, the streamwise velocity at two points varies periodically. In the paper, the repeatability is attained after 37 cycles' iteration (approximately 44,000 time's iteration) for Case A, and 39 cycles' iteration (approximately 46,000 time's iteration) for Case B. When this repeatability is attained, the simulation results at any time instant during the cycle can be treated as equivalent to the phase-averaged results from the experiment. Results at twenty equally-spaced phases in an actuation cycle are extracted to compute the time-averaged flow filed.

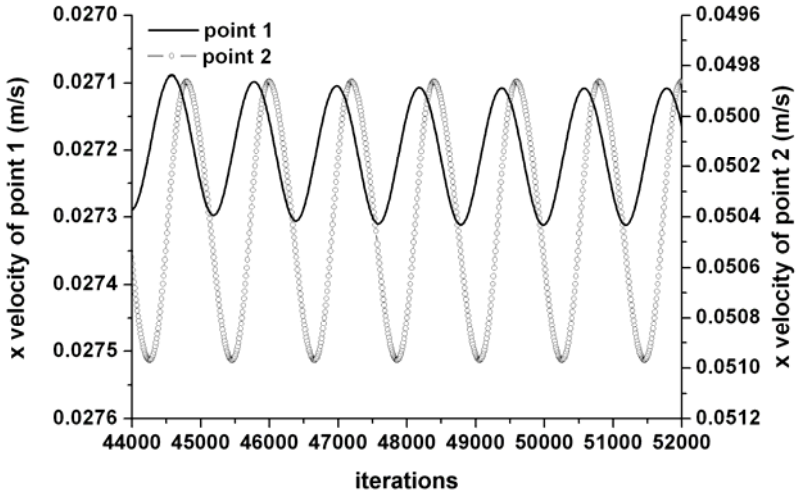

Figure 5.9. Variation of streamwise velocity at two points in Case A showing periodical repeatability of the simulation (point 1 is in the boundary layer whereas point 2 is in the freestream).

5.2.2.4 Validation of Computational Results

The capacity of FLUENT in simulating synthetic jets in a boundary layer is assessed in terms of particle movement, surface shear stress footprint, jet trajectory and boundary layer velocity profile. The trace of particle lines released at the orifice exit produced with the simulation data are equivalent to timelines and appears to be very similar to the dye visualization pattern (see Figs. 5.3 (i), (ii) and Figs. 5.4 (i), (ii)). In addition, by the Reynolds Analogy the surface shear stress distribution shows qualitatively similar patterns as revealed by temperature-sensitive liquid crystal coating (see Figs. 5.3 (iii) and 5.4 (iii)). A good agreement between the computed and measured jet trajectories on the streamwise central plane is also observed (see Fig. 5.10). Finally, the computed time-averaged and phase-averaged velocity profiles at $x = 3D_o$ on the central plane are compared with the PIV data, as shown in Figs.

5.11 and 5.12 respectively. It can be seen that the computed profiles match the measured profiles reasonably well. Therefore, FLUENT is believed to be fully capable of simulating the behavior of synthetic jets in a laminar boundary layer.

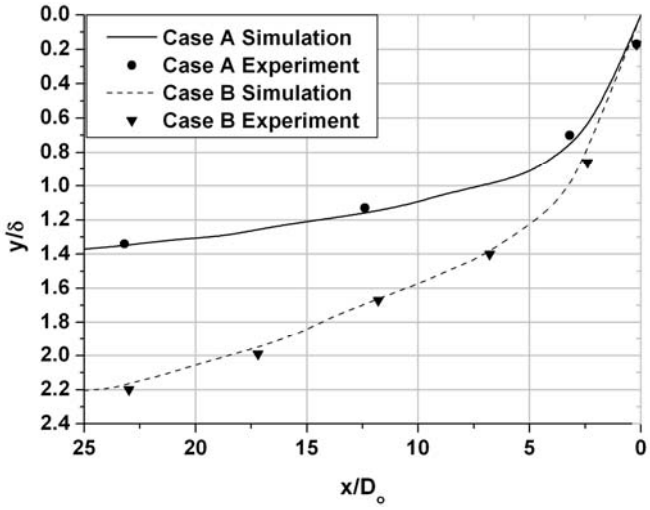

Figure 5.10. A comparison of jet trajectory from experiment and simulation.

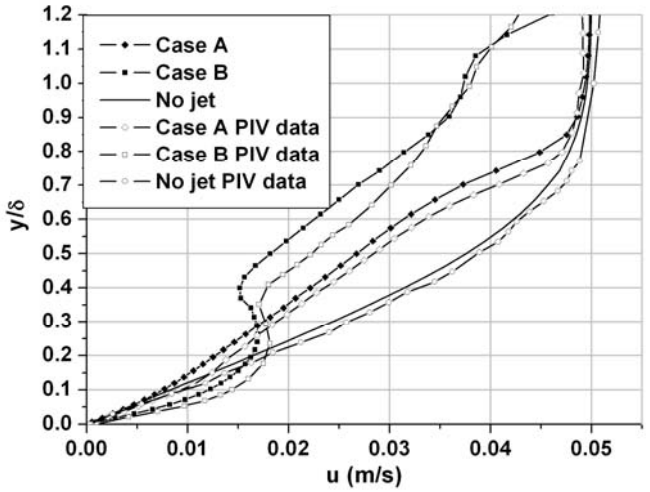

Figure 5.11. A comparison of simulated and measured time-averaged velocity profile at $x = 3D_o$. δ is the local boundary layer thickness.

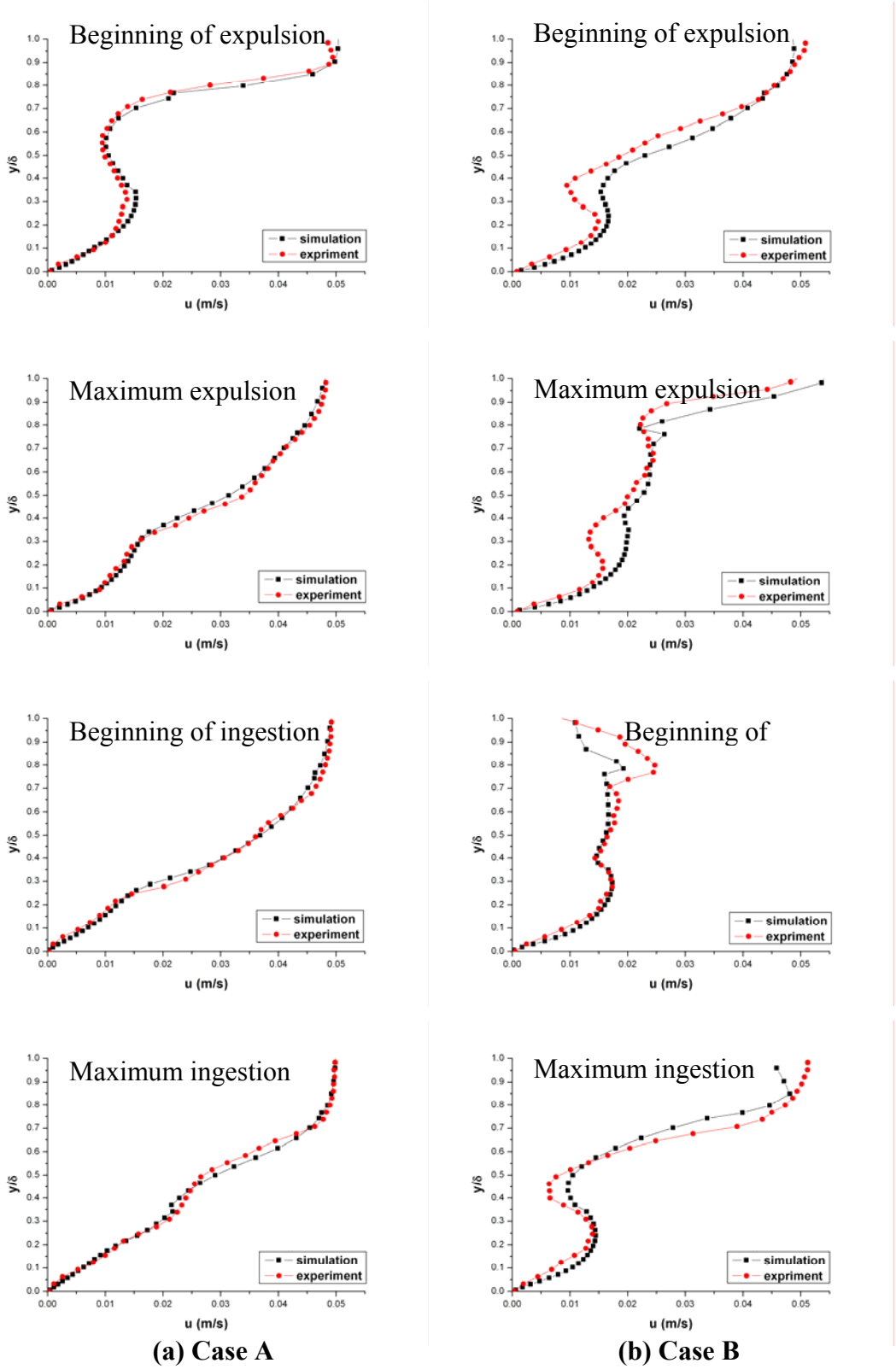

(a) Case A **(b) Case B**

Figure 5.12. A comparison of simulated and measured phase-averaged velocity profiles at $x = 3D_o$. δ is the local boundary layer thickness.

5.3 Results and Discussion

5.3.1 The *Q* criterion

The numerical simulation produces temporal variations of the 3D velocity field from which the information about the coherent structures produced by the interaction between synthetic jets and the boundary layer can be extracted. These coherent vortices are associated with high level of vorticity. However, they tend to be hidden in the vorticity field of the wall-bounded shear layer. In order to let these coherent vortices stand out, in this paper the *Q*-criterion (Hunt et al, 1988) is used to define an eddy structure.

The *Q*-criterion has been commonly used to identify coherent structures during the post-processing of numerical and experimental data. *Q*, the positive second invariant of velocity gradient tensor ∇u , is defined as

$$Q = 0.5(\|\Omega\|^2 - \|S\|^2) \tag{5.7}$$

where $\|S\| = \left[Tr(SS^t)\right]^{1/2}$, $\|\Omega\| = \left[Tr(\Omega\Omega^t)\right]^{1/2}$, $\|\cdot\|$ is the matrix norm, and $\boldsymbol{S}$ and $\boldsymbol{\Omega}$ are the symmetric and asymmetric component of ∇u . Thus Q represents the local balance between the rotation rate $\|\Omega\|^2$ and the strain rate $\|S\|^2$. It implies that positive Q iso-surfaces isolate areas where the strength of rotation overcomes the strain, thus a coherent vortex can be defined as a region where $Q > 0$. Dubief and Delcayre (2000) utilized *Q*-criterion to investigate a large panel of coherent vortices generated by DNS and LES, and they presented a comparison of four vortex-eduction methods of isotropic turbulence, mixing layer, channel flow and backward-facing step flow. It is found that the Q criterion is superior over ω (high vorticity) and low pressure criteria in free and wall-bounded turbulent flow, and agrees with the λ_2 criterion well due to the mathematical relation between them.

The Q criterion requires a user-defined threshold to visualize the coherent structures. In the present study, after a comparison of the iso-surfaces produced with a range of threshold values, $Q = 0.1$ is selected which allows the energetic vortical structures to be captured.

5.3.2 Evolution of Vortical Structures

In order to understand the formation of vortical structures as the result of the interaction between synthetic jets and the boundary layer in detail, their temporal evolution in the near field of the orifice is examined. Figures 5.13 and 5.14 show the time sequences of the $Q = 0.1$ iso-surface in Case A and B which are equally spaced in an actuation cycle. Here, phase 1 corresponds to the instant when the diaphragm is in its neutral position. The test surface is shown facing upwards to allow the vortical structure to be observed.

In the case of hairpin vortices (Case A, Fig. 5.13), it is seen that a new vortex ring begins to emerge from the orifice at Phase 3. As it fully emerges from the orifice at phase 5, there seems to be a pair of secondary structures trailing behind it which become more obvious at Phase 6. These structures are believed to be formed as the result of the extra vorticity which can not be entrained into the primary vortex ring. The threshold value of dimensionless stroke length when the primary vortex ring becomes saturated is found to be about 4 for synthetic jets issued into a quiescent flow (Gharib et al, 1998; Rosefeld et al, 1998). Although the dimensionless stroke length of 2.7 in the present experiment is much smaller than this value, it is believed, this threshold value is likely to drop in the presence of a cross flow. Sau and Mahesh (2007) also observed this kind of secondary structures in their DNS simulations at $L = 3$. At Phase 6, the ring experiences a tilt due to the Magus effect resulting in its upstream branch being closer to the wall than its downstream branch. At Phase 7, it is evident that the upstream branch of the vortex ring is weakened by the residential vorticity in the boundary layer which has the opposite sign. The upstream branch disappears at Phase 8 as the result the trailing structure appears as the legs of the main ring and the vortex ring-like structure that was observed initially at Phase 3 is eventually transformed into a hairpin vortex. This hairpin structure is seen to become more stretched as it propagates downstream at later phases. It is also noticed that a pair of weaker secondary streamwise vortical structures are induced by the legs of the hairpin structure which was produced by the previous diaphragm oscillation cycle (see Phase 7). These secondary structures grow in size under the combined influence of the previous and the newly formed hairpin vortex as they propagate downstream. Furthermore, a structure in the shape of a growing crescent is formed just upstream of the orifice as the new vortex ring emerges. This structure is believed to be induced by the emerging vortical structure which acts as an obstacle to the incoming flow and is known as horseshoe vortex

(Simpson, 2001; Fric and Roshko, 1994; Kelso et al, 1996). It is shed shortly before the next vortex ring is formed and it diminishes before it reaches a distance of two diameters downstream of the orifice.

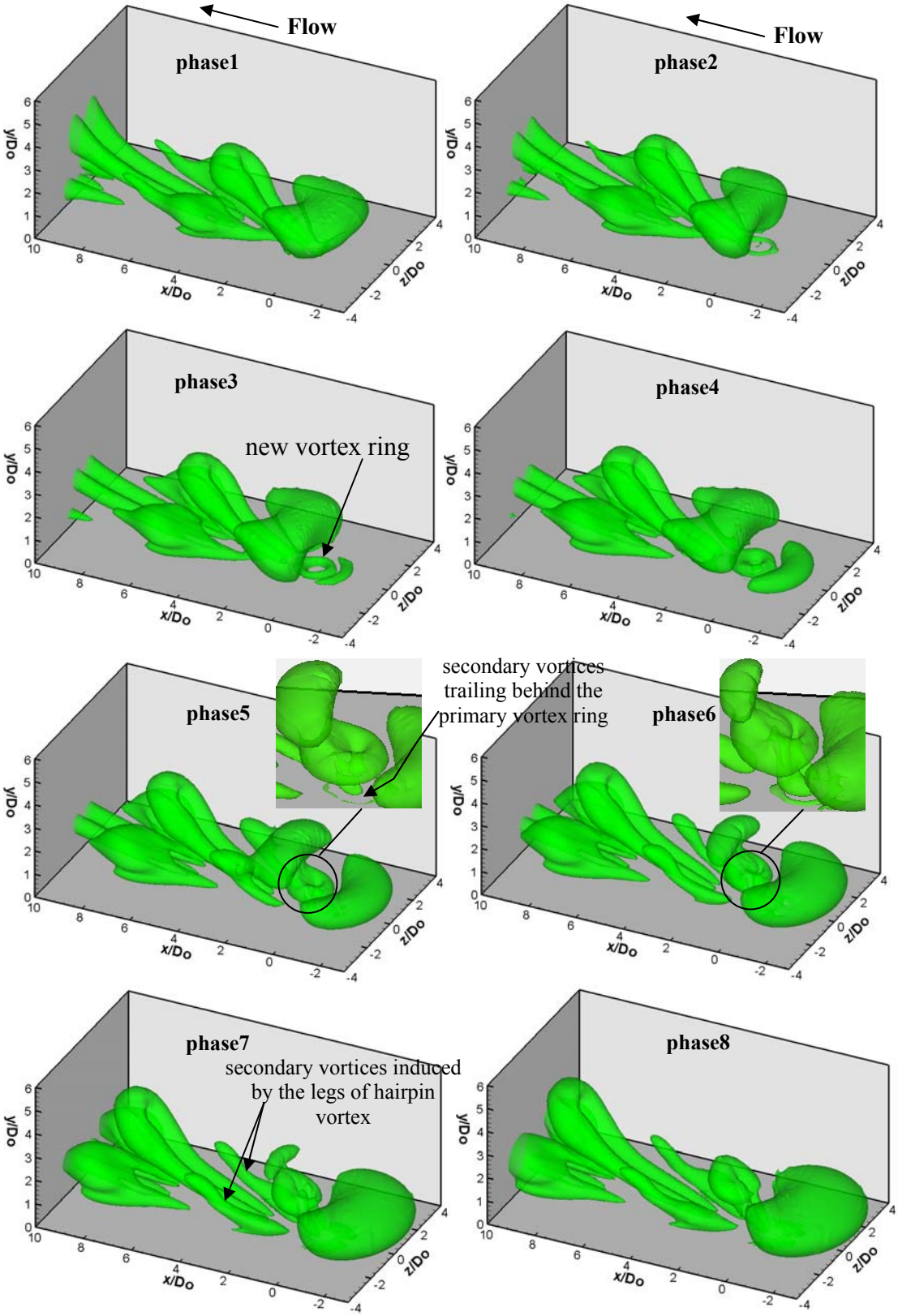

For caption see overleaf

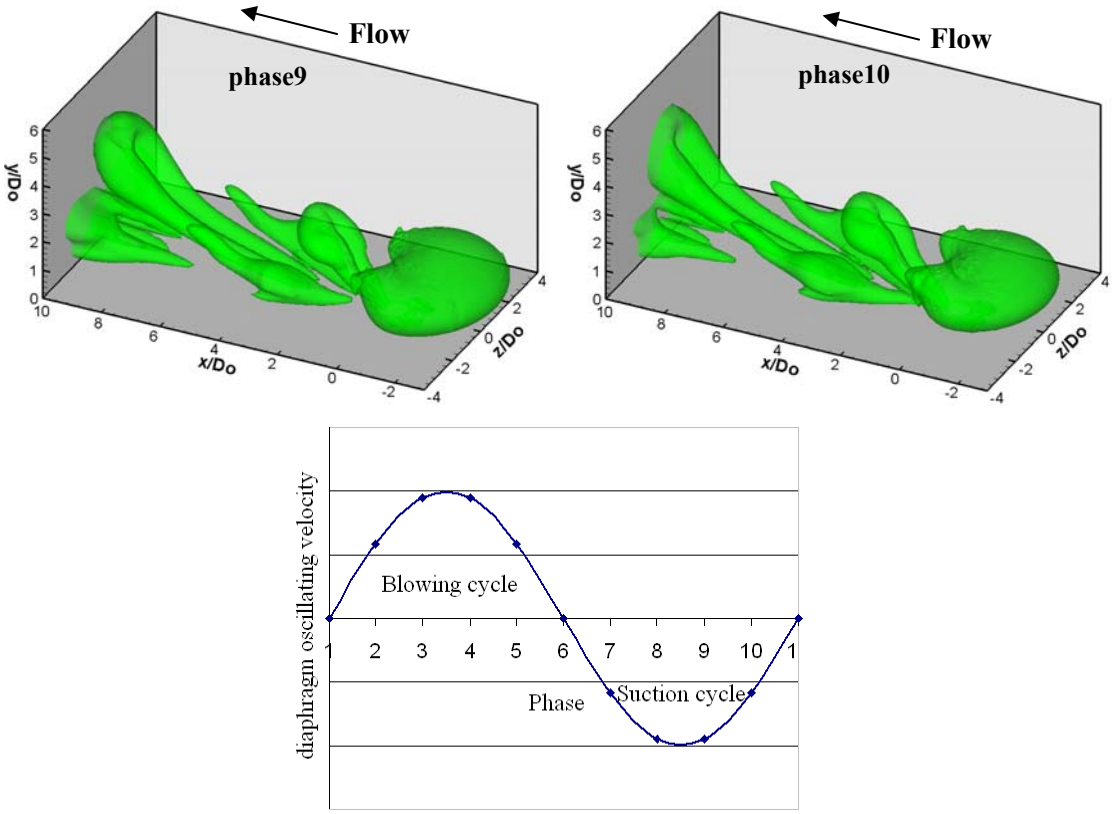

Figure 5.13. Time sequence of iso-surface of Q = 0.1 showing the formation of hairpin vortices (Case A).

Figure 5.14 shows the time sequences of the Q = 0.1 iso-surface of the tilted vortex rings (Case B) in an actuation cycle. Clearly, the tilted vortex rings exhibit a very different behaviour from that of hairpin vortices (Case A). Two main differences are observed during the formation and evolution of these structures. Firstly, due to its higher strength as the result of a higher Re_L, the upstream branch of the tilted vortex ring is capable of surviving from the attack of the residential vorticity in the boundary layer such that the vortex ring retains its ring shape. Secondly, as a result of the main vortex ring retaining its ring shape, the secondary vortices trailing behind the vortex ring remains their separate identity. These secondary vortices are highly stretched by the shear in the boundary layer. They in turns induce a pair of tertiary structures outboard and beneath their legs (see Phase 8). The newly formed tilted vortex ring accompanied by a trailing column appears similar to the vortical structure produced by a pulsed jet as observed by Sau and Mahesh (2007).

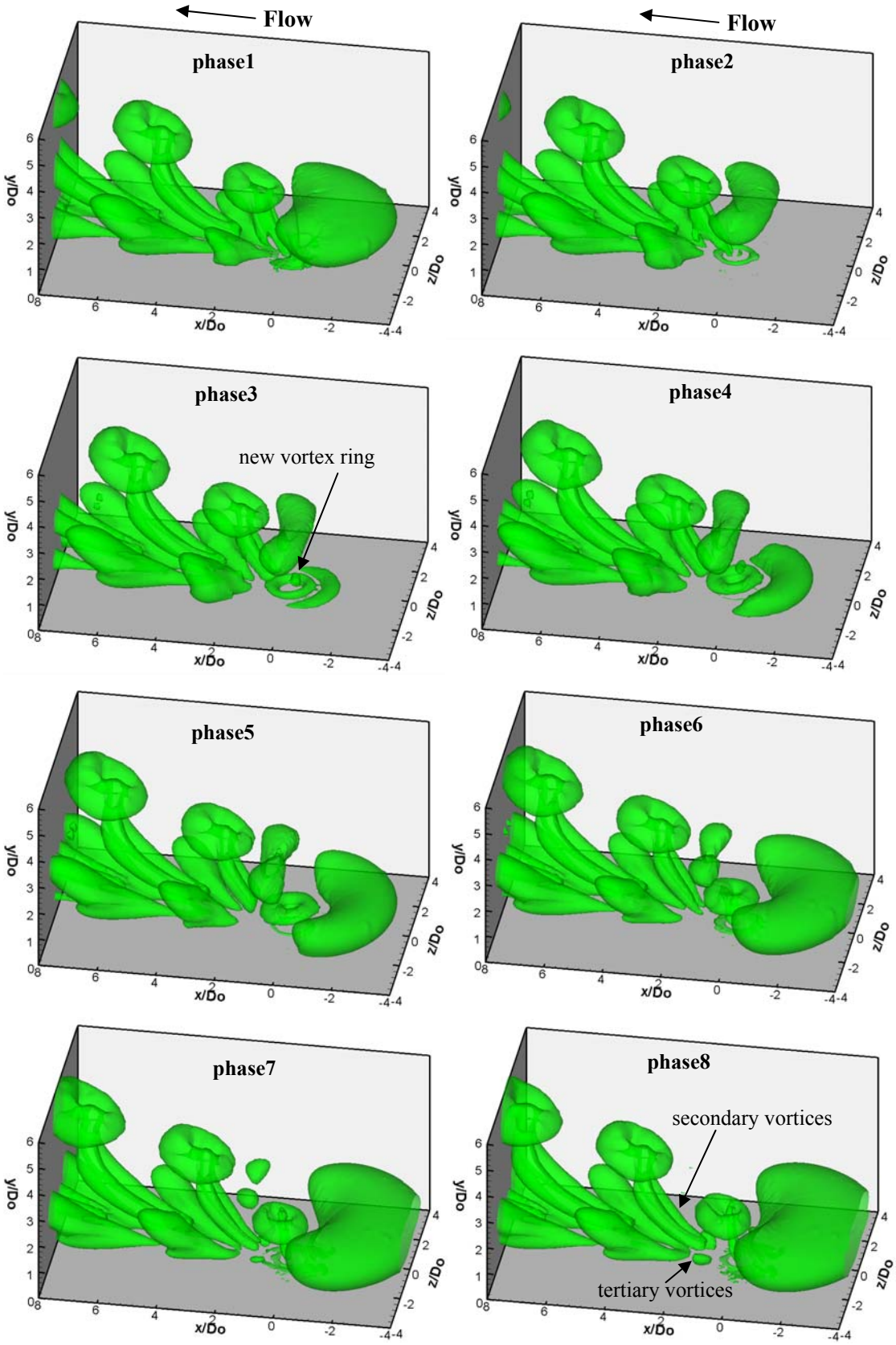

For caption see overleaf

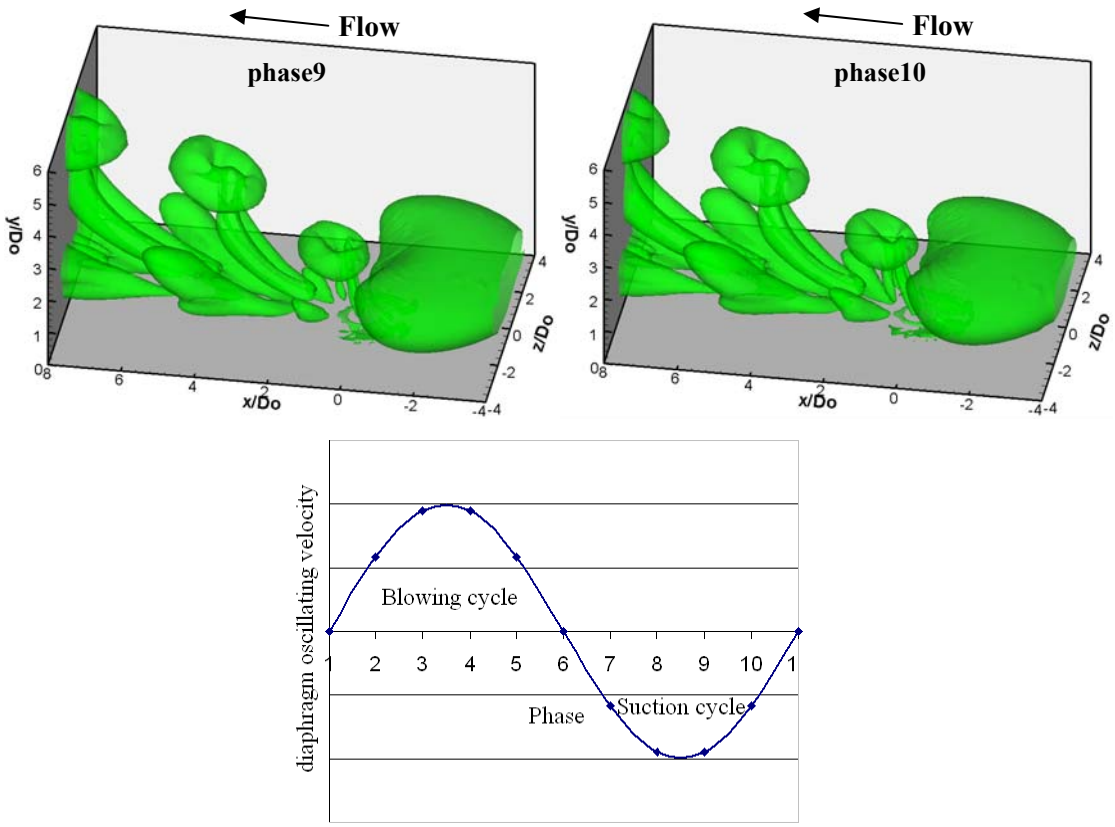

Figure 5.14. Time sequence of iso-surface of Q = 0.1 showing the formation of tilted vortex ring (Case B).

5.3.3 Instantaneous Coherent Structures

In Fig. 5.15, the instantaneous iso-surface of Q = 0.1 is presented at the time instant when the blowing cycle begins. For Case A, the dominant structures within a distance of $30D_o$ downstream of the orifice are highly stretched hairpin vortices along with their associated secondary structures (see Fig. 5.15a). The velocity vectors superimposed on the contours of streamwise velocity difference between the instantaneous and undisturbed local value at a spanwise plane ($x = 4D_o$) is provided in the insert. The velocity vectors indicate the sense of vortex circulation whereas the contour of velocity difference indicates the extent of fluid mixing due to the presence of the vortical structures. In the graph, the red region corresponds to the area with an increased velocity whereas blue to a decreased velocity. It can be seen that the upwash caused by the counter-rotating legs of hairpin vortices results in a reduced streamwise velocity around the central plane between the two legs. On the other hand, the downwash motion brings fast moving fluid in the outer part of the boundary layer to the near-wall region producing an increased local velocity. Outboard to each of the counter-rotating legs, a secondary streamwise vortex with an

opposite sense of rotation is also observed which enhances the mixing locally. The pattern of two high surface shear stress regions as shown in Fig. 5.15a reflects the combined effect produced by the counter-rotating legs of the hairpin vortices and the secondary structure induced by them. Similar hairpin vortices are observed by Acarlar and Smith (1987b) in their study of hairpin vortices formation in a laminar boundary layer. It is believed that the longitudinal vortices are generated due to the distortion and intensification of vorticity by the inrush of fluid outboard of the counter-rotating legs.

For Case B, the dominant structures in the boundary layer appear to be the tilted vortex rings and their secondary and tertiary structures. The inclined secondary vortex pair has the same sense of rotation as that of the sides of the primary vortex ring and it extends from the ring to the near-wall region (see Fig. 5.15b). The tertiary structures have an opposite sense of rotation and are located in the vicinity of the wall beneath the secondary structures. It can be seen that both the primary and secondary vortices produce a strong upwash in the central plane and a downwash in their outboard. However, as both the primary and secondary structures are located at least $1D_o$ away from the wall, their direct impact in the near flow is expected to be limited. This is supported by the fact that the single streak of high shear stress around the central plane can only be produced by the tertiary structures which are much closer to the wall and generate a common flow down.

Although the presence of the secondary structures trailing behind the tilted vortex ring is visible in the dye visualisation images shown in Fig. 5.4a(i) and appears to be correlated with the region of a velocity deficit between 0.3 and 1δ in the time-averaged velocity profile shown in Fig. 5.11, due to the limitation of the experimental techniques in probing the flow in the near-wall region and the lack of experimental data on the spanwise plane, the presence of the tertiary structure is not revealed. Here the high spatial resolution in the near-wall region and 3D nature of the simulation results overcome some of the limitations of the experimental data, leading to an improved understanding of the resultant structures of the interaction process and a credible explanation of the wall shear stress pattern observed in both the experiment and the simulation.

5.3.4 Wall Shear Stress Distribution

The variation in wall shear stress is considered to be a useful indictor of the effectiveness of a flow control device for potential flow separation delay. The spanwise distribution of wall shear stress at $x = 5D_o$ and $x = 50D_o$ are shown in Fig. 5.16. It is found that due to their steeper trajectory in the boundary layer the peak of wall shear stress produced by tilted vortex rings in Case B is reduced by 30 % at $x = 50D_o$ compared to a 12.5 % decrease for hairpin vortices in Case A. This indicates that the tilted vortex rings may be a less suitable candidate for delaying flow separation if the near-wall persistency of the structures is more beneficial than its absolute strength. Nevertheless, further studies of the interaction of synthetic jets with a separating boundary layer should be undertaken to verify the above statement.

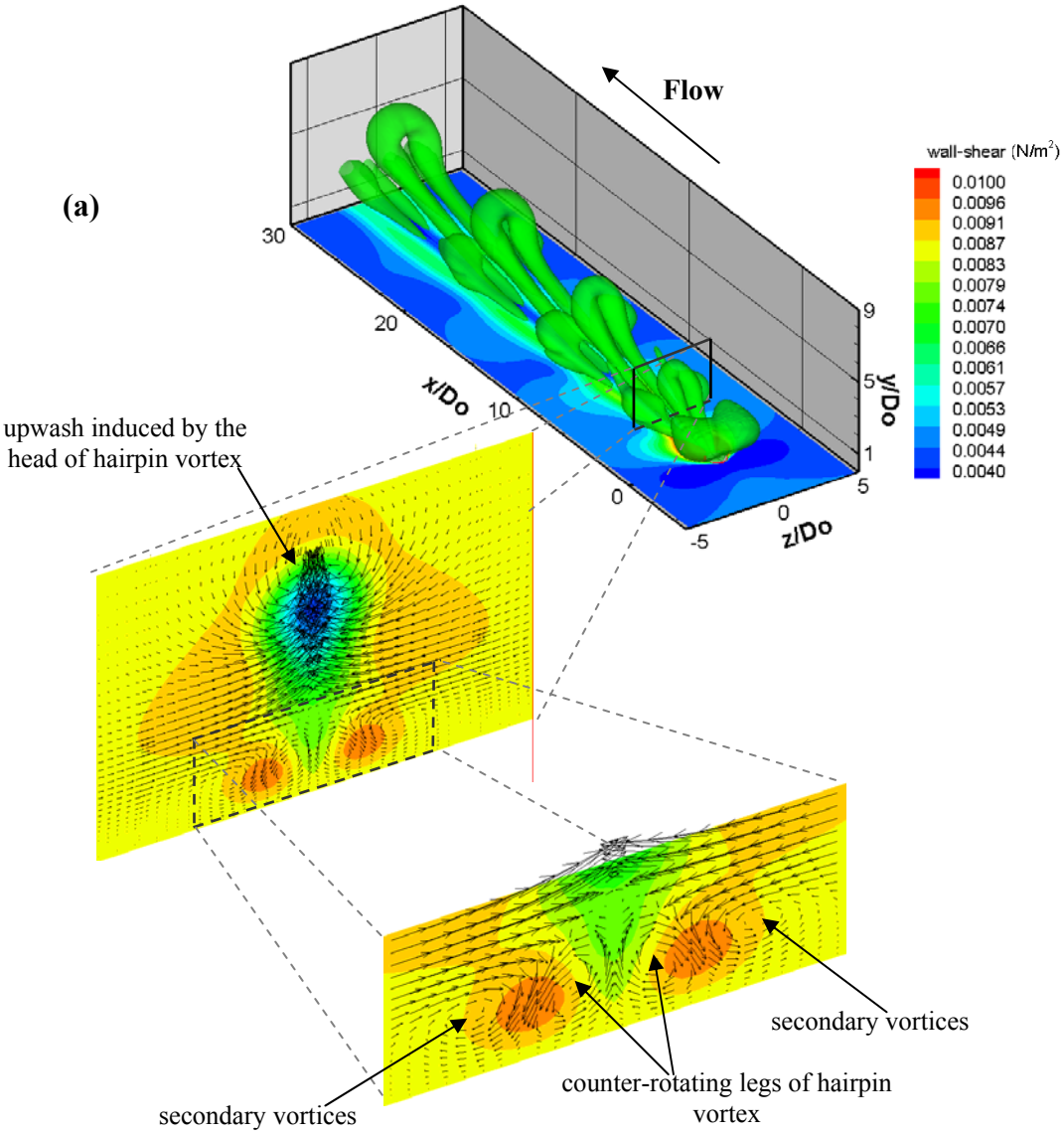

For caption see overleaf

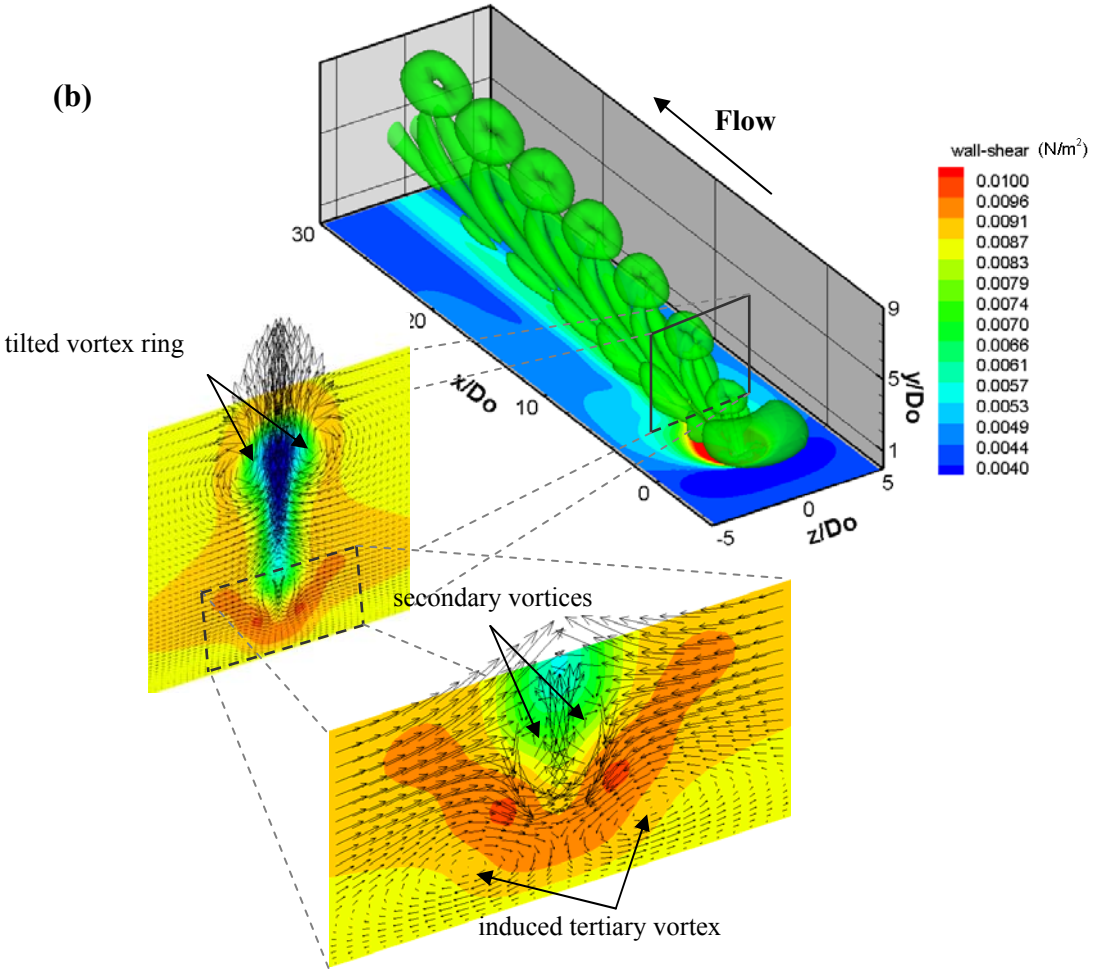

Figure 5.15. Instantaneous iso-surface of $Q = 0.1$ of (a) hairpin vortices (Case A) and (b) tilted vortex rings (Case B).

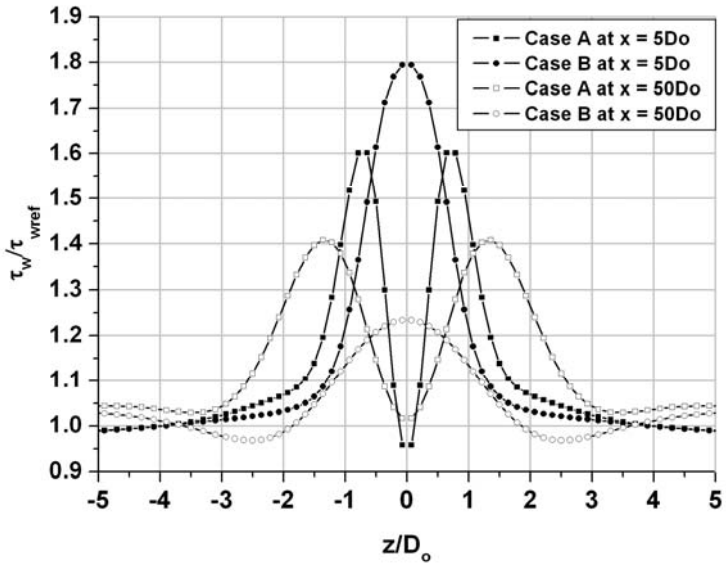

Figure 5.16. Spanwise distribution of wall shear stress at $x = 5D_o$ and $50D_o$.

5.4 Conclusions

In this work, a 3D numerical simulation of circular synthetic jets issued into a laminar boundary layer developing over a flat plate was undertaken in a complementary manner alongside with an experimental study with the aim of achieving an improved understanding of the interaction process between the synthetic jets and the boundary layer and the resultant vortical structures. The simulation was carried out in FLUENT at two diaphragm operating conditions, which produced two distinctly different vortical structures, i.e. the hairpin vortices (Case A) and tilted vortex rings (Case B). In Case A the passage of the structures produces two streamwise streaks of high surface heat transfer, whereas in Case B a single streak of high surface heat transfer is observed. The simulation results were validated using experimental data and a good agreement was achieved.

The temporal evolution and the hierarchy of coherent structures formed as the result of the interaction between synthetic jet and the boundary layer were examined using the Q-criterion. It is found that in Case A the vortex ring-like structure that was observed in the initial formation process is eventually transformed into a stretched hairpin vortex under the influence of shear in the near-wall boundary layer. The counter-rotating legs of the hairpin vortices and their secondary structures are responsible for producing the two streamwise streaks of high surface heat transfer observed in both the simulation and the experiment. In Case B, the dominant structures produced by the interaction consist of the tilted vortex rings, their secondary and tertiary structures. The single streak of high shear stress around the central plane is believed to be produced by the tertiary structures which are located much closer to the wall.

The high spatial resolution in the near-wall region and 3D nature of the simulation results provide the information about the flow field which is not only consistent with but also additional to that from the experiment, leading to an improved understanding of the interaction process between the synthetic jets and the boundary layer and its resultant structures.

Paper title:

Coherent Structures Produced by the Interaction between Synthetic Jets and a Laminar Boundary Layer and Their Surface Shear Stress Patterns

Authors:

Jue Zhou and Shan Zhong

Reformatted version of paper originally published in:

Computers and Fluids, Vol. 39, No. 8, pp. 1296-1313, 2010

Corrections:

1. Figure 6.2 is from Zhou and Zhong (2009).
2. The flow evolution for the case at $VR = 0.64$, $L = 4.1$ can be summarized as follows:

   The vortical structures generated at $VR = 0.64$, $L = 4.1$ appear as tilted vortex rings trailed by a pair of counter-rotating legs when they emerge from the orifice exit. As they develop downstream, the secondary hairpin vortices form from the counter-rotating legs and travel with the dominant tilted vortex rings until they gradually lose their coherence further downstream.
3. Some further explanation of Figs. 6.17, 6.18 and 6.19 is provided.

   In these three figures, the hairpin vortices are marked by the black symbol, while the tilted vortex rings are marked by the red symbol. A transitional boundary marked by the red dash line goes through all the transitional cases, and separates the two types of vortical structures and their corresponding shear stress patterns. Based on Figs. 6.17 and 6.18, it can be found that the location of transitional boundary correlates with $0.3 < VR < 0.4$ closely for $Str < 1$. For $Str > 1$, the boundary approaches a horizontal line of $L = 1.6$. In addition, Fig. 6.19 indicates that the hairpin vortices can occur at a high Reynolds number up to 1040. Hence, in the current study, the Reynolds number is a less important parameter in determining the vortical structure type and the surface shear stress pattern.

Chapter 6 Coherent Structures Produced by the Interaction between Synthetic Jets and a Laminar Boundary Layer and Their Surface Shear Stress Patterns

Jue Zhou and Shan Zhong

School of Mechanical, Aerospace and Civil Engineering, University of Manchester, UK

Abstract

In this paper, the results from 3D numerical simulations of circular synthetic jets issued into a zero-pressure-gradient laminar boundary layer developing along a flat plate are reported. The simulations are undertaken using FLUENT at a wide range of actuator operating conditions. The formation and development of the coherent structures produced as a result of the interaction between the synthetic jets and the boundary layer were examined using the Q-criterion. Non-dimensional parameter space maps were established to illustrate the variations in the appearance of these resultant structures and their shear stress footprints upon the changes in the operating conditions of synthetic jets. Finally, the parameter boundary separating the two distinct types of vortical structures and surface shear stress patterns is identified. It is found that the location of this boundary correlates closely with the jet-to-freestream velocity ratio of $VR = 0.4$ when the Strouhal number (Str) is less than 1, whereas for $Str > 1$ the boundary deviates from this trend, approaching the line of dimensionless stroke length of $L = 1.6$. In order to investigate the potential impact of the synthetic jets on the boundary layer, the increase in the space- and time-averaged skin friction coefficient relative to the baseline case without the synthetic jets is calculated. It appears that in order to maximise the impact on the near-wall flow while keeping the energy expenditure down, it is wise to maximise the accumulated effect of hairpin vortices by keeping the spacing between consecutive hairpin vortices similar to the local boundary layer thickness upstream of the separated flow instead of producing stronger individual structures.

6.1 Introduction

There has been an intense research on synthetic jets since 1990s due to their promising potential in delaying flow separation (Smith and Glezer, 1998; Glezer and Amitay, 2002; Seifert et al, 2004; Zhong et al, 2007; Tang et al, 2007). They are particularly attractive for aircraft applications due to their ability to inject momentum to an external flow without net mass flux and the relative ease in being integrated in MEMS through micro-fabrication (Gad-el-Hak, 2006; Warsop, 2004; Kral, 2000).

Synthetic jets issued from circular orifices are known to produce vortex rings (Glezer and Amitay, 2002) and therefore can be regarded as a special type of vortex generating jets. Experimental evidence shows that the interaction of the train of vortices produced by a synthetic jet with a boundary layer results in the formation of pairs of counter-rotating streamwise vortical structures (Crook, 2002), similar to those produced by vane vortex generators (Lin, 1999). These streamwise vortical structures are capable of delaying flow separation by entraining faster moving fluid from the freestream to the near-wall region.

Crook et al. (2001) undertook dye visualisation of circular synthetic jets issued into a uniform crossflow. They hypothesized that these streamwise vortical structures were produced by overlapping stretched vortex rings. The dye visualisation of synthetic jets issued into a laminar boundary layer conducted by Zhong et al. (2005) showed, for the first time that, depending on the magnitudes of the dimensionless stroke length and the jet-to-freestream velocity ratios, the vortical structures produced by synthetic jets may take different shapes. As the dimensionless stroke length and the jet-to-freestream velocity ratio increase, the primary vortical structures first appear as hairpin vortices that are attached to the wall, then as stretched vortex rings that gradually move towards the edge of the boundary layer, and finally as tilted or distorted vortex rings that penetrate the edge of the boundary layer shortly downstream. Using temperature-sensitive liquid crystal surface coating, Jabbal and Zhong (2008) found that the hairpins and stretched vortex rings produce two longitudinal streaks of high surface shear stress downstream of the each side of the orifice whereas the tilted or distorted vortex rings produce a single longitudinal streak directly downstream of the orifice. Zhou and Zhong (2009) examined the formation of typical hairpin type structures and typical tilted vortex ring type structures using their simulated results obtained with FLUENT. They not only

reproduced the primary structures observed in the experiment in their numerical simulations but also revealed a hierarchy of coherent vortices consisting of primary, secondary and tertiary structures hence providing a further insight of the formation of the two different patterns of surface shear stress observed in the experiment by Jabbal and Zhong (2008).

The work reported in this paper is an extension of the work by Zhou and Zhong (2009) aimed at undertaking a systematic investigation of how the nature of the vortical structures produced by the synthetic jets and their associated surface shear stress patterns vary as the jet operating condition changes over a large parameter space using numerical simulations. To the best knowledge of the authors, although a considerable amount of numerical simulations of synthetic jets has been undertaken, attempts have not been made along this line.

In the present work, the interaction of synthetic jets with a zero-pressure-gradient laminar boundary layer is studied for which the commercial CFD software is capable of producing results with credibility. It is believed that some commonalities exist in the interaction mechanisms between synthetic jets and a boundary layer irrespective if it is laminar or turbulent. First, the basic effect of shear in a boundary layer and the effect of suction cycle on the formation of coherent structures produced by synthetic jets in the boundary layer are similar regardless of whether the boundary layer is laminar or turbulent. Second, the entrainment brought about by the coherent vortices produced by the synthetic jets is an important flow separation mechanism in both flows. In the authors' opinion, understanding the behaviour of synthetic jets in a laminar flow is the first logical step towards understanding the complex behaviour of synthetic jets in a turbulent flow. Furthermore, although the present study is undertaken in a zero-pressure-gradient boundary layer, the potential flow control effectiveness of synthetic jets can be evaluated by some measureable changes to the flow, such as a gain of averaged surface shear stress. Therefore, the knowledge gained from this study should be useful to understanding the effect of synthetic jets on a separated flow to which flow separation control can be applied.

6.2 Dimensionless Parameters of Synthetic Jets in a Boundary Layer

Based on the dimensional analysis, Jabbal and Zhong (2008) suggested the impact of synthetic jets issued into a boundary layer depends on five dimensionless parameters as shown in Eq. 6.1. These parameters are the dimensionless stroke length (L), Reynolds number based on the stroke length (Re_L), the jet-to-freestream velocity ratio (VR), the ratio of orifice diameter to boundary layer thickness (d), and the surface friction coefficient (c_f), i.e.

$$\text{Jet impact on boundary layer} = Fn(L, \mathrm{Re}_L, VR, d, c_f) \tag{6.1}$$

This functional relationship is also supported by the numerical finding by Raju et al. (2005). For a given laminar boundary layer and an actuator with fixed geometry such as the case in the present study, d and c_f do not change. Hence the number of independent dimensionless parameters specified in Eq. 6.1 can be reduced to three; only the dimensionless stroke length, Reynolds number and the jet-to-freestream velocity ratio need to be considered.

The dimensionless stroke length is defined as

$$L = \frac{L_o}{D_o} = \frac{\overline{U}_o T}{D_o} \tag{6.2}$$

where L_o is the stroke length, which, according to the slug model (Glezer, 1988), represents the length of the fluid column expelled during the blowing stroke, $\overline{U}_o$ is the time-averaged blowing velocity over the entire cycle

$$\overline{U}_o = \frac{1}{T}\int_0^{T/2} \tilde{u}_o(t)dt \tag{6.3}$$

where $\tilde{u}_o(t)$ is the instantaneous space-averaged velocity at the orifice exit. The effect of L on the synthetic jet formation was discussed by Jabbal and Zhong (2008). In brief, for circular synthetic jets issued into a quiescent fluid, a minimum L of 0.5 is required to overcome the impact of the suction cycle and ensure the formation of a jet (Holman et al, 2005; Milanovic and Zaman, 2005), and there is a threshold of L = 4 beyond which secondary vortices will be formed behind the primary vortex (Gharib et al, 1998; Jabbal et al, 2006). For a synthetic jet issued into a boundary layer, the effect of suction would be confined to the upstream branch of vortex ring, leading to an asymmetric structure when the dimensionless stroke length is small (Jabbal and Zhong, 2008). The threshold value of L for the formation of secondary vortices is likely to decrease since the primary vortex also has to entrain vorticity in

the boundary layer. Sau and Mahesh (2007) observed the presence of secondary structures in their DNS simulations at a dimensionless stroke length down to 3.

The Reynolds number based on the stroke length is defined as

$$\mathrm{Re}_L = \frac{\overline{U}_o L_o}{\nu} \tag{6.4}$$

which is proportional to the vortex circulation in the synthetic jets hence quantifies the strength of a vortex ring (Tang and Zhong, 2006). Re_L is therefore an important parameter where fluid entrainment and mixing in the near-wall region via the generation of coherent vorticity is ultimately required.

The jet-to-freestream velocity ratio is defined as

$$VR = \frac{\overline{U}_o}{U_\infty} \tag{6.5}$$

where U_∞ is the freestream velocity. *VR* indicates the relative strength between the jet and freestream velocity and it affects the trajectory of the vortical structures as they propagate through the boundary layer (Milanovic and Zaman, 2005). Hence at low *VR* the vortical structures will reside in the boundary layer for a longer period of time. In the current study, as the geometry of synthetic jet is fixed and the freestream velocity is constant, *VR* depends on the jet velocity only and therefore it is determined by the displacement and frequency of the oscillating diaphragm.

The Strouhal number based on the freestream velocity and the thickness of the undisturbed boundary layer at the orifice is defined as

$$Str = \frac{f\delta}{U_\infty} = \frac{VR}{Ld} \tag{6.6}$$

which is a useful dimensionless frequency for synthetic jets issued into a boundary layer. Assuming that the structures travel at the freestream velocity, *Str* is a measure of the distance between the consecutive structures produced by the synthetic jets as a fraction of the boundary layer thickness. But as seen from Eq. 6.6, it is not an independent parameter.

6.3 Numerical Method

The synthetic jet actuator used in the numerical study is identical to that used in the experiment of Jabbal and Zhong (see Fig. 6.1). The cavity of the actuator has a

diameter of D_c = 45 mm and a height of H = 25 mm. The orifice diameter D_o is 5 mm and its height h is also 5 mm. The rubber diaphragm is pre-stretched and clamped circumferentially to the back of the cylindrical cavity. The centre of the diaphragm is made to oscillate in a sinusoidal manner by being attached to a permanent magnetic shaker via a steel rod.

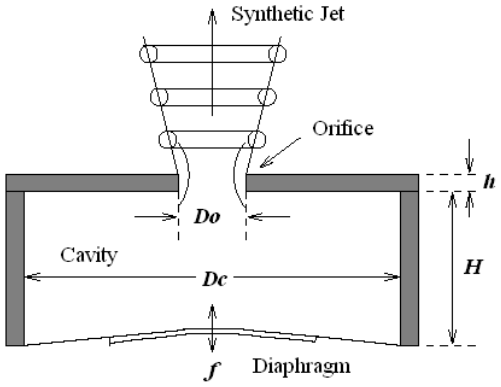

Figure 6.1. Schematic of synthetic jet actuator (modified from Crook, 2002).

The experiment is conducted in a tilting water flume. The orifice centre of the synthetic jet actuator is located at 0.7 m downstream of the leading edge of the flat test plate along which a laminar boundary layer develops. In the present study, the freestream velocity is set as 0.05 m/s and the local boundary layer thickness is about four times of the orifice diameter at the orifice, i.e. $d \approx 0.25$. The flow characteristics of the synthetic jet are varied by changing the diaphragm oscillation displacements and frequencies.

In the present study, the commercial CFD software, FLUENT 6.3, is utilized to compute the unsteady 3D incompressible flow. Since the Reynolds numbers of the jet in the present study are much lower than the critical value (around 5×10^4) above which the jet becomes turbulent at the orifice exit (Glezer, 1988), the laminar model is employed to compute the flow field.

The computational domain and boundary conditions used in this study are shown in Fig. 6.2. In order to save on computational time, only half width of the flow field is modelled. Both the orifice duct and actuator cavity are included in the simulation and a velocity boundary condition is applied at the neutral position of the diaphragm. Assuming that the diaphragm exhibits a cone shape instantaneously, the moving velocity of diaphragm can be expressed as,

$$v(r,t) = \pi \Delta f \left(1 - \frac{r}{r_c}\right) \cos(2\pi f t) \tag{6.7}$$

where f is the diaphragm oscillation frequency, Δ is the peak-to-peak displacement at the centre of diaphragm, r is the distance from the centre of diaphragm and r_c is the radius of the diaphragm. The velocity boundary condition is specified using user-defined functions (UDFs) supported by FLUENT.

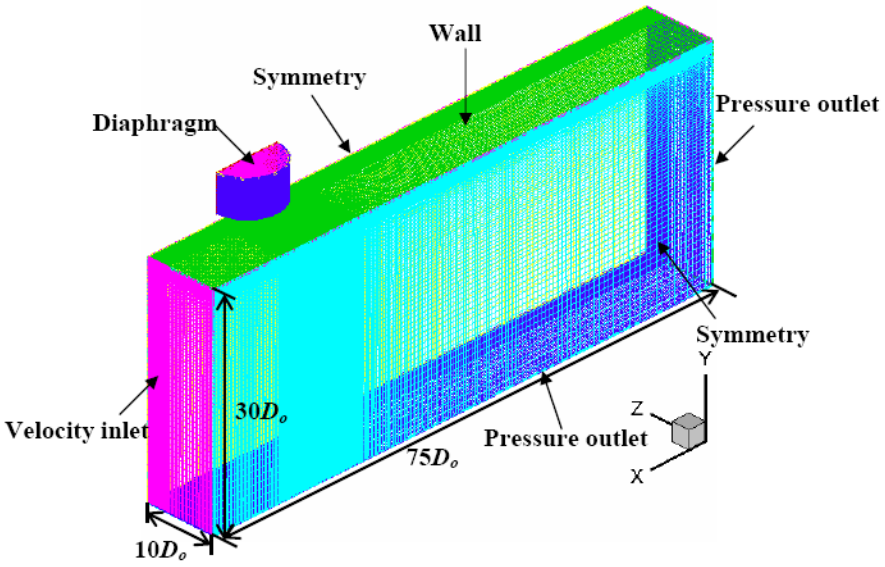

Figure 6.2. Geometry of computational domain and boundary conditions.

The computational domain contains 1.4 million mesh cells. The mesh distributions in the synthetic jet cavity, orifice and outflow domain are listed in Table 6.1. The time step size is set as 1/120 of the diaphragm oscillation cycle as a compromise between computational accuracy and computational time. These settings are identical to those used by Zhou and Zhong (2009) in their previous studies of the same actuator in the same boundary layer (There is a typo error in Zhou and Zhong (2009). The cavity height H should be 25 mm instead of 20 mm). In their studies, the adequacy of the choices of computational domain and boundary conditions has been validated and a sensitivity study of grid and time step size has been undertaken, confirming that the chosen grids and time step size are adequate. Furthermore, they also conducted a comparison of their simulated results with the PIV data from Jabbal and Zhong (2008) for two test cases. The good agreement between the simulation and the measurement confirms that the capability of the

numerical method used here is capable of capturing the key characteristics of the flow.

Table 6.1 Mesh partition of the simulation cases

	Cavity	Orifice	Out flow domain	Total mesh
Mesh number	80×30×75	20×30×20	264×56×85	1,434,796

In the present study, the flow in the actuator can be adequately assumed as incompressible. It can be proved that the mean time-averaged blowing velocity during the entire oscillation cycle across the orifice exit can be expressed as (Tang and Zhong, 2006)

$$\overline{U}_o = \alpha f \Delta \left(\frac{D_c}{D_o} \right)^2 \tag{6.8}$$

The coefficient α is equal to 1/3 for the rubber diaphragm used in this study. In some studies, the peak exit velocity is used to define the velocity ratio and Reynolds number. For the present actuator, it can be proved that the peak velocity is $\pi \overline{U}_o$. Eq. 6.8 indicates that $\overline{U}_o$ is proportional to the diaphragm oscillation frequency and displacement. Substituting Eq. 6.8 into Eq. 6.2, one can show that the dimensionless stroke length is independent of the diaphragm frequency and it is proportional to the displacement only. Hence Eq. 6.8 is useful for illustrating the relationships between the dimensionless parameters and the actuator operating conditions. In the present study, $\overline{U}_o$ used for calculating the dimensionless parameters is computed from Eq. 6.8.

6.4 Results and Discussions

In the present study, a total of 34 cases have been computed to cover a reasonably wide range of dimensionless parameters with $1.6 \le L \le 6.5$ and $0.16 \le VR \le 0.81$. The choice of the maximum values of L and VR is restricted by the use of the laminar flow model. Nevertheless, the maximum value of VR (equivalent to a velocity ratio based on the jet peak velocity of 2.5) is thought to be close to the top range of VR which would be of interest in practical setting (Schaeffler, 2003;

Dandois et al, 2006). In addition, based on the finding by Jabbal and Zhong (2008), the parameter range selected in this study is sufficient to cover the parameter space within which transition from the hairpin type to tilted vortex ring type of vortical structures occurs. Due to space limitation, however, only 12 cases are selected for discussion in this paper which distribute themselves across the parameter space covered by this study. These test cases are chosen such that the effect of changing L at constant VR can be examined and vice versa. A summary of the 12 selected cases is illustrated in Fig. 6.3 and the magnitudes of the dimensionless parameters for each case can be found in Table 6.2.

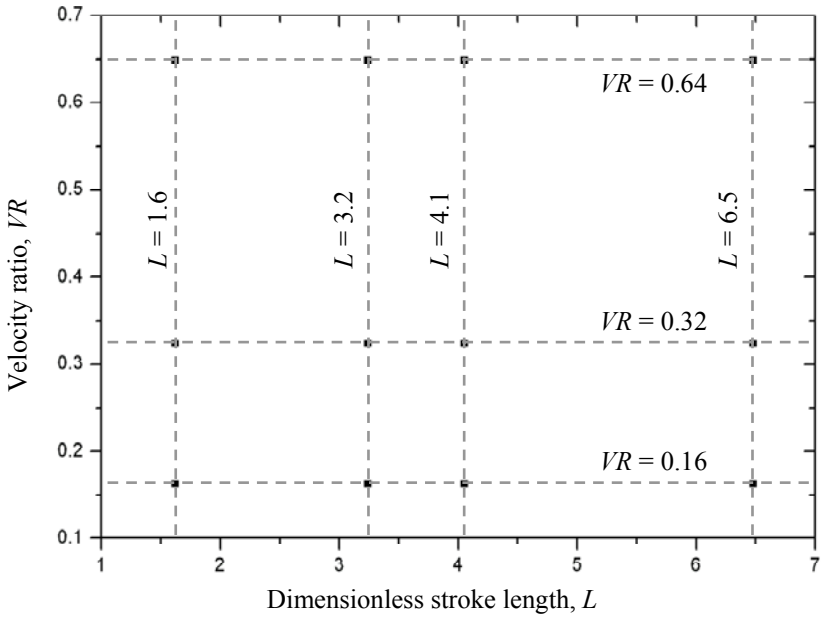

Figure 6.3. Summary of selected test cases in *VR-L* parameter map.

6.4.1 Vortical Structures Produced by the Synthetic Jets

Figures 6.4a to 6.6a show the instantaneous coherent structures identified by the Q-criterion at four different dimensionless stroke lengths at VR = 0.16, 0.32 and 0.64 respectively. The iso-surface of Q is chosen as Q = 0.1. To maintain a constant VR while L increases, the diaphragm frequency (i.e. Strouhal number) is reduced while the displacement is increased.

Table 6.2 Parameters of the simulated cases

Δ (mm)	f (Hz)	VR	L	Re_L	Str
0.3	1	0.16	1.6	65	0.4
0.6	0.5	0.16	3.2	130	0.2
0.75	0.4	0.16	4.1	163	0.16
1.2	0.25	0.16	6.5	261	0.1
0.3	2	0.32	1.6	130	0.8
0.6	1	0.32	3.2	261	0.4
0.75	0.8	0.32	4.1	326	0.32
1.2	0.5	0.32	6.5	521	0.2
0.3	4	0.64	1.6	261	1.6
0.6	2	0.64	3.2	521	0.8
0.75	1.6	0.64	4.1	652	0.64
1.2	1	0.64	6.5	1040	0.4

At VR = 0.32 and L = 1.6 (see Fig. 6.5a1), the dominant structures consist of typical hairpin vortices each accompanied by a pair of streamwise vortices with an opposite sense of rotation located outboard of the counter-rotating legs of the hairpin. The hairpin vortices remain embedded within the boundary layer due to their low VR. As such, their counter-rotating legs experience a degree of stretching as they propagate downstream. At the same time, the streamwise vortices, which are believed to be induced by the counter-rotating legs, gradually become weaker and disappear as they propagate downstream.

As L increases to 3.2 while VR is kept the same (Fig. 6.5a2), the spacing between successive structures increases due to a decrease in frequency. Although the jet exit velocity $\overline{U}_o$ is the same, a larger L leads to a higher Re_L hence a stronger vortex ring. Nevertheless, the primary structure still appears as hairpin vortices. Due to a higher self-induced velocity, the head of the structure is lifted-up higher in the boundary layer. As such the legs become highly tilted and stretched due to the local shear. In contrast, the head of the hairpin appears more upright since it is located in the outer part of the boundary layer where the shear is almost negligible. The difference between the structures at L = 4.1 (Fig. 6.5a3) and L = 3.2 (Fig. 6.5a2)

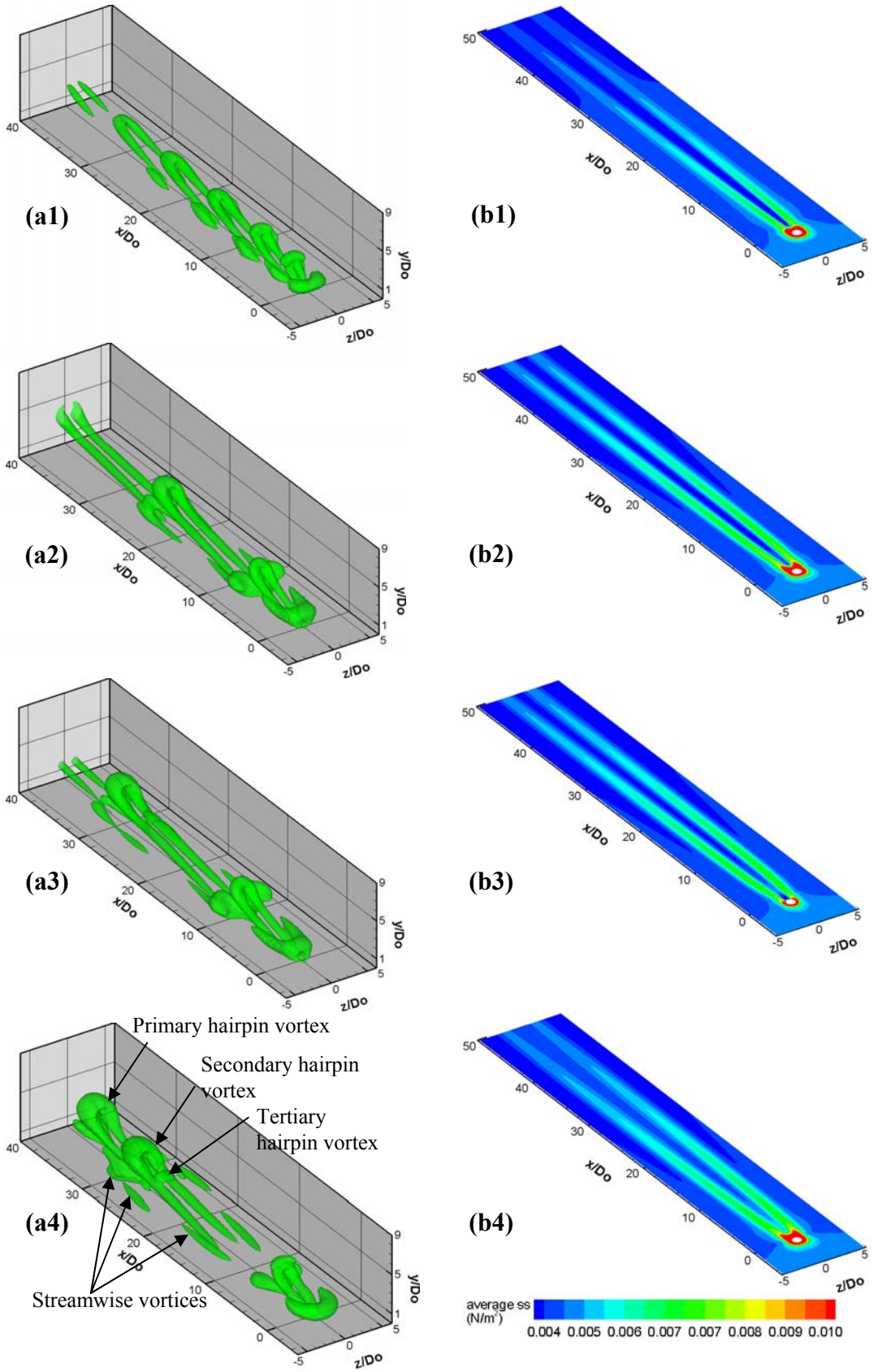

Figure 6.4. (a) Instantaneous coherent structures and (b) their corresponding time-averaged surface shear stress at *VR* = 0.16, (1) *L* = 1.6, (2) *L* = 3.2, (3) *L* = 4.1, and (4) *L* = 6.5.

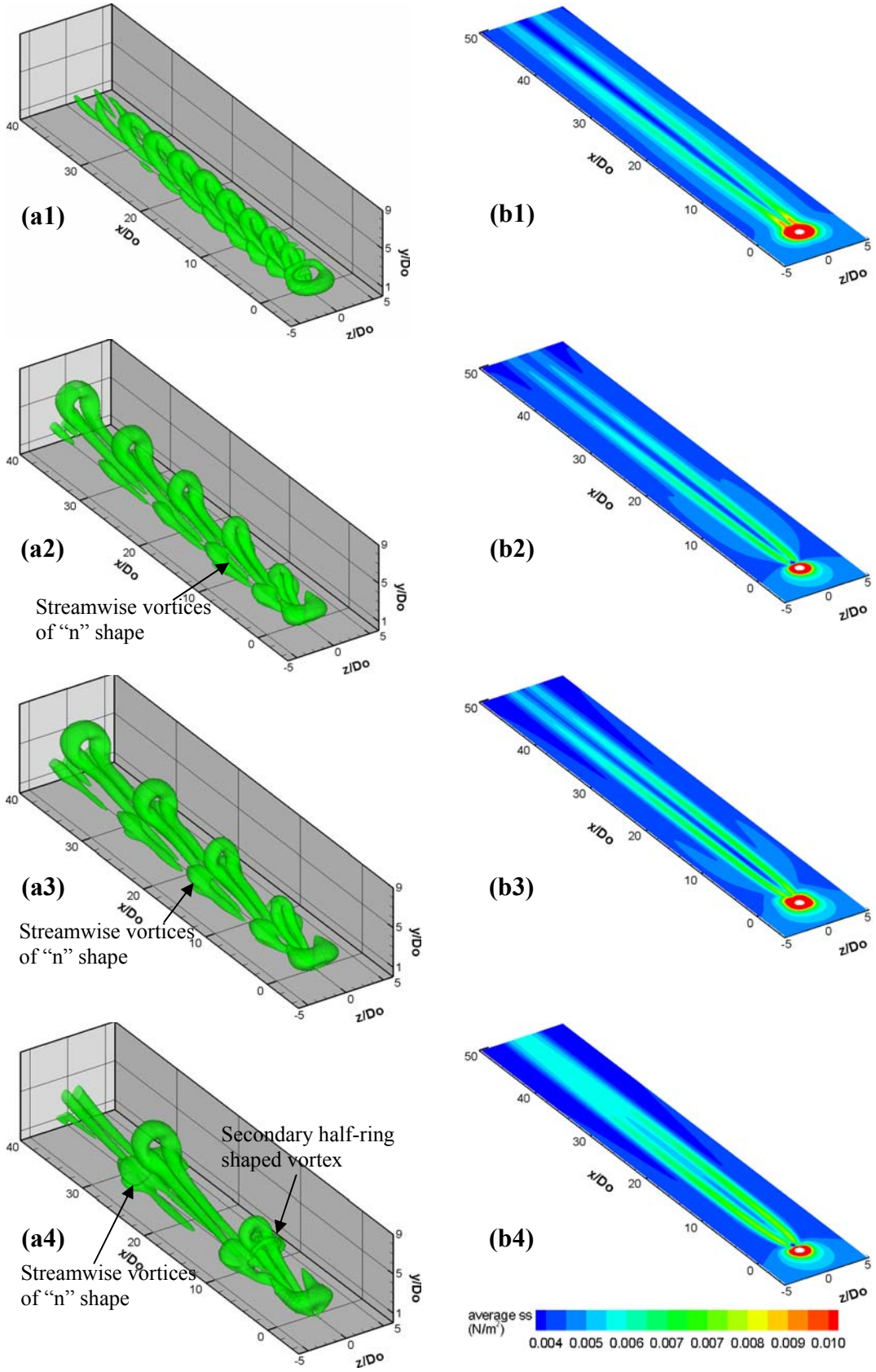

Figure 6.5. (a) Instantaneous coherent structures and (b) their corresponding time-averaged surface shear stress at *VR* = 0.32, (1) *L* = 1.6, (2) *L* = 3.2, (3) *L* = 4.1, and (4) *L* = 6.5.

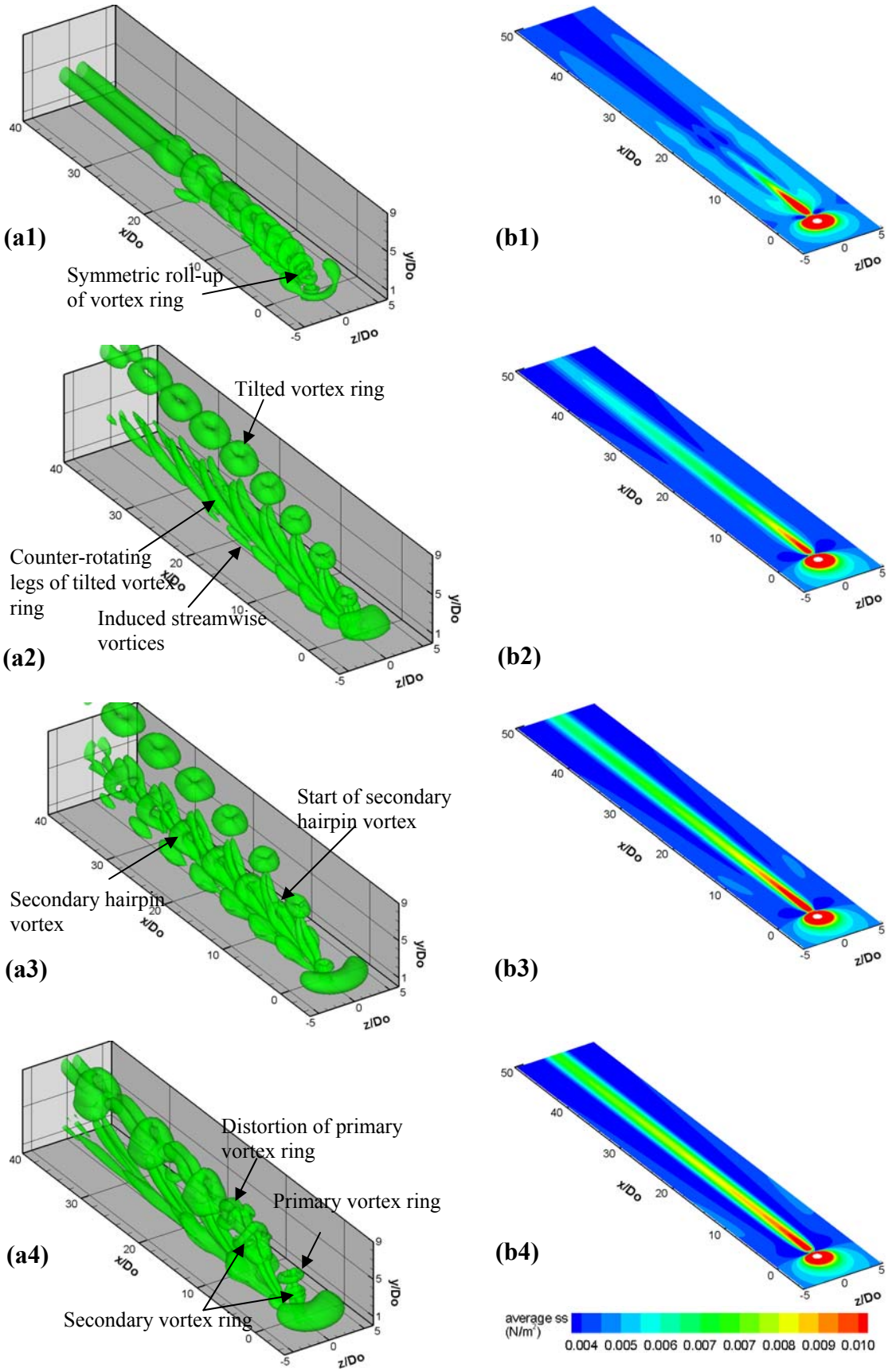

Figure 6.6. (a) Instantaneous coherent structures and (b) their corresponding time-averaged surface shear stress at *VR* = 0.64, (1) *L* = 1.6, (2) *L* = 3.2, (3) *L* = 4.1, and (4) *L* = 6.5.

is not evident except that the hairpins appear to have more remarkably elongated counter-rotating legs and a larger head.

The formation of hairpin vortices is examined in detail using the time-sequence shown in Fig. 6.7. It is found that the newly formed vortex ring appears to be nearly symmetrical as it emerges from the orifice outlet (Fig. 6.7a). The upstream branch of the new vortex ring is gradually weakened by the resident vorticity in the boundary layer, which is of the opposite sense of rotation (Fig. 6.7b), and it eventually disappears (Fig. 6.7c). On the contrary, its downstream branch is enhanced and the structure turns into a hairpin vortex within an actuation cycle. In the paper by Jabbal and Zhong (2008), these structures are called stretched vortex rings due to their initial ring like shape and the intention of differentiating this case from those in which hairpin vortices are observed at the orifice outlet as the result of the upstream branch being inhaled by the suction at a lower L.

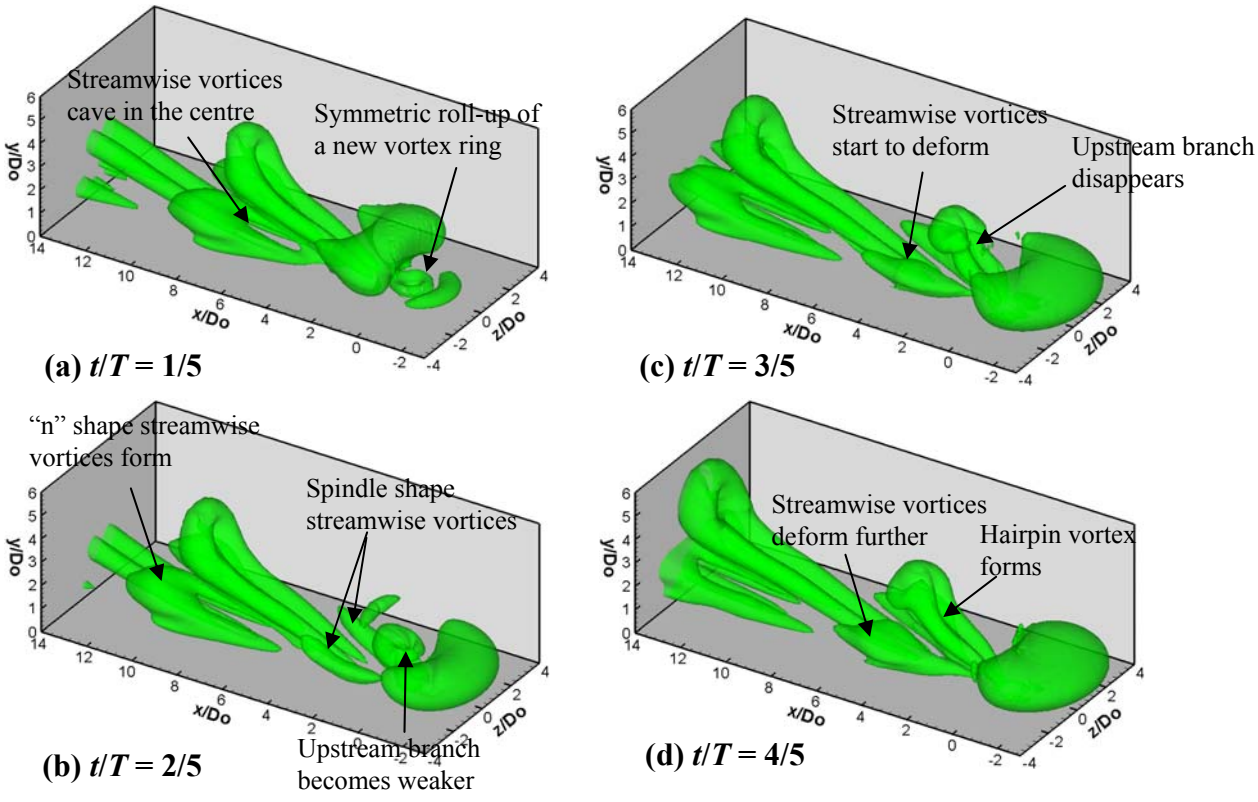

Figure 6.7. Sequence from iso-surface of Q = 0.1 showing the formation of hairpin vortex and the deformation of the induced streamwise vortices at VR = 0.32, L = 4.1.

In addition, it is found that in the near field the induced streamwise vortices appear to change from a spindle shape (see Figs. 6.7c and d) to an "n" shape as the

structure becomes flattened and cave in at its centre (see Figs. 6.7a and b). The presence of those "n" shape streamwise vortices is also evident at L = 3.2 and it is even more obvious at L = 4.1. An examination of the velocity vector field and vorticity field on selected cross flow planes reveals that the deformation of the induced streamwise vortices are caused by the combined shearing action of the legs of hairpin formed in the current and previous cycles. Nevertheless, as the primary hairpin vortices play a dominant role in the near-wall flow the effect of changing shape in the induced streamwise vortices is negligible hence will not be further explored.

As L increases further to 6.5, it is observed that a half ring-shaped spanwise secondary vortex occurs over the counter-rotating legs, just behind the upright head (Fig. 6.5a4). A closer examination of the time-sequence shown in Fig. 6.8 indicates that it is originated from the secondary vortex ring formed at the orifice. As shown in Fig. 6.8a, a secondary vortex ring is formed below the primary ring. At L = 6.5, the vorticity generated by the synthetic jet has exceeded the critical level of vorticity that can be entrained into the primary vortex ring, and thus the excessive vorticity is shed as a secondary vortex. Within a short distance from the orifice, the upstream branch of both the primary and secondary ring disappears due to the effect of the resident vorticity in the boundary layer (Figs. 6.8b and c). Subsequently, the primary vortex ring evolves into a hairpin vortex with the downstream branch of the secondary ring riding over the legs of the primary hairpin (Fig. 6.8f). The strength of the secondary vortex becomes gradually weaker and it eventually disappears as the entire structure propagates downstream, as shown in Fig. 6.5a4.

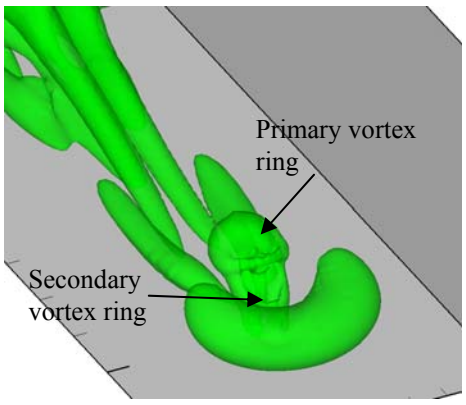

(a) t/T = 7/20

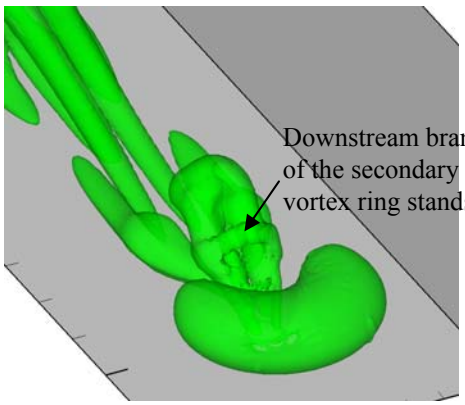

(d) t/T = 10/20

For caption see overleaf

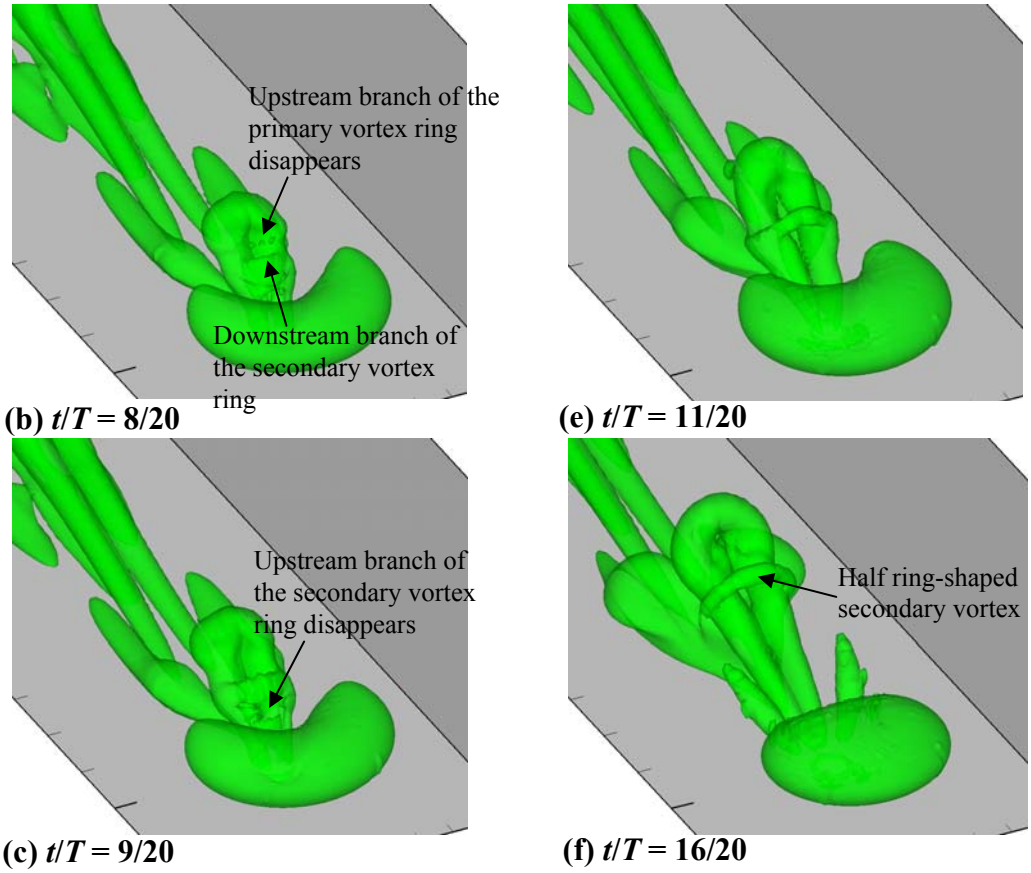

Figure 6.8. Sequence from iso-surface of Q = 0.1 showing the formation of the secondary hairpin vortices at VR = 0.32, L = 6.5.

Figure 6.4a shows the instantaneous coherent structures at four different dimensionless stroke lengths at a lower VR of 0.16. Here a lower VR is achieved by reducing the diaphragm frequency while maintaining the same displacement at the corresponding L. The dominant structures in these four cases appear to be highly stretched hairpin vortices owing to a lower actuation frequency hence a longer resident time in the boundary layer. Since the upstream branch of vortex ring is located in the near-wall region, its circulation is quickly cancelled out by the resident shear with the opposite sense of rotation. This process is similar to that observed at VR = 0.32, but proceeds much more quickly. At VR = 0.16, the heads of hairpin vortices do not appear upright even at a higher L since the vortical structures are embedded in the lower part of the boundary layer with a strong shear. Furthermore, it is noticed that secondary and tertiary hairpin vortices appear as L increases (Figs. 6.4a3 and a4). A close examination of the time sequence at L = 6.5 reveals that the new secondary and tertiary hairpin vortices are not formed at the orifice, but during the evolvement process as the primary hairpin vortices propagate downstream (Fig. 6.9). Therefore, it is believed that the formation mechanism of the secondary and

tertiary hairpin vortices is different from that at VR = 0.32 and L = 6.5 which is due to the presence of a secondary vortex ring formed from the orifice. It is believed that they are produced by the roll-up of the high-shear layer that develops between the lifted-up, low-momentum, near-wall fluid and the higher-momentum, outer-boundary freestream flow. Acarlar and Smith (1987b) observed a similar phenomenon in their study of hairpin vortices in a laminar boundary layer, which were formed owing to the breakup of the synthetic low-speed streak generated by steady fluid injection. The mechanism forming the secondary hairpin vortex structure has been explained clearly by Haidari and Smith (1994) who also used controlled fluid injection to create hairpin vortices. Although the mechanism generating the hairpin vortices in their study is different from that used in the present study, the interaction between the hairpin vortices and fluid flow in the near-wall region once they are formed is believed to be similar hence the formation mechanism of the secondary hairpin vortices. The induced streamwise vortices and "n" shape vortices observed at VR = 0.32 are still present at VR = 0.16, as shown in Fig. 6.4a2.

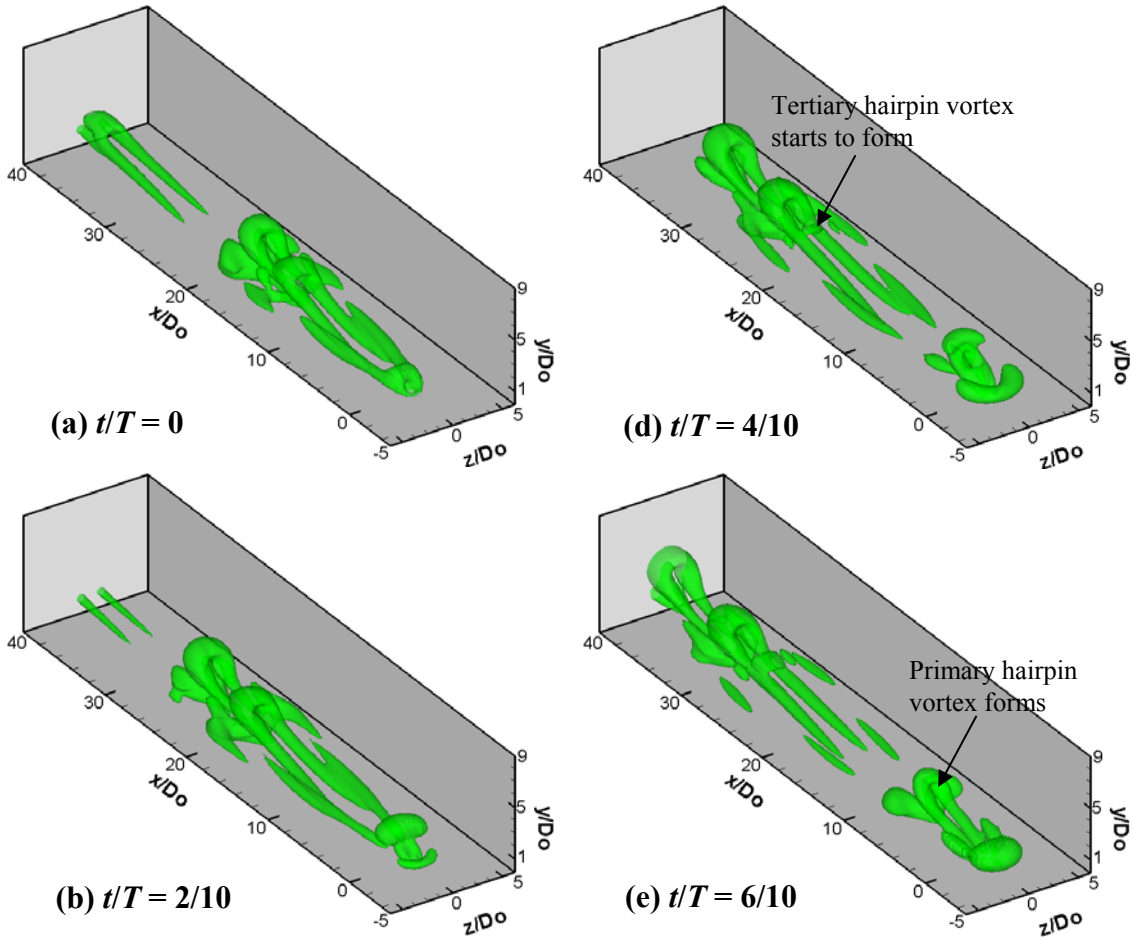

For caption see overleaf

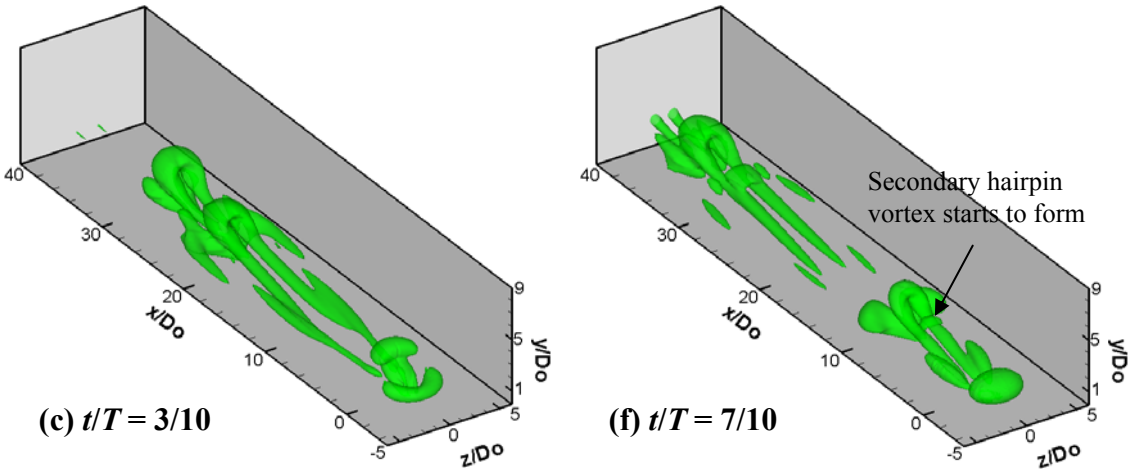

Figure 6.9. Instantaneous coherent structures at *VR* = 0.16, *L* = 6.5 showing the formation of the secondary and tertiary hairpin vortices.

When *VR* increases to 0.64, the appearance of the coherent structures changes more dramatically as shown in Fig. 6.6a. A close observation of the formation process of vortical structures at *VR* = 0.64 and *L* = 1.6 (Fig. 6.6a1) reveals that the upstream branch of the primary vortex ring is weakened by the combined effect of the resident vorticity in the boundary layer and the downstream branch of the newly formed vortex ring, both of which have the opposite sense of rotation and it eventually disappears after two actuation cycles. Because of the high actuation frequency, the vortical structures in the near field of the orifice appear as a train of hairpin vortices which stay closely together. Further downstream, the hairpin vortices agglomerate to form larger hairpin vortices. The spanwise vorticity of those large hairpin vortices becomes weaker then disappears and the vortical structures eventually transform into a pair of streamwise vortices. The hairpin vortices also induce streamwise vortices outboard of their counter-rotating legs. These induced streamwise vortices are weakened and they dissipate quickly within a distance of $20D_o$ from the orifice.

Very different from the structures observed at *VR* = 0.64 and *L* = 1.6, the coherent structures at *VR* = 0.64 and *L* = 3.2 appear to be consistent with a typical tilted vortex ring with its trailing counter-rotating legs and a pair of streamwise vortices induced by the legs (Fig. 6.6a2). In this case, due to its high *L* and *VR* the vortex ring has survived from both the impact of the suction cycle and the resident shear and retains its ring shape. The formation and evolvement of the tilted vortex rings have been explained in an earlier paper by the authors (Zhou and Zhong, 2009).

As L increase to 4.1, secondary hairpin vortices begin to emerge between the consecutive structures (Fig. 6.6a3). Figure 6.10 is the sequence from a close-up view of the iso-surface of $Q = 0.1$ showing the formation process of the secondary hairpin vortices. It is seen that after two actuation cycles, a spanwise vortex filament emerges, bridging over the counter-rotating legs of the primary structures (Fig. 6.10a). The spanwise vortex filament gains strength as the main structure moves downstream (Fig. 6.10b) and evolves into the head of the secondary hairpin vortex (Fig. 6.10d). The legs of the secondary hairpin vortex appear to split from the counter-rotating legs of the tilted vortex ring at about $35D_o$ downstream of orifice outlet. The formation mechanism of the secondary hairpin vortices at $VR = 0.64$, $L = 4.1$ is similar to that at $VR = 0.16$ and $L = 6.5$, which was discussed earlier.

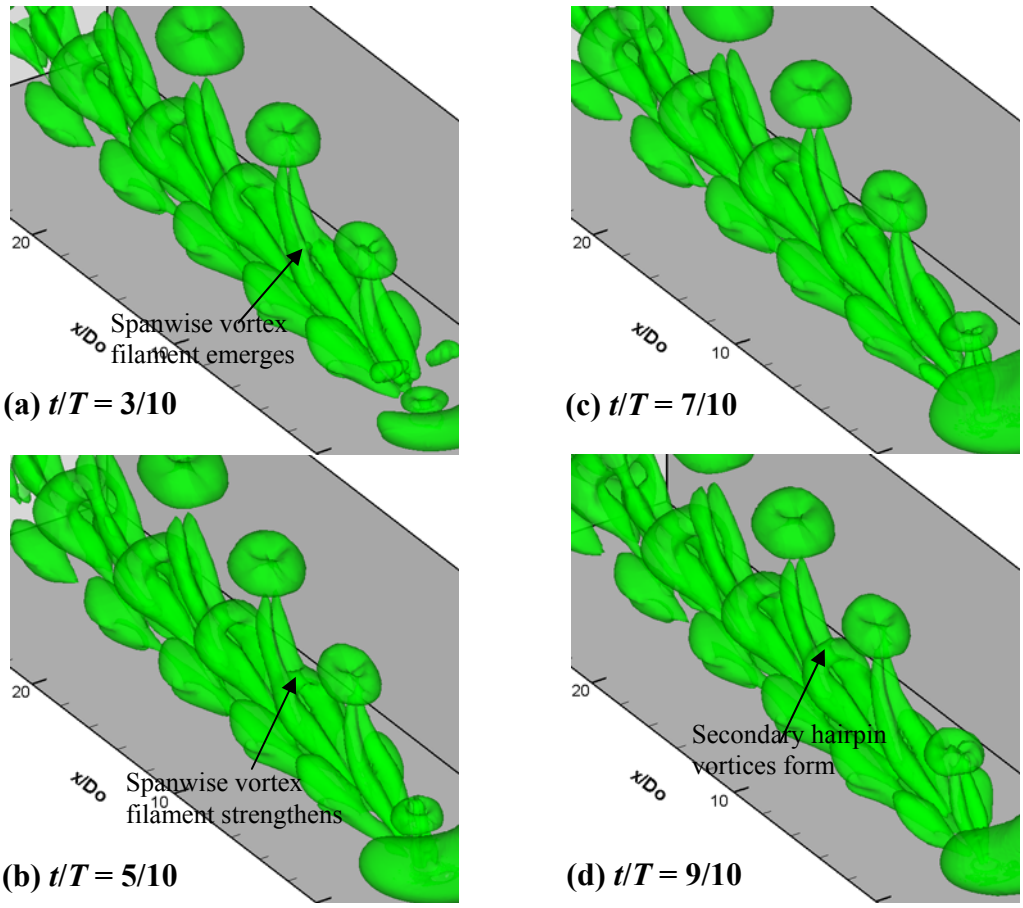

Figure 6.10. Sequence from iso-surface of $Q = 0.1$ showing the formation of the secondary hairpin vortices at $VR = 0.64$, $L = 4.1$.

At $L = 6.5$, the tilted vortex rings become distorted due to the mutual interaction between the different parts of the vortical structures (Fig. 6.6a4). At such a large L, a secondary vortex ring is seen to form below the primary vortex ring and

it travels together with the primary vortex ring (see Fig. 6.11). The deformation of the structures due to the interaction between them is quite complex. However, the head of the structure evolved from the secondary vortex ring appears to retain its ring shape. On the other hand, the head of the primary vortex ring becomes a passive tongue-shape vortex attached to the secondary vortex ring from downstream. This downstream vortical tongue is also observed by Zhou et al. (1999) for a single hairpin vortex-like structure evolved in a low-Reynolds number channel flow.

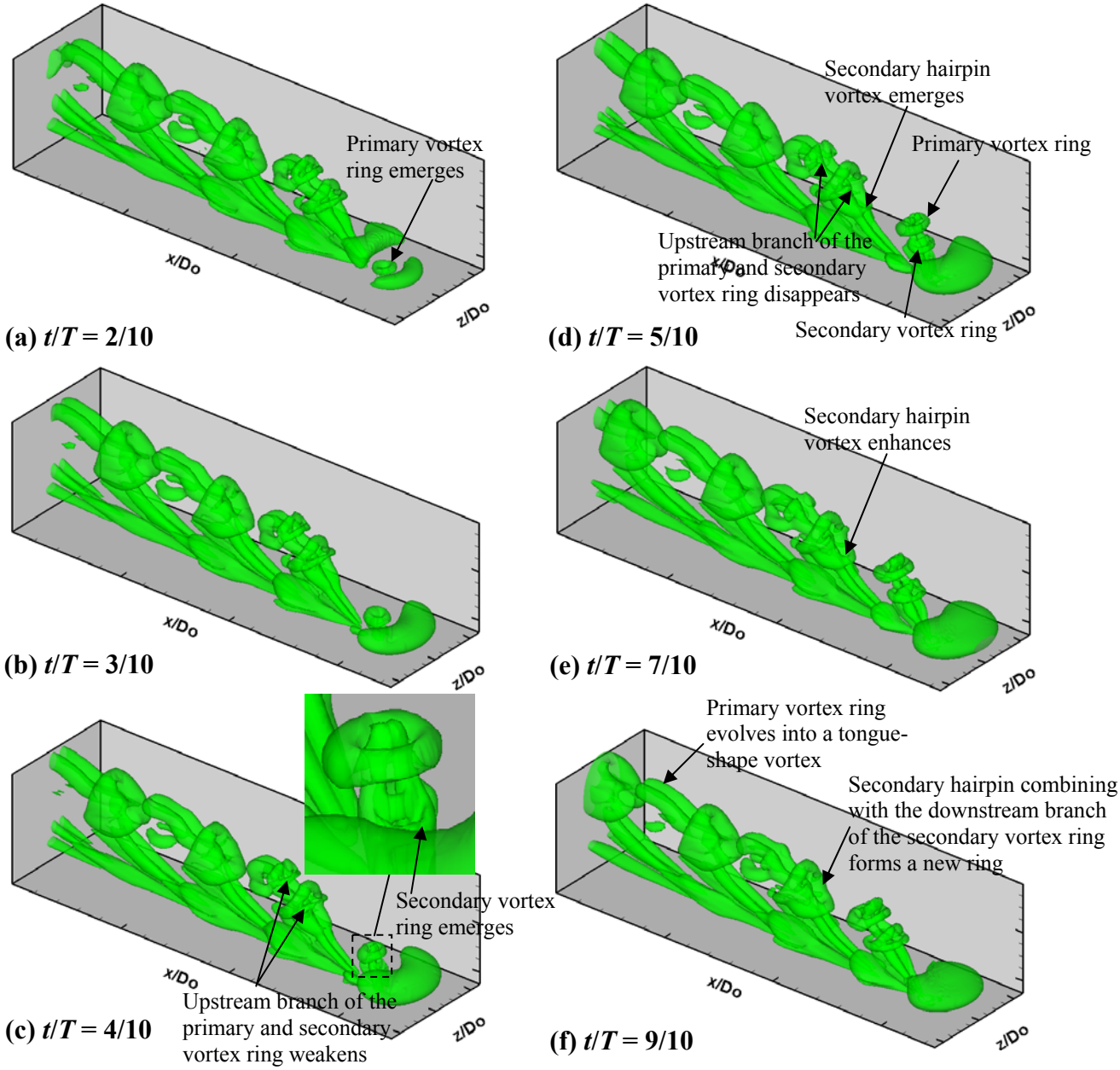

Figure 6.11. Sequence from iso-surface of $Q = 0.1$ showing the evolvement of the primary and secondary vortex rings and the formation of secondary hairpin vortex at $VR = 0.64$, $L = 6.5$.

6.4.2 Patterns of Surface Shear Stress

It is believed that a key mechanism of separation delay is to increase mixing by introducing coherent structures into the boundary layer which subsequently entrain high-speed fluid from the outer part of the boundary layer to the near-wall region. Therefore the level of surface shear stress is a useful indicator of the potential of vortical structures in delaying boundary layer separation. In this section, the patterns of surface shear stress produced by different vortical structures are investigated.

The distributions of time-averaged surface shear stress at the corresponding test conditions for those cases discussed earlier are shown in Figs. 6.4b, 6.5b, and 6.6b. It can be seen that in general the hairpin vortices produce a streak of high surface shear stress on each side of the orifice (Fig. 6.4b), whereas the tilted/distorted vortex rings produce a streak of high surface shear stress downstream of the orifice centreline (Figs. 6.6b2-b4). The mechanisms of producing the above two types of shear stress patterns have been explained in an earlier paper by the authors (Zhou and Zhong, 2009) hence the discussion will not be repeated here in detail. In brief, in the case of the hairpins, the two streaks of high surface shear stress are produced by the downwash induced by the counter-rotating legs of the hairpin and its induced streamwise vortices outboard of the legs of the hairpin (see Fig. 6.12). This downwash motion brings the high momentum fluid from outer region of the boundary layer towards the wall outboard of the hairpin legs resulting in an increase in the local velocity hence the surface shear stress. In the case of tilted/distorted vortex rings, the single streak of high surface shear stress on the orifice central plane is due to the downwash produced by the streamwise vortices which are induced by the trailing legs of the vortex ring, as shown in Fig. 6.13.

A comparison of Figs. 6.4b2 and b4, indicates that the presence of secondary/tertiary hairpin vortices seems to have no obvious influence on the pattern of surface shear stress. This could be attributed to the weak nature of the secondary/tertiary hairpin vortices, and their further distance from the wall than the counter-rotating legs.

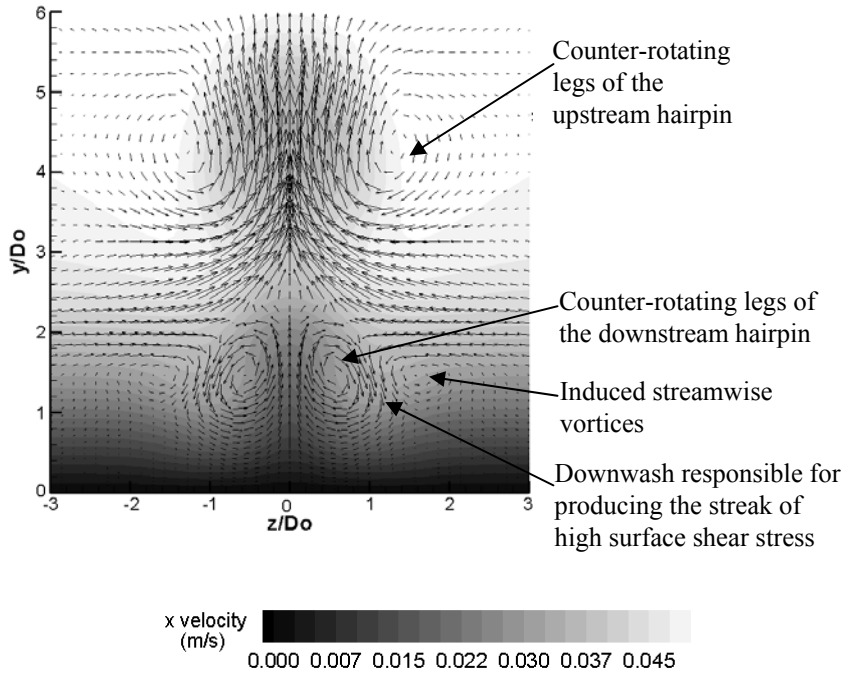

Figure 6.12. Velocity vector superimposed on streamwise velocity at x/D_o = 20 for the structures at VR = 0.32, L = 3.2.

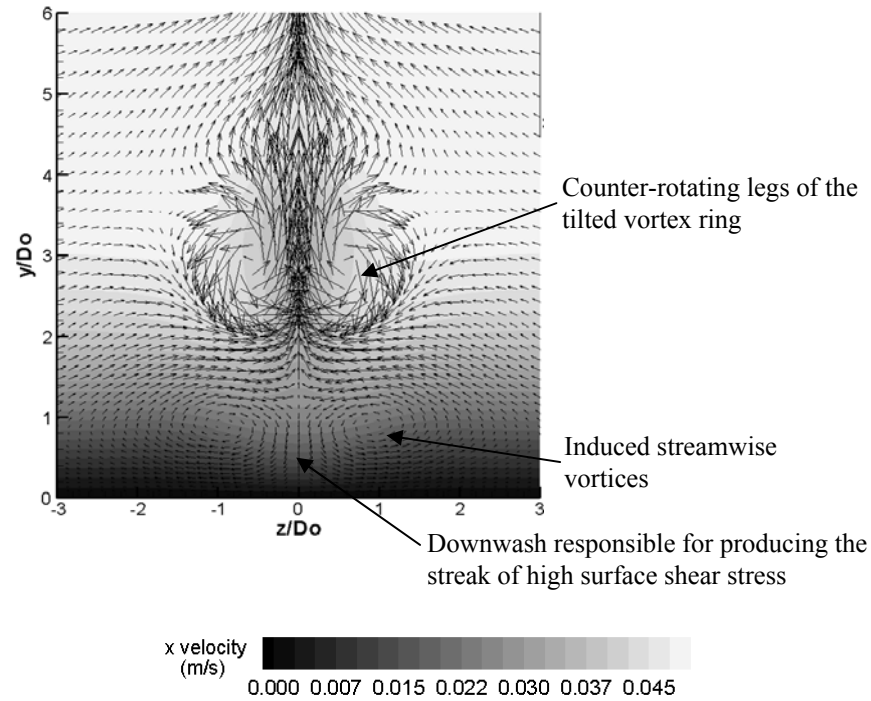

Figure 6.13. Velocity vector superimposed on streamwise velocity at x/D_o = 20 for the structures at VR = 0.64, L = 3.2.

In addition to the above two distinct patterns of surface shear stress, a changeover from two streaks to a single streak or vice versa in the streamwise direction is observed. For example, at VR = 0.64 and L = 1.6 (Fig. 6.6a1) a central

streak emerges in the near field of the orifice and it becomes weaker downstream. The central streak is due to the downwash produced by the induced streamwise vortices as shown in Fig. 6.14a. The two faded side streaks, however, are believed to be caused by the strong induced inrush towards the central plane by the agglomerated hairpins rather than by any near-wall features. As the induced streamwise vortices dissipate downstream, the downwash flow on the central plane is replaced by the upwash produced by the agglomerated hairpins, thus the central streak disappears and only the two faded side streaks remain (Fig. 6.14b).

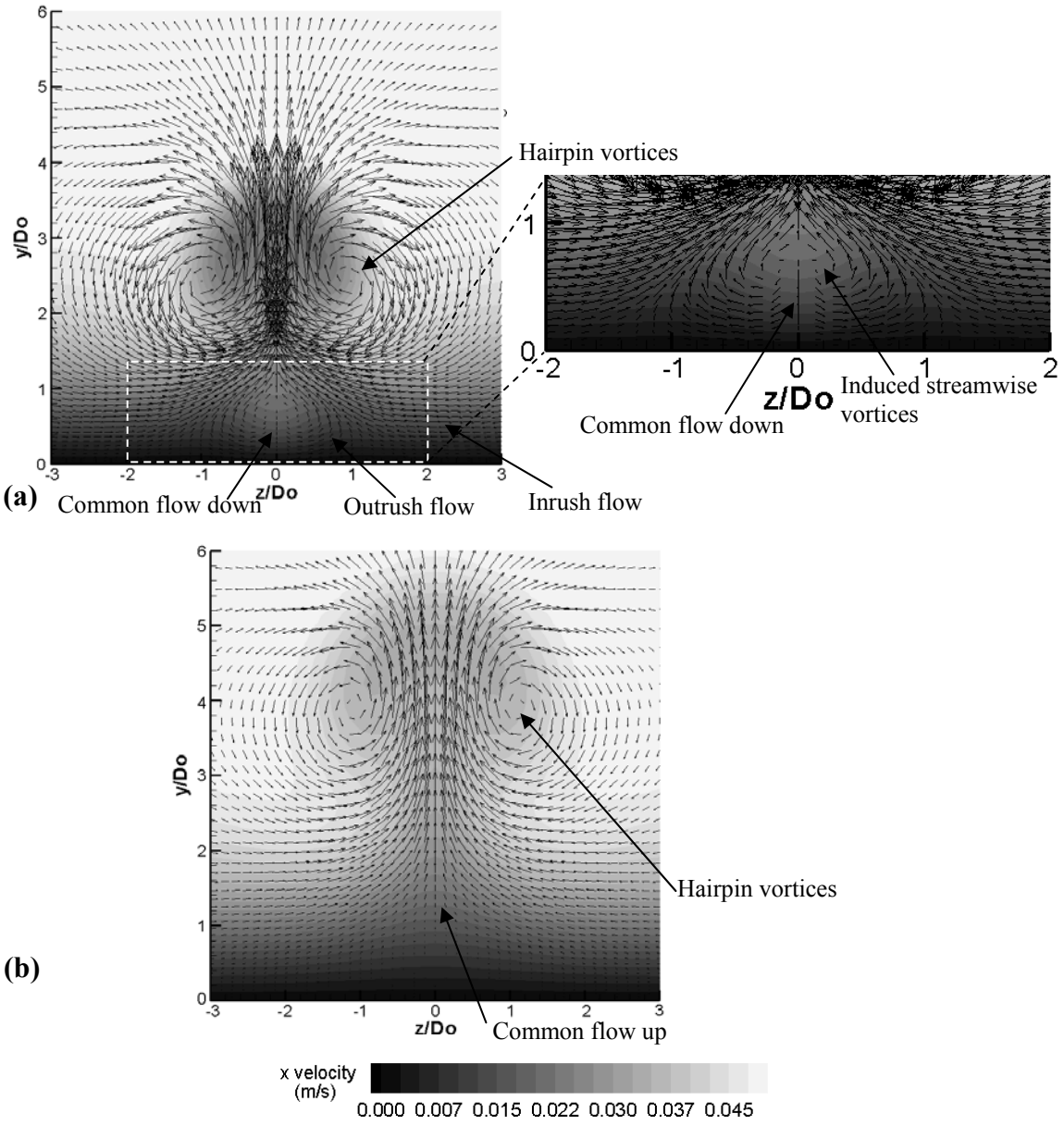

Figure 6.14. Velocity vector superimposed on streamwise velocity at (a) x/D_o = 10 and (b) x/D_o = 40 for the structures at VR = 0.64, L = 1.6.

An additional case is also simulated at the same L but a higher VR = 0.81 (i.e. a higher frequency) in which a single central streak persists further downstream, as shown in Fig. 6.15b. Its instantaneous coherent structures in Fig. 6.15a indicate that at a higher frequency, the interaction between adjacent vortical structures is stronger which accelerates the agglomeration of vortical structures and enhances the persistency of the single-steak surface shear stress pattern downstream. Hence the case at VR = 0.64 and L = 1.6 can be taken as a transitional case between the two-streak pattern and the single-streak pattern. The disappearance of the two-streak pattern as VR increases is associated with the disappearance of hairpin vortices due to the deconstructive interaction among themselves since they are too close to each other. A single-streak pattern sets in as the agglomeration of the successive vortical structures generates a pair of large-scale streamwise vortices accompanied by another pair of induced streamwise vortices with the opposite sense underneath. The pair of induced streamwise vortices is closer to the wall and they produce a downwash motion between themselves hence a high shear stress streak on the central plane (see Fig. 6.15c). As VR increases, the induced streamwise vortices become stronger and produce a more persistent central streak.

On the other hand, the footprint for the structures at VR = 0.32, L = 6.5 exhibits an opposite transition process (Fig. 6.5b4), i.e. the two streaks seen at upstream transforming into a significant central streak further downstream. Velocity contours on two spanwise planes at x/D_o = 10 and 40 are used to find the cause. At x/D_o = 10 (Fig. 6.16a), the head of the hairpin vortex appears at $4D_o$ above the wall and its induced streamwise vortices with an opposite sense of rotation are located underneath and outboard. The pair of weaker vortices beneath the induced streamwise vortices at about $0.5D_o$ above the wall is the highly stretched counter-rotating legs of the hairpin formed in the previous cycle. The induced streamwise vortices and the legs of the downstream hairpin produce a downwash outboard of the latter (see the zoom-in contour). At the same time, the upwash produced between the legs of the downstream hairpin dominates on the central plane, resulting in a local low shear stress. Hence the two streaks of high surface shear stress are formed. However, as the vortical structures propagate further downstream, the counter-rotating legs of the downstream hairpin are weakened. Therefore, only the upstream hairpin vortex and its induced streamwise vortices can be observed at x/D_o = 40 (Fig. 6.16b). The downwash produced by induced streamwise vortices hence dominates

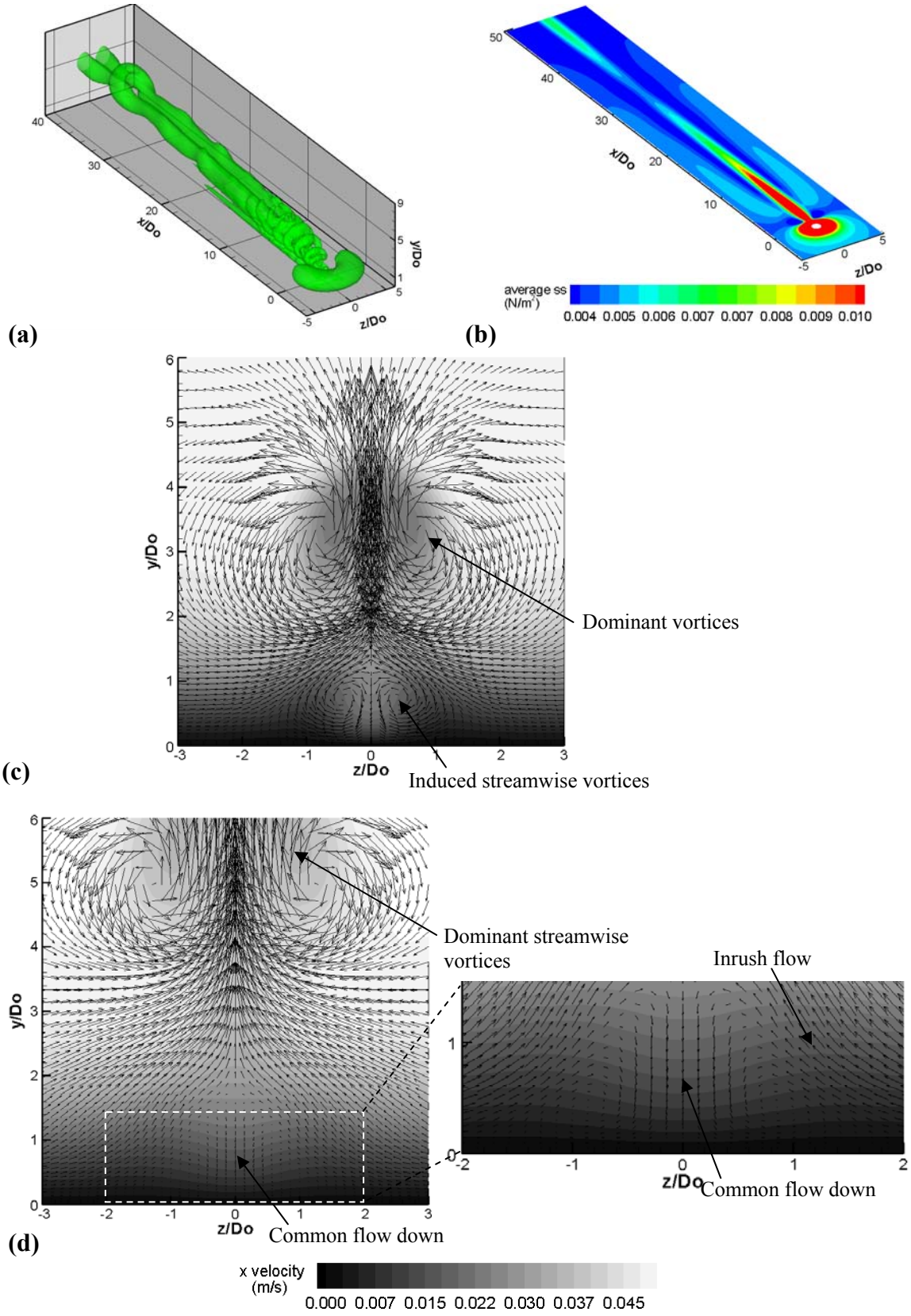

Figure 6.15. (a) Instantaneous coherent structures, (b) its corresponding time-averaged surface shear stress, and velocity vector superimposed on streamwise velocity at (c) x/D_o = 10 and (d) x/D_o = 40 for the structures at VR = 0.81, L = 1.6.

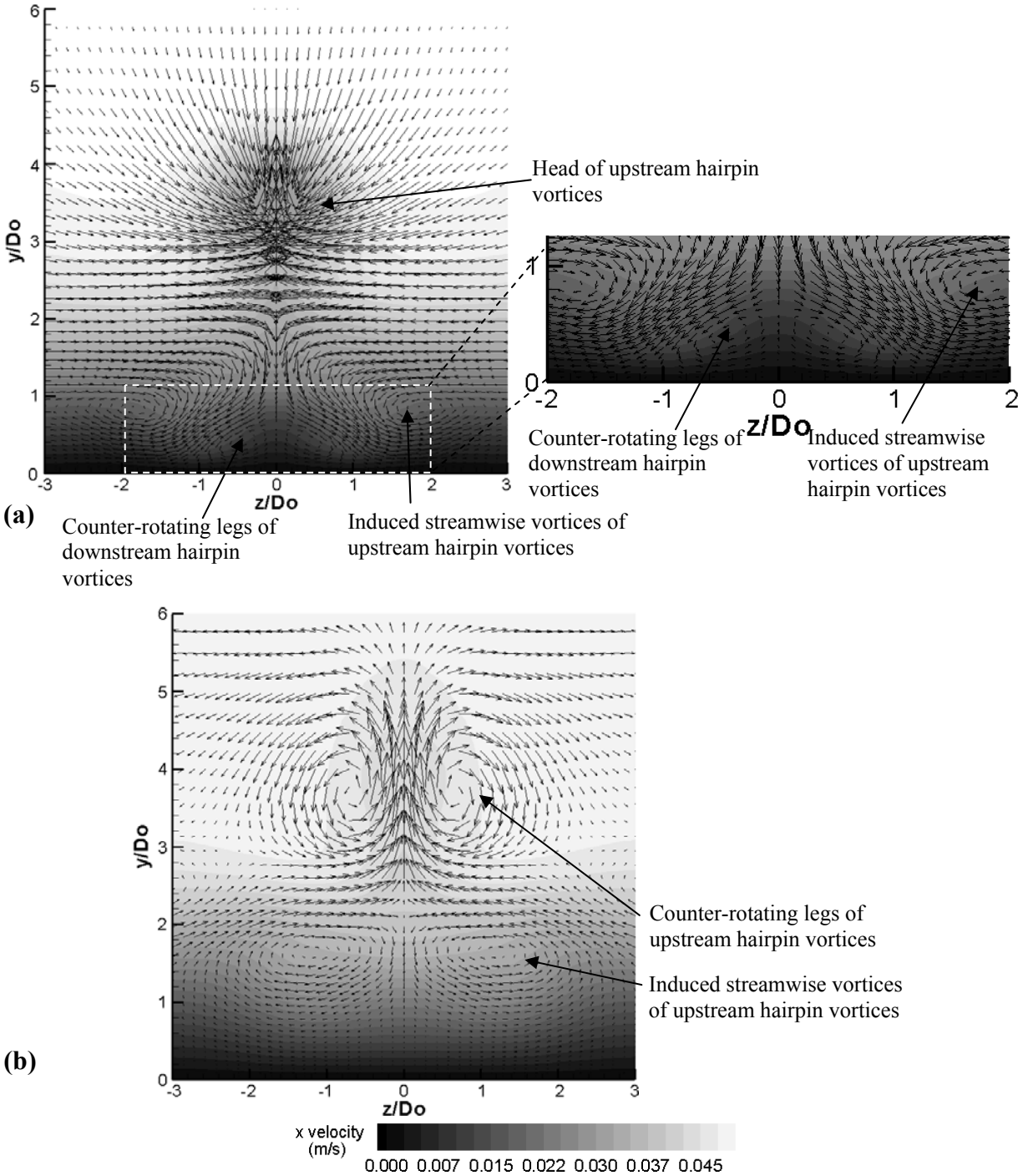

Figure 6.16. Velocity vector superimposed on streamwise velocity at (a) x/D_o = 10 and (b) x/D_o = 40 for the structures at VR = 0.32, L = 6.5.

the near-wall region and due to their further distance from the wall a weak plateau of high surface shear stress is produced.

Overall, it is found that the pattern of the surface shear stress produced by the synthetic jets is essentially determined by the position of the induced streamwise vortices relative to the vortical structures that induce them. In the cases where the

two-streak pattern is observed, the pair of induced streamwise vortices is separated by the legs of the downstream hairpin vortex. Therefore a downwash and a high local surface shear is produced between each induced streamwise vortex and the leg of the hairpin on the corresponding side (Figs. 6.12 and 6.16a). In the case where a single-streak pattern is observed, the pair of induced streamwise vortices is located directly underneath the vortical structures which induce them. As such, the pair of induced streamwise vortices is close to each other around the central plane producing a downwash hence a high surface shear there (Figs. 6.13 and 6.14a). When the induced streamwise vortices are weakened and eventually disappear (Fig. 6.14) or the relative position between the induced streamwise vortices and the main structures changes (Fig. 6.16), the surface shear stress pattern will alter accordingly.

6.4.3 Parameter Map of Vortical Structures and Patterns of Surface Shear Stress

In the previous two subsections, the effect of dimensionless stroke length and velocity ratio on the appearance of vortical structures and the distribution of surface shear stress produced by synthetic jets are studied. In order to illustrate the transformation of vortical structures of synthetic jets and their near-wall effect, the results from all the cases simulated in the present study are incorporated into three parameter spaces defined by different combinations of the dimensionless parameters.

The *VR*-*L* parameter map is shown in Fig. 6.17. The instantaneous coherent structures and patterns of time-averaged surface shear stress of these cases are inserted in Fig. 6.17 to aid the comparison. The lines of constant *Str* are also added which correspond to lines of constant diaphragm frequencies as the freestream velocity and the boundary layer thickness are fixed. According to the shape of the primary vortical structures, the *VR*-*L* parameter map can be divided into two regimes, i.e. the regime of hairpin vortices and that of tilted/distorted vortex rings (see Fig. 6.17). It is found that hairpin vortices tend to exist at lower *VR* (<0.32) or lower *L* (<1.6), since at these conditions the upstream branch of the initial vortex rings is either destroyed or weakened by the impact of the suction cycle and the shear in the boundary layer because of their proximity to the wall. In addition, a high *L* (>4) also results in the formation of secondary vortices since the excessive vorticity ejected during the blowing cycle cannot be contained in the primary vortex ring. The vortical

structures subsequently appear more distorted at large stroke lengths due to the mutual interaction between the primary and secondary structures.

The patterns of surface shear stress change accordingly as the nature of vortical structures produced by the synthetic jets varies (see Fig. 6.17). In general, hairpin vortices produce a pair of high shear stress streaks downstream of the jet orifice whereas the tilted vortex rings produce a single streak of high shear stress with an exception when the actuator frequency is high enough to cause the agglomeration of hairpin vortices. A transitional boundary which goes through all the cases exhibiting the transitional surface shear stress pattern and separates the one-streak and two-streak pattern of surface shear stress is shown as a dash line in the parameter space. Above the line, the tilted vortex ring type of vortices and the one-streak surface shear stress pattern are observed. Contrarily, below the line hairpin type of vortices and the two-streak surface shear stress pattern are seen. The transitional boundary in the *VR*-*L* parameter map is nearly a vertical line at *L* around 1.6 and it turns sharply into a horizontal line at $VR \approx 0.32$. The coherent structures and their surface shear stress patterns shown in Fig. 6.17 are similar to those observed by Jabbal and Zhong (2008). They also provided a parameter space marking the different vortical structures, classified as no vortex formation, hairpin vortices, stretched vortex rings and tilted and distorted vortex rings, for the parameter range $0.2 < Str < 0.8$, $0.04 < VR < 0.7$ and $0.8 < L < 5.1$. The boundary separating the stretched vortex rings and the tilted vortex rings in their parameter space is located between $0.3 < VR < 0.4$, which is similar to the boundary obtained from the simulations. In this paper, the stretched vortex rings are classified as hairpin vortex type structures as they both produce a two-streak surface shear stress pattern.

The *L*-*Str* parameter map is shown in Fig. 6.18 with lines of constant *VR* added to assist the interpretation of data. It can be seen that the location of transitional boundary correlated with $VR = 0.4$ closely for $Str < 1$. For $Str > 1$, the boundary deviates from the *VR* contour lines, approaching a horizontal line of $L = 1.6$. This deviation at higher *Str* is believed to be caused by the agglomeration of hairpin structures due to their close proximity to each other resulting the formation of the one-streak surface shear stress pattern at higher *VR*.

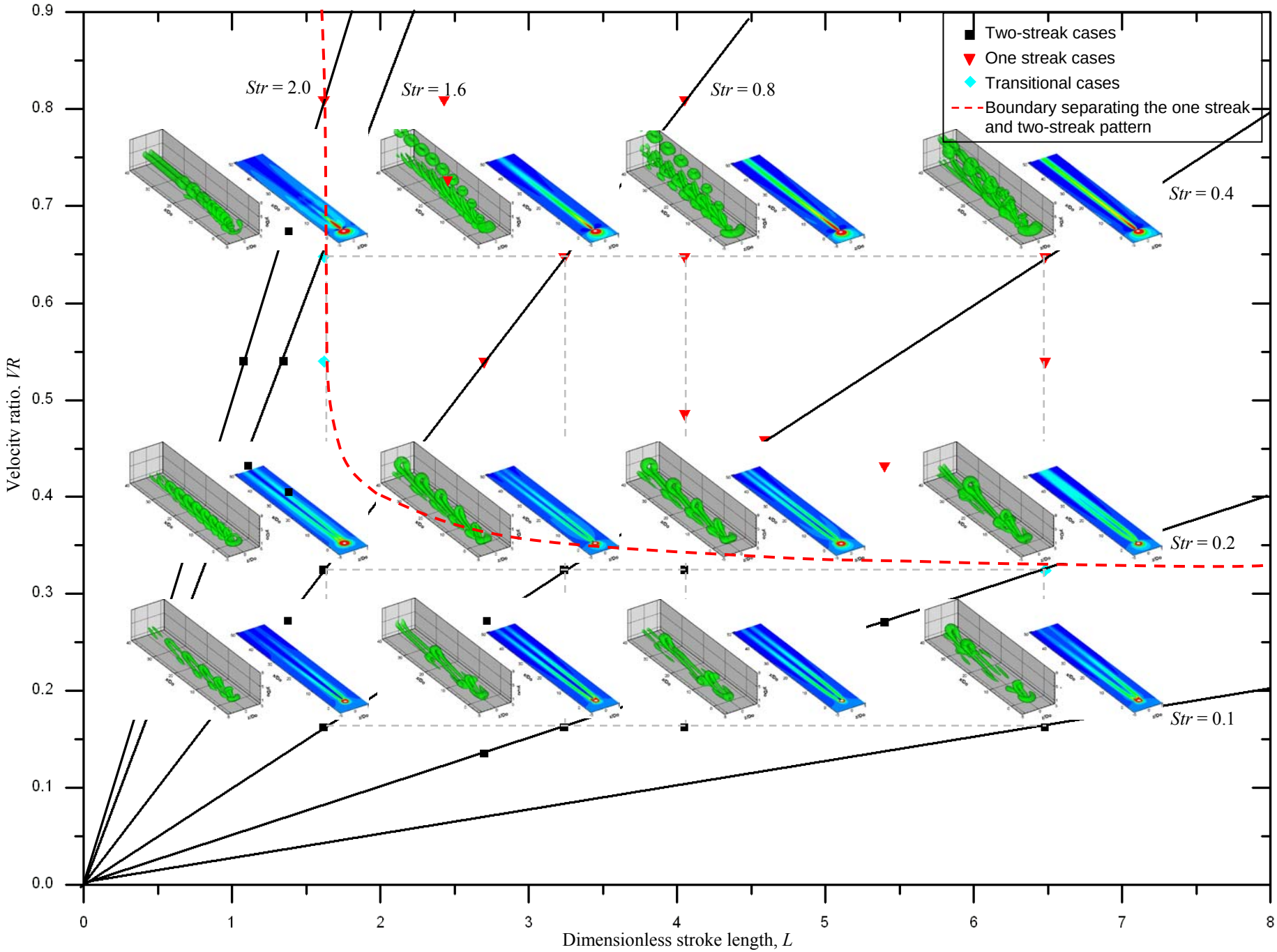

Figure 6.17. *VR-L* parameter map of different vortical structures and their corresponding time-averaged surface shear stress.

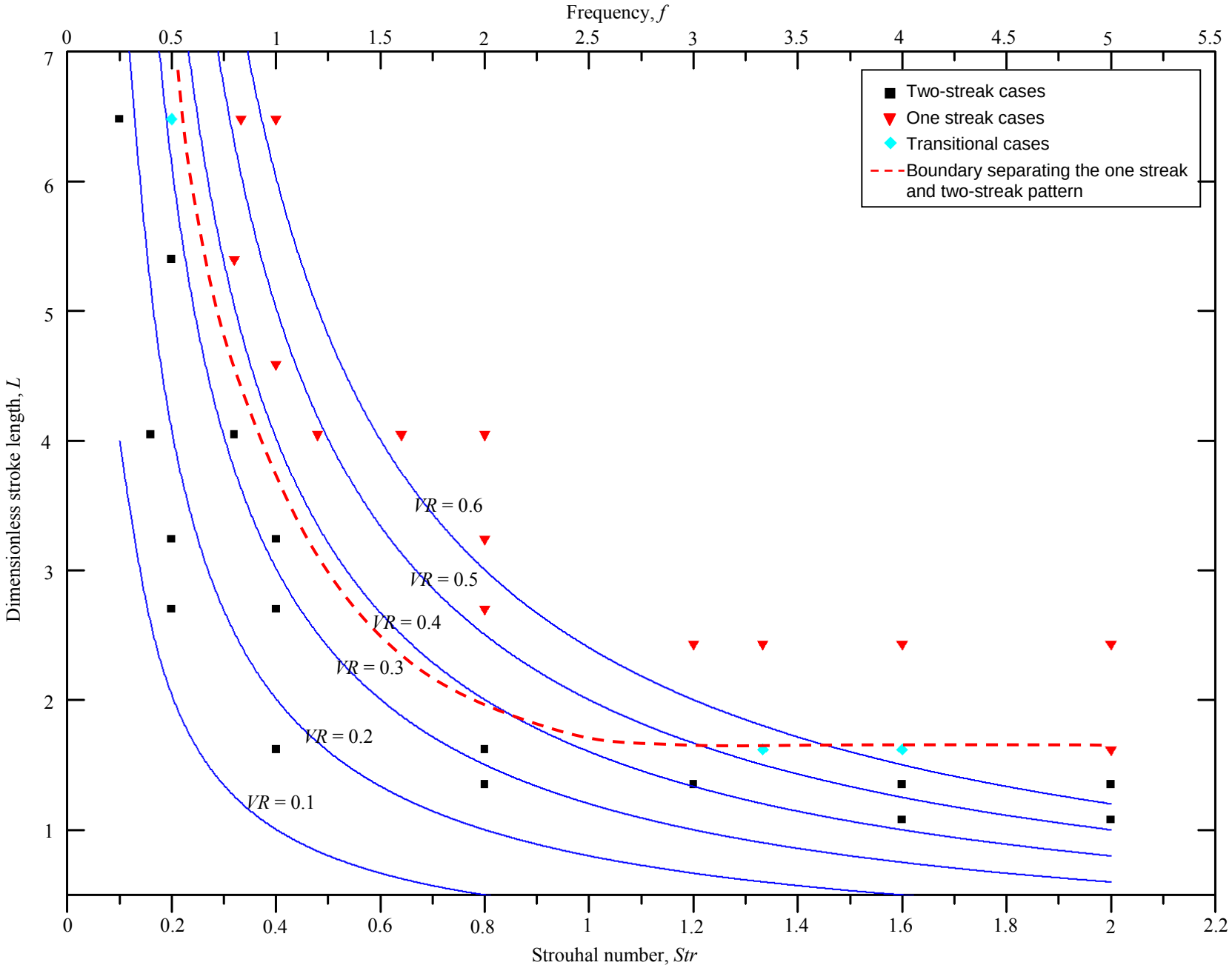

Figure 6.18. *L-Str* parameter map of different vortical structures and their corresponding time-averaged surface shear stress patterns.

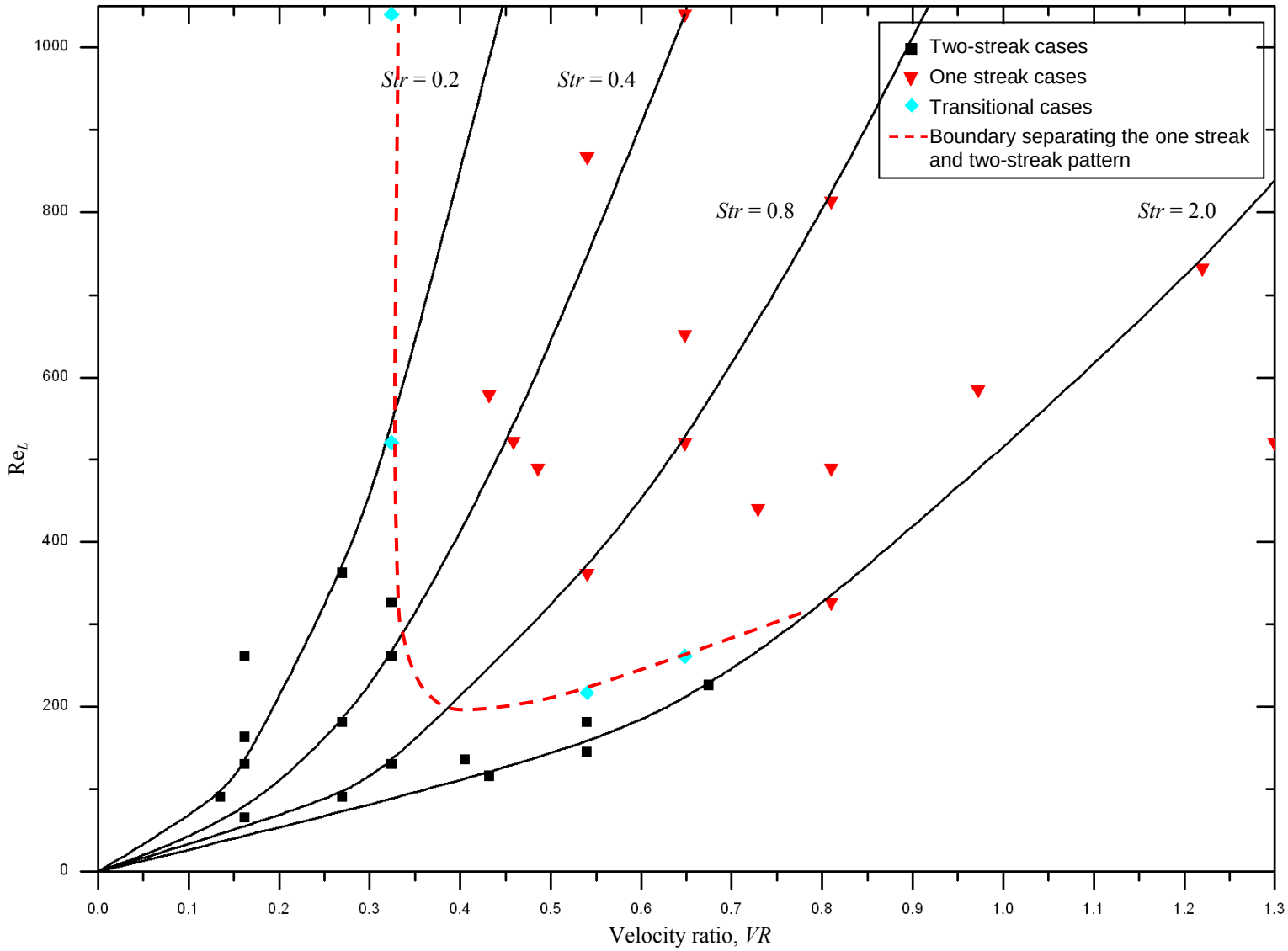

Figure 6.19. Re_L-*VR* parameter map of different vortical structures and their corresponding time-averaged surface shear stress patterns.

The Re_L-*VR* map (Fig. 6.19) seems to indicate that the hairpin vortices and the two-streak surface shear stress pattern can occur at a Reynolds number up to 1040. Therefore, the Reynolds number plays a less dominant role in determining the vortical structure type hence the pattern of surface shear stress for the range of parameters examined in the present study.

Based on Figs. 6.17 to 6.19, it can be concluded that the appearance of vortical structures and patterns of surface shear stress produced by the synthetic jets is mainly determined by *VR* for *Str* < 1, and by *L* for *Str* > 1. The knowledge gained from this study presents a considerable improved understanding of how the nature of the vortical structures and their associated surface shear stress patterns produced by the synthetic jets vary as the operating condition of the jet changes. For synthetic jets in a turbulent boundary layer, it is expected that the types of vortical structures would be similar to those observed in a laminar boundary layer. However, the operating conditions at which a specific type of vortices is generated are likely to shift. Jabbal (2008) suggested that the vortical structures issued into a turbulent boundary layer will need to be of higher stroke length and higher Reynolds number relative to those in a laminar boundary layer, in order to overcome the higher friction velocity and higher rate of viscous dissipation.

6.4.4 The Potential Impact of Vortical Structures Produced by Synthetic Jets

In the current study, in order to investigate the potential impact of the synthetic jets on the boundary layer, the increase in the space- and time-averaged skin friction coefficient relative to the baseline case without the synthetic jets is defined as

$$\Delta c_f = \frac{\tau_w - \tau_{ref}}{0.5\rho U_\infty^2} \tag{6.9}$$

Here τ_w is the magnitude of the time- and area-averaged surface shear stress, τ_{ref} is the magnitude of the time- and area-averaged surface shear stress for the baseline case, and ρ is the density of water. The area average is obtained for the area from $5D_o$ to $50D_o$ downstream of the orifice which extends to $10D_o$ on each side of the orifice centreline where τ_w is approaching its level in the baseline case.

It is seen that all the cases simulated in the present study produce an increase in the time- and space-averaged surface shear stress relative to the baseline case, i.e. $\Delta c_f > 0$ (see Fig. 6.20). Nevertheless, Δc_f remains to be low at $VR < 0.3$ due to a limited amount of momentum flux injected by the synthetic jet. A high Δc_f is achieved at $VR > 0.6$ except at $L < 2$ due to the relatively strong strength of the jet and a high momentum flux injection. In these cases, the distorted tilted vortex ring type structures are observed. Interestingly, a relative high Δc_f is also obtained in an isolated region with a medium VR between 0.3 and 0.55 and L around 2. In this region, the hairpin vortices are observed with spacing close to the local boundary layer thickness at the location of the jet orifice (Str around 1). It appears that a further increase in VR accompanied by a reduction in the spacing between consecutive hairpin vortices will adversely result in a decrease in Δc_f due to a strong mutual interaction between them. Furthermore, an increase in L while keeping the same VR also leads to a decrease in Δc_f due to an increase in the spacing between consecutive hairpins although each individual structure is stronger.

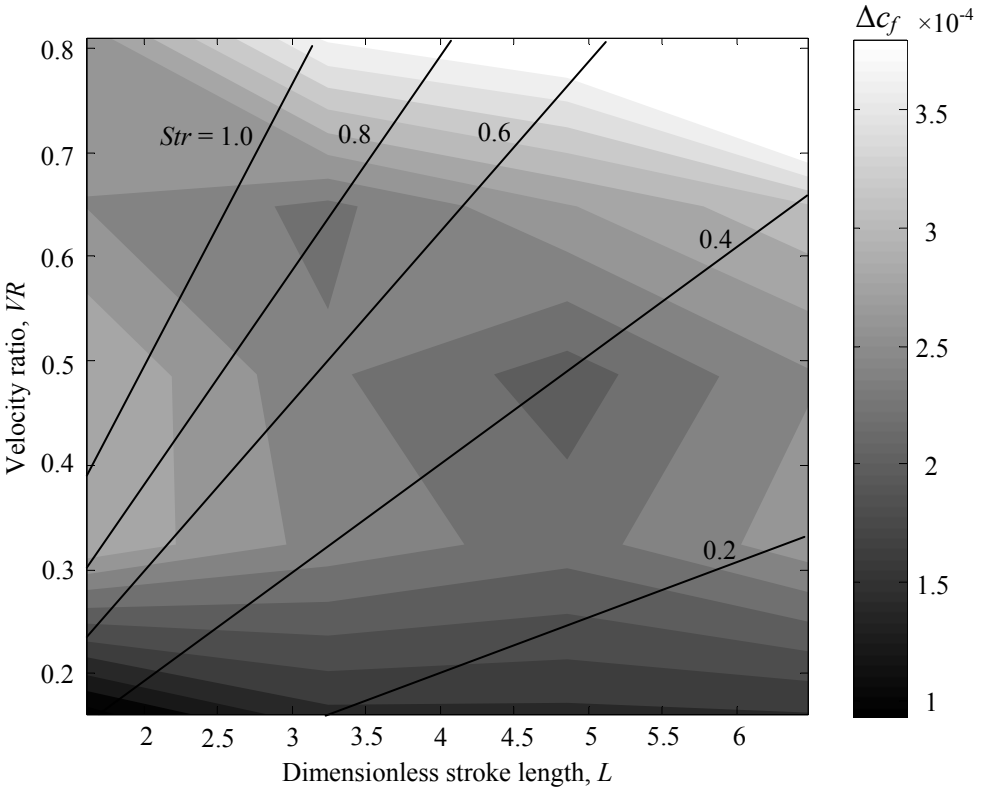

Figure 6.20. Map of the area- and time-averaged gains of skin friction coefficient, Δc_f.

In practical flow control applications, for a given external flow it would be desirable to operate the synthetic jets at a condition which yields the maximum flow separation delay with the least energy expenditure. In general, operating the synthetic jets at a high VR, particularly at a large L requires high energy input. Therefore the region with a medium VR between 0.3 and 0.55 and L around 2 is very attractive due to its relatively high near-wall impact and low energy requirement. Based on the results from the present study, it appears that in order to maximise the impact on the near-wall flow while keeping the energy expenditure down, it is wise to maximise the accumulated effect of hairpins by keeping the spacing between consecutive hairpin vortices similar to the local boundary layer thickness upstream of the separated flow instead of producing stronger individual structures. This hypothesis is supported by the experimental results from Zhang and Zhong (2009) who studied the flow control effectiveness of an array of three synthetic jets issued into a flat plat boundary layer which separates further downstream. The optimal operating condition of the synthetic jets found in their experiment is $L \approx 2$, $VR \approx 0.5$ and $Str \approx 1.6$ where relatively weak hairpin vortices with spacing around half of the local boundary layer thickness at the jet array are observed.

Further numerical studies of an array of synthetic jets issued into a boundary layer which separates further downstream have been undertaken by the authors. In these studies, the streamwise variations in the phase-averaged surface shear stress distributions across the span are examined and the flow control effectiveness in relation to the power consumption is addressed. These results will be presented in their follow-on publications.

6.5 Conclusions

In this paper, the results from 3D numerical simulations of circular synthetic jets issued into a zero-pressure-gradient laminar boundary layer developing along a flat plate are reported. The simulations are undertaken using FLUENT at a wide range of actuator operating conditions. The formation and development of these coherent structures were examined using the Q-criterion. Three non-dimensional parameter spaces were established to illustrate the variations in the appearance of these

resultant structures and their shear stress footprints upon the changes in the operating conditions of synthetic jets.

According to the shape of the primary vortical structures, the parameter map can be divided into two regimes, i.e. the regime of hairpin vortices and that of tilted/distorted vortex rings. Correspondingly, two distinct patterns of shear stress are produced by the vortical structures in the near-wall region. In general, hairpin vortices produce a pair of high shear stress streaks downstream of the jet orifice whereas the tilted/distorted vortex rings produce a single streak of high shear stress with an exception when the actuator frequency is high enough to cause the agglomeration of hairpin vortices. The location of transitional boundary correlated with $VR = 0.4$ closely for $Str < 1$. For $Str > 1$, the boundary deviates from the VR contour lines, approaching a horizontal line of $L = 1.6$.

In order to investigate the potential impact of the synthetic jets on the boundary layer, the increase in the space- and time-averaged skin friction coefficient relative to the baseline case without the synthetic jets is calculated. It appears that in order to maximise the impact on the near-wall flow while keeping the energy expenditure down, it is wise to maximise the accumulated effect of hairpin vortices by keeping the spacing between consecutive hairpin vortices similar to the local boundary layer thickness upstream of the separated flow instead of producing stronger individual structures.

Paper title:

A Numerical Investigation of the Interaction of an Array of Synthetic Jets with a Separated Laminar Boundary Layer

Authors:

Jue Zhou and Shan Zhong

Paper submitted to:

Computers and Fluids, 2010

Chapter 7 A Numerical Investigation of the Interaction of an Array of Synthetic Jets with a Separated Laminar Boundary Layer

Jue Zhou and Shan Zhong

School of Mechanical, Aerospace and Civil Engineering, University of Manchester, UK

Abstract

In this work, flow separation control using an array of three round synthetic jets issued into a zero-pressure-gradient laminar boundary layer that separates further downstream over an inclined plate is investigated using a 3D numerical simulation. The simulation results are validated using experimental data and a reasonable agreement is achieved. The simulations are undertaken at three synthetic jet operating conditions, i.e. Case A: L = 2, VR = 0.32; Case B: L = 4, VR = 0.64 and Case C: L = 5, VR = 0.81. Two distinct types of vortical structures, i.e. hairpin vortices (Case A) and tilted vortex rings (Case B and C), are generated by each synthetic jet. Case A exhibits two streaks of high surface shear stress downstream of each jet whereas Case B and C show only one streak of high surface shear stress downstream of each jet. These patterns of surface shear stress are observed in the zero-pressure-gradient boundary layer developing along the horizontal plate upstream to the inclined plate and they persist further downstream resulting in a wavy separation line in the separated flow region. The impact of the middle synthetic jet in the array on the boundary layer prior to separation is evaluated by examining the spatial variations of surface shear stress. It is found that Case A produces the largest space- and time-averaged surface shear stress, whereas Case C produces the highest local peak surface shear stress due to its high velocity ratio. The flow control effectiveness of the middle synthetic jet is also quantified by the size of the surface area over which the flow remains attached. Among the three cases tested here, Case A is found to be most effective as it produces a considerable flow separation delay and a smoother separation line while consuming less energy than the other two cases.

The finding from this study suggests that hairpin vortical structures produced at a relatively low *VR* are more desirable structures for effective flow control.

7.1 Introduction

Synthetic jet actuators (SJAs), as a promising method in delaying boundary layer separation on aircraft, have received much research attention in recent years (Smith and Glezer, 1998; Seifert et al, 2004; Zhong et al, 2007; Tang et al, 2007). They are capable of imparting momentum to the external flow through an array of orifices on the wall without requiring a compressed air supply. It has been demonstrated in many laboratory experiments that SJAs are capable of delaying or eliminating flow separation on circular cylinders (Crook and Wood, 2001; Glezer and Amitay, 2002; Tensi et al, 2002) and aerofoil models (McCormick, 2000; Amitay and Glezer, 2002; Amitay et al, 2001). It is believed that the streamwise-aligned vortices, produced by the interaction between synthetic jets and the boundary layer, entrain the fast, high-momentum fluid from the freestream to the near-wall region, and therefore result in the delay of flow separation.

Extensive experimental studies aimed at understanding the fluid mechanics of synthetic jets have been undertaken at Manchester University since 1998. It has led to an improved understanding of the structure of circular synthetic jets under quiescent conditions as well as the behaviour of a synthetic jet issued into a uniform cross-flow and a boundary layer (Zhong et al, 2005; Jabbal and Zhong, 2008; Crook, 2002; Garcillan et al, 2005) The dye visualization of synthetic jets issued into a laminar boundary layer by Zhong et al. (2005) showed, for the first time, that depending on magnitudes of the dimensionless stroke length and the jet-to-freestream velocity ratios the vortical structures produced by synthetic jets may take different shapes. As the dimensionless jet stroke length and the jet-to-freestream velocity ratio increase, these vortical structures first appear as hairpin-like vortices that are attached to the wall, then as stretched vortex rings that gradually move towards the edge of the boundary layer, and finally as tilted vortex rings that emerge out of the boundary layer shortly downstream. Using temperature-sensitive liquid crystal surface coating, Jabbal and Zhong (2008) found that both the hairpin and stretched vortex ring type structures produce a longitudinal streak of high wall shear

stress downstream of each side of the orifice, whereas the tilted vortex ring type structures produce a single longitudinal streak directly downstream of the orifice.

Numerical simulations of synthetic jets issued into a laminar boundary layer have been undertaken in a complementary manner in parallel with the ongoing experiments at Manchester. Once validated with the existing experimental data, the three-dimensional data produced by the simulations, which are often not available from the experiments, can be used to provide a further insight into the nature of vortical structures produced by the synthetic jets. Using numerical simulations in FLUENT, Zhou and Zhong (2009) reproduced the primary structures observed by Jabbal and Zhong in their experiment (Jabbal and Zhong, 2008). Based on their simulation results, a credible explanation of the two different patterns of wall shear stress observed in the experiment is provided. Furthermore, a series of non-dimensional parameter spaces were established to illustrate the evolution of these resultant structures and their shear stress footprints upon the changes in the operating conditions of synthetic jets. An evaluation of the impact of the synthetic jets on the boundary layer measured by the increase in the space- and time-averaged skin friction coefficient relative to the jet-off case is also made (Zhou and Zhong, 2010a).

More recently, Zhang and Zhong (2010a) conducted an experimental investigation of flow separation control using an array of three round synthetic jets issued into a laminar flow that separates further downstream on an inclined plate in a water channel. In the experiment, PIV data obtained on a plane parallel to the inclined plate near its surface are used to evaluate the flow control effect. The objectives of the complementary numerical simulation reported in this paper are two-fold; a). to investigate the nature of the vortical structures and surface shear stress patterns produced by the synthetic jets prior to separation; b) to examine how the extent of separation delay is related to the impact of the synthetic jets on the boundary layer prior to separation. The availability of the surface shear stress information from the simulation is expected to provide further insight of the interaction of synthetic jets with a boundary layer for the purpose of identifying the desired synthetic jet actuator conditions for flow control.

In order to simplify the measurements and computations, the present study was undertaken in a laminar boundary layer. However, it is believed that some commonalities exist in the interaction mechanisms between synthetic jets and a boundary layer no matter it is laminar or turbulent. Firstly, the basic effect of shear

in a boundary layer and the effect of suction cycle on the formation of coherent structures produced by synthetic jets in the boundary layer are similar regardless of whether the boundary layer is laminar or turbulent. Secondly, the entrainment brought about by the coherent vortices produced by the synthetic jets is an important flow separation mechanism in both flows. In the authors' opinion, understanding the behaviour of synthetic jets in a laminar flow is the first logical step towards understanding the complex behaviour of synthetic jets in a turbulent flow, and the finding from this work could shed some light on the design of synthetic jet actuators for flow control at practical settings.

7.2 Experimental and Computational Methods

7.2.1 Experimental Methods

In this study, synthetic jet array used in the simulation is identical to that used in the experiment (Zhang and Zhong, 2010a). The actuator consists of a cylindrical cavity with a diameter D_c = 45 mm and height H = 12 mm, and an orifice plate and an oscillating diaphragm (Fig. 7.1). The three parallel circular orifices on the orifice plate have a diameter D_o = 2 mm and depth h = 3 mm and they are spaced 12 mm ($6D_o$) apart. The thin rubber diaphragm, which is sandwiched between two metal disks, is clamped circumferentially to the end of the cylindrical cavity and the centre of the diaphragm is attached to a permanent magnetic shaker via a steel rod. The diaphragm is made to oscillate in a sinusoidal manner at predetermined diaphragm oscillation displacements and frequencies. With this arrangement, the diaphragm mimics a piston-like motion.

The experiments are conducted in a tilting water flume with a cross-section of 0.3 m×0.3 m. Figure 7.2 shows the sketch of the test plate and its coordinate system. The test plate consists of three 10 mm thick aluminium flat plates with the same width which are connected with each other sequentially using hinges. The test surface faces downwards to allow the synthetic jet actuator to be mounted above the free surface of water. The most upstream plate is 530 mm in length with an elliptical leading edge. It is mounted horizontally across the whole width of the test section. The middle plate is 200 mm in length and it is inclined 5˚ upwards relative to the horizontal plane. The boundary layer developing along the horizontal plate will

separate at about 40 mm ($20D_o$) downstream of the start of the inclined plate based on the dye flow visualization, creating a separated boundary layer to which flow control with synthetic jets can be applied. Finally, a 150 mm long plate is attached to the end of the inclined plate. The incidence angle of this plate can be altered to ensure that the flow is attached at the leading edge of the horizontal plate.

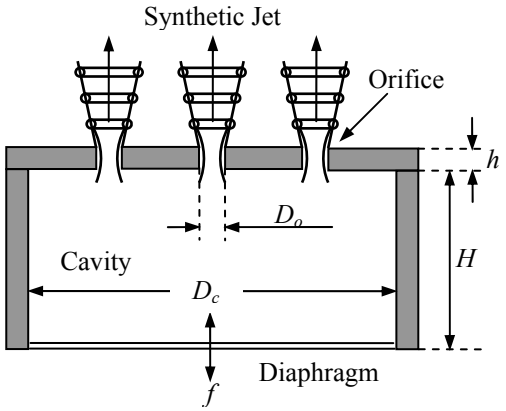

Figure 7.1. A schematic of the synthetic jet actuator.

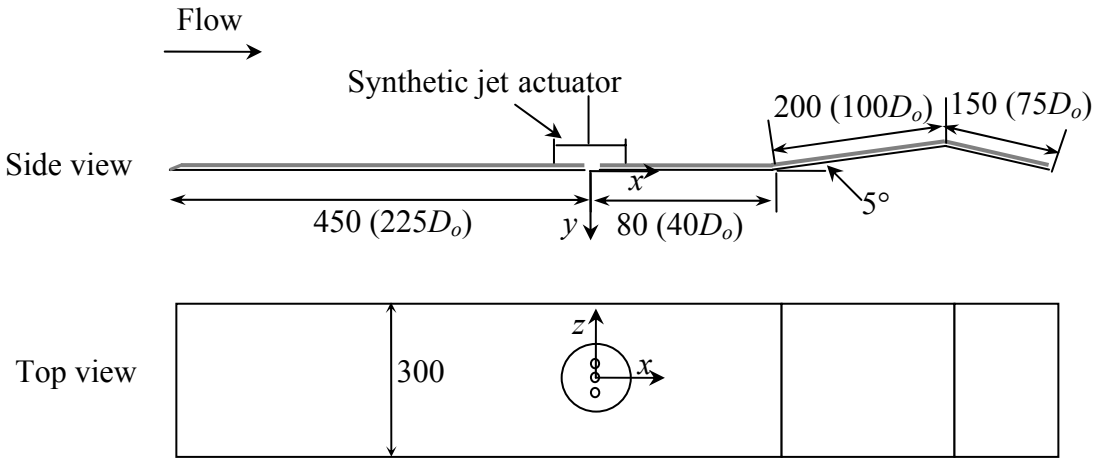

Figure 7.2. A schematic of the experimental setup (all dimensions are in mm, D_o = 2 mm).

The array of synthetic jets is located 450 mm downstream of the leading edge of the horizontal plate. The distance between the centres of orifices and the start of the flap is 80 mm ($40D_o$). The freestream velocity in the experiment is fixed at 0.1 m/s, and the local boundary layer thickness at the location of the orifices is 10 mm ($5D_o$) approximately.

To provide the information of three-dimensional interaction of the synthetic jet array with the separated boundary layer, PIV measurements were undertaken on a plane parallel to the inclined plate at a distance of 1.5 mm below the surface. The time-averaged velocity field of the separated flow is obtained in an area of 160 mm×160 mm with a spatial resolution of 2.5 mm in both streamwise and spanwise directions. In addition, to reveal the characteristics of the vortical structures produced by the synthetic jets which are responsible for the separation delay, phase-averaged PIV images were also taken on the streamwise central plane of the middle orifice at 20 equally-spaced phases during one actuation cycle.

7.2.2 Synthetic Jet Operating Conditions

The dimensional analysis carried out by Jabbal and Zhong (2008) reveals that the behaviour of synthetic jets in a given laminar boundary layer is determined by three key non-dimensional parameters, i.e. the jet-to-freestream velocity ratio *VR*, dimensional stroke length *L*, Reynolds number based on the stroke length Re_L.

The jet-to-freestream velocity ratio is defined as

$$VR = \frac{\overline{U}_o}{U_\infty} \tag{7.1}$$

where U_∞ is the freestream velocity, and $\overline{U}_o$ is the time-averaged blowing velocity over the entire cycle.

$$\overline{U}_o = \frac{1}{T}\int_0^{T/2} \tilde{u}_o(t)dt \tag{7.2}$$

where $\tilde{u}_o(t)$ is the instantaneous spatial-averaged velocity at the orifice exit and *T* is the period of the actuation cycle. For the present synthetic jet actuator, the diaphragm undergoes a piston-like motion and the flow is incompressible. It can be proved that the time-averaged blowing velocity over the entire cycle of each jet in the jet array is given by

$$\overline{U}_o = \frac{1}{3}\Delta f\left(\frac{D_c}{D_o}\right)^2 \tag{7.3}$$

where Δ is the peak-to-peak displacement of the diaphragm and *f* is the diaphragm oscillation frequency in Hertz, $f = 1/T$. The dimensional stroke length is defined as

$$L = \frac{L_o}{D_o} = \frac{\overline{U}_o}{fD_o} \tag{7.4}$$

where L_o is the stroke length, which, according to the slug model (Smith and Glezer, 1998), represents the length of the fluid column expelled during the blowing stroke. Finally, the Reynolds number is defined as

$$\mathrm{Re}_L = \frac{\overline{U}_o L_o}{\nu} \tag{7.5}$$

In the present study, the flow characteristics of the synthetic jets are varied by changing the diaphragm oscillation displacements and frequencies. Three cases are selected in which the diaphragm oscillation frequency is fixed at 8 Hz whereas the diaphragm peak-to-peak displacements are varied, Case A: $L = 2$, $VR = 0.32$; Case B: $L = 4$, $VR = 0.64$ and Case C: $L = 5$, $VR = 0.81$. The actuator operating conditions and non-dimensional parameters are listed in Table 7.1. These three cases are chosen such that typical hairpin vortices are obtained in Case A whereas weak tilted vortex ring type of structures are observed in Case B and strong tilted vortex ring type of structures occur in Case C. The choice of the settings in Case C also ensures that the synthetic jets remain to be laminar such that the use of the laminar flow model in the simulation is valid.

Table 7.1 Operating conditions and dimensionless parameters of three test cases

Case	f (Hz)	Δ (mm)	VR	L	Re_L
A (Hairpin vortices)	8	0.023	0.32	2	127
B (Tilted vortex rings)	8	0.047	0.64	4	508
C (Tilted vortex rings)	8	0.059	0.81	5	796

7.2.3 Computational Methods

7.2.3.1 The Numerical Solver

3D unsteady incompressible flow simulations are performed using the commercial CFD software, FLUENT 6.3. The laminar equations are solved as the Reynolds number of the synthetic jet in the current study is much lower than the critical value above which the jet becomes turbulent (Glezer, 1988). The second-order implicit scheme is selected for the unsteady formulation. The pressure and velocity are coupled using the Pressure-Implicit with the Splitting of Operators (PISO) algorithm. The second-order scheme and second-order upwind scheme are selected for pressure discretization and momentum discretization, respectively.

7.2.3.2 Geometry and Boundary Conditions

The computational geometry and boundary conditions used in the current study are shown in Fig. 7.3a. The inlet of the flow domain is located 20 mm ($10D_o$) upstream of the centres of the orifices. The outlet is set at the end of the final plate which is 430 mm ($215D_o$) downstream of the orifices. The height of the computational domain is 70 mm ($35D_o$) above the horizontal plate. Since the flow field is expected to be symmetric relative to the central plane of the middle orifice, only a half of the flow field is modelled in order to save the computation time.

To assist the choice of the domain width, a comparison of the spanwise distributions of time-averaged surface shear stress using three different domain widths (z/D_o = 16, 21 and 26) for Case A is made at two streamwise positions (x/D_o = 5 and 40). It is found that these distributions are nearly identical for $z/D_o < 10$ with a maximum difference of less than 1 % at both streamwise positions (Fig. 7.4). Although the difference increases towards the side boundary of the domain, since our study is focused on the central synthetic jet which is more representative of a jet in an array, a domain width of $21D_o$ is chosen as a compromise of computational time and accuracy.

The flow inlet condition is specified using the Blasius velocity profile. The flow at the top surface of the domain (y/D_o = 35) is not at a constant freestream condition due to the presence of the inclined plate and the final plate. In order to improve the accuracy of the boundary condition, this velocity distribution is obtained from a separate simulation of a 2D laminar flow which includes the bottom wall of the test section of the water tunnel. The pressure outlet condition is applied at the outlet of the flow domain assuming that a static (gauge) pressure at the outlet is zero, which is same as that at the inlet. All other flow quantities at the pressure outlet are extrapolated from the interior. The symmetric boundary condition is used on the streamwise plane bisecting the middle orifice since the flow domain is symmetric relative to that surface. The side boundary parallel to the streamwise central surface is also set as symmetry since this boundary is located far enough from the orifices such that the flow does not change in the spanwise direction.

Both the cavity and orifice are included in the simulation, and a velocity boundary condition is applied at the neutral position of the diaphragm. The

instantaneous displacement of the oscillating diaphragm $\delta(t)$ relative to its neutral position is given by:

$$\delta(t) = \frac{\Delta}{2}\sin(2\pi ft) \tag{7.6}$$

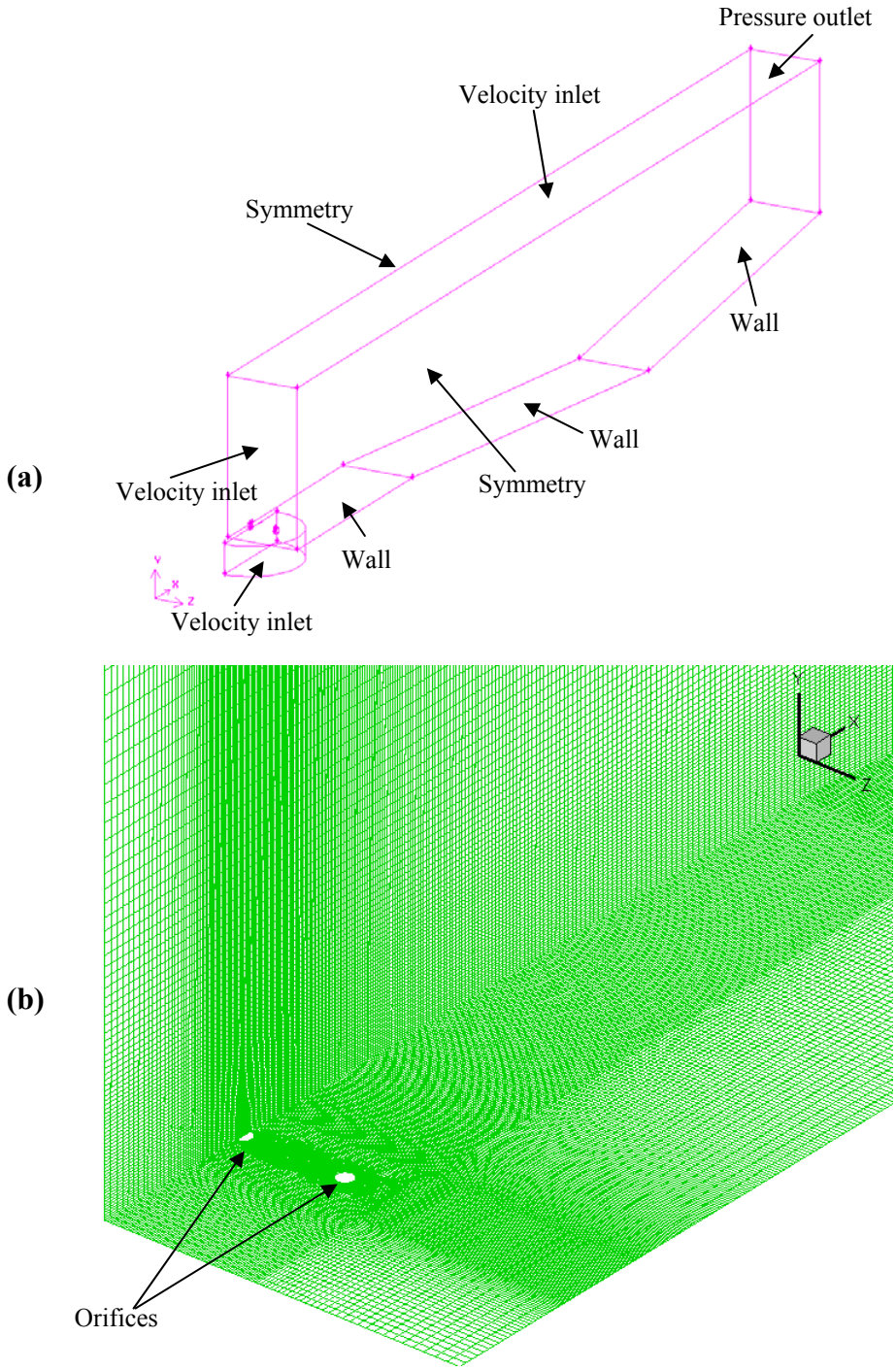

Figure 7.3. (a) The geometry and boundary conditions of numerical simulation, (b) medium grid in the orifice region.

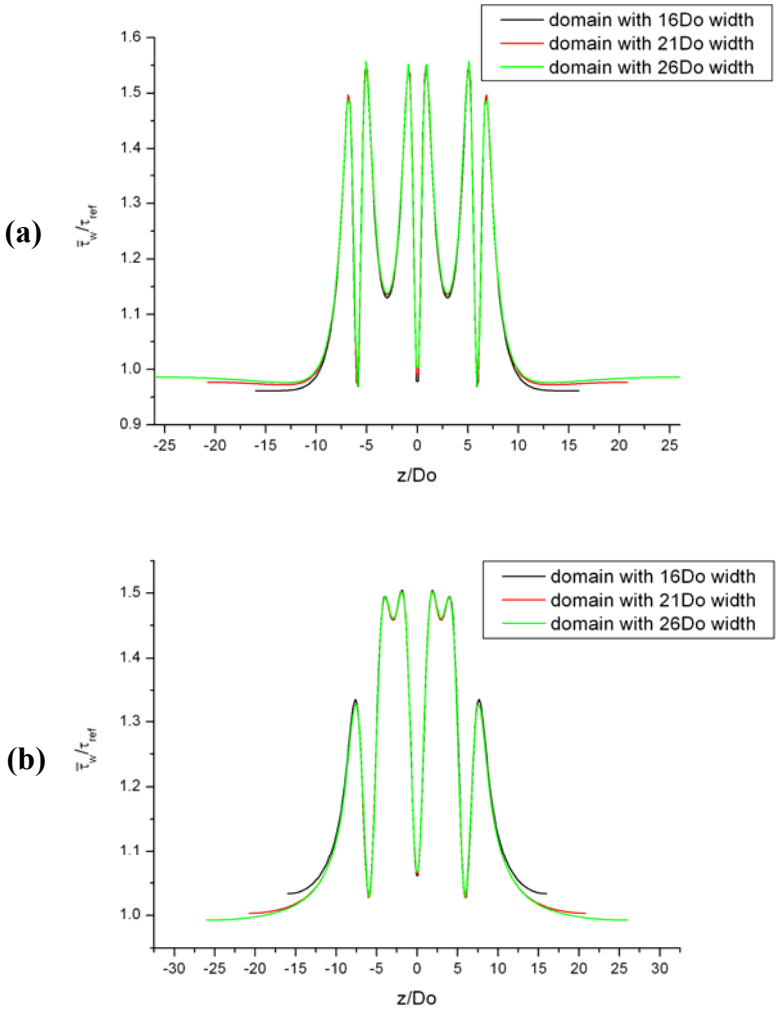

Figure 7.4. A comparison of the time-averaged surface shear stress using different domain widths of Case A at (a) x/D_o = 5 and (b) x/D_o = 40.

The moving velocity of the diaphragm can be obtained by differentiating Eq. 7.6 with respect to time,

$$v(t) = \pi \Delta f \cos(2\pi f t) \tag{7.7}$$

The velocity boundary condition is specified using user-defined functions (UDFs) supported by FLUENT.

7.2.3.3 Sensitivity Study of Mesh Size and Time Step Size

To assist the selection of the mesh size and time step size, a sensitivity study has been undertaken using three different mesh sizes and time step sizes. The mesh size of all the test cases is listed in Table 7.2. Finer meshes are generated in the orifice, boundary layer, and the region of $z/D_o < 9$ to obtain a high spatial resolution. Figure 7.3b illustrates the typical medium mesh used in the simulation. The spanwise

distribution of the time-averaged surface shear stress at x/D_o = 40 in Case A is examined. As shown in Fig. 7.5a, the results using the medium mesh are reasonably close to those using the fine mesh with a maximum difference of 2.2 % at z/D_o = 0.95, whereas the results using the coarse mesh exhibit a difference of 5.6 %. Therefore, as a compromise of the computational accuracy and time, the medium mesh is chosen for the current study.

Table 7.2 Mesh numbers used in the mesh density sensitivity study

Mesh designation	Coarse	Medium	Fine
Cavity	112×100×32	142×130×40	172×156×48
Orifice	10×16×10	12×20×12	16×24×15
Out flow domain	358×81×60	448×102×75	498×116×90
Total mesh	1,937,812	3,818,215	6,206,790

Similarly, Fig. 7.5b shows a comparison of the surface shear stress for the three test cases with a time step size of $T/60$, $T/120$ and $T/240$. The difference between these results is very small, confirming that the choice of $T/120$ is reasonable.

7.2.3.4 Validation of Computational Results

The capability of FLUENT in simulating the baseline flow without the actuation of synthetic jets and the interaction of a single synthetic jet issued from a 5mm diameter orifice with a laminar boundary layer has been validated using experimental data by Zhou and Zhong (2009). Here, the simulation results of an array of three 2mm diameter synthetic jets issued upstream to a laminar boundary layer which separates further downstream are compared with the existing experimental results.

The simulation is started with the baseline case without the actuation of synthetic jets. The velocity profiles along the centreline at a distance of 5, 15 and $25D_o$ downstream of the synthetic jet array are compared, as shown in Fig. 7.6. It can be seen that the velocity profiles from the numerical simulation are very close to that from the experiment indicating that FLUENT is capable to model the upstream flow prior to separation of the baseline case. According to the image of dye which is injected upstream to the separation line on the central plane of the flap, the baseline flow separates at about $60D_o$ downstream of the synthetic jet array or $20D_o$

downstream of the start of the flap as shown in Fig. 7.7a. Based on the distribution of the streamwise velocity from the simulation, the reverse flow occurs at $19.5D_o$ downstream of the flap as shown in Fig. 7.7b, which is very close to that found in the dye visualisation experiment, The separation line extracted from the PIV data obtained over the flap is located further downstream than that indicated by the dye, around $65D_o$ downstream of the start of the jets (Fig. 7.7c). On the other hand, the location of the separation line revealed by the contour of time-averaged streamwise velocity on the spanwise plane parallel to the flap, where the centre of the laser sheet located, is about $70D_o$ downstream of the jets (Fig. 7.7d). Consider the finite thickness of the laser sheet and the difficulty in measuring the precise location of the laser sheet, the slight difference between the measured and computed locations of separation line is acceptable.

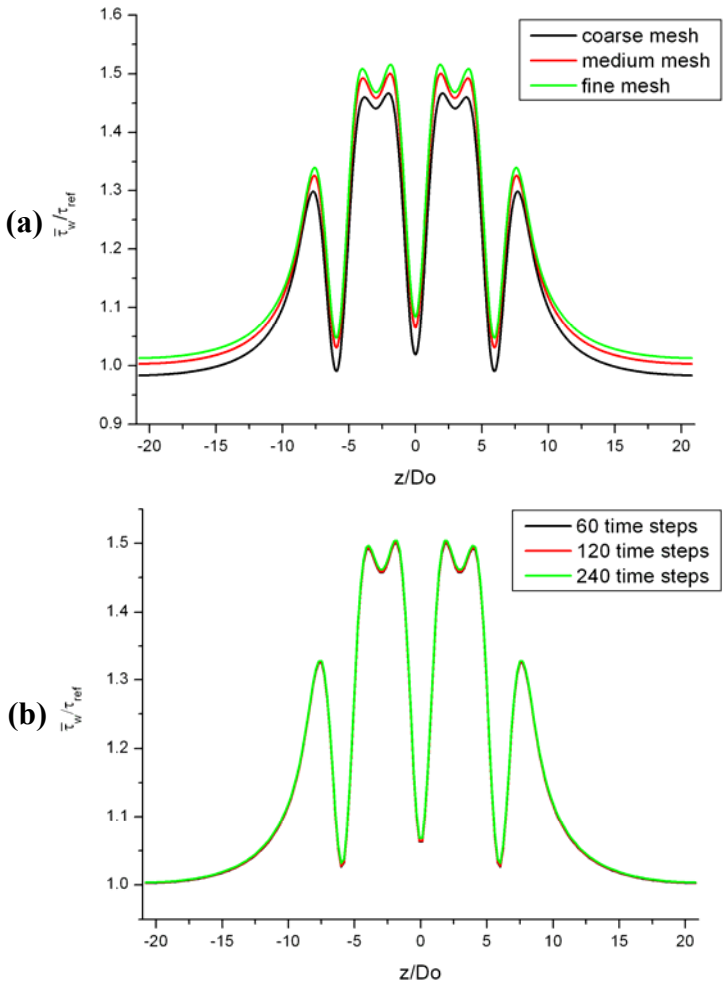

Figure 7.5. A comparison of the time-averaged surface shear stress of Case A at x/D_o = 40 using (a) different mesh sizes and (b) different time steps per cycle.

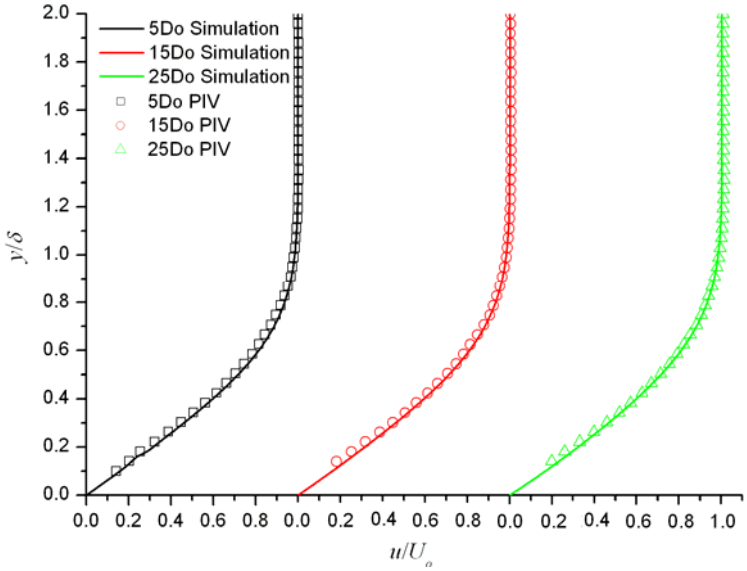

Figure 7.6. A comparison of boundary layer velocity profiles of the baseline flow at 5, 15 and 25D_o downstream of the synthetic jet array.

In the simulation, the synthetic jets are activated when the baseline flow converges. The solution is then allowed to evolve through a sufficient number of actuation cycles until the flow field exhibits a stable periodic characteristic. The process of convergence is monitored at two points on the central plane at x/D_o = 60 where the flow separation starts at baseline flow: point 1 is in the boundary layer (y/D_o = -0.75) and point 2 is in the freestream (y/D_o = 7.5). Figure 7.8 shows the variation of streamwise velocity with the number of iterations for Case A at these two points. It is evident that after a certain number of iterations, the streamwise velocity at these two points exhibits a periodicity.

After the simulation achieves a stable periodic condition, one more actuation cycle is computed to yield the time- and phase-averaged values of flow variables. Figure 7.9 shows the contours of the computed and measured instantaneous spanwise vorticity on the streamwise central plane of the middle jet in Case A and B. The comparison for Case C is not made here as PIV data on the streamwise central plane of the middle jet are not available. In Case A, it can be seen from the computed results that the boundary layer (y/D_o < 5) is being periodically disturbed by the presence of successive vortical structures embedded in it (See Fig. 7.9a). The pair of positive and negative spanwise vorticity in the newly formed vortex ring can be seen clearly near the orifice exit. The upstream branch of the ring with the positive vorticity disappears shortly as the positive vorticity is cancelled by the negative

vorticity resident in the boundary layer. On the other hand, the remaining downstream branch with the negative spanwise vorticity persists downstream and appears to be increasingly stretched in the streamwise direction. The above description of the spanwise vorticity field matches well with what is expected from typical hairpin vortex type of structures (Zhou and Zhong, 2009).

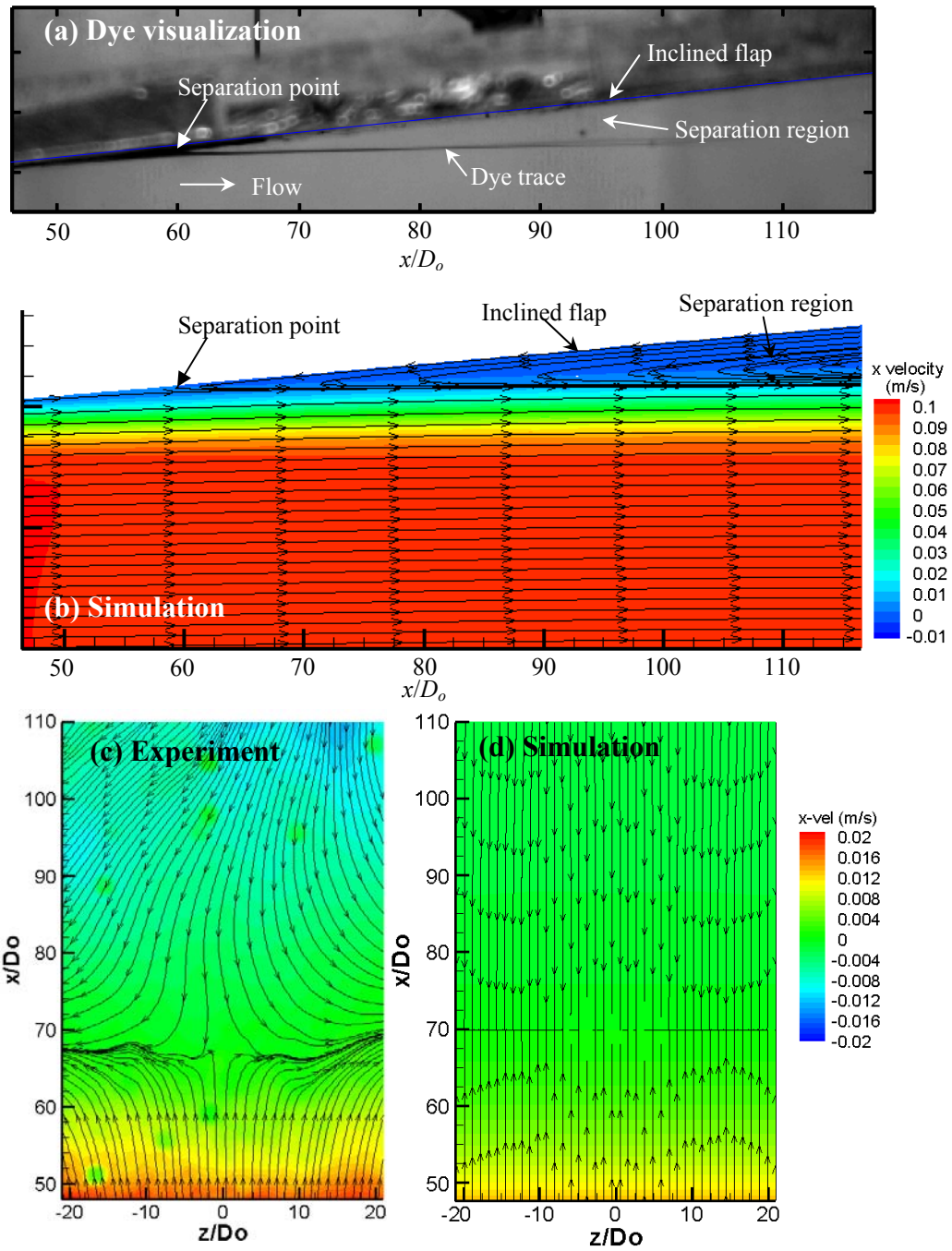

Figure 7.7. Flow separation on the flap for the baseline case: (a) dye visualization of the flow separation; (b) streamwise velocity contour and streamlines on the central plane from the simulation; streamwise velocity contour and streamlines on a plane parallel to the flap from (c) the experiment and (d) the simulation.

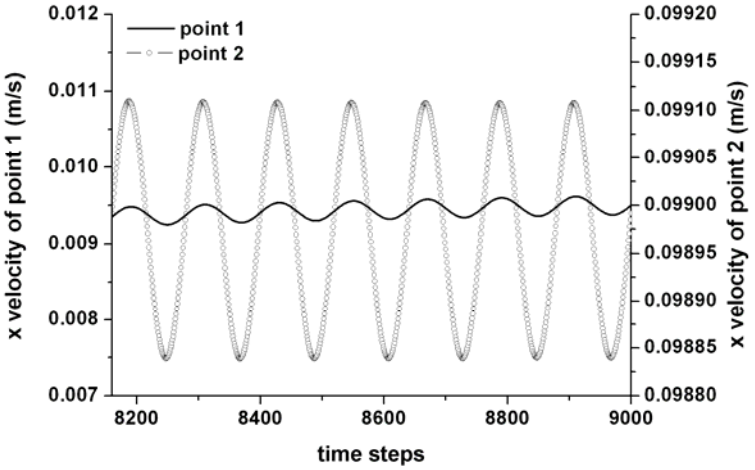

Figure 7.8. Variations of the streamwise velocities with the number of time steps for Case A at the two monitor points.

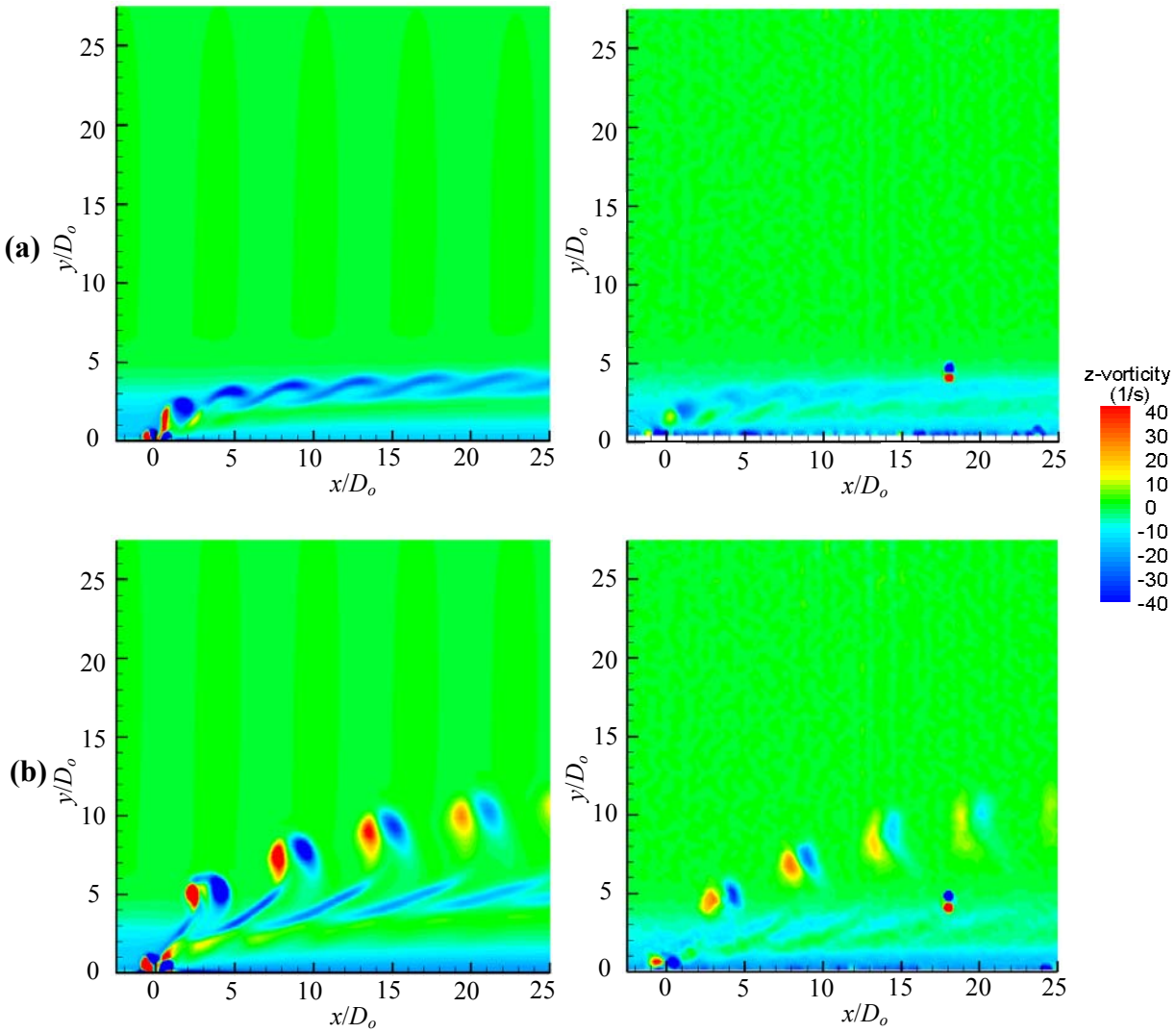

Figure 7.9. A comparison of the instantaneous spanwise vorticity on the central plane of the middle jet at t/T = 1/4 (a) Case A and (b) Case B.

In Case B, the vortical structures generated by the synthetic jets are much stronger (see Fig. 7.9b). The pairs of negative and positive vorticity associated with the downstream and the upstream branches of the vortex rings remain distinct after x/D_o > 20 and they emerge out of the boundary layer within a short distance downstream of the orifice. The elongated patch of negative spanwise vorticity behind each vortex pair is believed to be associated with the trailing legs of the primary ring, which exhibits a certain degree of spanwise vorticity. The spanwise vorticity field observed in this case matches well with what is expected from typical tilted vortex ring type of structures (Zhou and Zhong, 2009). In comparison, the computed results for Case A and B are in qualitative agreement with the PIV data despite that the strength of the vortical structures extracted from the experiment is generally weaker. Furthermore, the comparison between the computed and measured jet trajectory based on the maximum spanwise vorticity on the central plane indicates that the agreement for Case A and B is excellent (Fig. 7.10).

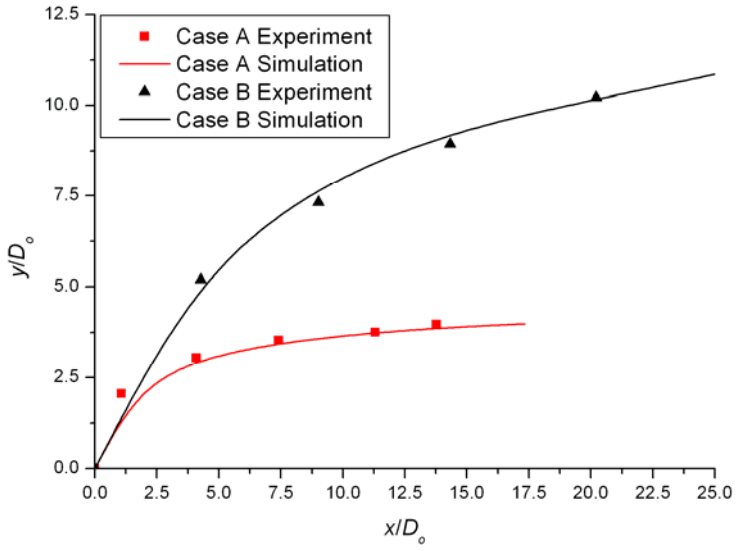

Figure 7.10. A comparison of the jet trajectory on the central plane of the middle jet.

The computed time-averaged velocity profiles on the central plane of the middle jet at x/D_o = 5, 15 and 25 for Case A and B are shown in Fig. 7.11. It can be seen that although the measured and computed velocity profiles exhibit a similar trend at all the locations, the measured velocity profiles exhibit much less variations across the boundary layer.

(a) Case A

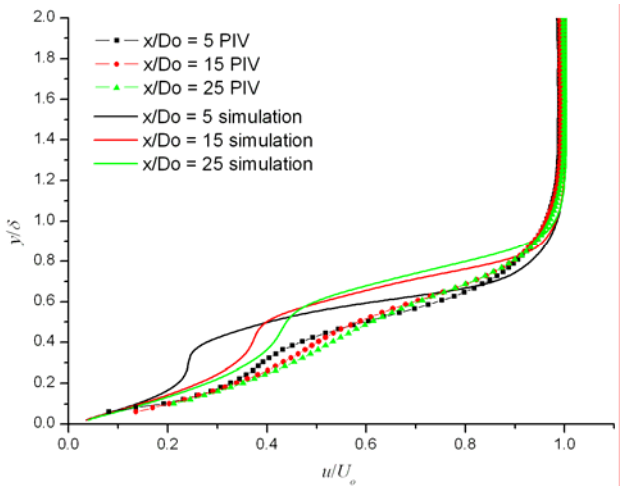

(b) Case B

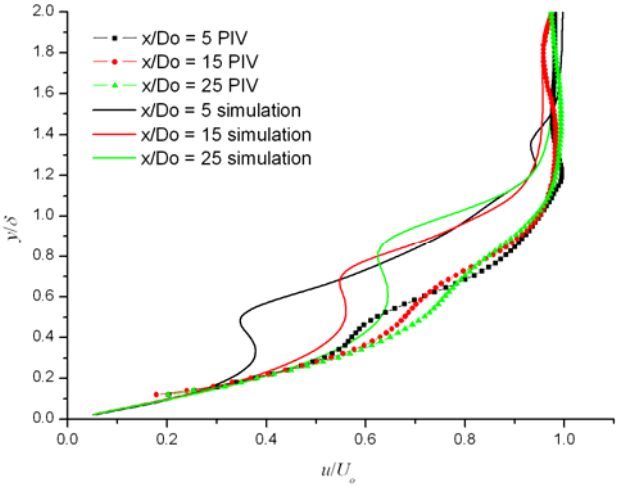

Figure 7.11. A comparison of time-averaged velocity profiles on the central plane of the middle jet at (a) Case A and (b) Case B.

The contours of time-averaged streamwise velocities on the spanwise plane where the PIV measurements were taken over the flap are also compared as shown in Fig. 7.12. For Case A, two strong high velocity streaks appear at the spanwise locations mid way between the consecutive orifices (around $z/D_o = \pm 3$). Two weaker streaks are also observed at around $z/D_o = \pm 9$. A qualitative agreement between the computed and measured results is obtained in terms of the number and the location of the high velocity streaks (see Fig. 7.12a). For Case B, three strong high velocity streaks can be observed directly downstream of each jet orifice from the computed results. However, due to the weak nature of vortical structures in Case B, the flow separation delay is not obvious and the high velocity streaks are not well defined from the PIV data (see Fig. 7.12b). For Case C, again three strong high velocity streaks can be observed directly downstream of each jet orifice from the computed results. Although less distinct in the PIV data, a noticeable flow separation delay can

be seen and three high velocity streaks also appear at the same locations in the measured results (see Fig. 7.12c).

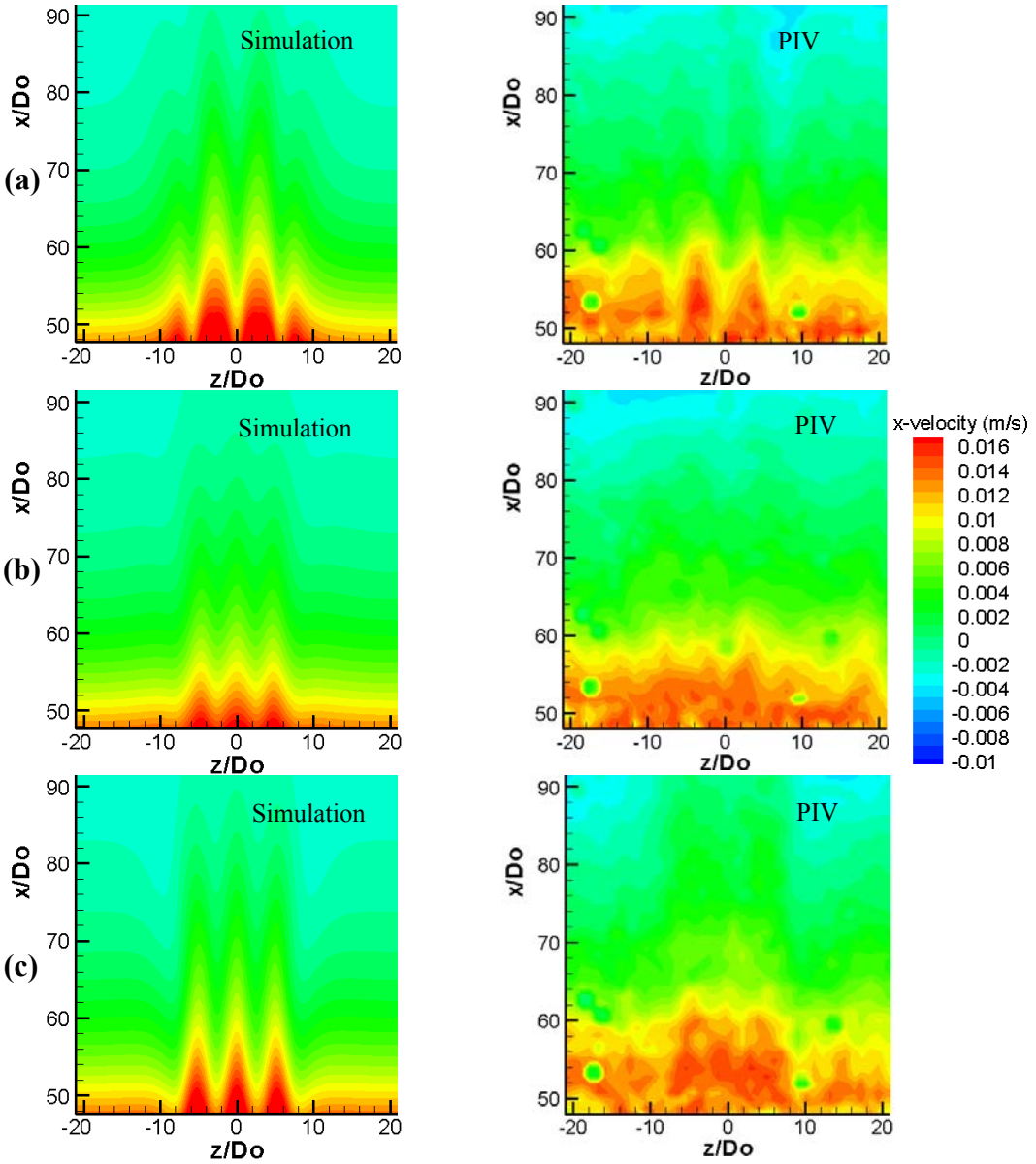

Figure 7.12. A comparison of the time-averaged streamwise velocity on the plane 1.5 mm below the inclined flap (a) Case A, (b) Case B and (c) Case C.

The weaker strength of vortical structures and lower level of velocity fluctuations captured by PIV are believed to be caused by three factors. First, the orifice diameter is only 2mm whereas the thickness of the laser sheet is about 1mm. This can result in a considerable spatial averaging across the central plane of the jet. Second, in order to obtain the flow information over a large area, a large viewing area was used in the PIV measurement. This has resulted in a lower spatial resolution of measurement which is less desirable for a flow field disturbed by the jets of such a

small diameter. Third, there are also some variations in the synthetic jets produced in different diaphragm actuation cycles, making the phase-averaged contours less well defined.

Overall, although the level of agreement with experimental data is not ideal due to the issues related to the experimental data, it is seen that FLUENT is still capable of reproducing the key characteristics of a synthetic jet array and its interaction with a separated laminar boundary layer.

7.2.3.5 The *Q*-Criterion

In this paper, the *Q*-criterion is used to illustrate the vortical structures produced by the synthetic jets. The *Q*-criterion has been commonly used to identify coherent structures during the post-processing of numerical and experimental data. *Q*, the second invariant of velocity gradient tensor ∇u , is defined as

$$Q = 0.5\left(\|\Omega\|^2 - \|S\|^2\right) \tag{7.8}$$

where $\|S\| = \left[Tr(SS^t)\right]^{1/2}$, $\|\Omega\| = \left[Tr(\Omega\Omega^t)\right]^{1/2}$, $\|\cdot\|$ is the matrix norm, and S and Ω are the symmetric and asymmetric component of ∇u . Thus Q represents the local balance between the rotation rate $\|\Omega\|^2$ and the strain rate $\|S\|^2$. It implies that positive Q iso-surfaces identify the areas where the strength of rotation overcomes the strain, thus a coherent vortex can be defined as a region where $Q > 0$. Dubief and Delcayre (2000) utilized the *Q*-criterion to investigate a large panel of coherent vortices generated by DNS and LES, and they made a comparison of four different vortex-eduction methods, including the low pressure criterion, the high vorticity modulus, the negative λ_2 method and the Q criterion. It is found that the Q criterion is superior over the ω (high vorticity) and the low pressure criterion in free and wall-bounded turbulent flows, and it agrees with the λ_2 criterion well due to the mathematical relation between them. Nevertheless, the Q criterion requires a user-defined threshold to visualize the coherent structures. In the present study, after a comparison of the iso-surfaces produced with a range of threshold values, Q = 1 is selected which allows the energetic vortical structures to be captured.

7.3 Results and Discussions

7.3.1 Vortical Structures

Figure 7.13a shows the instantaneous coherent structures in Case A (L = 2 and VR = 0.32) using the Q-criterion. Three trains of typical hairpin vortices produced by the synthetic jets are seen to develop in parallel. The hairpin vortices, accompanied by a pair of induced streamwise vortices, are embedded in the boundary layer and thus experience a high degree of stretching. As these structures propagate downstream, the induced streamwise vortices become weaker and are barely visible at the end the flat plate (x/D_o = 40). The heads of the remaining hairpin vortices are also weakened as they enter the separated flow and they disappear at about $10D_o$ downstream of the start of the inclined flap.

The vortical structures produced in Case B (L = 4, VR = 0.64) are totally different from that in Case A, as shown in Fig. 7.13b. Three trains of tilted vortex ring type of structures, each consist of a whole vortex ring with a pair of highly-stretched counter-rotating legs, are observed. The induced streamwise vortices underneath of the trailing legs are also visible and they disappear just before the start of the flap. Due to their higher velocity ratio, the tilted vortex rings penetrate the boundary layer just $4D_o$ downstream of the orifice. These structures appear to persist further downstream over the inclined flap than the hairpin type of structures observed in Case A.

For Case C (L = 5, VR = 0.81), the vortical structures appear to be more complex as indicated by the presence of secondary hairpin vortices between consecutive trailing legs of the tilted vortex rings (Fig. 7.13c). The tilted vortex rings come out of the boundary layer about $3D_o$ downstream of the orifice exits. The zoom-in view shows that the head of the secondary vortex first appears as a ridge across the trailing legs of the second tilted vortex ring. This hairpin vortex becomes a separate structure located under the trailing legs of the primary vortex ring further downstream. This secondary hairpin subsequently causes another hairpin vortex to form across the trailing legs which initially is seen as a ridge across the trailing legs on the fourth tilted vortex ring. The formation mechanism of both secondary vortices is same. It is believed that they are produced by the roll-up of the high-shear layer that develops between the lift-up, low-momentum, near-wall fluid and the higher-momentum, out-boundary freestream flow as observed by Haidari and Smith (1994) who used controlled surface fluid injection to create hairpin vortices. Between the

two secondary hairpin vortices, the early secondary vortices which are located near to the wall dissipate quickly and it is hardly visible at the end of the flat plate whereas the later secondary vortices remain well-defined. The counter-rotating trailing legs of the primary vortex ring, on the other hand, are weakened significantly after having given birth to the two secondary hairpin vortices and they disappear eventually. Therefore, only the primary vortex rings and the later secondary hairpin vortices along with the induced streamwise vortices survive and persist downstream into the separated flow region.

7.3.2 Surface Shear Stress Patterns

Hairpin vortices and tilted vortex rings have been found to produce distinctly different shear stress patterns (Jabbal and Zhong, 2008; Zhou and Zhong, 2009). The former generates two streaks of high surface shear stress, one on each side of the orifice centreline, whereas the latter produces a single streak at the centreline. The detailed formation mechanisms in both cases have been explained by Zhou and Zhong (2009).

The patterns of the time-averaged surface shear stress on the flat plate in the three test cases are shown in Fig. 7.14. It can be seen that the patterns of surface shear stress produced by each jet are consistent to those observed in a single jet. In the case of hairpin vortices (Case A), the two streaks formed out of each orifice spread outwards in the spanwise direction as they propagate downstream. For the jet spacing specified in the present study, the streaks from adjacent jets overlap downstream, forming one thicker and stronger streak on each side of the middle orifice (see Fig. 7.14a). The phase-averaged cross-sectional velocity vectors superimposed on the phase-averaged streamwise vorticity contours can be used to explain the surface shear stress patterns. As shown in Fig. 7.15a, it can be seen that the counter-rotating legs of hairpin vortices in Case A create a downwash motion outboard to each leg which brings the high-speed fluid from the outer part of the boundary layer to the near-wall region, leading to a higher local surface shear stress, and at the same time an upwash movement on the central plane results in a lower local surface shear stress. The action of counter-rotating legs persists further downstream forming two streaks of high surface shear stress, one on each side of the

orifice centreline, along the streamwise direction. Figure 7.16 is the schematic drawing of hairpin vortices and the corresponding shear stress pattern.

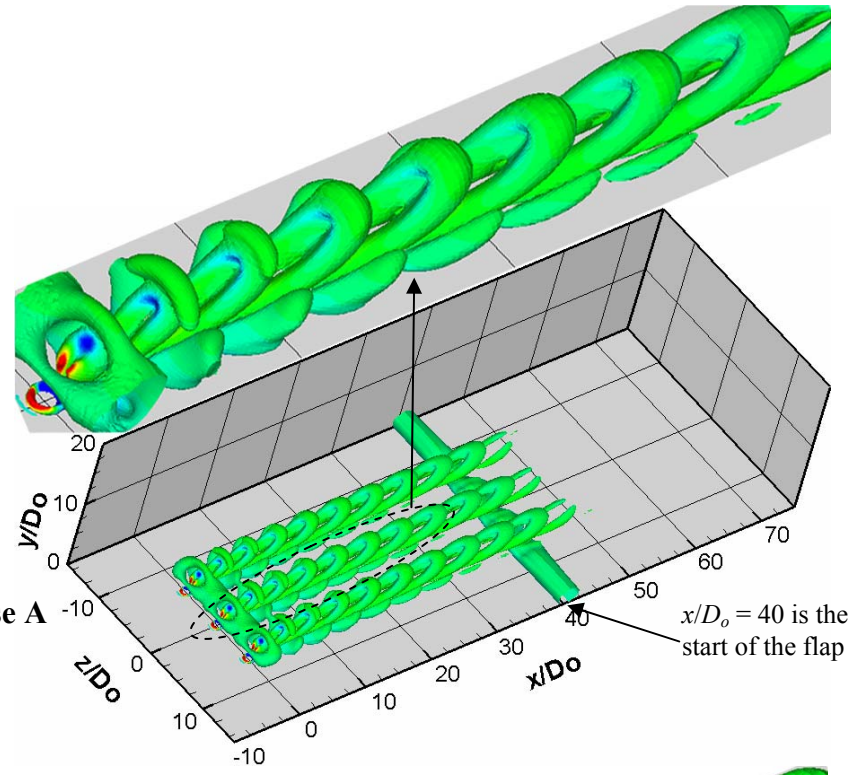

(a) Case A

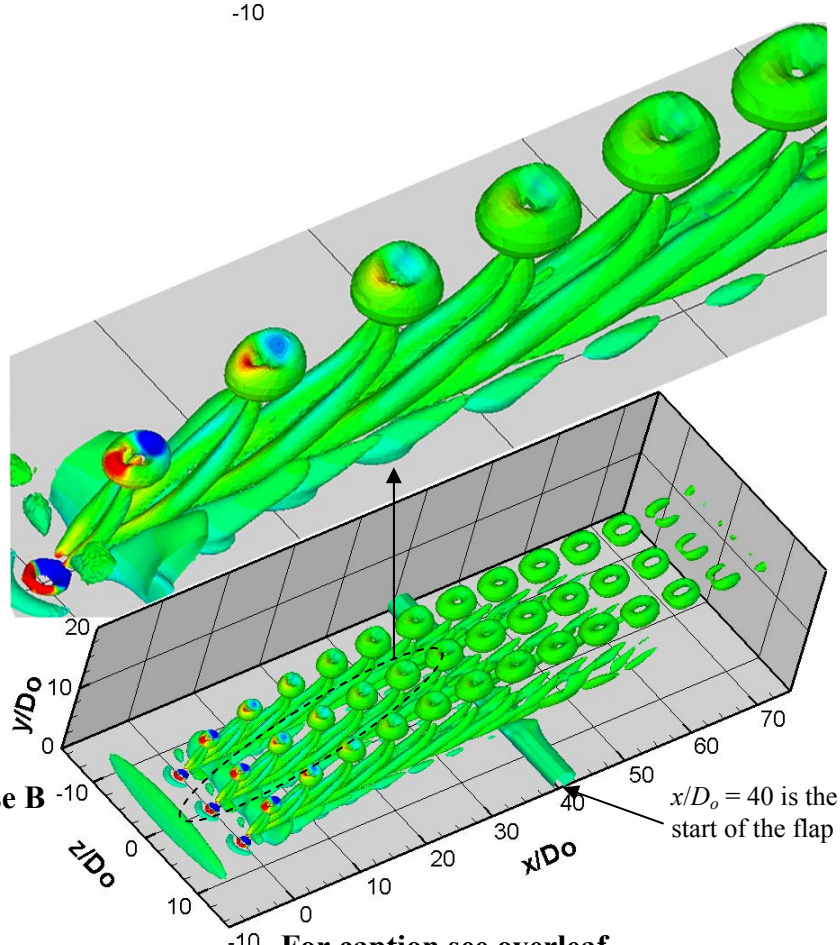

(b) Case B

For caption see overleaf

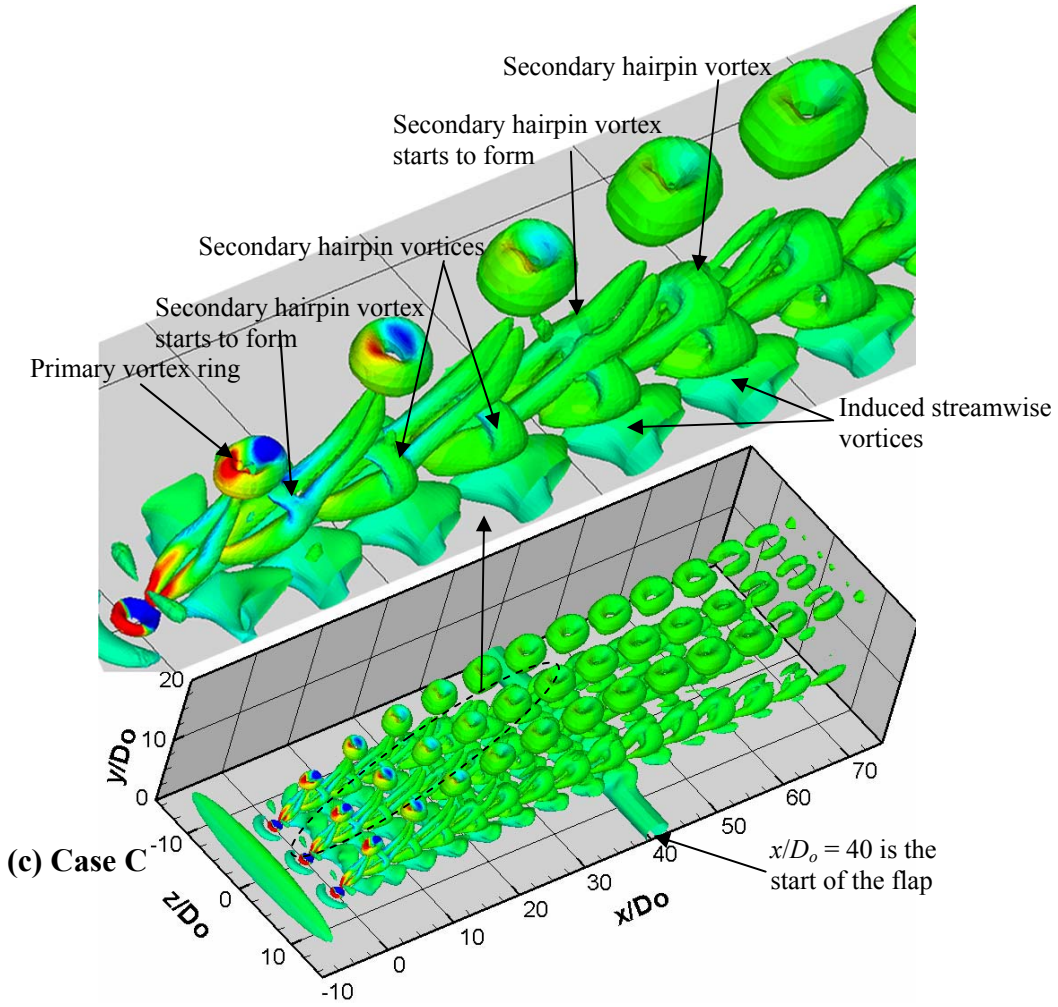

Figure 7.13. Iso-surfaces of Q = 1 showing the downstream development of coherent structures (the inclined flap starts at x/D_o = 40, and the colour on the vortical structures indicates the value of spanwise vorticity).

In the case of tilted vortex rings (Case B), the single high surface shear stress streaks formed out of each orifice also appear to grow in width as they propagate towards the flap resulting in some degree of overlapping between streaks from adjacent jets. Nevertheless the peak surface shear stress associated with each of three jets is still discernable at the start of the flap (see Fig. 7.14b). The formation of single streak shear stress pattern of each orifice is due to the downwash motion produced by the induced streamwise vortices which are located directly underneath the trailing legs of the tilted vortex ring. This downwash motion brings the high-speed fluid from the outer part of the boundary layer to the near-wall region on the streamwise central plane of the jet (Fig. 7.15b). Similarly, the schematic drawing of tilted vortices and their formed shear stress pattern is shown in Fig. 7.17. In Case C, despite the dominant structures being more complex, the location and action of the

induced streamwise vortices are similar (Fig. 7.15c), and hence the pattern of surface shear stress is comparable to Case B (Fig. 7.14c). The strength of the three streaks produced by the jets appears to be stronger than that in Case B with no obvious overlapping.

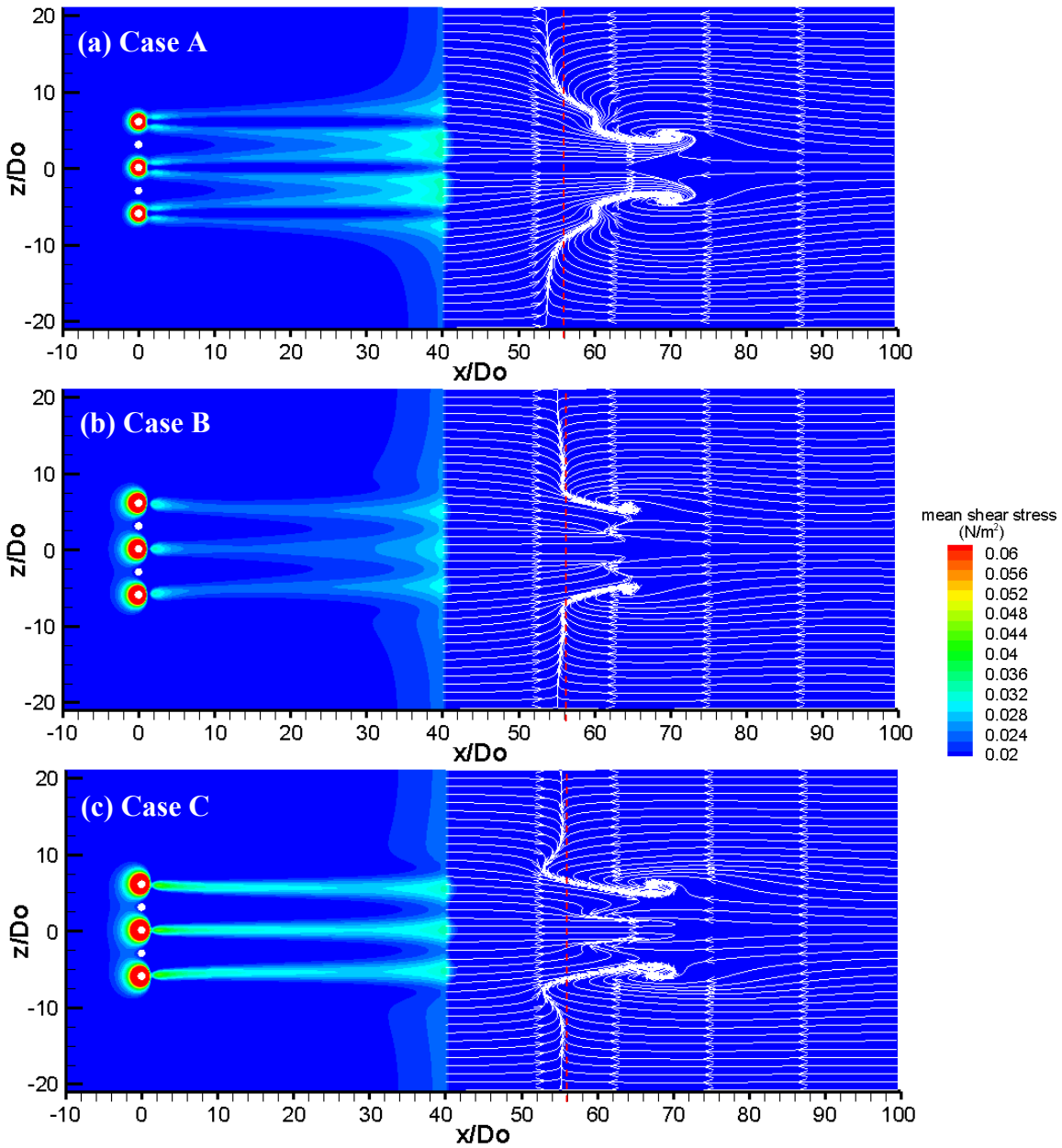

Figure 7.14. Patterns of time-averaged surface shear stress on the horizontal plate and separation regions indicated by skin friction lines superimposed on the contours of time-averaged surface shear stress (The red dash line is the separation line of the baseline flow based on the skin friction and $x/D_o = 40$ is the start of the inclined flap).

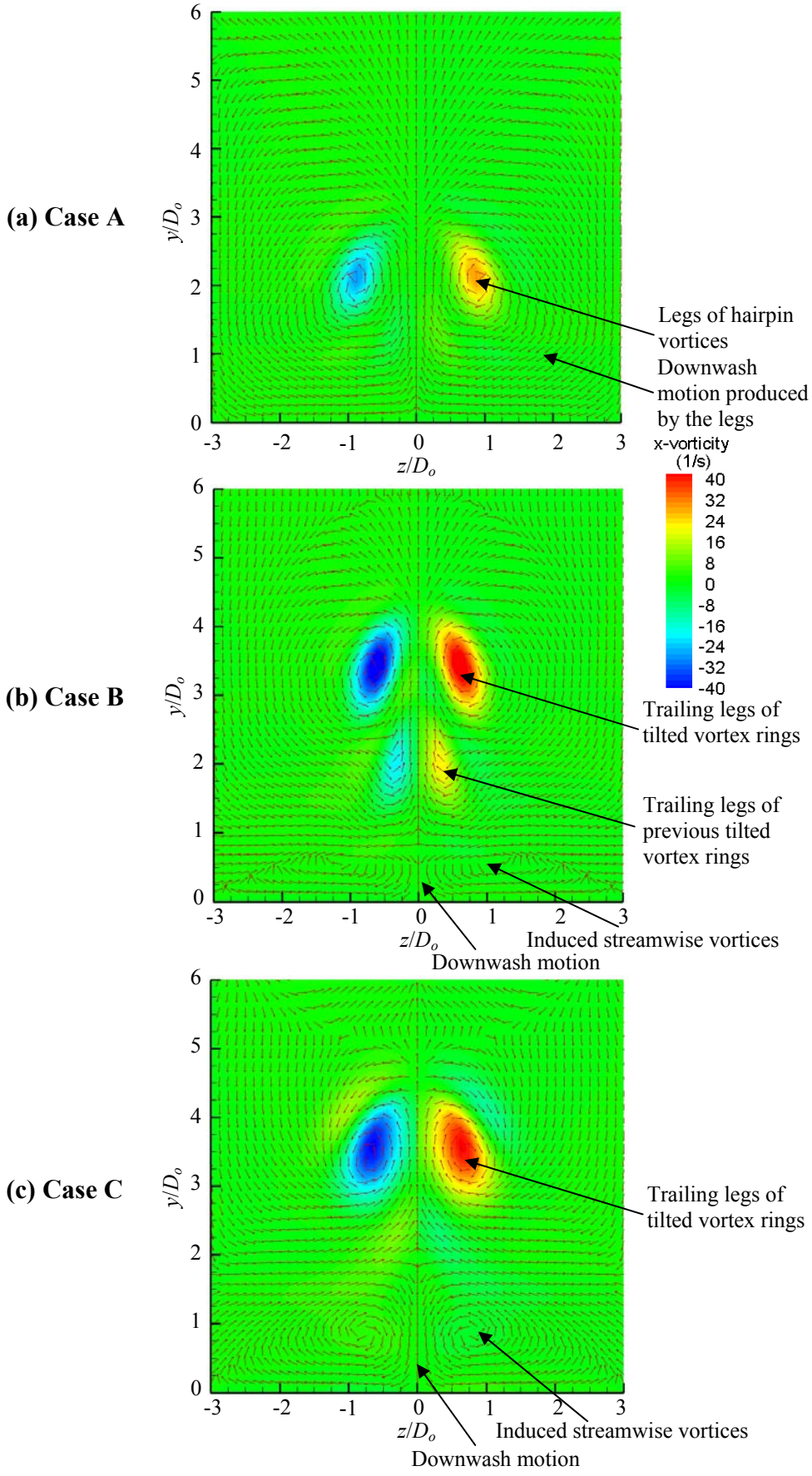

Figure 7.15. Phase-averaged velocity vectors superimposed on the phase-averaged streamwise vorticity at $x/D_o = 10$ for (a) Case A, (b) Case B and (c) Case C.

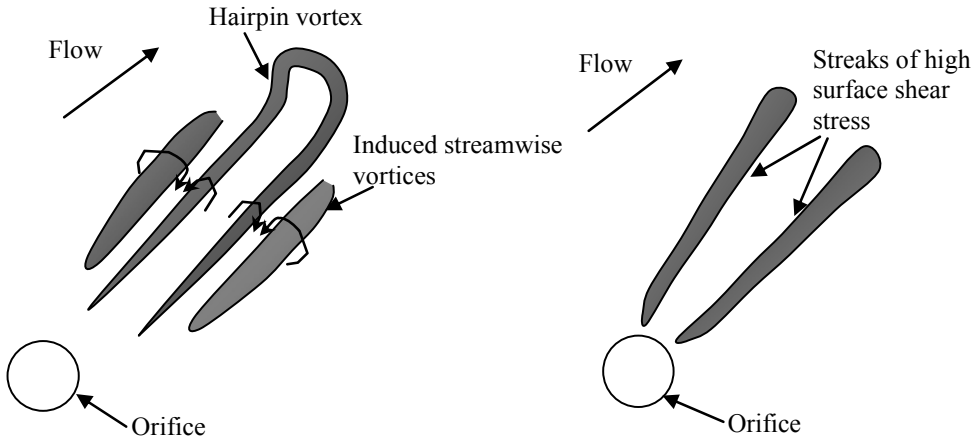

(a) **(b)**

Figure 7.16. A schematic drawing of (a) the hairpin vortex and its induced vortices (b) the production of two streaks of high surface shear stress.

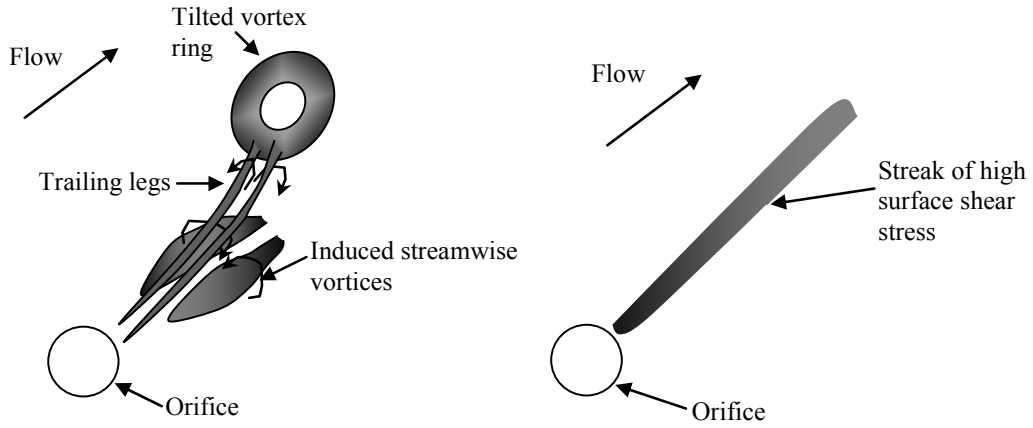

(a) **(b)**

Figure 7.17. A schematic drawing of (a) the tilted vortex ring and its induced vortices (b) the production of one streak of high surface shear stress.

The spanwise distributions of time-averaged surface shear stress are consistent with the patterns of surface shear stress shown in Fig. 7.14 in terms of the number of local peaks (see Fig. 7.18). It appears that the local peak shear stress in the near-field of the orifice exit (x/D_o = 2) increases as the velocity ratio increases as shown in Fig. 7.18a. This agrees with the finding of Kostas et al. (2009) from a co-rotating pulsed jets array. Nevertheless, this trend is not maintained further downstream as the maximum shear stress of Case A exceeds that of Case B (Figs. 7.18b and c) and is nearly same as that of Case C at the end of the flat plate (Fig. 7.18c). From Fig. 7.18, it is seen that due to the spanwise growth of individual streaks and the overlapping of neighbouring streaks, the peaks are broadened and the

surface shear stress further away from the orifice central plane is increased. Consequently, the level of spatial fluctuations in the local shear stress decreases.

It is also noted that the level of the surface shear stress away from the central plane in the near field drops significantly below that of the baseline value in Case B and C (Fig. 7.18a). Nevertheless, the extent of this surface shear stress deficit decreases further downstream such that the level of surface shear stress is even above that of the baseline case (Fig. 7.18b). In contrast, in Case A the level of the surface shear stress away from the central plane is always above that of the baseline case as a result of the downwash generated by the hairpin vortices outboard which brings the high speed fluids towards the wall. Furthermore, the surface shear stress in that region is even enhanced further downstream due to the overlapping of downwash caused by hairpins from two adjacent jets (compare Fig. 7.18b and Fig. 7.18c).

Since the surface shear stress of each case varies considerably in the spanwise direction, the space-averaged shear stress, covering a width of $3D_o$ on each side of the central plane of the middle jet is hence calculated. The reason, that a spanwise width of $3D_o$ (one half of the spanwise spacing between jets) on each side is chosen, is to focus on the middle jet which has the minimum end effect in the array. Figure 7.19 shows the variation of the space-averaged shear stress in each case with the streamwise distance from the orifice. The baseline case is also added to aid the comparison. In general, the level of surface shear stress increases as the flow accelerates towards the flap. A substantial increase in surface shear stress in comparison to the baseline case is obtained in all the three cases except at $x/D_o = 2$ in Case C. It is found that, among the three cases, Case A maintains a high surface shear stress, which is most likely due to the close proximity of the legs of hairpins to the wall. It is also interesting to note that although Case B and C have a higher local peak at $x/D_o = 2$, the space-averaged shear stress is lower than that of Case A at the same location since the vortical structures also cause a reduction in surface shear stress off the orifice centreline relative to the baseline case. As a result, the space-averaged shear stress of Case C is even lower than that of the baseline case at $x/D_o = 2$. However, the shear stress in Case C increases rapidly further downstream, achieving a level which is similar to that of Case A around $x/D_o = 10$. From Fig. 7.18b, it is seen that this dramatic increase in surface shear stress in Case C at that location is associated with a rapid rise in surface shear stress off the orifice centreline

and a broadening of the central peak, indicating a strong local interaction between the synthetic jets and the boundary layer. The increase in the surface stress then slows down significantly between x/D_o = 10 and 30 before it peaks up again as the flow approaches the flap. A similar trend is observed in Case B, although the changes are more gradual.

(a)

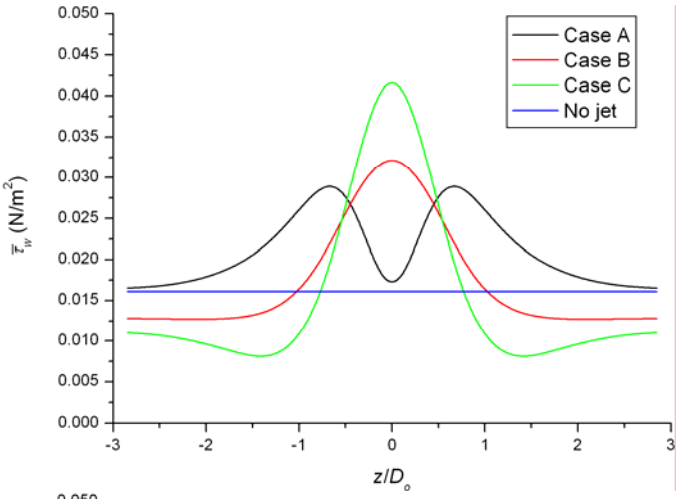

(b)

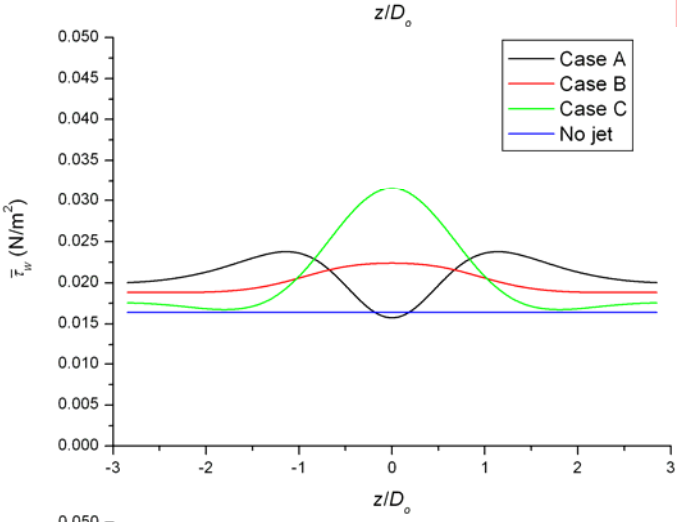

(c)

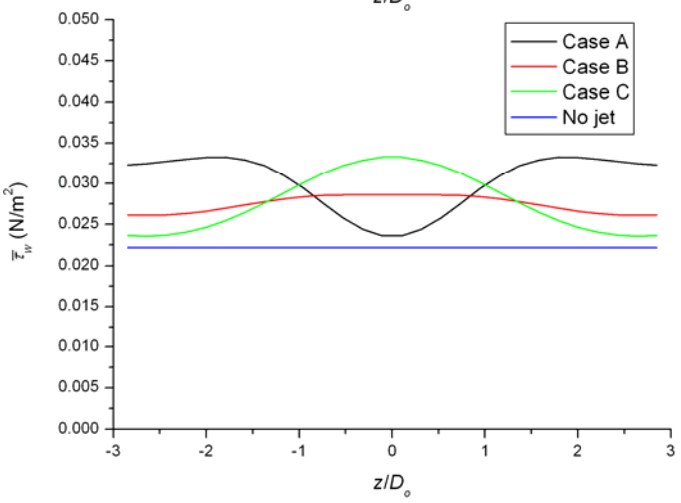

For caption see overleaf

(d)

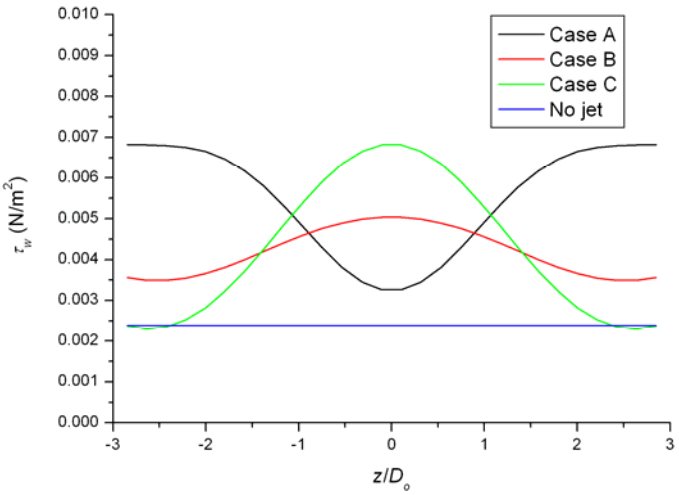

Figure 7.18. Spanwise distributions of the time-averaged surface shear stress at (a) x/D_o = 2; (b) x/D_o = 10; (c) x/D_o = 40 and (d) x/D_o = 50.

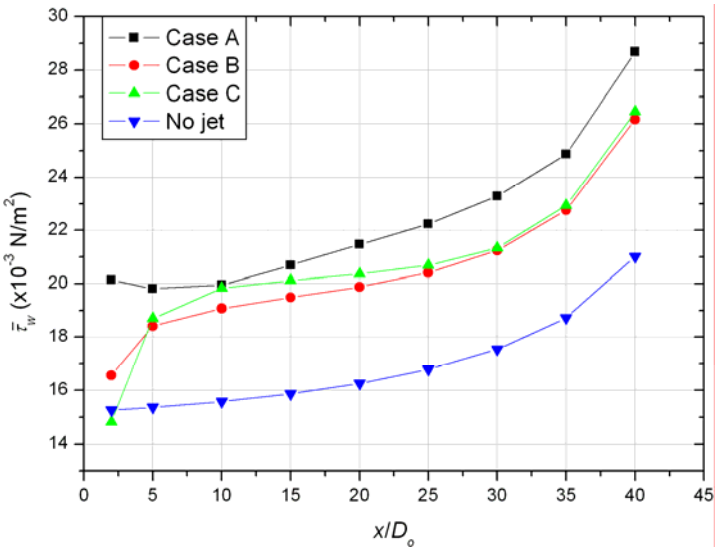

Figure 7.19. Variations of the space-averaged surface shear stress. in the streamwise direction.

As a measure of the overall effect of the synthetic jets on the boundary layer upstream of the flap, the space- and time-averaged surface stress in the area bounded by x/D_o = 2 to 40 and z/D_o = -3 to 3 normalised by that of the baseline flow for the three cases is calculated and presented in Fig. 7.20. The averaged shear stress appears to decrease sharply from 1.32 to 1.21 as L increases from 2 to 4, and then increases more gradually to 1.23 when L increases to 5, indicating that the hairpin vortices in Case A produces the highest space- and time-averaged shear stress. The reason for despite the level of shear stress level in Case C being either higher or similar to that of Case A the space- and time-averaged shear stress in Case A is still higher, is that the overlapping near-wall effect produced by neighbouring hairpin

structures from adjacent orifices has produced a larger region with a higher surface shear stress.

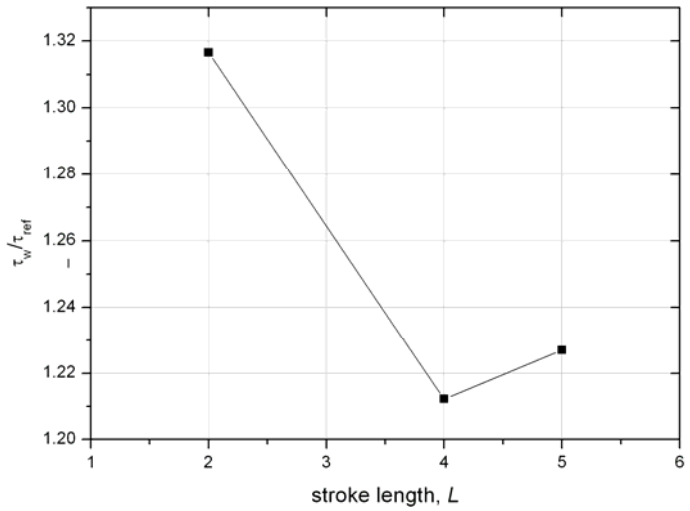

Figure 7.20. Variations of the non-dimensional space and time-averaged surface shear stress versus the dimensionless stroke length.

7.3.3 Flow Control Effect

In the present study, skin friction lines superimposed on the contours of time-averaged surface shear stress on the flap are used to evaluate the flow control effect of the synthetic jet array at the three test conditions (Fig. 7.14). The skin friction lines show the direction of surface shear stress vectors hence they provide a visual indication of the region of attached and separated flow. The location of separation line can be taken as the location where the skin friction lines coming from upstream and those coming from downstream meet and redirect themselves tangentially. To aid the comparison, the separation line of the baseline flow based on the skin friction is shown as the red dash line. It is noticed that the streamwise locations of separation line at the edge of the computational domain are not identical to that in the baseline case in these three cases. The maximum deviation occurs in Case A which is about $2.5D_o$. This deviation is likely to be caused by the current domain being not wide enough to allow the effect of the side boundaries on the flow field to be neglected. On the other hand, since it is the performance of the middle jet which is of interest in this study and the accuracy of simulation for $z/D_o < 10$ is shown to be acceptable in section 7.2.3.3, the results presented here should still be valid.

In Case A, four high surface shear stress streaks are observed upstream of the separation region with the two dominant streaks aligned with the middle points

between the middle jet and each side jet and a weaker streak outboard of each side jet (Fig. 7.14a). The pattern of skin friction lines in the separated flow region shows a clear correspondence to the shear stress pattern observed on the upstream flat plate, in that the flow remains attached further downstream in the spanwise locations where the streaks of high surface shear stress from upstream are located. A much strong separation delay is produced by the two dominant streaks such that the attached flow extends to $x/D_o = 73$ as shown in Fig. 7.14a.

The pattern of skin friction in the separation region in Case B also corresponds to the shear stress pattern observed on the upstream flat plate (Fig. 7.14b). Three streaks of attached flow with comparable strength are observed on the downstream inclined flap, whose spanwise locations are approximately aligned with the centre of each synthetic jet orifice. The extent of flow separation delay is less than that in Case A with the attached flow reaching $x/D_o = 66$ as shown in Fig. 7.14b.

Similar but much profound skin friction pattern is observed in Case C due to its high velocity ratio. The three streaks of attached flow are seen to extend to $x/D_o = 70$ as shown in Fig. 7.14c. On the other hand, flow reversal in the regions between the streaks appears to be significant, resulting in a highly fluctuated separation line.

Considering the fact that the vortical structures are much weaker when they reach the separated flow region in Case A than in the other two cases, the considerable flow separation delay produced in Case A is unlikely to be due to the local interaction of these structures with the separated flow but the accumulated effect of the these structures on the boundary layer as they propagate downstream once they are formed. Since the local surface shear stress can be taken as a measure of this accumulated effect, the distributions of surface shear stress at $x/D_o = 50$, a location just before the separation line in the baseline case, is examined (see Fig. 7.18d). It can be seen that although the overall level of surface shear stress is reduced significantly at this location, the peak surface shear stress in Case A and C remains to be higher in a similar level whilst that in Case B stays as the lowest. From Figs. 7.14 and 7.18d, it appears that the level of peak surface shear stress just before the baseline separation line and the extent by which the separation line is pushed downstream locally among these three cases is correlated.

For practical applications, the space-averaged flow control effect across the span of a typical jet in a synthetic jet array is of more interest than the local effect. In order to evaluate such an effect quantitatively, in the present study the size of the

area from the start of the flap to the time-averaged separation line with a spanwise width of $3D_o$ on each side of the central plane of the middle jet is calculated and it is then normalised by the corresponding area in the baseline case. From Fig. 7.21, it can been seen that the control effect firstly decreases as L increases from 2 to 4 and then increases by a certain extent when L increases from 4 to 5. The reduction of control effect from L = 2 to 4, is believed to be associated with the change of vortical structures from hairpin vortices to tilted vortex rings while the latter is still weak. As L increases further, the control effect increases as the tilted vortex rings gain their strength. Among the three cases, Case A is found to produce the strongest separation delay. From Figs. 7.20 and 7.21, there appears to be a clear correlation between the averaged surface shear stress along the horizontal plate behind the middle jet and the extent of separation delay among these three cases, i.e. a higher averaged surface shear stress along the horizontal plate results in a stronger separation delay further downstream.

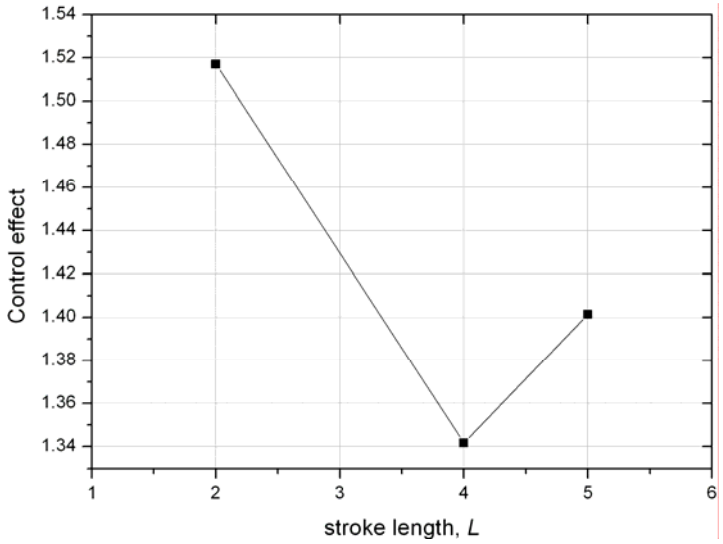

Figure 7.21. Flow control effect versus the dimensionless stroke length.

For the three cases considered here, since the actuation frequency is the same a higher diaphragm displacement implies higher power consumption in producing the synthetic jets. Therefore, among the three cases Case A is most effective since it produces the strongest flow separation delay while consumes the least amount of energy. The finding from this study suggests that hairpin vortical structures produced at a relatively low VR are more desirable structures for effective flow control. This is

most likely because the input energy has been used more effectively in producing coherent structures that are closer to the wall. In addition, the present setup also benefits from the overlapping near-wall effect produced by neighbouring hairpin structures from adjacent orifices. This implies that, for a given distance between the synthetic jets and the separation line, the jet spacing is an important parameter to be considered in order to maximize the effect of flow control. Further investigations of more test cases are being undertaken in order to identify the actuator operating condition that delivers the optimal control effect over a wider range of parameter space.

7.4 Conclusions

In this work, flow separation control using an array of round synthetic jets issued into a laminar flow that separates further downstream over an inclined plate is investigated using a 3D numerical simulation. The simulation results are validated using experimental data and a reasonable agreement is achieved.

Three operating conditions are examined in which the diaphragm displacement is varied while the oscillating frequency is kept constant. Two distinct types of vortical structures, i.e. the hairpin vortices (Case A) and tilted vortex rings (Case B and C), are generated by each synthetic jet which are similar to those found from a single synthetic jet. Case A exhibits two streaks of high surface shear stress downstream of each jet whereas in Case B and C, only one streak of high surface shear stress is observed downstream of each jet. These patterns of surface shear stress are observed in the zero-pressure-gradient boundary layer developing along the horizontal plate upstream to the flap and they persist further downstream resulting in a wavy separation line in the separated flow region.

The impact of the middle synthetic jet in the array on the boundary layer prior to separation is evaluated by examining the spatial variations of time-averaged surface shear stress. It is found that Case A produces the largest space- and time-averaged surface shear stress whereas Case C produces the highest local peak surface shear stress due to its high velocity ratio.

The flow control effectiveness of the middle synthetic jet is also quantified by examining the size of the surface area over which the flow remains attached.

Among the three cases tested here, Case A is found to be most effective since it produces a considerable flow separation delay and a smoother separation line while consuming the least amount of energy among the three cases. The finding from this study suggests that hairpin vortical structures produced at a relatively low *VR* are more desirable structures for effective flow control. Further investigations of more test cases are being undertaken in order to identify the actuator operating conditions that will deliver the optimal control effect over a wider parameter space.

Paper title:

The Near-Wall Effect of an Array of Synthetic Jets and Their Control Effect in a Separated Laminar Boundary Layer

Authors:

Jue Zhou and Shan Zhong

Paper submitted to:

Computers and Fluids, 2010

Chapter 8 The Near-Wall Effect of an Array of Synthetic Jets and Their Control Effect in a Separated Laminar Boundary Layer

Jue Zhou and Shan Zhong

School of Mechanical, Aerospace and Civil Engineering, University of Manchester, UK

Abstract:

In this paper, flow separation control using an array of circular synthetic jets issued into a flat plate laminar boundary layer which separates downstream over an inclined plate is investigated using 3D numerical simulations. The simulations are undertaken using FLUENT at a wide range of actuator operating conditions. Based on the large number of cases simulated, a parameter map illustrating the nature of the primary vortical structures in the orifice near-field is established. The parameter map can be divided into two regimes separated by a well-defined boundary; one regime is characterised by hairpin vortices and the other by tilted vortex rings. The impact of the middle synthetic jet in the array on the boundary layer prior to separation is evaluated by examining the space- and time-averaged surface shear stress. Two regions with a high surface shear stress increment relative to the baseline case are identified; one is associated with the appearance of hairpin vortices and the other is featured by the presence of tilted vortex rings. The flow control effect of the middle jet is also quantified by examining the time-averaged location of the separation line. It is found that the hairpin vortex type of structures is capable of delivering a stronger flow control effect than the tilted vortex ring type of structures and this is correlated with the fact that the former also produces a higher surface shear stress increment upstream. It is found that the best flow control effect occurs when the maximum height of the hairpin structures is about that of the boundary layer with their limbs located at about a half of the boundary layer height. Among all the conditions examined in the current study, operating the synthetic jets at $L = 2$ and $VR = 0.36$ which yields hairpin-like structures with a streamwise spacing about 70% of the local boundary layer thickness at the jet orifices is found to produce the best flow control effect with the lowest power consumption. The evidence from this study also

suggests that the flow separation delay produced by the synthetic jet array investigated here is due to the accumulated effect of the vortical structures on the boundary layer as they propagate downstream, rather than the local interaction of these structures with the separated flow.

8.1 Introduction

Synthetic jet actuators, as a novel method of delaying flow separation with a potential application on the aircraft high-lift systems, have received much research attention since 1990s (Smith and Glezer, 1998; Crook et al, 1999; Glezer and Amitay, 2002; Seifert et al, 2004). The capability of synthetic jets in delaying flow separation has been demonstrated on aerodynamic bodies with various shapes in a number of experiments (Amitay et al, 2001; McCormick, 2000; Crook and Wood, 2001; Tensi et al, 2002). A good understanding of the behaviour of synthetic jets issued into a quiescent flow and a boundary layer has been achieved (Crook, 2002; Garcillan et al, 2005; Zhong et al, 2005; Jabbal and Zhong, 2008; Zhong et al, 2007; Tang et al, 2007). Nevertheless, in order to use synthetic jet actuators effectively in practical settings, one of the key issues that remain to be addressed is at which dimensionless parameters they should be operated in order to maximize their flow control effect for a given external flow condition.

Existing experimental evidence shows that the interaction of the vortices produced by a circular synthetic jet with a boundary layer results in the formation of streamwise vortical structures, which are capable of delaying flow separation by entraining faster moving fluid to the near-wall region (Crook and Wood, 2001). In order to obtain a better understanding of the nature of these vortical structures, both experiments and numerical simulations have been undertaken on a single circular synthetic jet issued into a zero-pressure-gradient laminar boundary layer (Jabbal and Zhong, 2008; Zhong et al, 2007; Tang et al, 2007). It is shown that as the dimensionless jet stroke length and the jet-to-freestream-velocity ratio increase, the primary vortical structures produced by the interaction between the synthetic jet and the boundary layer first appear as hairpin-like vortices that are located close to the wall then as tilted vortex rings that come out of the boundary layer shortly downstream. Using temperature-sensitive liquid crystal surface coating, Jabbal and

Zhong (2008) found that the hairpin type structures produce a pair of streamwise streaks associated with a high heat transfer rate downstream of the orifice whereas the tilted vortex ring type structures produce a single streamwise streak directly downstream of the orifice. By the Reynolds analogy, an area of high heat transfer rate is associated with a local high surface shear stress or a local high flow velocity in the near-wall region.

The presence of hairpin vortices is also confirmed in the CFD simulations of Zhou and Zhong (2009) who found that the legs of the hairpins trailing along the wall also induce a pair of streamwise vortices of the opposite sign outboard (Fig. 8.1a). According to Zhou and Zhong, the tilted vortex rings are located outside the boundary layer and connected to the wall via a pair of counter-rotating legs. The counter-rotating legs further induce a pair of tertiary streamwise vortices of an opposite sense directly underneath as shown in Fig. 8.1b.

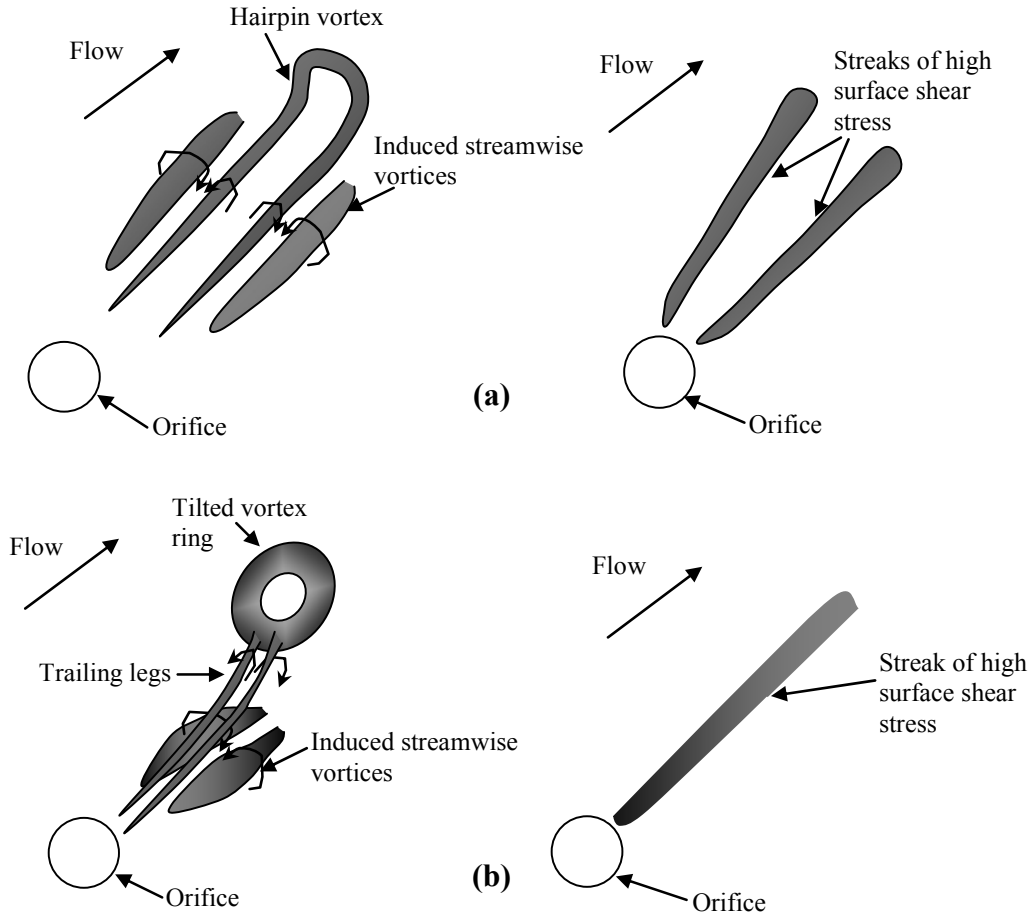

Figure 8.1. A schematic drawing of (a) the hairpin vortex and its induced vortices producing a two-streak pattern of surface shear stress (b) the tilted vortex ring and its induced vortices producing a single-streak pattern of surface shear stress.

The formation and development of the aforementioned two types of vortical structures have been explained by Jabbal and Zhong (2008) and Zhou and Zhong (2009). Furthermore, Zhou and Zhong (2010a) also presented a parameter map showing the different types of vortical structures observed based on the dimensionless stroke length and the frequency of the synthetic jet. The hairpin vortices are found to occur when the velocity ratio is less than about 0.4. This is also consistent with the observation made by Jabbal and Zhong (2008) in their experiment.

On the basis of understanding the interaction of a single synthetic jet with a zero-pressure-gradient boundary layer, Zhang and Zhong (2010a) conducted an experimental study of flow control using an array of three synthetic jets in a separated laminar flow over an inclined plate in a water channel. PIV measurements were made on a spanwise plane parallel to the inclined plate at a distance of 1.5mm from its surface to obtain the information about the extent of flow separation delay at different synthetic jet operating conditions. Laser induced florescence (LIF) flow visualisation technique was used to reveal the characteristics of the vortical structures produced by the synthetic jets which result in a delay of separation. It is found that for the range of actuator operating conditions tested in this study, a profound flow control effect is obtained for $0.3 < VR < 0.5$ where hairpin-like vortical structures are observed.

In the present work, numerical simulations of a large number of cases for an identical synthetic jet actuator and incoming flow conditions are undertaken. The 3D vortical structures produced by the interaction between the synthetic jets and the boundary layer are examined using the Q-criterion. The results are collated to produce a parameter map showing the variations in the nature of vortical structures with changing synthetic jet operating conditions. The flow control effectiveness of the synthetic jets is then evaluated and the regions with good flow control effect as well as the associated flow structures are identified. Furthermore, by making use of the surface shear stress data the impact of the vortical structures on the boundary layer prior to separation is examined and its possible correlation with the flow control effect is investigated. Finally, a small selection of cases is examined in more details so as to indentify the characteristics of vortical structures that yield the best flow separation delay.

In order to simplify the simulations, the present study was undertaken in a laminar boundary layer. However, the authors believe that the results from this work will provide an insight of the fluid mechanics of synthetic jets for practical applications since some commonalities exist in the interaction mechanisms between synthetic jets and a boundary layer no matter it is laminar or turbulent. Furthermore, experimental evidence has already revealed that similar vortical structures identified in laminar flows also exist in turbulent flows and are responsible for the delay of flow separation (Zhang and Zhong, 2010b). In the authors' opinion, understanding the behaviour of synthetic jets in a laminar flow is the first logical step towards understanding the more complex behaviour of synthetic jets in a turbulent flow.

8.2 The Synthetic Jets

In this study, the synthetic jet array and its test conditions used in the simulation are identical to that used in the experiment of Zhang and Zhong (2010a) (Fig. 8.2). The jet array consists of three jets which are issued through three circular orifices aligned normally to the orifice plate. The orifices have a diameter of D_o = 2 mm and a depth of h = 3 mm. The three jets are produced by an oscillating diaphragm attached to a single cylindrical cavity with a diameter of 45 mm and a height of 12 mm. Driven by a permanent magnetic shaker, the diaphragm is made to oscillate in a sinusoidal manner at predetermined oscillation displacements and frequencies and mimics a piston-like motion.

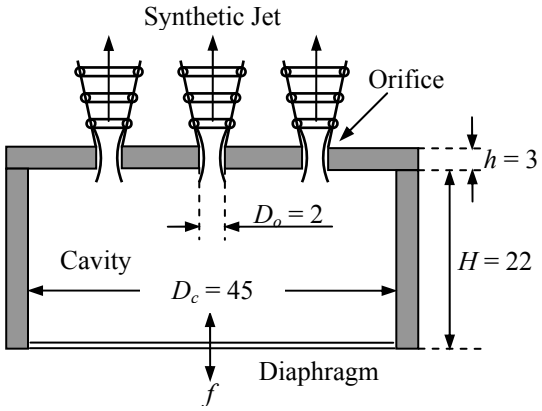

Figure 8.2. A schematic of the synthetic jet actuator (all dimensions are in mm).

The experiments were conducted in a water flume. The sketch of the test plate and its coordinate system are shown in Fig. 8.3. The laminar boundary layer developing along the horizontal plate subsequently separates at some point along the inclined plate which is tilted 5° upwards relative to the horizontal direction, creating a separated boundary layer to which flow control with synthetic jets can be applied. In this experiment, in order to focus on the study of the flow control effect of changing actuator operating conditions, the jet spacing and the distance between the jet array and the baseline separation line are fixed. The spacing between synthetic jets is 12 mm ($6D_o$). The array is located at 450 mm downstream of the leading edge of the horizontal plate, leaving a distance of 80 mm to the start of the inclined plate ($40D_o$) and a distance of about 120 mm to the baseline separation line ($60D_o$). Detailed description of the synthetic jet array and the experimental settings can be found in Zhang and Zhong (2010a).

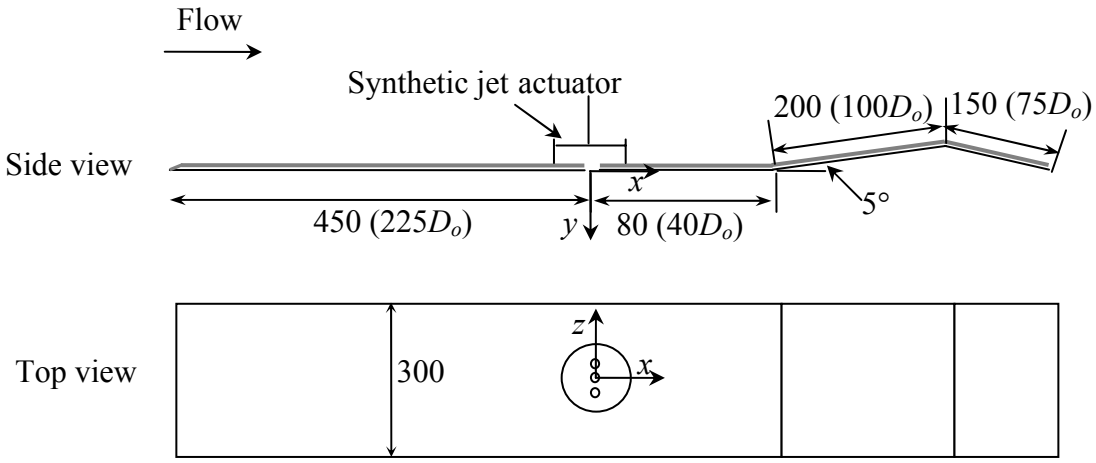

Figure 8.3. A schematic of the experimental setup (all dimensions are in mm, D_o = 2 mm).

The dimensionless analysis done by Jabbal and Zhong (2008) and the experiments by Zhang and Zhong (2010a) indicated that for a synthetic jet with a fixed geometry embedded in a given boundary layer, the jet effectiveness, which is defined in terms of the strength and persistency of fully formed vortical structures in the near-wall region of a boundary layer, is determined by the dimensionless stroke length L, jet-to-freestream-velocity ratio VR, Reynolds number based on the stroke length Re_L and the Strouhal number based on the freestream velocity and local boundary layer thickness Str. In the present work, the same definitions of the

dimensionless parameters as those used by Zhang and Zhong (2010a) are adapted. Note that the velocity ratio used here is defined based on the time-averaged jet blowing velocity over the entire actuation cycle.

In the experiment, the freestream velocity is fixed at 0.1 m/s. The local boundary layer thickness is about five times of the orifice diameter at the location of the jet array. The flow characteristics of the synthetic jets are varied by changing the displacements and frequencies of the oscillating diaphragm. In total, sixty-three cases are simulated, among which the oscillating frequency is varied from 2 to 14 Hz and the displacement is varied independently from the frequency to yield a range of dimensionless stroke length from 1 to 8. Accordingly, the velocity ratio changes from 0.08 to 1.12, the Reynolds number based on the stroke length from 24 to 1020 and the Strouhal number from 0.2 to 1.4. The simulations are undertaken to cover a reasonably large parameter range within the capability of the flow solver. The maximum velocity ratio in the present study is cut off at 1.12 because that it is found in the experiments synthetic jets with a higher velocity ratio become turbulent, making them unsuitable to be modelled with a laminar flow model. A summary of all the test cases is illustrated in Fig. 8.4.

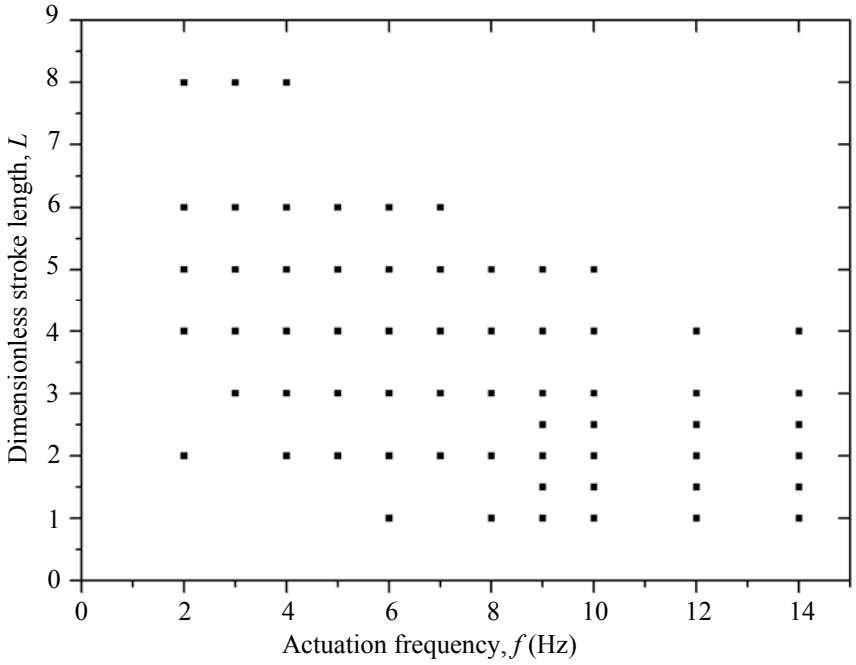

Figure 8.4. Summary of test cases in *f-L* parameter map.

8.3 The Numerical Methods

The commercial CFD package, FLUENT 6.3, is utilized to computer the 3D unsteady incompressible flow. The laminar model is employed to model the flow field due to the low jet Reynolds numbers in the present study. The second-order implicit scheme is selected for the unsteady formulation. The pressure and velocity are coupled using the Pressure-Implicit with the Splitting of Operators (PISO) algorithm. The second-order scheme and second-order upwind scheme are selected for pressure discretization and momentum discretization, respectively.

The computational domain and boundary conditions used in this study are shown in Fig. 8.5. The computation domain contains 3.8 millions mesh cells. The inlet of the flow domain is located at 20 mm ($10D_o$) upstream of the centres of the orifices. The outlet is set at the end of the test plate which is 430 mm ($215D_o$) downstream of the orifices. The height of the computational domain is 70 mm ($35D_o$) above the horizontal plate. Since the flow field is expected to be symmetric relative to the central plane of the middle orifice, only a half of the flow field is modelled in order to save on computational time. A domain width of $21D_o$ is chosen as a compromise of computational time and accuracy. The time step size is set as 1/120 of the diaphragm oscillating cycle.

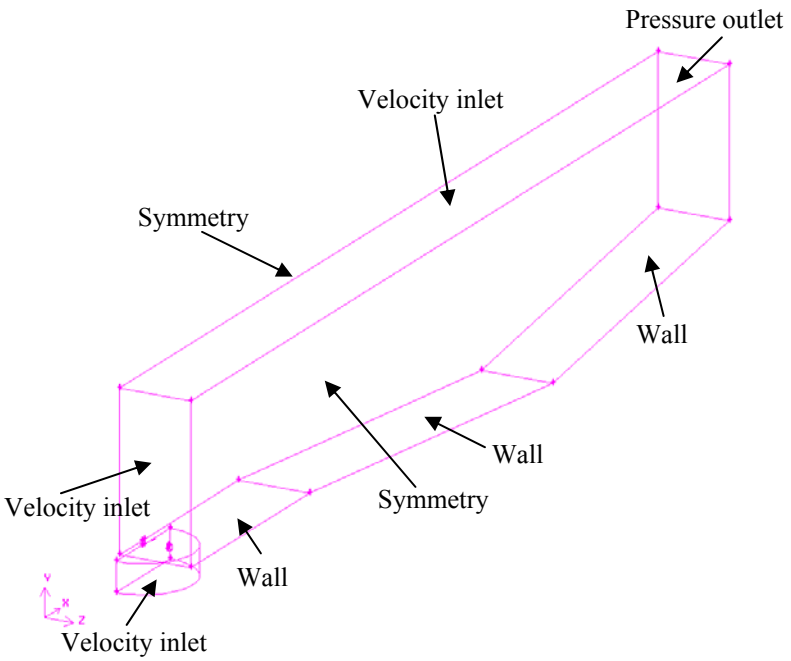

Figure 8.5. The geometry and boundary conditions of numerical simulation.

All the aforementioned settings are identical to those used by Zhou and Zhong for modelling the same synthetic jet array in the same boundary layer in their previous work. A detailed description of the domain size and the specifications of the boundary conditions can be found in Zhou and Zhong (2010b). The adequacy of the computational domain size and boundary conditions used this study has been validated and a sensitivity study of grid and time step size has been undertaken by Zhou and Zhong (2010b), confirming that the chosen mesh size and time step size are reasonable. Furthermore, they also conducted a comparison of their simulation results with the measured data from Zhang and Zhong (2010a) for the baseline case without the actuation of synthetic jets and three test cases with the actuation of synthetic jets. A number of parameters were compared, including the instantaneous spanwise vorticity and the time-averaged velocity profiles on the streamwise central plane of the middle synthetic jet, the jet trajectory on the central plane, and the contours of time-averaged streamwise velocities on the spanwise plane parallel to the inclined plate where the PIV measurements were taken. The reasonable agreement between the simulation and the experiment confirms that the numerical method used here is capable of capturing the key characteristics of a synthetic jet array and its interaction with a separated laminar boundary layer.

8.4 Results and Discussions

8.4.1 Vortical Structures

Figure 8.6 shows the coherent structures produced by the interaction of synthetic jet array with the laminar boundary layer, for a selection of cases at f = 5, 9 and 14 Hz, using the Q criterion. Here, in order to capture the energetic vortical structures the Q value of iso-surfaces is selected as 1. The operating conditions and dimensionless parameters of these cases can be found in Table 8.1.

It can be seen that at f = 9 Hz, as L increases from 2 to 5, the dominant vortical structures change from hairpin vortices (Fig. 8.6b1) to tilted vortex rings (Fig. 8.6b3). The hairpin vortices are accompanied by a pair of induced streamwise vortices outboard of the counter-rotating legs and they remain embedded in the boundary layer within a substantial distance downstream of the jet orifices. On the other hand, the tilted vortex ring type structures, which are characterised by a whole

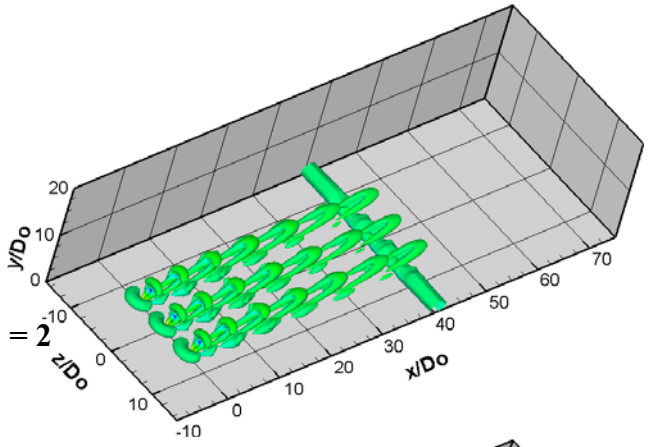

(a1) f = 5 Hz, L = 2

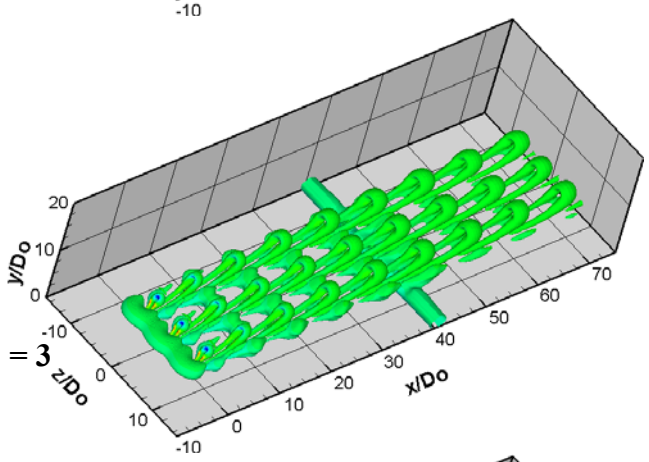

(a2) f = 5 Hz, L = 3

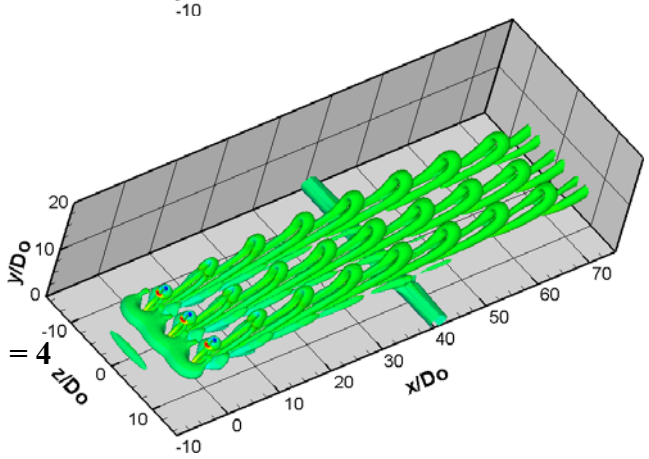

(a3) f = 5 Hz, L = 4

For caption see overleaf

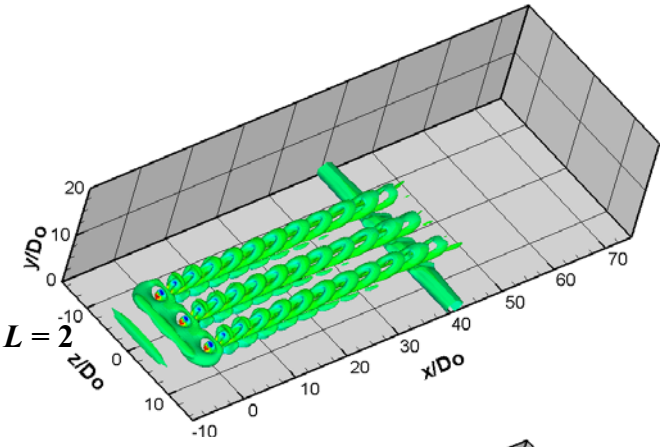

(b1) f = 9 Hz, L = 2

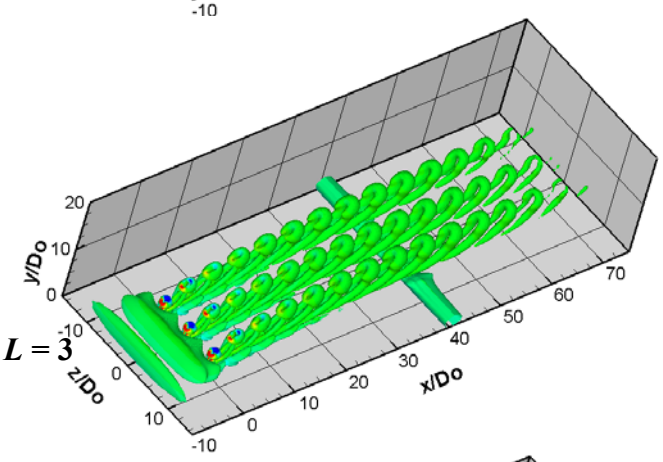

(b2) f = 9 Hz, L = 3

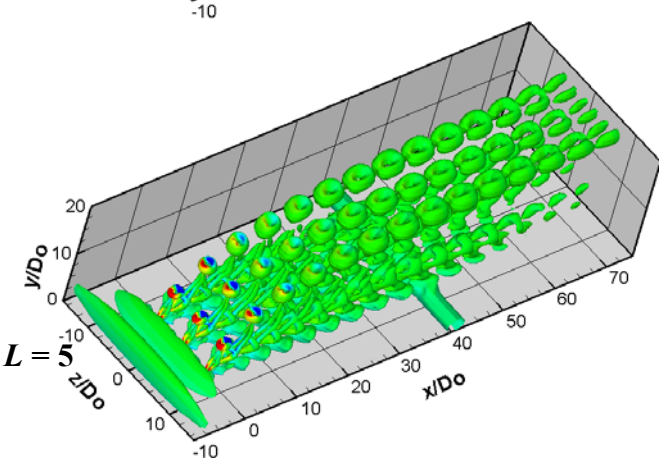

(b3) f = 9 Hz, L = 5

For caption see overleaf

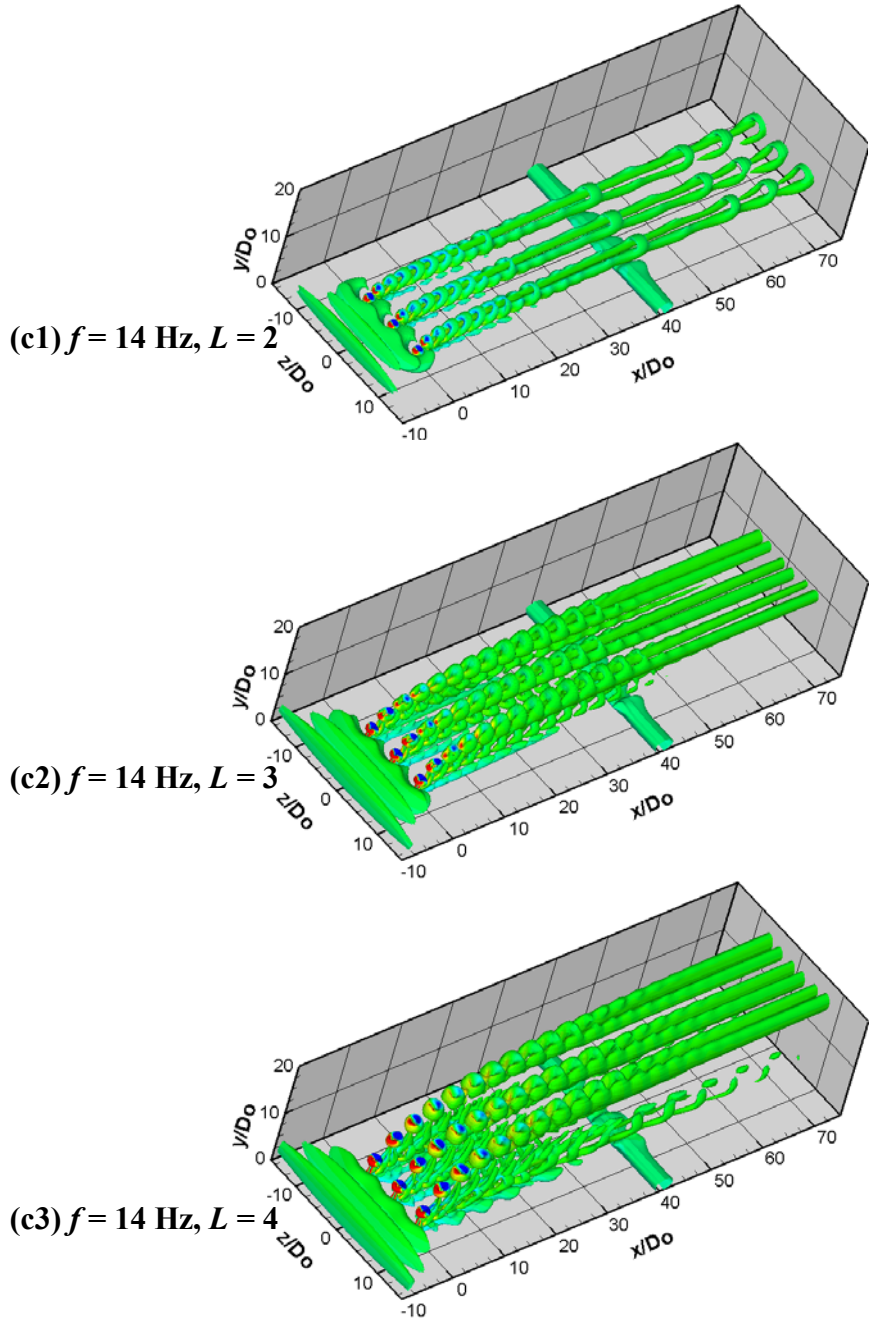

Figure 8.6. Iso-surface of Q = 1 showing the downstream development of coherent structures at (a) f = 5 Hz, (b) f = 9 Hz and (c) f = 14 Hz.

vortex ring trailed by a pair of counter-rotating legs, come out of the boundary layer within a short distance downstream. The formation and evolution of each type of vortical structures have already been discussed by the authors in their previous paper (Zhou and Zhong, 2009) hence will not be repeated here. At L = 2, the structures appear as hairpin vortices. At L = 3, the newly formed vortical structure has an intact vortex ring (Fig. 8.6b2). However, its upstream branch disappears gradually and only the downstream branch remains, resulting in a transformation for the structures from

tilted vortex rings to hairpin vortices further downstream. The transition from tilted vortex rings to hairpin vortices as the structures propagate downstream is caused by the upstream branch of the vortex rings being weakened and eventually cancelled out by the resident vorticity of the opposite sign in the boundary layer. At L = 5, secondary hairpin vortices are generated from the trailing legs of the tilted vortex ring structures, making the structures appear complex. The streamwise vortices induced by the counter-rotating trailing legs of the vortex ring in the near-wall region can also be observed.

Table 8.1 Operating conditions and dimensionless parameters of three group cases

Case	f (Hz)	Δ (mm)	VR	L	Re_L
Group 1	5	0.0237	0.2	2	79
		0.0355	0.3	3	178
		0.0474	0.4	4	318
Group 2	9	0.0237	0.36	2	143
		0.0356	0.54	3	321
		0.0593	0.9	5	895
Group 3	14	0.0237	0.56	2	222
		0.0356	0.84	3	499
		0.0474	1.12	4	889

At f = 5 Hz, the spacing between the consecutive structures increases as a result of a decrease in frequency. The dominant vortical structures at L = 2 to 4 are hairpin vortices with an increasing strength as L increases. The transition from tilted vortex rings to hairpin vortices observed at f = 9 Hz, L = 3 (Fig. 8.6a1) also takes place at f = 5 Hz, L = 4 but at a more upstream location. Although not shown here, tilted vortex ring type structures are seen to persist downstream at L > 5.

At f = 14 Hz, the agglomeration of consecutive structures is clearly seen as a result of the strong interaction between them. At L = 2, the closely spaced hairpin vortices agglomerate with each other to form a pair of streamwise vortices which subsequently breakdown into individual hairpin vortices further downstream over the inclined plate (Fig. 8.6c1). Similarly, at L = 3 and 4, closely spaced tilted vortex rings also transform into a pair of streamwise vortices (Figs. 8.6c2 and c3). It can be

seen that as L increases the downstream vortical structures are located further away from the inclined plate. In addition, the near-wall structures lose their coherence as they propagate downstream due to viscous dissipation, although their persistency is enhanced with an increase of L.

A parameter map showing the variations of vortical structures in the near-field of the jet orifices with the actuation frequency f and the dimensionless stroke length L for the present synthetic jet array is given in Fig. 8.7. The lines of constant VR are added to aid the comparison. The variations of the vortical structures produced by the synthetic jet array with changing actuator operating conditions are similar to those observed in a single jet issued from a 5 mm diameter orifice into a laminar boundary layer over a flat plate (Zhou and Zhong, 2010a).

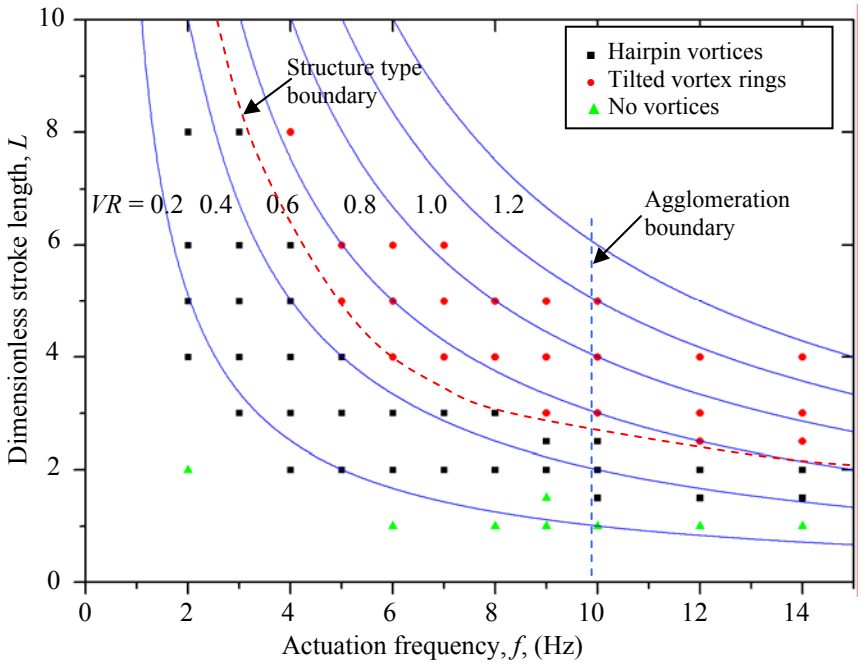

Figure 8.7. The parameter map showing the variations of vortical structures with changing synthetic jet operating conditions.

Overall, it can be seen that at $L < 2$, the vortical structures either are barely visible or disappear quickly soon after emerging out of the orifice exit due to the strong impact of the suction stroke. At $L \geq 2$, two types of vortical structures can be observed, i.e. hairpin vortices and tilted vortex rings based on the shape of the primary vortical structures. As shown by the red dash line, the approximate boundary between hairpin vortices and tilted vortex rings is located between $VR = 0.5$ and 0.6 for all frequencies examined here, with a trend of the boundary moving towards a

higher *VR* at $f > 8$ Hz. This trend can be explained as follows. In order to acquire the same *VR,* the dimensionless stroke length required at higher frequencies is lower resulting in the vortical structures being weaker. Therefore the upstream branch of the initial vortex ring tends to be weakened by the combined impact of the suction stroke and the resident vorticity in the boundary layer, favouring the formation of hairpin vortices. The agglomeration of consecutive vortical structures is observed at $f \geq 10$ Hz (equivalent to $Str \geq 1$). The agglomeration is seen to occur at a shorter distance downstream of the orifice exits at higher frequencies. After the agglomeration, the primary vortical structures transfer into pairs of quasi streamwise vortices.

8.4.2 Surface Shear Stress Patterns

The surface shear stress patterns produced by a single synthetic jet developing over a flat plate has been discussed in detail in the authors' previous papers (Zhou and Zhong, 2009, 2010a). It was found that hairpin vortices and tilted vortex rings produce two distinctly different surface shear stress patterns; the former generates two streaks of high surface shear stress outboard of the centreline of the orifice whereas the latter generates a single streak along the centreline. The formation mechanism of such different shear stress patterns has been explained by the authors (Zhou and Zhong, 2009). The two-streak pattern associated with the hairpin vortices is caused by the counter-rotating legs, which produce a downwash movement outboard of each leg bringing the fast, high momentum fluid from the outer part of the boundary layer to the near-wall region (Fig. 8.1a). Contrarily, the formation of a single streak by the tilted vortex rings is owing to the downwash movement on the streamwise central plane of the jet produced by the streamwise vortices which are induced by the trailing legs of the primary structure (Fig. 8.1b).

Figure 8.8 shows the corresponding time-averaged surface shear stress distributions of the cases shown in Fig. 8.6. It can be seen that for a synthetic jet array the pattern of surface shear stress downstream of each orifice is consistent with that observed in a single jet as described above. Nevertheless, depending on the pattern and strength of vortical structures, as they propagate downstream the streaks from adjacent orifices may merge as a result of their spanwise growth.

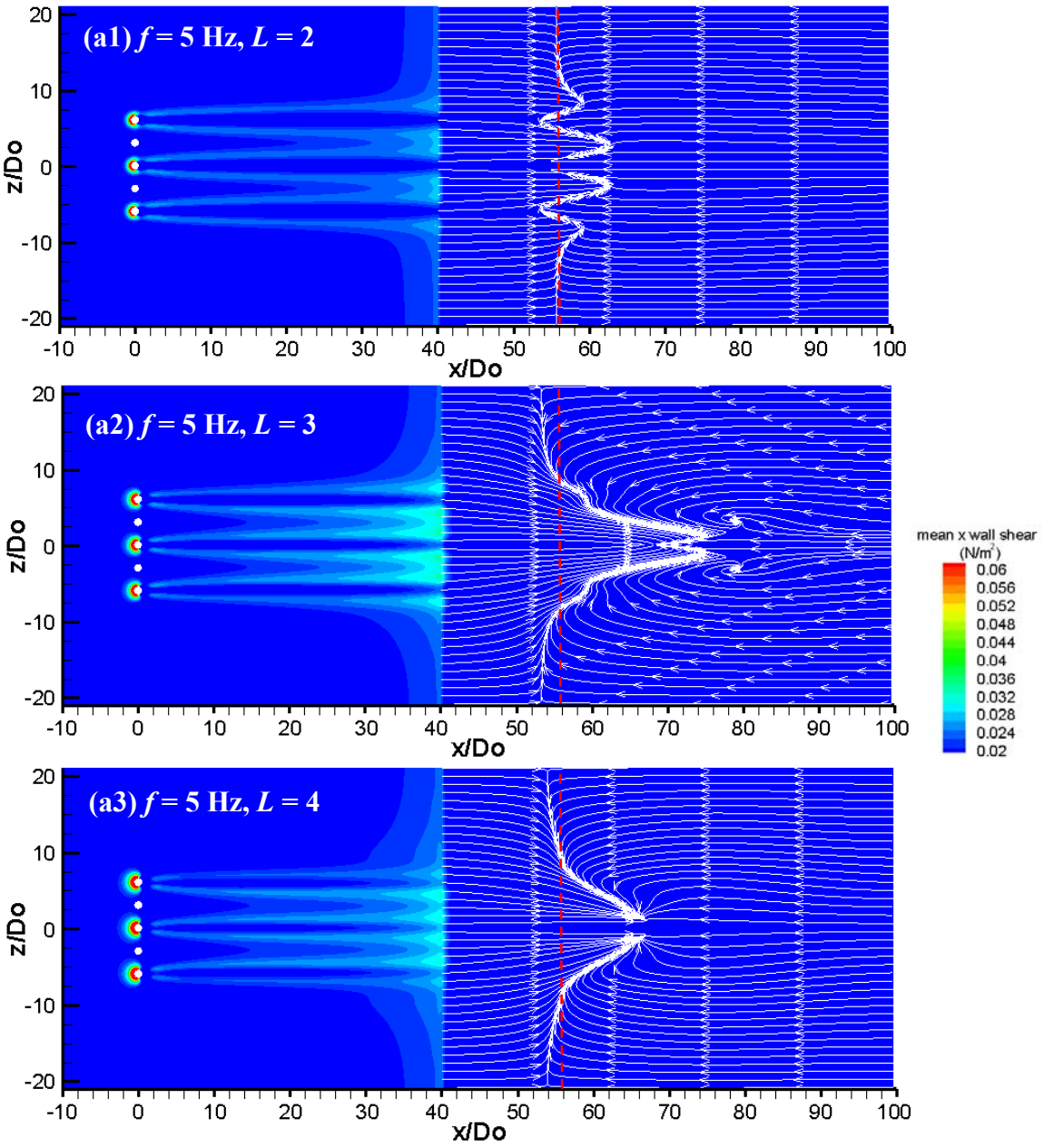

For caption see overleaf

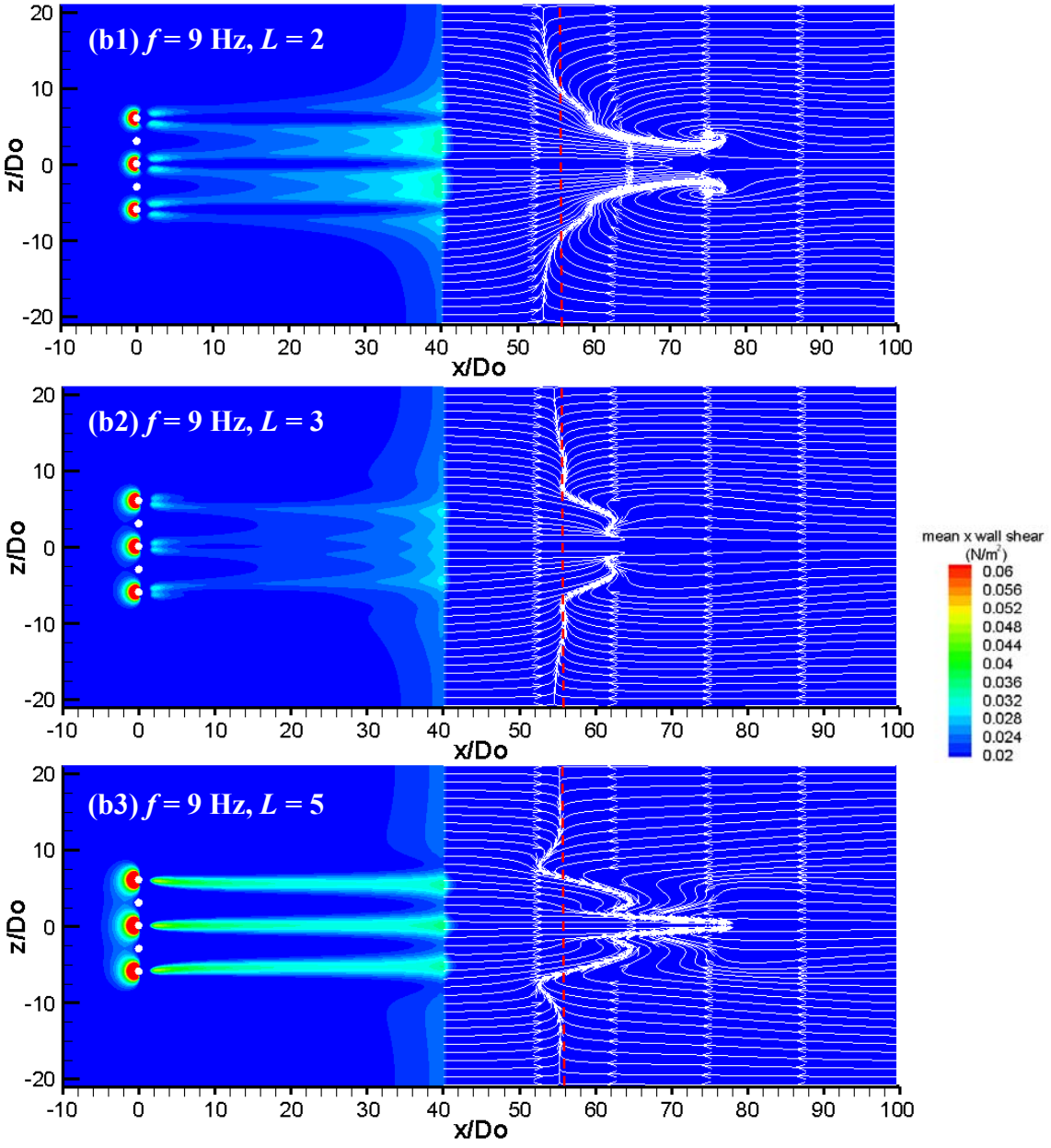

For caption see overleaf

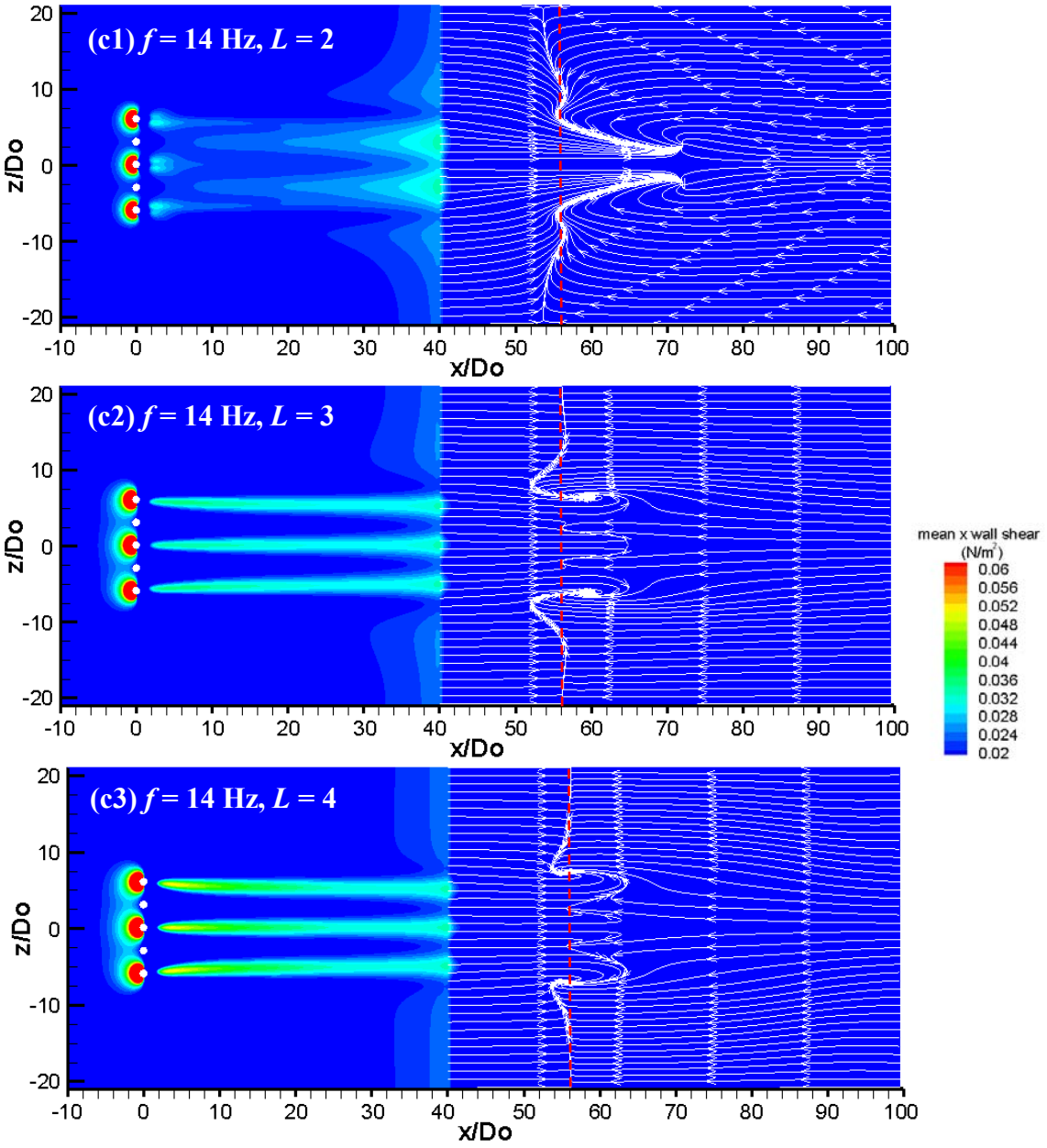

Figure 8.8. Patterns of time-averaged surface shear stress on the horizontal plate and skin friction lines over the inclined plate at (a) f = 5 Hz, (b) f = 9 Hz and (c) f = 14 Hz (The red dash line is the separation line of the baseline flow and x/D_o = 40 is the start of the inclined flap).

At the lowest dimensionless stroke lengths of the cases at f = 5 and 9 Hz, the hairpin type of vortical structures generated at each orifice produces the typical two-streak pattern as expected (Figs. 8.8a1 and b1). The streaks from the neighbouring orifice merge with each other downstream producing two stronger and thicker streaks at the end of the horizontal plate, one on each side of the middle jet. At f = 14 Hz, L = 2, the pattern of the surface shear stress changes, at some distances

downstream, from the typical two streaks behind each orifice to a single streak between two adjacent orifices due to vortex agglomeration (Fig. 8.8c1). The merger of streaks from adjacent orifices is also evident towards the end of the horizontal plate. In the case of the highest dimensionless stroke lengths at f = 9 and 14 Hz, strong tilted vortex ring type of structures is produced. The single streak of high shear stress from each orifice does not merge with each other hence remains distinct downstream (Figs. 8.8b3 and c3). The pattern of surface shear stress at f = 5 Hz, L = 4 and f = 9 Hz, L = 3 is also similar to that at the lower stroke lengths, but the level of surface shear stress is lower, reflecting the transitional nature of the vortical structures between the hairpin vortices and tilted vortex rings at these particular actuator operating conditions (Figs. 8.8a3 and b2).

To assess the accumulated impact of the synthetic jets on the boundary layer, the time-averaged surface stress in the area bounded by x/D_o = 2 to 40 and z/D_o = -3 to 3 is calculated for all the cases. The value is normalized by the corresponding value of the baseline case. The region of interest is chosen so as to focus on the effect of the middle jet and also to exclude the region with large fluctuations in surface shear around and immediately downstream of the jet orifice. From Fig. 8.9, it can be seen that a high surface shear stress increment (20% increase above the baseline value) only occurs with $VR > 0.2$ for $f < 6$ Hz and $L > 1.7$ for $f > 6$ Hz when the strength of the vortical structures becomes appreciable. The region of higher shear stress increment (shown in orange and red) can be divided into two zones; one is associated with the appearance of hairpin vortices with $VR < 0.6$, the other is featured by the presence of tilted vortex rings with $VR > 0.8$. There is a deduction in the increment of surface shear stress between these two zones across the entire frequency range due to the fact that the vortical structures undergo transition from one type to the other and tilted vortex rings have not yet gained a sufficient strength.

8.4.3 Flow Control Effect

8.4.3.1 Patterns of Skin Friction Lines on the Inclined Plate

In the current study, skin friction lines on the inclined plate are used to evaluate the long time-averaged flow control effect of the synthetic jet array. The skin friction lines indicate the direction of surface shear stress vectors, and thus they provide a visual description of the regions of attached and separated flow. The location of the

time-averaged separation line can be determined by the skin friction lines to which the shear stress vector as well as the skin friction vector is everywhere tangential (Lighthill, 1963). To aid the comparison, the separation line of the baseline flow which is located at $56D_o$ downstream of the orifices is also shown (the red dash line). The patterns of skin frictions lines for the cases shown in Fig. 8.6 are presented in Fig. 8.8.

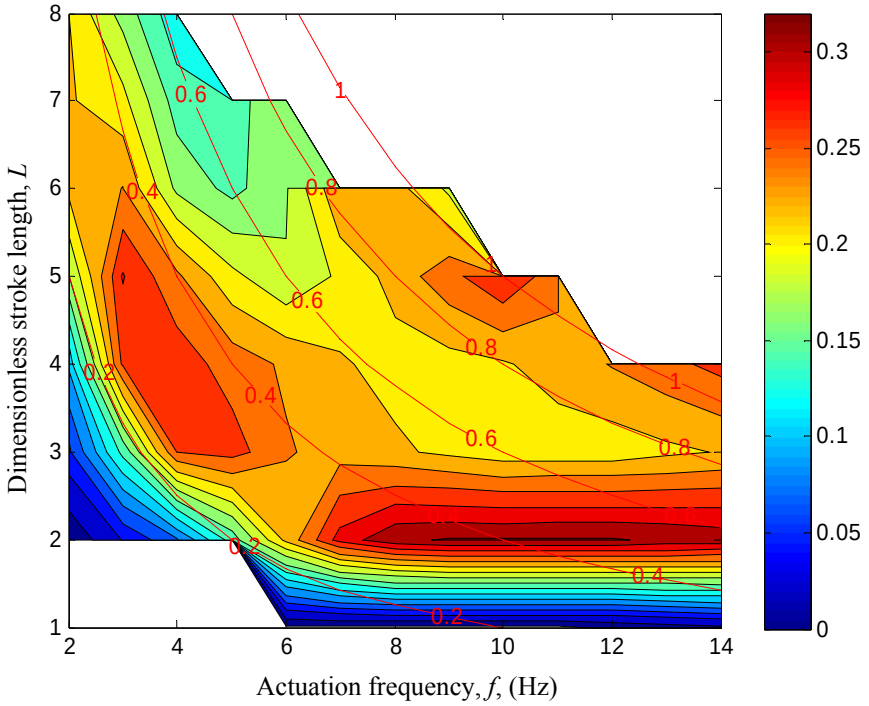

Figure 8.9. The gain of non-dimensional time-averaged surface shear stress in the specified area.

At f = 9 Hz, L = 2, the pattern of skin friction lines shows a clear correspondence to the shear stress pattern observed on the flat plate (Fig. 8.8b1); two strong streaks of attached flow accompanied by two weak outboard streaks extrude downstream, whose spanwise locations are nearly aligned with the streaks of high surface shear stress upstream of the flap. The separation line exhibits a wavy manner in the spanwise direction with the attached flow extending up to $77D_o$ downstream of the orifice exit, approximately. At L = 5, three streaks of attached flow are observed. The pattern of the skin friction lines also shows a clear correspondence to the shear stress pattern at the end of the plate, although the middle streak stretches much further downstream to x/D_o = 78 (Fig. 8.8b3). This is probably because the induced streamwise vortices from the two side jets are weakened more significantly due to

the end effect. In comparison to the above two cases, the flow pattern on the flap at L = 3 is relatively smoother due to a less fluctuated shear stress pattern from upstream (Fig. 8.8b2). The maximum extruding length of the streaks is smaller in comparison to the case at L = 2, to about x/D_o = 63. The smoother separation line at L = 3 reflects the transitional nature from two streaks of attached flow to three streaks of this case.

For the cases at f = 5 Hz, the pattern of skin friction lines and its variation with the increase of L is similar to that at f = 9 Hz. Due to the weak nature of vortical structures, the level of separation delay at L = 2 is only marginal. Benefiting from the merger of the high surface shear stress streaks from adjacent orifices, a significant separation delay downstream of the middle jet with the attached flow reaching up to x/D_o = 75 can be observed at L = 3 (Fig. 8.8a2). The separation line at L = 4 becomes smoother due to the transition of vortical structures in the near-field. However, the delay in flow separation becomes worse with the attached flow only extending to x/D_o = 67 (Fig. 8.8a3).

At f = 14 Hz, despite of the formation of large-scale streamwise vortices downstream of the jet orifices as a result of agglomeration of consecutive structures, the pattern of skin friction lines experiences a similar change with an increasing in L as discussed above. The two-streak pattern is observed at L = 2 with the attached flow extending to x/D_o = 72 due to the proximity of the large-scale streamwise vortices to the wall. Whereas at L = 3 and 4, the three-streak pattern can be seen with the attached flow extending to x/D_o = 64. It is noted that an increase of L from 3 to 4 does not produce a further delay in separation at this frequency.

8.4.3.2 Time-Averaged Flow Control Effect

In order to evaluate the flow control effect of the synthetic jet array quantitatively, the streamwise coordinate of the space-averaged separation line along a spanwise width of $6D_o$ across the middle jet is calculated. Then the difference between this coordinate and the streamwise coordinate of the separation line in the region unaffected by the synthetic jet array is found. Finally, the flow control effectiveness is obtained as the ratio between the above coordinate difference and the length of the flap. The flow control effectiveness as defined above for all the cases examined in this study is presented as a contour in the space of dimensionless stroke length and diaphragm frequency in Fig. 8.10.

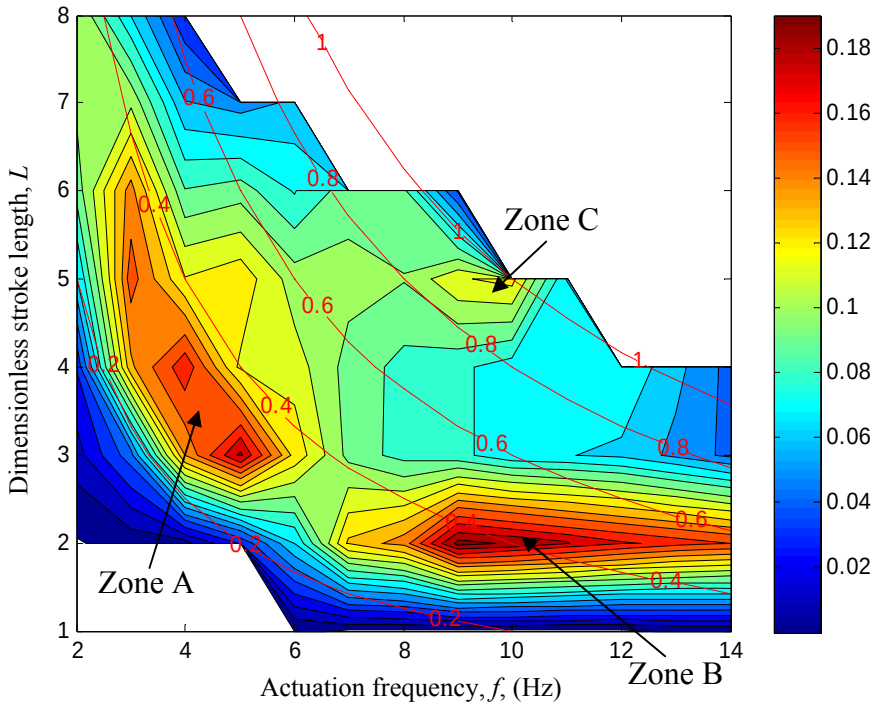

Figure 8.10. Contours of non-dimensional flow control effect.

The regions with noticeable flow control effect can be divided into three zones. For $f < 6$ Hz, a region of good control effect occurs at around $0.25 < VR < 0.4$ (Zone A). For $f > 6$ Hz, it occurs at around $L = 2$ with $0.3 < VR < 0.6$ (Zone B). There is also an additional small region with a less significant flow control effect with f around 9 Hz and $0.8 < VR < 1$ (Zone C). According to the flow patterns shown in Fig. 8.7, the primary structures in both Zone A and Zone B are hairpin vortices and those in Zone C are tilted vortex rings.

The gap between Zone A and Zone B associated with a weaken flow control effect can be explained as follows. At low frequencies ($f < 6$ Hz), a dimensionless stroke length greater than 3 is required to produce $VR = 0.25$~0.4, resulting in the formation of relatively strong individual hairpin structures. As the frequency increases, the value of L required for producing $VR = 0.25$~0.4 reduces and thus the strength of the hairpin vortices weakens such that the control effect decreases. Nevertheless, as the frequency increases further ($f > 8$ Hz), the consecutive hairpin vortices become closely packed together, resulting in a stronger effect in the near-wall region even though they are relatively weak individually. Similar observations are also made in the experiments by Zhang and Zhong (2010a).

Overall, based on Fig. 8.10 the flow control effectiveness of hairpin vortex type of structures appears to be stronger than that of the tilted vortex ring type of structures. Comparing Figs. 8.9 and 8.10, some correlations seem to exist between the level of increment of surface shear stress on the upstream flat plate and the time-averaged control effect over the downstream flap. It is seen that at $VR < 0.6$ the regions of good control effect (Zone A and Zone B) coincide with the regions of high surface shear stress. However, for the region at $VR > 0.8$ (Zone C), despite of the gain of surface shear stress on the upstream plate being reasonably large, the control effect on the flap is comparably weaker.

8.4.4 Analyses of Selected Cases

Based on the discussions in the above section, a general consensus can be obtained, i.e. hairpin vortices produced at relatively low *VR* are the more promising candidate for delivering an effective flow separation delay. This seems to suggest that, although the induced streamwise vortices produced by the trailing legs of tilted vortex rings are located close to the wall, they are less effective than the hairpin vortices in enhancing near-wall mixing. On the other hand, the flow control effect of hairpin vortices does vary as the synthetic jet operating condition changes indicating that hairpin structures of certain characteristics are more favourable. In this section, the location and strength of the vortical structures of a few selected cases will be examined and the possible link between the desired flow control effect and characteristics of the vortical structures will be investigated. These cases are chosen around the three zones where a good flow control effect is observed, which include three cases at $f = 5$ Hz ($L = 2$, 3 and 4) in Zone A and three cases at $f = 9$ Hz ($L = 2$, 3 and 5) which stretches across both Zone B and Zone C. Note that among them the case at $f = 5$ Hz, $L = 3$ is the best flow control case in Zone A, that at $f = 9$ Hz, $L = 2$ is the best flow control case in Zone B and that at $f = 9$ Hz, $L = 5$ is close to the best flow control case in Zone C.

The contours of phase-averaged spanwise vorticity for these cases are shown in Fig. 8.11 from which the trajectories of the primary vortical structures generated by the middle synthetic jet can be observed. For the cases at $f = 5$ Hz in Zone A, the strongest flow control effect occurs at $L = 3$. At $L = 3$, the vortical structures start to come out of the boundary layer from $x/D_o = 10$ and reach $y/\delta = 1.3$ before the start of

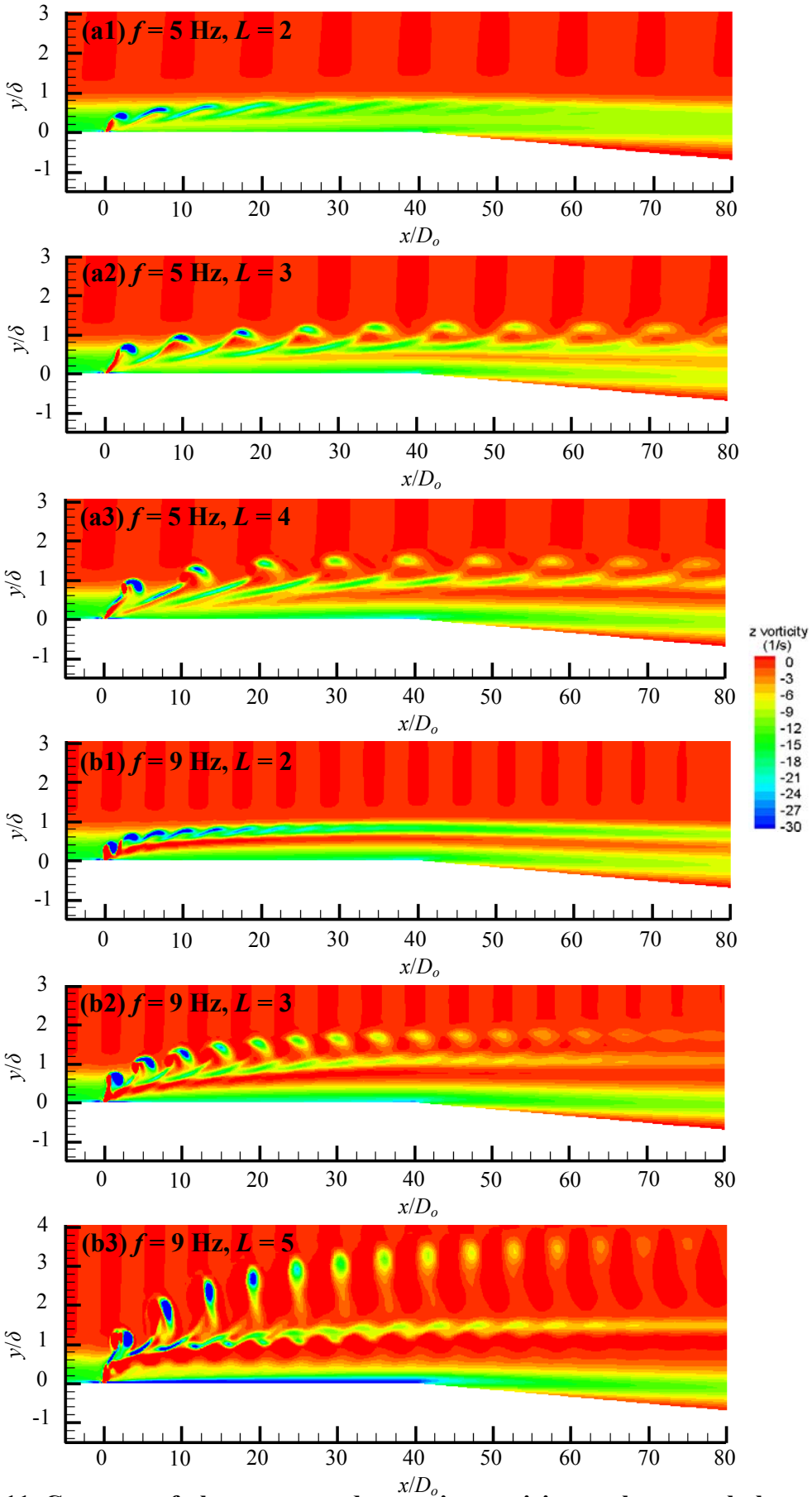

Figure 8.11. Contours of phase-averaged spanwise vorticity on the central plane of the middle jet for the cases at (a) $f = 5$ Hz and (b) $f = 9$ Hz.

the flap (Fig. 8.11a2). Compared to the cases at the same frequency but at different stroke lengths, it is clearly seen that at $L = 2$ the hairpin vortices are fully embedded in the boundary layer with a maximum height reaching $y/\delta = 0.8$ whereas at $L = 4$ the vortical structures are located further away from the wall reaching $y/\delta = 1.6$ at the end of the horizontal plate. For the case in Zone B at $f = 9$ Hz, at $L = 2$ the hairpin structures are confined within the boundary layer with a maximum height up to $y/\delta = 1$ (Fig. 8.11b1). As L increases to 3, the structures come out of the boundary layer within $5D_o$ downstream of the orifice exit (Fig. 8.11b2). At $L = 5$, the primary structures are tilted vortex rings which reach as far as $y/\delta = 3$ before the start of the flap (Fig. 8.11b3).

The information about the location and strength of the near-wall structures, which are responsible for entraining high momentum fluid from the outer part of the boundary layer to the near-wall region, can be extracted from the streamwise vorticity contours on cross-flow planes. The circulation magnitude and the location of the legs of hairpin vortices and the induced streamwise vortices as the structure passes a given streamwise plane during an actuation cycle are shown in Fig. 8.12. The circulation is found by integrating the streamwise vorticity over the region where the structure of interest occupies. The location of the structure from the wall is obtained as where the maximum vorticity is located. As shown in Fig. 8.12, for a given hairpin vortex the level of circulation of the hairpin leg decreases along its length in the upstream direction as it gets closer to the wall. As expected, the level of circulation increases as L increases which is particularly obvious for $f = 5$Hz at $x/D_o = 5$ (Fig. 8.12a1). When the structure propagate downstream to $x/D_o = 40$, its level of circulation is reduced substantially, especially for the weakest case of $f = 5$ Hz, $L = 2$.

It is understandable that, for a given boundary layer flow, streamwise vortical structures with both stronger vortex strength and a closer location to the wall, where the velocity gradient is larger, will favour the mixing in a boundary layer subsequently lead to a better flow control effect. It can be seen by comparing the three cases at $f = 5$ Hz (Fig. 8.12) that at a given frequency as L increases the strength of the hairpin vortices increases as the same time they move further away from the wall. This is also true for the two hairpin vortex cases at $f = 9$ Hz. In both Zone A and Zone B, the best flow control effect ($f = 5$ Hz, $L = 3$ and $f = 9$ Hz, $L = 2$) occurs when the limbs of the hairpin vortices are within $2D_o$ in the near-field and around $2.5D_o$ (about a half of the local boundary layer thickness) in the far-field. It is

believed that although the legs of hairpin vortices in the case of f = 5 Hz, L = 2 are closer to the wall, its strength is insufficient to be effective. Based on the above observations, it appears that a compromise exists between the location of the hairpin structures and their strength so as to produce a good control effect. In addition, the ability of the structures remaining in this location as they propagate further downstream also appears to be important. This ensures that the limbs of these structures stay in the region where a relatively high velocity gradient in the boundary layer is present, which is beneficial to enhancing mixing.

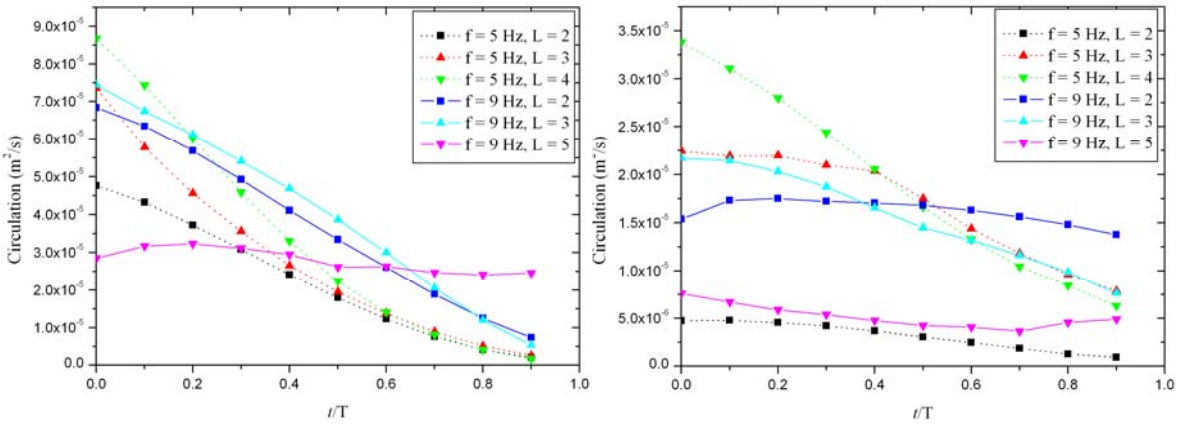

(a1) circulation at x/D_o = 5 **(a2) circulation at x/D_o = 40**

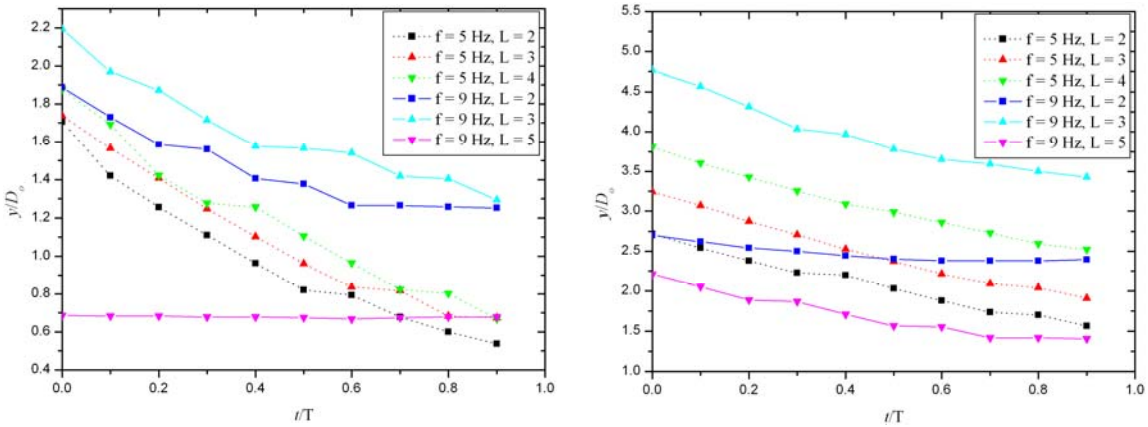

(b1) vortex location at x/D_o = 5 **(b2) vortex location at x/D_o = 40**

Figure 8.12. The strength and location of the near-wall structures at x/D_o = 5 and 40 for the cases at f = 5 and 9 Hz.

As the velocity ratio is a primary parameter which determines the trajectory of the vortical structures in a given boundary layer, it is therefore not surprised that the cases with a good flow control are correlated with the velocity ratio. Since the same range of desirable velocity ratio can be produced with either a combination of a low frequency and a high stroke length or a high frequency and a low stroke length,

the question remains to be addressed is which hairpin vortex generated in the above two scenarios would be more effective in delaying flow separation. Comparing the two best hairpin vortex cases at f = 5 and 9 Hz, one can see that the individual structures at f = 9 Hz, L = 2 are weaker due to the use of a lower L and the spacing between consecutive structures is smaller. The closer spacing also results in a mutual interaction which suppresses the uplifting of the vortex head. Since among the two cases, the flow control effect of the case with f = 9 Hz and L = 2 is stronger, it appears that a lower jet trajectory and a closer spacing are beneficial which compensates for the weaker nature of the structures. On the other hand, as shown in Fig. 8.6 if the spacing between consecutive structures continues to decrease as a result of an increase in frequency, these structures will interact and merge into large-scale streamwise vortices which are located further away from the wall leading to a reduction in the flow control effect.

For the case in Zone C at f = 9 Hz, L = 5, the induced streamwise vortices appear to be weaker than the trailing legs of the tilted vortex rings which produce them. Furthermore, in the orifice near-field the vorticity level of these induced streamwise vortices is much lower than that of hairpin vortices observed in the other selected cases. By the time they arrive at x/D_o = 40, their strength has been reduced considerably and become very dissipated. Nevertheless, these induced streamwise vortices are located much closer to the wall producing a high localised peak surface shear stress as shown in Fig. 8.8b3.

In order to examine the differences in the near-wall impact of hairpin vortex type and tilted vortex ring type of structures, the spanwise distributions of surface shear stress at x/D_o = 5, 40 and 50 of the cases at f = 5 Hz, L = 3; f = 9 Hz, L = 2 and f = 9 Hz, L = 5 are shown in Fig. 8.13. The blue line shows the shear stress of the baseline flow. It can be seen that the hairpin vortex type of structures obtained at f = 5 Hz, L = 3 and f = 9 Hz, L = 2 produce two peaks with one at each side of the middle jet whereas the tilted vortex ring type of structures obtained at f = 9 Hz and L = 5 produce a single peak downstream of the middle jet. It is also seen that at f = 9 Hz, L = 5 despite an initial high peak surface shear stress in the near-field as a result of a high momentum injection associated with a higher velocity ratio, the magnitude of the peak surface shear stress decreases rapidly and it is reduced to the same level as in the other two hairpin vortex cases by the end of the horizontal plate at x/D_o = 40 (Fig. 8.13b). Furthermore, although the peaks of surface shear stress broaden

downstream, the surface shear stress in the region between adjacent jets remains low at f = 9 Hz, L = 5. In contrast, in the case of hairpin vortices the level of shear stress between the adjacent jets is increased considerably downstream as a result of the overlapping of the effect of neighbouring jets for the given jet spacing examined in this work. As such, the space-averaged surface shear stress across the span in the tilted vertex ring case remains relatively lower over a substantial distance downstream along the horizontal plate (Fig. 8.14) and this results in a lower area-averaged surface shear stress as shown in Fig. 8.9. It is also can be seen in Fig. 8.13c that at streamwise location over the flap just before the baseline separation line the surface stress between the adjacent jets for the tilted vortex ring case remains to be low and even falls below the level of the minimum surface shear stress of the hairpin vortex cases. Consequently, on a spanwise averaged sense the increment in the surface shear stress is lower and the ability of the tilted vortex ring structures in delaying flow separation is hampered.

(a)

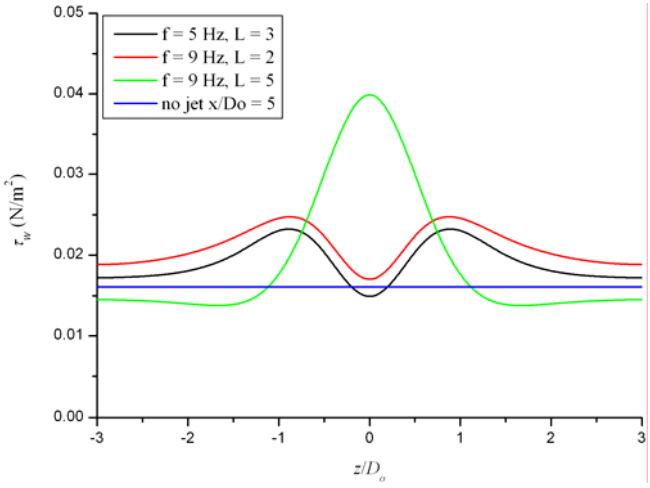

(b)

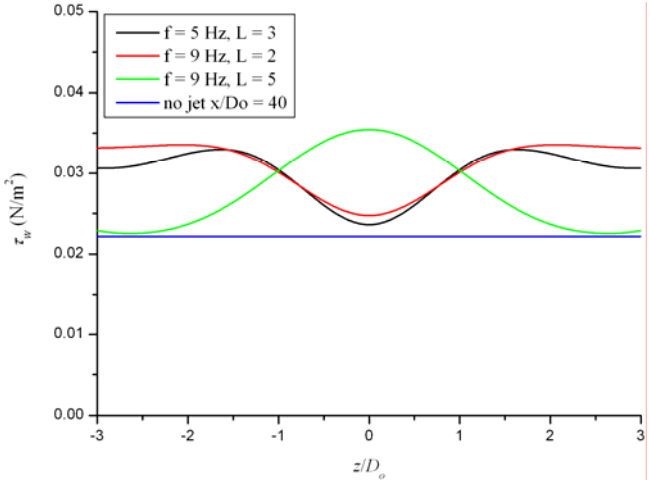

For caption see overleaf

(c)

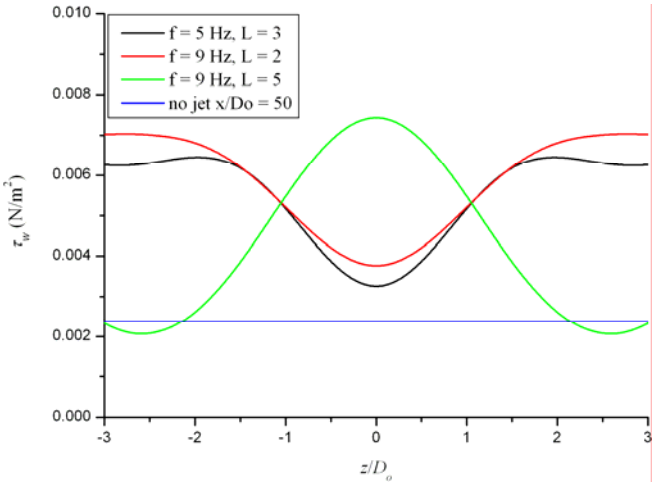

Figure 8.13. Spanwise distributions of the time-averaged surface shear stress at (a) x/D_o = 5, (b) x/D_o = 40 and (c) x/D_o = 50 for the cases at f = 5 Hz, L = 3; f = 9 Hz, L = 2 and f = 9 Hz, L = 5.

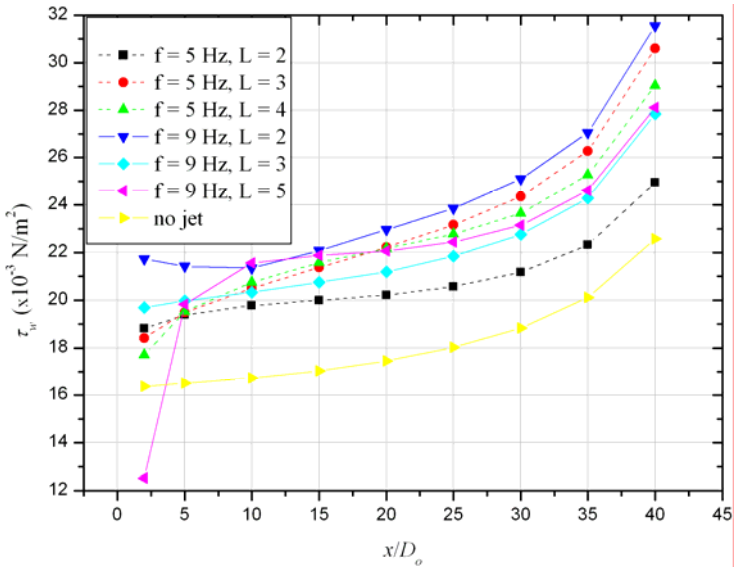

Figure 8.14. Streamwise distributions of spanwise-averaged surface shear stress for the cases at f = 5 Hz, L = 2, 3 and 4, and f = 9 Hz, L = 2, 3 and 5.

To investigate the role of vortical structures in producing the separation delay, the development of the instantaneous coherent structures produced by the middle jet over the inclined plate and the separation bubble indicated by the iso-surface of zero streamwise velocity are presented in Fig. 8.15. Here, the Q value is decreased to 0.1 so as to reveal all the possible beneficial structures. It is found that the hairpin vortices generated at f = 5 Hz, L = 3 are capable of maintaining their coherence over a significant distance downstream over the flap (Fig. 8.15a2). Contrarily, the hairpin vortices at f = 9 Hz, L = 2 evolve into a pair of streamwise vortices shortly after

arriving at the flap, and lose their coherence before reaching above the separation bubble (Fig. 8.15b1). In all cases no coherent structures are revealed in the separated shear layer (Fig. 8.15). These observations seem to suggest that the flow separation delay produced in these cases is more likely to be caused by the accumulated impact of these structures on the boundary layer upstream rather than the local interaction of these structures with the separated flow.

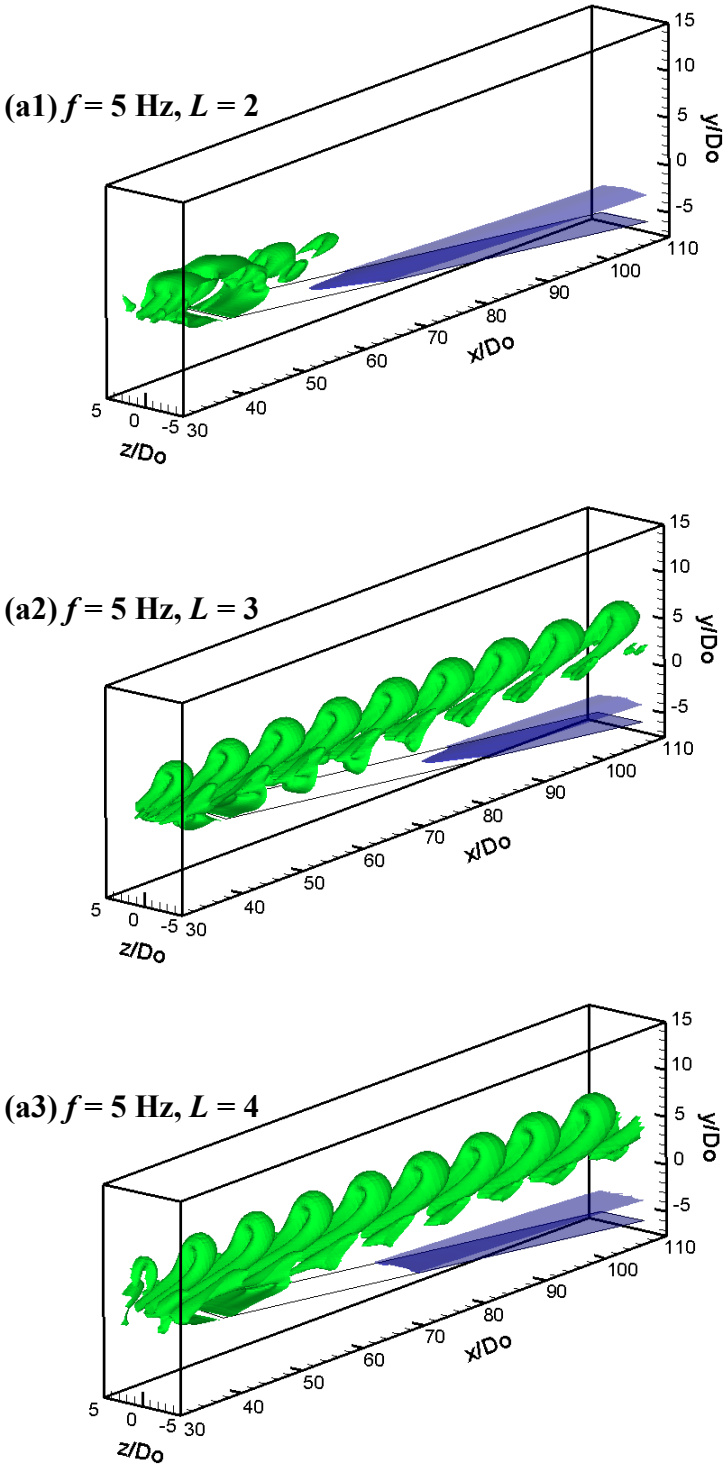

For caption see overleaf

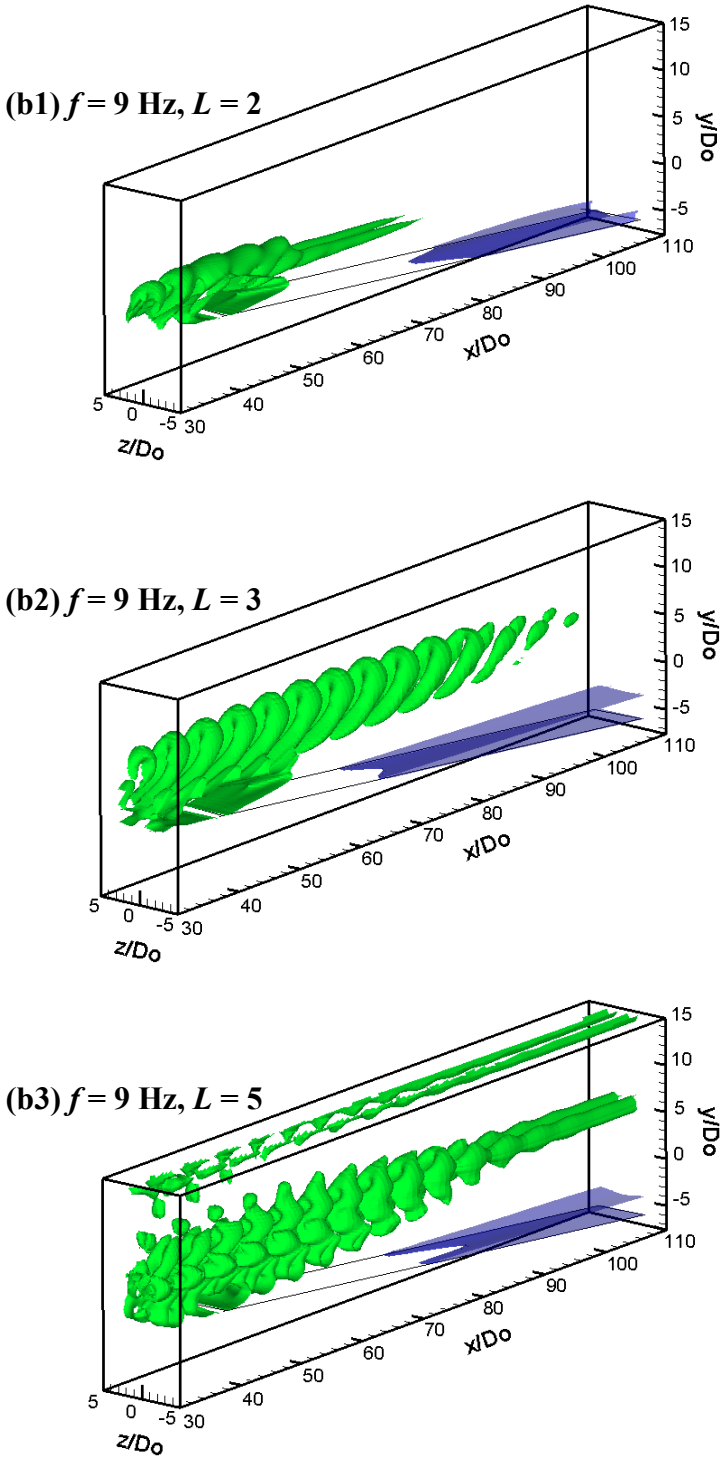

Figure 8.15. Iso-surface of $Q = 0.1$ showing the instantaneous coherent structures produced by the middle jet in relation to the separation bubble over the flap for the cases at (a) $f = 5$ Hz and (b) $f = 9$ Hz.

8.4.5 Power Consumption for Synthetic Jets

For practical applications, it is not only the extent of flow separation delay but also the power required for the synthetic jet actuator to deliver the flow control effect that

should be considered. The desired synthetic jet operating conditions would be those which produce a given control effect with a minimum amount of input power.

The acoustic power required for oscillating diaphragm at a given displacement and frequency has been taken as a measure of the energy consumption of an actuator by a number of researchers. It can be calculated as (Swift, 2002)

$$\dot{E} = \frac{1}{T}\int_0^T p(t)\dot{V}(t)dt \tag{8.1}$$

where p is the pressure acting on the area of the diaphragm at its neutral position, and $\dot{V}$ is the volume flow rate at the corresponding area. Essentially, the acoustic power represents the power that is required to oscillate the diaphragm at the prescribed conditions by working against the pressure difference between the front and back side of the diaphragm. From Fig. 8.16, it can be seen that the required acoustic power increases with an increase of VR and the operating conditions having the same VR appear to require a similar level of acoustic power.

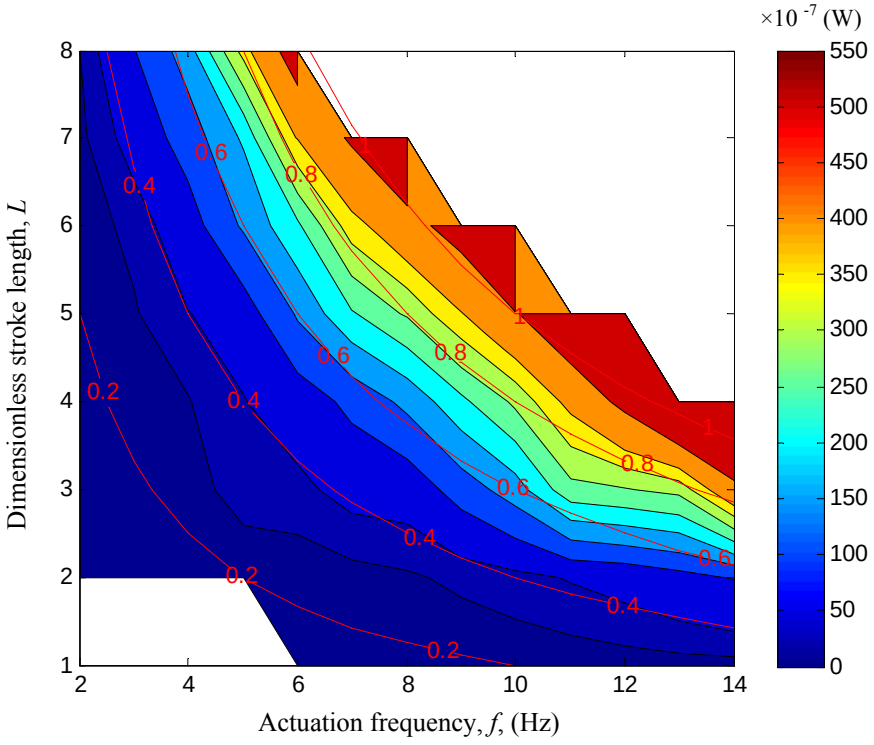

Figure 8.16. Contours of acoustic power required for oscillating the diaphragm.

The time-averaged electrical power consumption was also obtained in the experiments by measuring the temporal variations of current and voltage supplied to the shaker (Zhang and Zhong, 2010a), as shown in Fig. 8.17. It includes the power

required to overcome the pressure difference across the oscillating diaphragm, to drive the mass of the diaphragm assembly to undergo a sinusoidal motion at a given frequency and displacement, to work against the deformation of the rubber diaphragm and to overcome the mechanical and electrical losses in the shaker. As shown in Fig. 8.17, over the experimental range the power consumption increases more sharply with an increasing diaphragm displacement than with an increasing frequency such that at the same *VR* the power consumption is lower when the actuator is operated at a higher frequency.

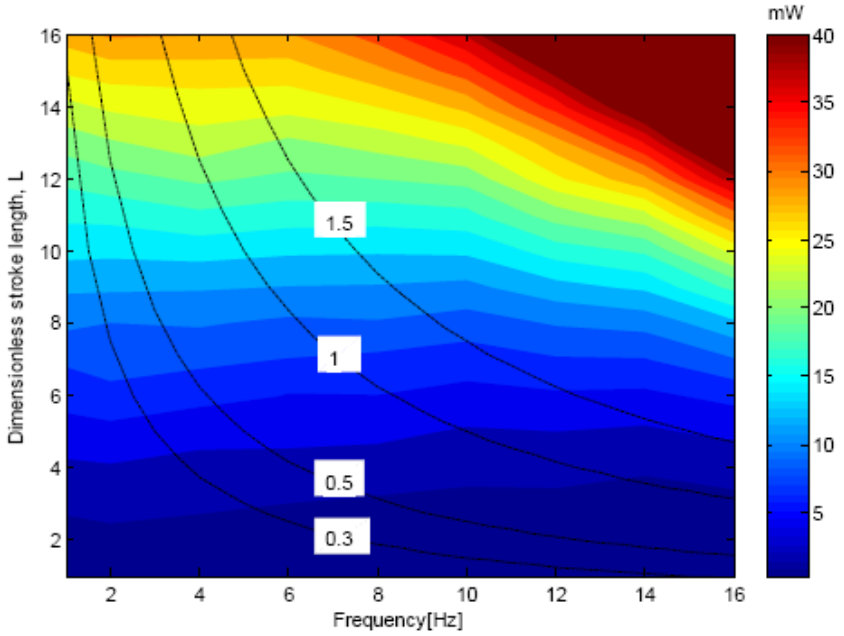

Figure 8.17. Contours of power consumption of the synthetic jet actuator (Zhang and Zhong, 2010a).

It is noted that in the current study, the acoustic power is almost three orders of magnitude smaller than that of the electrical power consumption. This is because the acoustic power does not take into account of all the types of power assumptions as mentioned above, except for the power required to overcome the pressure difference across the oscillating diaphragm. Hence the acoustic power is insufficient to characterise the energy requirement for the synthetic jets, at least for the shaker driven actuator used in the present study. Consequently, the time-averaged electrical power consumption will be used to evaluate the flow control efficiency.

Among the three best cases discussed in section 8.4.4, the performance of the case at f = 9 Hz, L = 2 appears to be most efficient, because that it not only yields a

maximal separation delay but also consumes a less amount of energy (Table 8.2). The tilted vortex rings at f = 9 Hz, L = 5 is less efficient among the three cases because of two reasons. Firstly, most of the energy input to the actuator is used to create vortical structures which move out the boundary layer quickly once they are formed. Secondly, although the induced streamwise vortices are located very close to the wall, they are found to produce a localised effect which restrict the impact of the jet in the spanwise direction whereas the hairpin vortex type structures are likely to benefit from the overlapping of the effect from the adjacent jets in the array.

Table 8.2 Power consumption and flow control effect of the synthetic jet actuator for the three best cases.

case	f = 5 Hz, L = 3	f = 9 Hz, L = 2	f = 9 Hz, L = 5
Power consumption (mW)	2.2	0.8	4.1
Non-dimensional Flow control effect	0.18	0.19	0.12

Overall, the operating condition at around f = 9 Hz, L = 2 is the optimal one among all the conditions examined in the current study, due to its significant control effect and high control efficiency. The operating conditions specified using dimensionless parameters for this case is L = 2 and VR = 0.36. The Strouhal number is 0.9 corresponding to a streamwise spacing between the consecutive hairpin-like structures of about 70% of the local boundary layer thickness at the jet orifices. Nevertheless, as the level of interaction between neighbouring synthetic jets and their flow control effectiveness are expected to alter upon changes in the jet spacing and the distance between the orifices and the baseline separation line, the generality of the above finding remains to be established in the future work.

8.5 Conclusions

In this paper, flow separation control using an array of circular synthetic jets issued into a laminar boundary layer which separates downstream over an inclined plate is investigated using 3D numerical simulations. The simulations are undertaken using FLUENT at a wide range of actuator operating conditions. The aims of this work are to identify the range of actuator operating conditions which yield the best flow

separation delay, and to examine the characteristics of the associated vortical structures and their near-wall effect with the aid of the simulation results.

Based on the large number of cases simulated, a parameter map illustrating the appearance of the primary vortical structures in the orifice near-field has been established. The parameter map can be divided into two regimes; one is characterised by hairpin vortices and the other by tilted vortex rings. The approximate boundary between these two types of vortical structures is located between $VR = 0.5$ and 0.6, with a trend of the boundary moving towards a higher VR at $f > 8$ Hz. The impact of the middle synthetic jet in the array on the boundary layer prior to separation is evaluated by examining the space- and time-averaged surface shear stress. The regions with high surface shear stress increment relative to the baseline case is divided into two zones; one is associated with the appearance of hairpin vortices with $VR < 0.6$, the other is featured by the presence of tilted vortex rings with $VR > 0.8$.

The flow control effect of the middle jet is also quantified by examining the time-averaged location of the separation line. It is found that the hairpin vortex type of structures is capable of delivering a stronger flow control effect than the tilted vortex ring type of structures and this is correlated with the fact that the former also produces a higher surface shear stress increment. By analysing selected cases at two actuation frequencies ($f = 5$ and 9 Hz), it is found that the best flow control effect occurs when the maximum height of the hairpin structures is about that of the boundary layer with their limbs located at about a half of the boundary layer height. Among all the conditions examined in the current study, operating the synthetic jets at $L = 2$ and $VR = 0.36$ which yields hairpin-like structures with a streamwise spacing about 70% of the local boundary layer thickness at the jet orifices is found to produce the best flow control effect with the lowest power consumption. The evidence from this study also suggests that the flow separation delay produced by the synthetic jet array investigated here is due to the accumulated effect of the vortical structures on the boundary layer as they propagate downstream, rather than the local interaction of these structures with the separated flow. Nevertheless, as the level of interaction between neighbouring synthetic jets and their flow control effectiveness are expected to alter upon changes in the jet spacing and the distance between the orifices and the baseline separation line, the generality of the above finding remains to be established in the future work.

Chapter 9 Conclusions and Recommendations

9.1 Conclusions

The aims of this thesis as given in Chapter 1 were:

> *To achieve an improved understanding of the parameters that affect the formation of vortex rings produced by synthetic jets in quiescent conditions towards developing a vortex roll-up criterion for synthetic jets, and the behaviour of synthetic jets issued into an attached laminar boundary layer and a separated laminar boundary layer in relation to the evolution of vortical structures, their impact on the boundary layer, and the flow control effect, such that the optimal operating conditions which produce the desired vortical structures with the highest flow control effectiveness and lowest power consumption for flow separation control can be identified.*

In order to achieve these aims, a series of objectives were specified using computational fluid dynamics (CFD) techniques to investigate synthetic jets issued into quiescent conditions, a zero-pressure-gradient laminar boundary layer and a laminar boundary layer which separates further downstream over an inclined plate. 2D and 3D simulations of circular synthetic jets with/without a cross flow were carried out by FLUENT. The adequacy of the chosen computational domain and boundary conditions has been validated and a sensitivity study of grid and time step size has been undertaken. For a single synthetic jet interacted with a zero-pressure-gradient laminar boundary layer, the capacity of FLUENT was evaluated for two typical test cases. The good agreement between the simulation results and the experimental data from Jabbal and Zhong (2008) confirmed that FLUENT is fully capable of capturing the key characteristics of synthetic jets in a laminar boundary layer. For an array of synthetic jets interacted with a laminar boundary layer which separates further downstream, the capacity of FLUENT was assessed by comparing the simulation results with the measured data from Zhang and Zhong (2010a) for both baseline flow and actuated flow. Both qualitative and quantitative agreements have been achieved proving that FLUENT is also capable of reproducing the key

features of an array of synthetic jets and its interaction with a separated laminar boundary layer.

In broad terms, the thesis has demonstrated an improved understanding of the behaviour of synthetic jets in quiescent conditions, the interaction of synthetic jets with an attached boundary layer and a separated boundary layer, and the capability of synthetic jets in delaying boundary layer separation.

Significant progresses have been achieved in establishing the criterion of vortex roll-up for synthetic jets, identifying the typical vortical structures and their corresponding surface shear stress patterns produced by the interaction of synthetic jets with an attached boundary layer, and establishing the relationship between the impact of synthetic jets on the boundary layer prior to separation and the extent of separation delay on the inclined flap. In addition, based on a number of numerical simulation results, a series of parameter maps have been provided concerning the different regimes of synthetic jets in quiescent conditions, different types of vortical structures and surface shear stress patterns for synthetic jets in an attached boundary layer and a separated boundary layer, the flow separation control effect of the synthetic jet array issued into a separated laminar boundary layer, and the acoustic power required for oscillating diaphragm. In the end, a guidance to select the optimal operating conditions under which the desired vortical structures form from the synthetic jets investigated in the current study for delaying flow separation has been provided.

In more details, the following conclusions related to the specific objectives are drawn:

- *To investigate the effect of dimensionless parameters on the formation and strength of vortex rings produced by synthetic jets, and to establish a parameter map classifying the different regimes of synthetic jets.*

Theoretical analysis of a fully developed laminar oscillating flow issued from an orifice opening indicates that the strength of vortex roll-up is determined by the Stokes number, S, since it affects the thickness of the Stokes layer inside the orifice duct and therefore the shape of velocity profile at the orifice exit. At $S < 10$, the maximum velocity occurs at the centre of the orifice exit hence the leading edge of the vortex sheet is unable to curl due to the axisymmetry and continuum of the flow. Whereas at $S > 10$, a potential core appears at the centre of the orifice, allowing the

vortex sheet to curl and a vortex ring to form. Results of numerical simulations confirm that for an orifice with a finite depth, S also plays an important role in determining the strength of vortex roll-up of a synthetic jet due to the same reason, which is consistent with the findings of theoretical analysis. However, the dimensionless stroke length, L appears to exert less effect on the exit velocity profile than S. Furthermore, based on the computational results, a L-S parameter map has been established, in which the different regimes of synthetic jets classified as no jet, jet formation without vortex roll-up and jet formation with vortex roll-up are identified for the present actuator. It is shown that a minimum S of about 8.5 is required to ensure the occurrence of an appreciable vortex roll-up at $L > 4$. For $L < 4$, the threshold of S for vortex roll-up increases as L decreases. In addition, a very low S can also suppress the formation of synthetic jets even at high L, and the threshold of S for jet formation increases as L decreases. These findings may be useful for designing more effective synthetic jet actuators where vortex roll-up is desired.

- *To study the nature of vortical structures produced by the interaction of a single synthetic jet with an attached laminar boundary layer and their near-wall effects, and to establish a parameter space identifying different types of vortical structures and surface shear stress patterns.*

3D numerical simulation has identified two main types of vortical structures, namely hairpin vortices and tilted vortex rings, from the interaction of a single synthetic jet with a zero-pressure-gradient laminar boundary layer. Hairpin vortices formed at lower velocity ratio embed in the boundary layer for a long time. Therefore, they experience an asymmetric development as the upstream branch of the vortices is cancelled under the influence of resident shear within the boundary layer. The counter-rotating legs of hairpin vortices and their induced streamwise vortices are responsible for producing two streamwise streaks of high surface shear stress downstream of each side of the orifice. Conversely, tilted vortex rings formed at higher velocity ratio penetrate the boundary layer in a short time after they generate from the orifice exit. Therefore, the upstream branch of the initial vortex ring is capable of surviving from the attack of the resident vorticity in the boundary layer such that the vortex ring retains its ring shape, and experiences a symmetric development. Tilted vortex rings consisting of the intact vortex rings, the counter-rotating legs and their induced streamwise vortices produce a single streak of high

surface shear stress directly downstream of the orifice. Non-dimensional parameter maps have been established to illustrate the variations in the appearance of these resultant structures and their shear stress footprints upon the changes in the operating conditions of synthetic jets. In addition, a transitional boundary dividing the regimes of these two types of vortical structures and their corresponding surface shear stress patterns has been identified. It is found that the location of this boundary correlates closely with the jet-to-freestream velocity ratio of VR = 0.4 when the Strouhal number (Str) is less than 1, whereas for $Str > 1$ the boundary deviates from this trend, approaching the line of dimensionless stroke length of L = 1.6.

- *To investigate the nature of vortical structures produced by an array of synthetic jets in a separated laminar boundary layer, the surface shear stress patterns prior to separation, and the relation between the impact of the vortical structures on the boundary layer prior to separation and the separation delay on the inclined plate.*

For an array of three circular synthetic jets issued into a laminar flow that separates further downstream over an inclined plate, two distinct types of vortical structures, i.e. hairpin vortices and tilted vortex rings, are generated by each synthetic jet, which are similar to those observed from a single synthetic jet. The patterns of surface shear stress of each synthetic jet are also consistent with those observed in a single jet. For hairpin vortices, two streaks of high surface shear stress form downstream of each jet, whereas for tilted vortex rings, only one single streak of high surface shear stress is observed downstream of each jet. These patterns of surface shear stress persisting along the horizontal plate upstream to the flap result in a wavy separation line in the separation flow region. The flow patterns in the separation region show a clear correspondence to the upstream surface shear stress patterns. Two streaks of attached flow extruding downstream are associated with the two streaks of high shear stress upstream of the separation region. While three streaks of attached flow are related to the three streaks of high shear stress. Hairpin vortices produce a high space- and time-averaged surface shear stress due to the close proximity of the vortical structures to the wall, while tilted vortex rings produce a high local peak surface shear stress due to their high velocity ratio.

- *To establish a series of parameter maps identifying the transition of vortical*

structures and surface shear stress patterns on the upstream flat plate, the gain of surface shear stress, the flow control effect and the power consumption of the synthetic jet array, to identify the optimal operating conditions of this synthetic jet array which yield the best flow separation delay, and to examine the characteristics of the associated vortical structures and their near-wall effect.

A parameter map illustrating the appearance of the primary vortical structures in the orifice near-field has been established. It can be divided into two regimes; one is characterised by hairpin vortices and the other by tilted vortex rings. The approximate boundary between these two types of vortical structures is located between $VR = 0.5$ and 0.6, with a trend of the boundary moving towards a higher VR at $f > 8$ Hz. The impact of the middle synthetic jet in the array on the boundary layer prior to separation is evaluated by examining the space- and time-averaged surface shear stress. The regions with high surface shear stress increment relative to the baseline case are divided into two zones; one is associated with the appearance of hairpin vortices with $VR < 0.6$, the other is featured by the presence of tilted vortex rings with $VR > 0.8$.

The flow control effect of the middle jet is also quantified by examining the time-averaged location of the separation line. It is found that the hairpin vortex type of structures is capable of delivering a stronger flow control effect than the tilted vortex ring type of structures and this is correlated with the fact that the former also produces a higher surface shear stress increment. By analysing selected cases at two actuation frequencies ($f = 5$ and 9 Hz), it is found that the best flow control effect occurs when the maximum height of the hairpin structures is about that of the boundary layer with their limbs located at about a half of the boundary layer height. Among all the conditions examined in the current study, operating the synthetic jets at $L = 2$ and $VR = 0.36$ which yields hairpin-like structures with a streamwise spacing about 70% of the local boundary layer thickness at the jet orifices is found to produce the best flow control effect with the lowest power consumption. The evidence from this study also suggests that the flow separation delay produced by the synthetic jet array investigated here is due to the accumulated effect of the vortical structures on the boundary layer as they propagate downstream, rather than the local interaction of these structures with the separated flow.

9.2 Recommendations for Future Work

This study has numerically investigated the vortex roll-up of synthetic jets in quiescent conditions and the behaviour of circular synthetic jets in a laminar boundary layer with/without flow separation, including the formed vortical structures, their near-wall effects on the flat plate, the relationship between the impact of these vortical structures on the boundary layer prior to separation and the downstream separation delay, and their flow separation control effect and efficiency. It works as a first logical step towards understanding the fluid mechanics of synthetic jets interacted with a turbulent boundary layer hence there is scope for future development of this research.

Firstly, it is necessary to extend the study to a turbulent boundary layer to verify the hypothesis that the types of vortical structures generated in a turbulent boundary layer are similar to those observed in a laminar flow. Consequently, the existing non-dimensional parameter maps illustrating the type of vortical structures, the surface shear stress patterns, and the flow separation control effectiveness should be extended and shifted to take account of a turbulent flow.

Secondly, the number of synthetic jets in an array should be increased to reduce the side effect and to make the array more representative. The location of the synthetic jet array relative to the baseline separation line, and the spacing between the adjacent synthetic jets should be changeable. Therefore the optimal location and spacing of the synthetic jets can be identified to achieve the best flow separation control effect.

Finally, considering the flow control efficiency of synthetic jets in practical application, the acoustic power studied in the current study is far insufficient. A more detailed analysis on the energy consumption and actuator power efficiency is required in order to develop more effective and efficient synthetic jet actuators for industrial application.

References

Abbott, I.H. and von Doenhoff, A.E.; Theory of Wing Sections; Dover Publications Inc., New York, 1959.

Acarlar, M.S. and Smith, C.R.; A study of hairpin vortices in a laminar boundary layer. Part 1. Hairpin vortices generated by a hemisphere protuberance; Journal of Fluid Mechanics, Vol. 175, pp. 1-41, 1987a.

Acarlar, M.S. and Smith, C.R.; A study of hairpin vortices in a laminar boundary layer. Part 2. Hairpin vortices generated by fluid injection; Journal of Fluid Mechanics; Vol. 175, pp. 43-83, 1987b.

Amitay, M. and Glezer, A.; Role of actuation frequency in controlled flow reattachment over a stalled airfoil; AIAA Journal, Vol. 40, No. 2, pp. 209-216, 2002.

Amitay, M., Kibens, V., Parekh, D. and Glezer, A.; The dynamics of flow reattachment over a thick aerofoil controlled by synthetic jet actuators; AIAA 1999-1001, 37th Aerospace Sciences Meeting & Exhibit, Reno, USA, 11-14 January 1999.

Amitay, M., Honohan, A.M., Trautman, M. and Glezer, A.; Modification of the aerodynamic characteristics of bluff bodies using fluidic actuators; AIAA 1997-2004, 28th Fluid Dynamics Conference, Snowmass Village, USA, 29 June - 2 July 1997.

Amitay, M., Smith, B.L. and Glezer, A.; Aerodynamic flow control using synthetic jet technology; AIAA 1998-0208, 36th Aerospace Sciences Meeting & Exhibit, Reno, USA, 12-15 January 1998.

Amitay, M., Smith, D.R., Kibens, V., Parekh, D.E. and Glezer, A.; Aerodynamic flow control over an unconventional airfoil using synthetic jet actuators; AIAA Journal, Vol. 39, No. 3, pp. 361-370, 2001.

Ashill, P.R., Fulker, J.L. and Hackett, K.C.; Studies of flows induced by subboundary layer vortex generators (SBVGs); AIAA 2002-0968, 40th Aerospace Sciences Meeting & Exhibit, Reno, USA, 14-17 January 2002.

Ashill, P.R., Fulker, J.L. and Hackett, K.C.; A review of recent development in flow control; The Aeronautical Journal, Vol. 109, No. 1095, pp. 205-232, 2005.

Bernard, A., Dupont, P., Foucaut, J.M. and Stanislas, M.; Identification and assessment of flow actuation and control strategies; AEROMEMS report FREP/CN18/MS001101, 2000.

Bremhorst, K. and Hollis, P.; Velocity field of an axisymmetric pulsed, subsonic air jet; AIAA Journal, Vol. 28, No. 12, pp. 2043-2049, 1990.

Carpy, S. and Manceau, R.; Turbulent modelling of statistically periodic flows: Synthetic jet into quiescent air; International Journal of Heat and Fluid flow, Vol. 27, No. 5, pp. 756-767, 2006.

Cater, J.E. and Soria, J.; The evolution of round zero-net-mass-flux jets; Journal of Fluid Mechanics, Vol. 472, pp. 167-200, 2002.

Chakraborty, P., Balachandar, S. and Adrian, R.J.; On the relationships between local vortex identification schemes; Journal of Fluid Mechanics, Vol. 535, pp. 189-214, 2005.

Chang, P.K.; Control of Flow Separation. Energy Conservation, Operational Efficiency and Safety; Hemisphere Publishing, 1976.

Chang, Y.K. and Vakili, A.D.; Dynamic of vortex ring in crossflow; Physics of Fluids, Vol. 7, No. 7, pp. 1583-1597, 1995.

Collis, S.S., Joslin, R.D., Seifert, A. and Theofilis, V.; Issues in active flow control: theory, control, simulation and experiment; Progress in Aerospace Sciences, Vol. 40, No. 4-5, pp. 237-289, 2004.

Comes, L., Crowther, W. and Wood N.; Towards a practical synthetic jet actuator for industrial scale flow control applications; IUTAM Proceedings on Flow Control and MEMS, Kluwer Academic Publishers, 2006.

Crook, A.; The control of turbulent flows using synthetic jets; PhD thesis, University of Manchester, UK, 2002.

Crook, A., Crowther, W.J. and Wood, N.J.; A parametric study of a synthetic jet in a cross flow; 22nd International Congress of Aeronautical Sciences, Harrogate, UK, 2000.

Crook, A., Sadri, A.M. and Wood, N.J.; The development and implementation of synthetic jets for the control of separated flow; AIAA 1999-3176, 17th Applied Aerodynamics Conference, Norfolk, USA, 28 June - 1 July 1999.

Crook, A. and Wood, N.J.; A parametric investigation of a synthetic jet in quiescent conditions; 9th International Symposium on Flow Visualization, Edinburgh, UK, 2000.

Crook, A. and Wood, N.J.; Measurements and visualizations of synthetic jets; AIAA 2001-0145, 39th Aerospace Sciences Meeting & Exhibit, Reno, USA, 8-11 January 2001.

Cui, J., Agarwal, R.K. and Cary, A.W.; Numerical simulation of the interaction of a synthetic jet with a turbulent boundary layer; AIAA 2003-3458, 33rd Fluid Dynamics Conference & Exhibit, Orlando, USA, 23-26 June 2003.

Dandois, J. and Garnier, E.; Unsteady simulation of a synthetic jet in a crossflow; AIAA Journal, Vol. 44, No. 2, pp. 225-238, 2006.

Dandois, J., Garnier, E. and Sagaut, P.; DNS/LES of active separation control by synthetic jets; AIAA 2006-3026, 3rd Flow control conference, San Francisco, USA, 5-8 June 2006.

Delery, J.M.; Shock wave/turbulent boundary layer interaction and its control; Progress in Aerospace Sciences, Vol. 22, No. 4, pp. 209-280, 1985.

Didden, N.; On the formation of vortex rings: Rolling-up and production of circulation; Journal of Applied Mathematics and Physics, Vol. 30, pp. 101-116, 1979.

Dubief, Y. and Delcayre, F.; On coherent-vortex identification in turbulence; Journal of Turbulence, Vol. 1, No. 1, pp. 1-22, 2000.

Fric, T.F. and Roshko, A.; Vortical structure in the wake of a transverse jet; Journal of Fluid Mechanics, Vol. 279, pp. 1-47, 1994.

Fugal, S.R., Smith, B.L. and Spall, R.E.; Displacement amplitude scaling of a two-dimensional synthetic jet; Physics of Fluids, Vol. 17, No. 4, 045103, 2005.

Gad-el-Hak, M.; Flow Control: Passive, Active and Reactive Flow Management; Cambridge University Press, 2000.
Gad-el-Hak, M.; The MEMS handbook (second edition); CRC Press, Boca Raton, 2006.

Gallas, Q., Holman, R., Raju, R., Mittal, R., Sheplak, M. and Cattafesta, L.; Low dimensional modeling of zero-net-mass-flux actuators; AIAA 2004-2413, 2nd AIAA Flow Control Conference, Portland, USA, 28 June – 1 July 2004.

Garcillan, L., Liddle, S., Sunneechurra, K., Crowther, B., Zhong, S. and Wood, N.J.; PIV measurements of the effect of pitch and skew on a circular orifice synthetic jet in a turbulent boundary layer; AIAA 2006-0318, 44th Aerospace Science Meeting & Exhibit, Reno, USA, 9-12 January 2006.

Garcillan, L., Liddle, S., Zhong, S. and Wood, N.J.; Time evolution of the interaction of synthetic jets with a turbulent boundary layer; CEAS/KATnet Conference on Key Aerodynamic Technologies, Bremen, Germany, 20-22 June 2005.

Gharib, M., Rambod, E. and Shariff, K.; A universal time scale for vortex ring formation; Journal of Fluid Mechanics, Vol. 360, pp. 121-140, 1998.

Gilarranz, J.L. and Rediniotis, O.K.; Compact, high-power synthetic jet actuator for flow separation control; AIAA 2001-0737, 39th Aerospace Sciences Meeting & Exhibit, Reno, USA, 8-11 January 2001.

Gilarranz, J.L., Traud, L.W. and Rediniotis, O.K.; A new class of synthetic jet actuators – Part II: Application to flow separation control; Journal of Fluids Engineering, Vol. 127, No. 2, pp. 377-387, 2005.

Glezer, A.; The formation of vortex rings; Physics of Fluids, Vol. 31, No. 9, pp. 3532-3542, 1988.

Glezer, A. and Amitay, M.; Synthetic jets; Annual Review of Fluid Mechanics, Vol. 34, pp. 503-529, 2002.

Glezer, A. and Coles, D.; An experimental study of a turbulent vortex ring; Journal of Fluid Mechanics, Vol. 211, pp. 243-283, 1990.

Godard, G., Foucaut, J.M. and Stanislas, M.; Control of a decelerating boundary layer. Part 2: optimization of slotted jets vortex generators; Aerospace Science and Technology, Vol. 10, pp. 394-400, 2006.

Godard, G. and Stanislas, M.; Control of a decelerating boundary layer. Part3: optimization of round jets vortex generators; Aerospace Science and Technology, Vol. 10, pp. 455-464, 2006a.

Godard, G. and Stanislas, M.; Control of a decelerating boundary layer. Part 1: Optimization of passive vortex generators; Aerospace Science and Technology, Vol. 10, pp. 181-191, 2006b.

Gomes, L., Crowther, W. and Wood N.J.; Towards a practical synthetic jet actuator for industrial scale flow control applications; IUTAM Symposium on Flow Control

and MEMS, Proceedings of the ITUAM Symposium, Vol. 7, London, 19-22 September, 2006.

Gordon, M., Cater, J.E. and Soria, J.; Investigation of the mean passive scalar field in zero-net-mass-flux jets in cross-flow planar-laser-induced fluorescence; Physics of Fluids, Vol. 16, No. 3, pp. 794-808, 2004.

Gordon, M. and Soria, J.; PIV measurement of a zero-net-mass-flux jet in cross flow; Experiments in Fluids, Vol. 33, No. 6, pp. 863-872, 2002.

Greenblatt, D. and Wygnanski, I.J.; The control of flow separation by periodic excitation; Progress in Aerospace Sciences, Vol. 36, No. 7, pp. 487-545, 2000.

Guo, F. and Zhong, S.; A PIV investigation of the characteristics of micro-scale synthetic jets; The Aeronautical Journal, Vol. 111, No. 1122, pp. 509-518, 2007. (Also presented as AIAA 2006-3183 at the 3rd Flow Control Conference, San Francisco, USA, 5-8 June 2006.)

Haidari, A.H. and Smith, C.R.; The generation and regeneration of single hairpin vortices; Journal of Fluid Mechanics, Vol. 277, pp. 135-162, 1994.

Harrison, T.J.; Separation control on high lift systems using vane vortex generators; PhD thesis, School of Mechanical, Aerospace and Civil Engineering, University of Manchester, UK, 2006.

Head, M.R. and Bandyopadhyay, P.; New aspects of turbulent boundary layer structures; Journal of Fluid Mechanics, Vol. 107, pp. 297-338, 1981.

Holman, R., Utturkar, Y., Mittal, R., Smith, B.L. and Cattafesta, L.; Formation criterion for synthetic jets; AIAA Journal, Vol. 43, No. 10, pp. 2110-2116, 2005.

Hong, G., Lee, C., Ha, Q.P., Mack, A. and Mallinson, S.; Effectiveness of synthetic jets enhanced by instability of Tollmien-Schlichting waves; AIAA 2002-2832, 1st Flow Control Conference, St. Louis, USA, 24-26 June 2002.

Hull, D.G.; Fundamentals of Airplane Flight Mechanics; Springer, 2007.

Hunt, J.C.R., Wray, A.A. and Moin, P.; Eddies, stream, and convergence zones in turbulent flows; In proceedings of the 1988 Summer Program of the Center for Turbulence Research, pp. 193-207, NASA Ames/Stanford University, 1988.

Ingard, U. and Labate, S.; Acoustic circulation effects and the nonlinear impedance of orifices; Journal of The Acoustical Society of America; Vol. 22, No. 2, pp. 211-218, 1950.

Jabbal, M.; Understanding the behaviour of synthetic jets in a boundary layer for flow separation control; PhD thesis, School of Mechanical, Aerospace and Civil Engineering, University of Manchester, UK, 2008.

Jabbal, M., Liddle, S.C. and Crowther, W.J.; Modelling the costs of implementing active flow control systems on civil transport aircraft; CEAS/KATnet II Conference on Key Aerodynamic Technologies, Bremen, 12-14 May 2009.

Jabbal, M., Wu, J. and Zhong, S.; The performance of round synthetic jets in quiescent flow; The Aeronautical Journal, Vol. 110, No. 1108, pp. 385-393, 2006.

Jabbal, M. and Zhong, S.; Flow measurement of synthetic jets in a boundary layer; AIAA 2007-3852, 37th AIAA Dynamics Conference & Exhibit, Miami, 25-28 June 2007.

Jabbal, M. and Zhong, S.; The near wall effect of synthetic jets in a boundary layer; International Journal of Heat and Fluid Flow, Vol. 29, No. 1, pp. 119-130, 2008.

Jeong, J. and Hussain, F.; On the identification of a vortex; Journal of Fluid Mechanics, Vol. 285, pp. 69-94, 1995.

Johari, H. and McManus, K.R.; Visualization of pulsed vortex generator jets for active control of boundary layer separation; AIAA 1997-2021, 28th Fluid Dynamics Conference, Snowmass Village, USA, 29 June - 2 July 1997.

Johari, H. and Rixon, G.S.; Effect of pulsing on a vortex generator jet; AIAA Journal, Vol. 41, No. 12, pp. 2309-2315, 2003.
Johnston, J.P. and Nishi, M.; Vortex generator jets – means for flow separation control; AIAA Journal, Vol. 28, No. 6, pp. 989-994, 1990.

Kelso, R.M.; Lim, T.T. and Perry, A.E.; An experimental study of round jets in cross-flow; Journal of Fluid Mechanics, Vol. 306, pp. 111-144, 1996.

Khodadoust, A. and Washburn, A.; Active flow control on a high-lift system with slotted flap at high Reynolds number; AIAA 2007-4424, 25th AIAA Applied Aerodynamics Conference, Miami, USA, 25-28 June 2007.

Kim, J., Moin, P. and Moser, R.; Turbulent statistics in fully developed channel flow at low Reynolds number; Journal of Fluid Mechanics, Vol. 177, pp. 133-166, 1987.

Kim, S.H. and Kim, C.; Separation control on NACA23012 using synthetic jet; Aerospace Science and Technology, Vol. 13, No. 4-5, pp. 172-182, 2009.

Kolář, Václav.; Vortex identification: New requirements and limitations; International Journal of Heat and Fluid Flow, Vol. 28, No. 4, pp. 638-652, 2007.

Kostas, J., Foucaut, J.M. and Stanislas, M.; The effects of pulse frequency and duty cycle on the skin friction downstream of pulsed jet vortex generators in an adverse pressure gradient turbulent boundary layer; Aerospace Science and Technology, Vol. 13, No. 1, pp. 36-48, 2009.

Kotapati, R.B. and Mittal, R.; Time-accurate three-dimensional simulations of synthetic jets in quiescent air; AIAA paper 2005-0103, 43rd AIAA Aerospace Sciences Meeting & Exhibit, Reno, USA, 10-13 Jan 2005.

Kotapati, R.B., Mittal, R. and Cattafesta, L.N.; Numerical study of a transitional synthetic jet in quiescent external flow; Journal of Fluid Mechanics, Vol. 581, pp. 287-321, 2007.

Kral, L.D.; Active flow control technology; ASME Fluids Engineering Technical Brief, 2000.

Kral, L.D., Donovan, J.F., Cain, A.B. and Cary, A.W.; Numerical simulation of synthetic jet actuators; AIAA 1997-1824, 4th Shear Flow Control Conference, Snowmass Village, USA, 29 June – 2 July 1997.

Lachmann, G.V.; Boundary Layer and Flow Control: Its Principles and Application. Vol. 1; Pergrmon Press, 1961.

Lawrence, P.; Meeting the challenge of aviation emissions: an aircraft industry perspective; Technology Analysis & Strategic Management, Vol. 21, No. 1, pp. 79-92, 2009.

Lee, C.Y. and Goldstein, D.B.; Two-dimensional synthetic jet simulation; AIAA Journal, Vol. 40, No. 3, pp. 510-516, 2002.

Lesbros, S., Ozawa, T. and Hong, G.; Numerical modelling of synthetic jets with cross flow in a boundary layer at an adverse pressure gradient; AIAA 2006-3690, 3rd Flow Control Conference, San Francisco, USA, 5-8 June 2006.

Liddle, S.C.; The use of synthetic jet actuators to enhance deflected surface controls; PhD thesis, School of Mechanical, Aerospace and Civil Engineering, University of Manchester, UK, 2007.

Liddle, S.C. and Crowther, W.J.; Systems and certification issues for active flow control systems for separation control on civil transport aircraft; AIAA 2008-518, 46th Aerospace Sciences Meeting & Exhibit, Reno, USA, 7-10 January 2008.

Liddle, S.C. and Wood, N.J.; Investigation into clustering of synthetic jet actuators for flow separation control applications; The Aeronautical Journal, Vol. 109, No. 1091, pp. 35-44, 2005.

Lighthill, M.J.; Introduction: Boundary layer theory. In: Laminar boundary layer theory; Oxford University Press, Oxford, 1963.

Lim, T.; On the role of Kelvin-Helmholtz-like instability in the formation of turbulent vortex rings; Fluid Dynamics Research, Vol. 21, No. 1, pp. 47-56, 1997.

Lin, J.C.; Control of turbulent boundary-layer separation using micro-vortex generators; AIAA 1999-3404, 30th Fluid Dynamics Conference, Norfolk, USA, 28 June - 1 July, 1999.

Lin, J.C.; Review of research on low-profile vortex generators to control boundary-layer separation; Progress in Aerospace Sciences, Vol. 38, No. 4-5, pp. 389-420, 2002.

Lin, J.C. and Howard, F.G.; Turbulent flow separation control through passive techniques; AIAA 1989-0976, 2nd Shear Flow Conference, Temp AZ, USA, 13-16 March 1989.

Lin, J.C., Howard, F.G. and Bushnell, D.M.; Investigation of several passive and active methods for turbulent flow separation control; AIAA 1990-1598, 21st Fluid Dynamics, Plasma Dynamics & Laser Conference, Seattle, USA, 18-20 June 1990.

Lin, J.C., Robinson, S.K., McGhee, R.J. and Valarezo, W.O.; Separation control on high-lift airfoils via micro-vortex generators; Journal of Aircraft, Vol. 31, No. 6, pp. 1317-1323, 1994.

Lin, J.C., Selby, G.V. and Howard, F.G.; Exploratory study of vortex-generating devices for turbulent flow separation control; AIAA 1991-0042, 29th Aerospace Sciences Meeting, Reno, USA, 7-10 January 1991.

Lombardo, D.; Advanced Aircraft Systems; McGraw-Hill, 1993.

Magill, J.C. and McManus, K.R.; Exploring the feasibility of pulsed jet separation control for aircraft configurations; Journal of Aircraft, Vol. 38, No. 1, pp. 48-56, 2001.

Mallinson, S.G., Hong, G. and Reizes, J.A.; Some characteristics of synthetic jets; AIAA 1999-3651, 30th Fluid Dynamics Conference, Norfolk, USA, 28 June – 1 July 1999.

Mallinson, S.G., Reizes, J.A. and Hong, G.; An experimental and numerical study of synthetic jet flow; The Aeronautical Journal, Vol. 105, No. 1043, pp. 41-49, 2001.

MaManus, K. and Magill, J.; Separation control in incompressible and compressible flows using pulsed jets; AIAA 1996-1948, 27th Fluid Dynamics Conference, New Orleans, USA, 17-20 June 1996.

McCormick, D.C.; Boundary layer separation control with directed synthetic jets; AIAA 2000-0519, 38th Aerospace Sciences Meeting & Exhibit, Reno, USA, 10-13 January 2000.

Milanovic, I.M. and Zaman, K.B.M.Q.; Synthetic jets in crossflow; AIAA Journal, Vol. 43, No. 5, pp. 929-940, 2005.

Milanovic, I.M., Zaman, K.B.M.Q. and Rumsey, C.L.; An isolated circular synthetic jet in crossflow at low momentum-flux ratio; AIAA 2005-1110, 43rd Aerospace Sciences Meeting & Exhibit, Reno, USA, 10-13 January 2005.

Mittal, R., Rampunggoon, R. and Udaykumar, H.S.; Interaction of a synthetic jet with a flat plate boundary layer; AIAA 2001-2773, 31st Fluid Dynamics Conference & Exhibit, Anaheim, USA, 11-14 June 2001.

Moin, P. and Bewley, T.; Feedback control of turbulence; Applied Mechanics Reviews. Vol. 47, No. 6, pp. S3-S13, 1994.

Müller, M.O., Bernal, L.P., Miska, P.K., Washabaugh, P.D., Chou, T-K.A., Parviz, B.A., Zhang, C. and Najafi, K.; Flow structure and performance of axisymmetric synthetic jets; AIAA 2001-1008, 39th Aerospace Sciences Meeting & Exhibit, Reno, USA, 8-11 January, 2001.

Prandtl, L.; Über Flüssigkeitbewegung bei sehr kleiner Reibung (On the motion of fluid with very small viscosity); Proceedings of the 3rd International Mathematical Congress, Heidelberg, Germany, pp. 484-491, 1904.

Pullin, D.I.; Vortex ring formation at tube and orifice openings; Physics of Fluids, Vol. 22, No. 3, pp. 401-403, 1979.

Raju, R., Gallas, Q., Mittal, R., and Cattafesta, L.; Scaling of pressure drop for oscillatory flow through a slot; Physics of Fluids, Vol. 19, No. 7, pp. 078107-1-4, 2007.

Raju, R., Mittal, R., Gallas, Q. and Cattafesta, L.; Scaling of vorticity flux and entrance length in zero-net mass-flux devices; AIAA 2005-4751, 35th Fluid Dynamics Conference & Exhibit, Toronto, Canada, 6-9 June 2005.

Rao, D.M. and Kariya, T.T.; Boundary-layer submerged vortex generators for separation control – An exploratory study; AIAA 1988-3546, ASME, SIAM, and APS, 1st National Fluid Dynamics Congress, Cincinnati, USA, 25-28 July 1988.

Rathnasingham, R. and Breuer, K.S.; Coupled fluid-structural characteristics of actuators for flow control; AIAA Journal, Vol. 35, No. 5, pp. 832-837, 1997.

Rathnasingham, R. and Breuer, K.S.; Active control of turbulent boundary layers; Journal of Fluid Mechanics, Vol. 495, pp. 209-233, 2003.

Ravi, B.R., Mittal, R. and Najjar, F.M.; Study of three-dimensional synthetic jet flowfields using direct numerical simulation; AIAA 2004-91, 42nd AIAA Aerospace Sciences Meeting & Exhibit, Reno, USA, 5-8 January 2004.

Rediniotis, O.K., Ko, J., Yue, X. and Kurdila, A.J.; Synthetic jets, their reduced order modelling and applications to flow control; AIAA 1999-1000, 37th Aerospace Sciences Meeting & Exhibit, Reno, USA, 11-14 January 1999.

Rehman, A. and Kontis, K.; Synthetic jet control effectiveness on stationary and pitching airfoils; Journal of Aircraft, Vol. 43, No. 6, pp. 1782-1789, 2006.

Reneaux, J.; Overview on drag reduction technologies for civil transport aircraft; European Congress on Computational Methods in Applied Sciences and Engineering, Jyväskylä, Finland, 24-28 July 2004.

Ritchie, B.D., Mujumdar, D.R. and Seitzman, J.M.; Mixing in coaxial jets using synthetic jet actuators; AIAA 2000-404, 38th Aerospace Sciences Meeting & Exhibit, Reno, USA, 10-13 January 2000.

Rizzetta, D.P., Visbal, M.R. and Stanek, M.J.; Numerical investigation of synthetic-jet flowfields; AIAA Journal, Vol. 37, No. 8, pp. 919-927, 1999.

Robinson, S.K.; Coherent motions in the turbulent boundary layer; Annual Review of Fluid Mechanics, Vol. 23, pp. 601-639, 1991.

Rosenfeld, M., Rambod, E. and Gharib, M.; Circulation and formation number of laminar vortex rings; Journal of Fluid Mechanics, Vol. 376, pp. 297-318, 1998.

Rudolph, P.K.C.; High-lift systems on commercial subsonic airlines; NASA CR 4746 report, 1996.

Rumsey, C.L., Gatski, T.B., Sellers, W.L., Vatsa, V.N. and Viken, S.A.; Summary of the 2004 CFD validation workshop on synthetic jets and turbulent separation control; AIAA 2004-2217, 2nd Flow Control Conference, Portland, USA, 28 June – 1 July 2004.

Rumsey, C.L., Gatski, T.B., Seller, W.L., Vatsa, V.N. and Viken, S.A.; Summary of the 2004 computational fluid dynamics validation workshop on synthetic jets; AIAA Journal, Vol. 44, No. 2, pp. 194-207, 2006.

Rumsey, C.L., Schaeffler, N.W., Milanovic, I.M. and Zaman, K.B.M.Q.; Time-accurate computations of isolated circular synthetic jets in crossflow; Computers and Fluids, Vol. 36, No. 6, pp. 1092-1105, 2007. (Also presented as AIAA 2005-5016 at the 35th Dynamics Conference & Exhibit, Toronto, Canada, 6-9 June 2005).

Sau, R. and Mahesh, K.; The effect of crossflow on vortex rings; AIAA 2007-1316, 45th Aerospace Sciences Meeting & Exhibit, Reno, USA, 8-11 January 2007.

Scglichting, H. and Gersten, K.; Boundary Layer Theory; Springer, 2000.

Schaeffler, N.W.; The interaction of a synthetic jet and a turbulent boundary layer; AIAA 2003-0643, 41st Aerospace Sciences Meeting & Exhibit, Reno, USA, 6-9 January, 2003.

Schaeffler, N.W. and Jenkins, L.N.; The isolated synthetic jet in crossflow: A benchmark for flow control simulation; AIAA 2004-2219, 2nd Flow Control Conference, Portland, USA, 28 June – 1 July 2004.

Schlichting, H.; Boundary-Layer Theory; McGraw-Hill, 1979.

Seifert, A., Bachar, T., Koss, D., Shepshelovich, M. and Wygnanski, I.; Oscillatory blowing, a tool to delay boundary layer separation; AIAA Journal, Vol. 31, No. 11, pp. 2052-2060, 1993.

Seifert, A., Darabi, A. and Wygnanski, I.; Delay of airfoil stall by periodic excitation; Journal of Aircraft, Vol. 33, No. 4, pp. 691-698, 1996.

Seifert, A., Greenblatt, D. and Wygnanski, I., Active separation control: an overview of Reynolds and Mach numbers effect; Aerospace Science and Technology, Vol. 8, No. 7, pp. 569-582, 2004.

Seifert, A. and Pack, L.G.; Oscillatory control of separation at high Reynolds numbers; AIAA Journal, Vol. 37, No. 9, pp. 1062-1071, 1999.

Seller, W.L. and Rumsey, C.L.; http://cfdval2004.larc.nasa.gov, 2004.

Shariff, K. and Leonard, A.; Vortex rings; Annual Review of Fluid Mechanics, Vol. 24, pp. 235-279, 1992.

Shuster, J.M., Pink, R.J., McEligot, D.M. and Smith, D.R.; The interaction of a circular synthetic jet with a cross-flow boundary layer; AIAA 2005-4749, 35th Fluid Dynamics Conference & Exhibit, Toronto, Canada, 6-9 June, 2005.

Shuster, J.M. and Smith, D.R.; A study of the formation and scaling of a synthetic jet; AIAA 2004-90, 42nd Aerospace Sciences Meeting & Exhibit, Nevada, USA, 5-8 January 2004.

Shuster, J.M. and Smith, D.R.; Experimental study of the formation and scaling of a round synthetic jet; Physics of Fluids, Vol. 19, No. 4, 045109, 2007.

Simpson, R.L.; Junction flows; Annual Review of Fluid Mechanics, Vol. 33: pp. 415-433, 2001.

Smith, B.L. and Glezer, A.; Vectoring and small-scale motions effected in free shear flows using synthetic jet actuators; AIAA 1997-213, 35th Aerospace Science Meeting & Exhibit, Reno, USA, 6-9 January 1997.

Smith, B.L. and Glezer, A.; The formation and evolution of synthetic jets; Physics of Fluids, Vol. 10, No. 9, pp. 2281-2297, 1998.

Smith, B.L. and Glezer, A.; Jet vectoring using synthetic jet actuators; Journal of Fluid Mechanics, Vol. 458, pp. 1-34, 2002.

Smith, B.L. and Swift, G.W.; Synthetic jets at large Reynolds number and comparison to continuous jets; AIAA 2001-3030, 31st AIAA Fluid Dynamics Conference & Exhibit, Anaheim, USA, 11-14 June 2001.

Smith, B.L. and Swift, G.W.; A comparison between synthetic jets and continuous jets; Experiments in Fluids, Vol. 34, pp. 467-472, 2003.

Smith, B.L., Trautman, M.A. and Glezer, A.; Controlled interactions of adjacent synthetic jets; AIAA 1999-0669, 37th Aerospace Sciences Meeting & Exhibit, Reno, USA, 11-14 January 1999.

Smith, C.R.; A synthesized model of the near-wall behavior in turbulent boundary layers; Proceedings of 8th Biennial Symposium on Turbulence, University of Missouri-Rolla, 1984.

Smith, C.R., Walker, J.D.A., Haidari, A.H. and Sobrun, U.; On the dynamics of near-wall turbulence; Philosophical Transactions: Physical Sciences and Engineering, Vol. 336, No. 1641, pp. 131-175, 1991.

Smith, D.R.; Interaction of a synthetic jet with a crossflow boundary layer; AIAA Journal, Vol. 40, No. 11, pp. 2277-2288, 2002.

Smith, D.R., Amitay, M., Kibens, V., Parekh, D. and Glezer, A.; Modification of lifting body aerodynamics using synthetic jet actuators; AIAA 1998-0209, 36th Aerospace Sciences Meeting & Exhibit, Reno, USA, 12-15 January 1998.

Spencer, R.F., Smith, B.L., and Spall, R.E.; A numerical study of 2-D synthetic jet formation; 2004 ASME Heat Transfer/Fluid Engineering Summer Conference paper HT-FED2004-56854, USA, July 2004.

Stanek, M.J., Raman, G., Ross, J.A., Odedra, J., Peto, J., Alvi, F. and Kibens, V.; High frequency acoustic suppression – The role of mass flow & The notion of superposition; AIAA 2002-2404, 8th AIAA/CEAS Aeronautics Conference & Exhibit, Breckenridge, USA, 17-19 June, 2002.

Stanek, M.J., Sinha, N., Senier, J.M., Pearce, B. and Jones, M.I.; Applying very high frequency excitation to the problem of tactical directed energy beam propagation; AIAA paper 2002-2272, 33rd Plasmadynamics & Laser Conference, Maui, USA, 20-23 May, 2002.

Swift, G.W.; Thermoacoustics: A unifying perspective for some engines and refrigerators; Acoustical Society of America, New York, 2002.

Tang, H.; Performance modelling of synthetic jet actuators for flow separation control; PhD thesis, School of Mechanical, Aerospace and Civil Engineering, University of Manchester, UK, 2006.

Tang, H., and Zhong, S.; The effect of actuator geometry on the performance of synthetic jets; CEAS/KATnet Conference on Key Aerodynamic Technologies, Bremen, Germany, June 2005a.

Tang, H. and Zhong, S.; 2D numerical study of circular synthetic jets in quiescent conditions; The Aeronautical Journal, Vol. 109, No. 1092, pp. 89-97, 2005b.

Tang, H. and Zhong, S.; Incompressible flow model of synthetic jet actuators; AIAA Journal, Vol. 44, No. 4, pp. 908-912, 2006.

Tang, H., Zhong, S., Jabbal, M., Guo, F., Garcillan, L., Wood, N. and Warsop, C.; Towards the design of synthetic jet actuators for full-scale flight conditions – part 2: low-dimensional performance prediction models and actuator design method; Flow, Turbulence and Combustion, Vol. 78, No. 3, pp. 309-329, 2007.

Taylor, H.D.; Application of vortex generator mixing principles to diffusers; Research Department Concluding Report No. R-15064-5, United Aircraft Corporation, 1948.

Tensi, J., Boue, I., Paille, F., Dury, G.; Modification of the wake behind a circular cylinder by using synthetic jets; Journal of visualization, Vol. 5, No. 1, pp. 37-44, 2002.

Theodorsen, T.; Mechanism of turbulence; Proceedings Second Midwestern Conference on Fluid Mechanics, Ohio State University, Columbus, Ohio, pp. 1-19, 1952.

Utami, T. and Ueno, T.; Experimental study on the coherent structure of turbulent open-channel flow using visualisation and picture processing; Journal of Fluid Mechanics, Vol. 174, pp. 399-440, 1987.

Utturkar, Y.; Holman, R., Mittal, R., Carroll, B., Sheplak, M. and Cattafesta, L.; A jet formation criterion for synthetic jet actuators; AIAA 2003-636, 41st Aerospace Sciences Meeting & Exhibit, Reno, USA, 6-9 January 2003.

Utturkar, Y. and Mittal, R.; Sensitivity of synthetic jets to the design of the jet cavity; AIAA 2002-124, 40th Aerospace Sciences Meeting & Exhibit, Reno, USA, 14-17 January 2002.

Vatsa, V.N. and Turker, E.; Simulation of synthetic jets using unsteady Reynolds averaged Navier-Stokes equations; AIAA 2004-4967, 22nd Applied Aerodynamics Conference & Exhibit, Providence, USA, 16-19 August 2004.

Viswanath, P.R.; Shockwave-turbulent boundary layer interaction and its control: A survey of recent developments; Sadhana, Vol. 12, No. 1-2, pp. 45-104, 1988.

Wallis, R.A.; The use of air jets for boundary layer control; Aerodynamics Research Laboratories, Australia, Aero Note 110, 1952.

Warsop, C.; MEMS and Microsystems technologies – their potential and status for drag reduction and separation control; European Congress on Computational Methods in Applied Science and Engineering (ECCOMAS), Jyväskylä, Finland, 24-28 July 2004.

Warsop, C., Hucker, M., Press, A.J. and Dawson, P.; Pulsed air-jet actuators for flow separation control; Flow, Turbulence and Combustion, Vol. 78, Nos. 3-4, pp. 255-281, 2007.

Watson, M., Jaworski, A.J. and Wood, N.J.; Contribution to the understanding of flow interactions between multiple synthetic jets; AIAA Journal, Vol. 41, No. 4, pp. 747-749, 2003.

Widnall, S.E., Bliss, D.B. and Tsai, C.Y. The instability of short waves on a vortex ring; Journal of Fluid Mechanics, Vol. 66, pp. 35-47, 1974.

Wilson, R.W. and Demuren, A.O.; Numerical simulation of turbulent jets with rectangular cross section; NASA CR-201642 ICASE Report No. 97-1, 1997.

Wood, N.J., Sadri, A.M. and Crook, A.; Control of turbulent flow separation by synthetic jets; AIAA 2000-4331, 18th AIAA Applied Aerodynamics Conference, Denver, USA, 14-17 August 2000.

Wu, D.K.L., and Leschziner, M.A.; Large-eddy simulation of synthetic jets in stagnant surroundings and turbulent cross-flow; IUTAM Symposium on Flow Control and MEMS, Proceedings of the ITUAM Symposium, Vol. 7, London, 19-22 September, 2006.

Wu, D.K.L. and Leschziner, M.A.; Large-eddy simulation of circular synthetic jets in quiescent surroundings and in turbulent cross-flow; International Journal of Heat and Fluid Flow; Vol. 30, No. 3, pp. 421-434, 2009.

Wu, J.Z., Xiong, A.K. and Yang, Y.T.; Axial stretching and vortex definition; Physics of Fluids, Vol. 17, No. 3, 038108, 2005.

Yao, C.S., Chen, F.J., Neuhart, D. and Harris, J.; Synthetic jets flow field database for CFD validation; AIAA 2004-2218, 2nd Flow Control Conference, Portland, USA, 28 June – 1 July 2004.

Zhang, S. and Zhong, S.; Experimental investigation of flow separation control using an array of synthetic jets; AIAA Journal, Vol. 48, No. 3, pp. 611-623, 2010a.(Also presented as AIAA 2009-4185 at the 39th Fluid Dynamics Conference, Texas, USA, 22-25 June 2009).

Zhang S. and Zhong, S.; Turbulent floe separation control by an array of synthetic jets; AIAA 2010-4582, 5th Flow Control Conference, Chicago, USA, 28 June-1 July 2010b.

Zhang, X. and Collins, M.W.; Flow and heat transfer in a turbulent boundary layer through skewed and pitched jets; AIAA Journal, Vol. 31, No. 9, pp. 1590-1599, 1993.

Zhong, S., Garcillan, L., Pokusevski, Z. and Wood, N.J.; A PIV study of synthetic jets with different orifice shape and orientation; AIAA 2004-2213, 2nd Flow Control Conference, Portland, USA, 28 June – 1 July 2004.

Zhong, S., Jabbal, M., Tang, H., Garcillan, L., Guo, F., Wood, N.J. and Warsop, C.; Towards the design of synthetic-jet actuators for full-scale flight conditions. Part 1: The fluid mechanics of synthetic-jet actuators; Flow, Turbulence and Combustion, Vol. 78, No. 3, pp 283-307, 2007.

Zhong, S., Millet, F. and Wood, N.J.; The behaviour of circular synthetic jets in a laminar boundary layer; The Aeronautical Journal, Vol. 109, No. 1100, pp. 461-470, 2005.

Zhou, J., Adrian, R.J., Balachandar, S. and Kendall, T.M.; Mechanisms for generating coherent packets of hairpin vortices in channel flow; Journal of Fluid Mechanics, Vol. 387, pp. 353-396, 1999.

Zhou, J., Tang, H. and Zhong, S.; Vortex roll-up criterion for synthetic jets; AIAA Journal, Vol. 47, No. 5, pp. 1252-1262, 2009.

Zhou, J. and Zhong, S.; Numerical simulation of the interaction of a circular synthetic jet with a boundary layer; Computers and Fluids, Vol. 38, No. 2, 393-405, 2009.

Zhou, J. and Zhong, S.; Coherent structures produced by the interaction between synthetic jets and a laminar boundary layer and their surface shear stress patterns; Computers and Fluids, Vol. 39, No. 8, 1296-1313, 2010a.

Zhou, J. and Zhong, S.; A numerical investigation of the interaction of an array of synthetic jets with a separated boundary layer; Under review by Computers and Fluids 2010b.